Technische Universität München
Institut für Energietechnik

Lehrstuhl für Thermodynamik

On Eulerian-Eulerian Large Eddy Simulation of Polydispersed, Reacting Spray Flows with Moment Methods

Patrick Dems

Vollständiger Abdruck der von der Fakultät für Maschinenwesen der Technischen Universität München zur Erlangung des akademischen Grades eines

DOKTOR – INGENIEURS

genehmigten Dissertation.

Vorsitzender:
Univ.-Prof. Dr.-Ing. Georg Wachtmeister
Prüfer der Dissertation:
1. Univ.-Prof. Wolfgang Polifke, Ph.D.
2. Univ.-Prof. Dr. rer. nat. Amsini Sadiki
Technische Universität Darmstadt

Die Dissertation wurde am 10. September 2014 bei der Technischen Universität München eingereicht und durch die Fakultät für Maschinenwesen am 03. Dezember 2014 angenommen.

Vorwort

Diese Arbeit entstand während meiner Zeit als Wissenschaftlicher Mitarbeiter am Lehrstuhl für Thermodynamik der Technischen Universität München im Rahmen der zweiten Phase der Forschungsinitiative 'Kraftwerke des 21. Jahrhunderts' (KW21) des Landes Baden-Württemberg und des Freistaates Bayern, finanziert durch das Ministerium für Wissenschaft, Forschung und Kunst Baden-Württemberg, dem Bayerischen Staatsministerium für Wissenschaft, Forschung und Kunst, dem Bayerischen Staatsministerium für Wissenschaft, Infrastruktur, Verkehr und Technologie sowie dem Teilprojekt zugehörigen Industriepartner ALSTOM Power Systems GmbH Mannheim.

Herrn Professor Polifke gilt mein ganz besonderer Dank für die Betreuung der Arbeit, für die Freiheiten bei der Wegfindung und das entgegengebrachte Vertrauen, dass so manche, scheinbar ergebnislose Phase dennoch für das Weiterkommen notwendig war. Herrn Professor Dr. rer. nat. Amsini Sadiki danke ich für die freundliche Übernahme des Co-Referates sowie Herrn Professor Dr.–Ing. Georg Wachtmeister für die Abwicklung des Promotionsprozesses und die Übernahme des Vorsitzes bei der mündlichen Prüfung.

Mein Dank gilt auch meinen Kolleginnen und Kollegen die sich trotz des teils abstrakten und fremden Themas wohlwollende Mühe gegeben haben mich in der ein oder anderen Fragestellung zu unterstützen. Insbesondere möchte ich mich bei Joao Carneiro bedanken, der mich als seinen Nachfolger in das Thema eingeführt und für die Problematiken des Momententransportes sensibilisiert hat, sowie Gary Jasor (mein Mathematiker) und Thomas Acher für die fachlichen Diskussionen und die Zusammenarbeit. Des Weiteren Frederik Collonval und Johannes Weinzierl für die wertvollen Tipps und den Erfahrungsaustausch bzgl. OpenFOAM sowie Alejandro Cardenas für die wesentliche Hilfe bei der Installation und dem Betrieb des Rechenclusters. Schlussendlich meinen Bürokollegen Christoph Jörg für das erfrischende Nachsinnen über die

"Master-Frage des Tages" und die gegenseitigen Mitleidsbekundungen beim Schreiben und Thomas Fiala für die Grundversorgung mit Knoppers und Schokolade.

München, im Januar 2015 Patrick Dems

Kurzfassung

Die vorliegende Arbeit leistet einen Beitrag zu der Herausforderung einen geeigneten Ansatz für die Grobstruktursimulation (Large Eddy Simulation) von polydispersen Sprayströmungen mit und ohne chemische Reaktion zu finden und zu etablieren. Hierbei wird zunächst ein stochastischer Ansatz verwendet, der die Partikelpopulation mit Hilfe einer Anzahldichtefunktion (NDF) über dem Eigenschaftsraum der Partikel (Grösse, Geschwindigkeit, Temperatur) beschreibt. Diese basiert auf einer theoretisch unendlichen Anzahl von Strömungsrealisierungen der Partikel für eine gegebene Realisierung der Gasphasenströmung. Die Transportgleichung der NDF wird zunächst räumlich gefiltert um der numerischen Methode Rechnung zu tragen sowie anschliessend über den Eigenschaftsraum integriert.

Zur Schliessung der unbekannten Terme, die sowohl die Partikeldynamik selbst als auch die Wechselwirkung mit der Gasphase betreffen, wird eine Momentenmethode basierend auf einer angenommenen Form der NDF angewendet. Hierbei werden drei bis vier Momente der NDF mit individuellen Geschwindigkeiten transportiert, welche wiederum durch einen Relaxationszeitansatz bestimmt werden. Die Verbrennung wird mit einer für Zweiphasenströmungen angepassten Variante des Thickend-Flame Model sowie einem einfachen Arrheniusansatz für die Chemie beschrieben. Zusätzlich wird ein für die Momentenmethode formulierter Ansatz der Einzeltropfenverbrennung vorgeschlagen.

Die mit OpenFOAM realisierten Simulationen zeigen für den polydispersen Ansatz bessere Ergebnisse für Spraydynamik und -verdampfung im Vergleich zu monodispersen Ergebnissen. Hierbei wurde eine Drallströmung sowie ein Partikel-beladener Freistrahl untersucht. Die Anwendbarkeit für polydisperse Sprayverbrennung wird nachgewiesen; das vergleichsweise einfache Modell offenbart jedoch grossen Bedarf an fortgeschritteneren Modellen und weiterer Forschungsarbeit. Dasselbe gilt für die Thematik der Partikel-Turbulenzinteraktion.

Abstract

The present work contributes to the challenge of finding and establishing an appropriate approach for the Large Eddy Simulation of polydisperse spray flows with and without chemical reaction. First, a stochastic approach is adopted which describes the particle population with the help of a number density function (NDF) spanned over the particle phase space including particle size, velocity and temperature. It is gained from a theoretical infinite number of particle phase realisations for a given flow realisation of the gas phase. The transport equation of the NDF is then spatially filtered due to the numerical method applied and subsequently integrated over the particle phase space.

For closure of the unknown terms, which are related to the dynamics of the particles itself but also their interaction with the gas phase, a moment method is applied, which presumes a certain type of the shape of the NDF. The temporal and spatial development of the NDF is calculated by transporting up to four moments of the NDF, each with its respective moment transport velocity. The latter are determined from a relaxation time approach. An adapted Thickened-Flame Model in conjunction with a simple Arrhenius mechanism is used to model the combustion. Additionally a method is proposed for single droplet combustion, which is adapted to be applicable in the framework of the moment model.

The numerical simulations are realised with OpenFOAM. A swirling flow configuration and a particle-laden jet have been investigated. Results obtained from the polydisperse approach show improved spray dynamics and evaporation rates compared to those resulting from a monodisperse description. The applicability of the combustion model is verified, however, the simplicity of the model demonstrates the need for more sophisticated approaches and further extensive research in this field. The same is true for the particle-turbulence interaction.

Contents

Nomenclature

Some indices, which does occur only once in combination with a specific quantity are not listed here separately but explained then. Different meanings for the same variable are separated with ";". For quantities, whose units depend on the associated index or superscript, the unit entry is noted as [var].

Latin Characters

B	Beta function
$\delta\mathbf{BB}_d$	Particle velocity correlations, also $\delta\mathbf{BC}_d$, $\delta\mathbf{CC}_d$ [$\mathrm{m}^2/\mathrm{s}^2$]
c_P	Specific heat capacity [$\mathrm{J}/(\mathrm{kg\,K})$]
$\mathbf{c}_p, c_p$	Velocity coordinate vector (components) of $\mathcal{I}$ [m/s]
dds	Droplet-droplet spacing (quantity) [m]
D	(Particle) diameter; size coordinate of $\mathcal{I}$ [m]
D_{ab}	Mean diameter [m]
e	Specific inner energy [J/kg]; Euler number [-]
$\mathbf{e}, e$	Unit vector (component) of spatial coordinates [m]
E	Specific total energy (without chemical energy) [J/kg]
$\mathbf{E}, \mathbf{F}$	Efficiency and thickening factor of the TFM [-]
f	Number density function (NDF) [var]
$\mathbf{F}$	Forces acting on a particle [N]
$\mathrm{F_T}, \mathrm{F_M}$	Correction factor for $\mathrm{B_M}$ and $\mathrm{B_T}$ [-]
$\mathbf{g}$	Gravity [m/s^2]
G	Filter kernel [$1/\mathrm{m}^3$]
h	Specific sensible enthalpy [J/kg]

Δh_v	Specific latent heat of vaporisation [J/kg]
j	Turbulent dispersion vector component [kg/(m^2 s)]
k	Volumetric kinetic energy [J/m^3]
K	Coefficient for vaporisation laws: $D^2(t) = D_0^2 - Kt$ [m^2/s]
l, L	Length; length scale [m]
m	Mass [kg]
$\dot{m}$	Mass flow rate [kg/s]
M	Moment about zero [var]
$\mathbf{M}, \mathrm{M}$	Vector (component) of volumetric forces between phases [N/m^3]
n_0	Number density (only in definition for Kn) [1/m^3]
N	Total number of particles (in a volume) [-]
p	Static pressure; vapour pressure [N/m^2]
p, q, C_0	Parameters of the Gamma distribution [m,-,1/m^3]/Beta distribution [-,-,1/m^3]
q	Specific heat [J/kg]
$\dot{Q}$	Heat transfer rate; heat release (of combustion) [W]
Q	Standard enthalpy of formation of species [J/kg]
ΔQ_c	Net heat of combustion [J/kg]
r	Radius [m]
R	Universal gas constant [J/(kg K)]
$\delta \mathbf{R}_d$	Random Uncorrelated Velocity tensor [m^2/s^2]
s	Flame speed [m/s]
S	Surface; general source term [m^2,var]
$\mathbf{S}$	SDC on/off switch [-]
t	Time coordinate [s]
T	Time interval; temperature [s,K]
$\mathbf{u}, u$	Velocity vector (component) [m/s]
$\mathbf{u}^{(k)}$	Transport velocity vector of moment $M^{(k)}$ [m/s]
$\mathbf{v}_p, v$	Velocity vector (component) of a particle/droplet [m/s]
V	Volume [m^3]
$\mathbf{V}, V$	Vector (component) of species diffusion velocity [m/s]
W	Molar mass; phase space density [kg/mol,var]
$\mathbf{x}$	Vector of space coordinates; position vector [m]

x, y, z	Space coordinates [m]
X	Phase indicator function [-]
Y	Mass fraction of species [-]

Greek Characters

α	Volume fraction (of particles) [-]
Γ	Mass exchange rate (volumetric mass flow rate or mass flow rate density) [kg/(m^3 s)]; Gamma function
$\Gamma_{M^{(k)}}$	Phase space average of Γ of order k [var]
δ	Residual component [var]; flame thickness [m]
$\delta()$	Dirac delta
δ_{ij}	Kronecker delta
Δ	Cut-off length scale [m]; interval indicator. See also other definitions in **Operators**
ϵ	Scalar dissipation rate [m^2/s^3]; fraction of total mass flux to species m [-]
ζ_p	Temperature coordinate of $\mathcal{I}$ [K]
η	Length scale [m]; dynamic viscosity [kg/(m^3 s)]
$\delta\theta_d$	Random Uncorrelated Energy [m^2/s^2]
θ	Volume fraction of the gas phase (void fraction) [-]
Θ	Volume occupied by a phase [m^3]
κ	RUM quantity [m^2/s]
λ	Thermal conductivity [W/(m K)]; mean free path of a molecule [m]
μ	Central moment, moment about the mean [var]
ν	Kinetic viscosity [m^2/s]; stoichiometric coefficient [-]
ξ	Spatial coordinate (notation in phase space integrals to distinguish between ξ and $\mathbf{x}$) [m]
π	3.1415...
ρ	Mass density [kg/m^3]
σ_0	Collision cross section [m^2]
σ^2	Variance [var]
τ	Time scale [s]; stress tensor component [N/m^2]

$\boldsymbol{\tau}$	Stress tensor [N/m^2]
ϕ	General quantity; equivalence ratio [-]
ψ	General quantity
$\dot{\omega}$	Chemical source term for species [1/s]; weighting factor

Indices, indicating...

0	... a reference value; integral scale
1, 2, 3	... coordinates
I, II	... different source terms S
ab	... different mean diameters D_{ab}, i.e. D_{10}, D_{32}, etc.
i, j	... a spatial coordinate
k	... a specific particle
m	... a specific species

Subscripts refer to variables or quantities related to...

AIR	... the air "species"
c	... the continuous phase; the critical point
d	... averaged quantities of the dispersed phase[1]
f	... a fluid (phase); the flame
fuel, F	... the fuel species
g	... gaseous phase/state
l	... liquid phase/state
M	... mass transfer
ox	... oxygen
p	... a particle/droplet (phase)
s	... a value at the surface
S,nS	... the Stokes/non-Stokes flow regime
t	... a turbulent state
T	... heat transfer
v	... vapour

[1] Even constant properties can change the subscript. For example, the mass density of the particle matter is named ρ_p before averaging procedures and ρ_d after, although it is the same constant.

Superscripts

$*, **$	Indicates an existing variable but based on a second or formally different definition.
$'$	Residual component between mean and actual value
$''$	Residual component between the Favre averaged mean and the actual value
$@\mathbf{x}_p^{(n)}$	Value of a quantity at the particle position.
(k, l, m)	Order of [3-dimensional] phase space averaged quantities, i.e. moments
(m)	Index for individual species
(n)	Index for individual particles/droplets
S,nS	Referring to the Stokes/non-Stokes flow regime
SDC	Referring to Single droplet combustion
t	Turbulent quantity

Dimensionless Numbers

B_M	Mass transfer number
B_T	Heat transfer number
Da	Damköhler number
Kn	Knudsen number
Nu	Nusselt number
Pr	Prandtl number
Re	Reynolds number
Sc	Schmidt number
Sh	Sherwood number
St	Stokes number

Abbreviations

Small typed abbreviations act as subscripts.

BML	Brass-Moss-Libby [combustion model]

boil	Boiling
CFD	Computational Fluid Dynamics
CMC	Conditional Moment Closure
comb	Combustion
dds	Droplet-droplet spacing
DIA	[Kraichnan's] Direct Interaction Approximation
DNS	Direct Numerical Simulation
DPM,S	Discrete Particle Method/Simulation
(D)QMOM	(Direct) Quadrature Method of Moments
E/S QMOM	Extended/Sectional Quadrature Method of Moments
DSMC	Direct Simulation Monte Carlo [method]
EbNDF	Ensemble [average] based NDF
EBU	Eddy-Break-Up [combustion model]
EE	Euler-Euler
eff	Effective
EL	Euler-Lagrange
ESDCM	Eulerian Single Droplet Combustion Model
FEbNDF	Filtered, ensemble [average] based NDF
FGM	Flamelet Generated Manifolds [based combustion model]
FNDF	Filtered NDF
heatup	Heat-up
IEM	Inter-Exchange [with the] Mean
ign	Ignition
LDI	Lean Direct Injection
LES	Large Eddy Simulation
LHDI	[Kraichnan's] Lagrangian History Direct Interaction
LODI	Local One-Dimensional Inviscid [boundary conditions]
LPP	Lean Premixed Prevaporised [combustion]
LS	Level Set [method]
max	Maximum
MEF	Mesoscopic Eulerian Formalism
MF	Multi-Fluid [method]
mix	Mixture
MOM	Method of Moments

MOMIC	Method of Moments with Interpolative Closure
NDF	Number density function
PaSR	Partially Stirred Reactor [model]
PD	Product-Difference [algorithm]
PDF	Probability density function
PDPA	Phase Doppler Particle Analyser
PMOM	Presumed [shape] Method of Moments
PTC	Particle Trajectory Crossing
QbMM	Quadrature based Moment Methods
rad	Radiation
RANS	Reynolds Averaged Navier Stokes
ref	Reference [state]
RMS	Root-Mean-Square [values]
RR	Rosin-Rammler [distribution]
RUM	Random Uncorrelated Motion
RUV	Random Uncorrelated Velocity
SDC	Single droplet combustion
SF	Stochastic Fields [method]
SPH	Smoothed Particle Hydrodynamics [method]
TFM	Thickened Flame Model
TH	Top hat [filter]
VAbM	Volume Average based Models
VOF	Volume of Fluid [method]

Operators

$\cdot$	Placeholder; inner product
:	Double inner product of two tensors
$\langle\cdot\rangle$	General notation for an averaging operation
$\langle\cdot\rangle^{E}$, $\langle\cdot\vert\boldsymbol{\mathcal{I}}\rangle^{\mathcal{E}}$	Ensemble average, ~ conditioned on phase space
$\langle\cdot\vert\boldsymbol{\mathcal{I}}\rangle^{\mathcal{E}\mathcal{F}}$	Combined ensemble average and spatial filtering operation conditioned on phase space
$\langle\cdot\rangle^{F}$, $\langle\cdot\vert\boldsymbol{\mathcal{I}}\rangle^{\mathcal{F}}$	Spatial filtering, ~ conditioned on phase space
$\langle\cdot\rangle^{T}$	Temporal average

$\langle\cdot\rangle^{V}$	Volume average for single phase flows
$\langle\cdot\rangle^{\mathcal{V}}$	Volume average for two-phase flows
$\langle\cdot\rangle^{\mathcal{VF}}, \langle\cdot\vert\boldsymbol{\mathcal{I}}\rangle^{\mathcal{VF}}$	Combined volume average and spatial filtering operation, ~ conditioned on phase space
$\Delta(\cdot)$	Laplace operator $\Delta = \nabla^2$
$\nabla(\cdot)$	Gradient operator
$\nabla\cdot(\cdot)$	Divergence operator
$\frac{\partial\cdot}{\partial\iota}, \frac{d\cdot}{dt}$	Partial derivative in coordinate ι, Total derivative
$\sum_i, \prod_i$	Sum/Product over index i
$\cdot\vert\phi$	Conditioned on ϕ
$(\cdot)^{(k)}$	Phase space average of order k to be applied to quantities $\cdot$
sgn()	Signum function
$\equiv$	... abbreviated/defined as...

Symbols

$.^{(k)}$	Phase space averaged quantity of order k
$\tilde{\cdot}$	Favre averaged quantity
$\bar{\cdot}$	Volume averaged quantity; spatially filtered quantity (i.e. weighted volume average)
$\breve{\cdot}$	Ensemble averaged quantity
$\breve{\bar{\cdot}}$	Ensemble averaged, filtered quantity
$\mathfrak{D}$	Diffusion coefficient [m^2/s]
$\mathcal{H}$	(Flow) realisation
$\boldsymbol{\mathcal{I}}$	Abbreviation for the particle phase space D, $\mathbf{c}_p$, ζ_p
j	Turbulent diffusion flux vector component [$\mathrm{kg}/(\mathrm{m}^2\,\mathrm{s})$]
$\mathcal{N}$	Number of (flow) realisations
$O()$	Terms of higher order
$\mathcal{R}$	dds to D ratio [-]
∞	Infinity
$\Delta_{0,1}, \Delta_{1,1}, \Delta_{k,l}$	Hankel-Hadamard determinants [var]

Units

cal	Calorie [4.185 kg m^2/s^2]
°	Degree (geometrical)
°C, °F	Degree Celsius/Fahrenheit
g	Gram
J	Joule [kg m^2/s^2]
K	Kelvin
kg	Kilogram
lb	Pound [453.6 g]
m	Metre
mm	Milli metre
µm	Micro metre
min	Minute
mol	Mole
Pa	Pascal [$kg/(m\,s^2)$]
s	Second

Chemical Species

$C_{12}H_{23}$	Surrogate species for kerosene
$C_{13}H_{26}$	Surrogate species for kerosene
CO_2	Carbon dioxide
H_2O	Water
N_2	Nitrogen
NOx	Nitrogen oxides
O_2	Oxygen

1 Introduction

Multiphase flows consist of at least two different phases, i.e. matter being in different thermodynamic state, which are *solid*, *liquid* or *gaseous*. Multiphase flows are encountered daily in any field of everyday occurences and environmental, technological and industrial application. As examples may be mentioned weather forecast (rain, snow, hail, fog, cloud physics), ocean waves, floods, volcano eruptions, avalanches, astrophysics, liquid fuelled combustion applications (diesel engines, coal furnaces, aero engine gas turbines), process industry (fluidised beds, bubble columns, sprays), oil and gas industry, nutrition industry (food production, drying, conditioning), spray applications (painting, varnishing, arts), interface/surface tension applications (lubrication, wave-ship interaction, rain-vehicle interaction), sprinklers, air conditioning, showers, movie industry (animated scenes or movies), etc. Besides the scientific observation and experimentation, nowadays the numerical simulation establishes as a powerful tool to understand the physics, to improve industrial processes and technology or to forecast nature phenomena including those having potentially harmful effect on the environment, either mankind, creature or nature.

1.1 Modelling of Multiphase Flows

The states of appearance of continuous single phase flows are numerous (i.a. laminar, turbulent, incompressible, compressible, subsonic, supersonic) and a variety of theoretical and numerical methods have been developed to meet the requirements given by the specific characteristics of these types of flow. Dealing with multiphase flows, numerous additional

types of flow arise, not because of the additional phases itself (since they can be considered usually to be continuous phases with previous mentioned states) but rather their interaction. On the one hand, the interface between two phases, i.e. the microscopic transition of the phase properties, and the interaction between two phases, i.e. the exchange of mass, momentum and energy, in general add new levels of scales to be considered, often smaller than those of the single phase flow. On the other hand, the macroscopic composition and dynamic of the phases strongly depend on the number of phases or fluids, their material properties and their interaction at the interface (surface tension, reaction), the flow conditions as well as inlet and boundary conditions.

While in single phase flows significant differences in the flow characteristic can be categorised mainly into sub- and supersonic states, multiphase flows require a more differentiated classification to do justice the multitude of flow types and phenomena. Accordingly, a large number of different numerical methods exists, where each of them is able to describe a specific choice for one of those flow types. Within the next two paragraphs, a rough classification of the most common types of multiphase flow and their numerical realisation is given, followed by an attribution of the class of multiphase flow that this thesis is concerned with.

1.1.1 Classification of Multiphase Flows

Multiphase flows can be classified into two main categories, namely *dispersed* and *separated* flows, where the former may be further split into two sub-classes, which are *homogeneous* and *heterogeneous* mixtures (Brennen, 2005). These three categories can be characterised as:

- homogeneous mixtures: all phases are uniformly[1] distributed throughout the mixture. Uniformly distributed means, that the average distance between disconnected regions of a phase as well as their

[1] ... on a scale far above the molecular level (in order to avoid a confusion with the definition in chemistry science)

individual spatial extent are orders of magnitude smaller than the integral length scale of the geometry, but not necessarily similar compared to each other. In other words, averaged values of the mixture quantities taken from averaging volumes much smaller than the integral length scales are statistically converged, locally isotropic and homogeneous. Examples are fog, mist, snowfall, bubble columns, etc.

- heterogeneous mixtures: the phases are actually similarly arranged as in homogeneous mixtures, however, the particle size or the length scale of connected regions/individual phase fragments becomes closer or even similar to that of the flow structures and the integral length scales of the geometry, e.g. splashing waves, disintegrating liquid jets, etc. In other words, averaged values of the mixture taken from averaging volumes much smaller than the integral length scales can vary significantly between neighbouring volumes.
- separated flows: phases are clearly separated at the integral length scale, and the resolution of the interface dynamics is of important significance, e.g. oceans, rivers, lubrication oil-air assembly in bearings, slug flows in pipes, etc.

Dilute, polydisperse sprays can be typically categorised as homogeneous mixtures, i.e. the focus of the thesis is on dispersed two-phase flows. Hence, the two-phase flow consists of a clearly defined dispersed phase, with a volume fraction small compared to that of the continuous phase in which it is dispersed in. Homogeneous, however, does not necessarily mean that all particles have the same size, velocity or temperature (monodisperse), but rather a wide spread of properties (polydisperse, polydispersity).

1.1.2 Simulation Methods for Multiphase Flows

Classification of the numerical methods applied to multiphase flows is not trivial, since too many aspects come into play. First, methods can be

classified by their specific application to one of the types of multiphase flows mentioned above, which is, however, not unique, since some methods can be applied to any of these types. Second, methods can be classified by the level of scales considered they have been developed for. Here again, some methods can be applied to any level of resolved or reduced modelling of scales. Furthermore, mathematical criteria can be used to characterise these methods, for example methods written in a Lagrangian frame, i.e. in coordinates connected to the particle, or an Eulerian frame, i.e. coordinates fixed in physical space. Both ways of describing the dynamics of the multiphase system are used due to their advantages for specific applications, but these are in turn not necessarily connected with any scales or flow types. Later on in Chapter 2, after having defined the temporal and spatial scales present in multiphase flows and the different averaging types, a comprehensive evaluation of the specific numerical methods with corresponding literature related to the development and the application is given. Furthermore, they are discussed additionally in a more mathematical background throughout the thesis, where additional details and references can be found. Although only a specific choice is finally made out of all those methods to produce the results shown in Chapter 7, it is helpful to mention these methods and to evaluate the specific characteristics at the different steps of the derivation of the two-phase equation system in order to enlarge the understanding and ability to clearly differentiate between all the methods.

1.1.3 Challenges in Multiphase Flow

Due to its additional complexity compared to single phase flows, practical application of multiphase flow simulation is a rather young discipline, which has not obtained the same sophisticated level of accuracy and user-optimised application as single phase flow simulation. Although theoretical effort has been undertaken for many decades and various methods and ideas can be used or adopted from single phase CFD, the specific characeristics of the multitude of multiphase flow modes, often require new concepts to find appropriate closure for the equation systems and

proper numerical algorithms. Especially the level of sophisticated closure models needed for the derivation of equation systems, which allow feasible implementation and efficient simulation, lags behind those of single phase flows. Hence, numerous methods and models have been developed for a wide range of multiphase flows during the last decades. A clear trend, however, which kind of methods seems to establish in each class of multiphase flows, can not be observed. There are several reasons. First, comprehensive methods, which satisfactorily capture the physics, are often way too costly for practical application and product development. Second, methods simplified in terms of the amount of physical phenomena considered, usually inherit similar closure problems as single phase flows do, but the differences in the underlying physics most often do not allow the adaption of single phase closure approaches or complicate them. Especially those methods, which are based on a comprehensive concept and formulation (for example PDF methods for dispersed two-phase flows), still require much effort to find appropriate closure. Third, some rather efficient methods, e.g. the two-fluid method, show shortcomings when coming to capture accurately complex flows in industrial configurations.

Simulation of multiphase flows also takes an important role to deepen the understanding of the physics itself as an alternative to theoretical and experimental investigations. On the one hand, the theoretical approach is even more complicated by the complexity of the mathematical description compared to single phase flows, which makes finding analytical solutions and theoretical predictions very challenging. On the other hand, experimental measurement and quantification of multiphase flows is often difficult regarding the separation of different effects and the accurate and explicit measurement of the quantity of interest. Therefore, the evaluation of the results of a direct simulation of the full physics, although only practicable for strongly reduced physical domains and rather simple flow conditions, can provide a better understanding of the processes. For practical applications, however, significant simplification of the physics considered has to be made to be able to simulate the phenomenon of interest with acceptable computational and temporal effort.

Beside the general challenges directly concerned with the description and numerical realisation of multiphase flows, related issues require increased attention. As example, spray combustion applications may be mentioned. Along with the development of methods descibing the spray dynamics, additional attention must be paid on the development of models to describe the adjacent physics, e.g. the different spray combustion modes, vaporisation, radiation, etc. Depending on the numerical method, closure must be found for terms which describe, e.g., the unresolved interaction of droplet motion, vaporisation and combustion. Embedded in this picture, the present work tries to contribute another piece to the puzzle as sketched next.

1.2 Scope and Structure of the Thesis

The objectives of this thesis were initiated as subsequent work of that done by Carneiro et al. (2008, 2009), which in turn remodelled and extended the work of Gharaibah and Polifke (2004), Gharaibah (2008). All these contributions were based on RANS equations derived with the help of the volume average. The initial concept of using mean and variance for the description of the particle size distribution as done in Gharabaih's work was discarded and replaced by using moments about zero[2] in order to avoid theoretical problems in the formulation of the corresponding moment transport equations. Additionally, Carneiro formulated the phase interaction source terms for spray application, i.e. drag and vaporisation, as well as the transcription of the relaxation time approach (Bollweg et al., 2007) to an integrated form to be used with the moment model.

Based on that work, the aim of this work has been the rigorous derivation of the moment model for the use with Large Eddy Simulation (LES) and its application to spray combustion test cases. To evaluate the influence of assumptions and simplifications made in order to obtain a closed and

[2]Definition in Section 4.1.1

numerically rather efficient model concerning implementation and computation effort, the equation system proposed had to be tested against experimental findings of non-vaporising, evaporating and combustion spray test cases.

In order to lay the foundation of the derivation of the aforementioned equation system, in Chapter 2 the multitude of multiphase flows is categorised using appropriate time and spatial scales, followed by an evaluation of the fundamental methods to derive dispersed two-phase flows with a detailed discussion of specific methods proposed in literature. With the knowledge of the characteristics, challenges, advantages and disadvantages of the options, two specific methods, which deliver a high level of generality and which can be customised properly to our needs, are used in Chapter 3 to comprehensively derive the gas phase and dispersed phase equations. These methods are based on a unified "volume average - spatially filtering" approach for the continuous phase, i.e. the gas phase, and an ensemble averaged, filtered number density fuction approach for the dispersed phase. The gas phase equation system is written in an Eulerian frame and can be solved with common finite volume techniques. To solve the transport equation of the number density function describing the statistics of the dispersed phase, the solution strategy remains optional until the end of that chapter, i.e. it is still possible to choose between Lagrangian and Eulerian methods.

Therefore, Chapter 4 presents the solution strategy of the transport equation of the number density function in an Eulerian frame, which is a method of moments in this work. Besides the closure of unknown correlations of the gas phase quantities discussed already in Chapter 3, the comprehensive discussion of closures for unknown terms due to the dispersed phase is given in Chapter 4, for both, those proposed in literature and the specific simplifications used in this work. At the end of the chapter, a closed two-phase equation system including particle transport, thermal dynamics and heat and mass exchange with the gas phase is obtained.

To describe the combustion of the fuel vapour, i.e. the gaseous state of

the dispersed liquid, Chapter 5 presents physical, experimental and numerical aspects of liquid spray combustion, with the detailed discussion of the specific methods used in this work. Although, the equation system is mathematically closed, the numerical implementation and solution require additional preparation, which is briefly given in Chapter 6.

Finally, numerical results obtained for different, mostly academically motivated experimental data sets for pure, polydisperse particle motion in a swirling flow field, for an evaporating gas-particle jet and a reacting spray are presented in Chapter 7. Keeping in mind the simplifications and assumptions made in the derivation of the underlying equation system, strengths and shortcomings of the numerical results compared to the experimental data are evaluated. The thesis closes with a summarising annotation of the capabilities of the methodology and the numerical results, and with a comprehensive proposal of aspects and issues which are significantly important to be dedicated to future research.

2 Modelling Dispersed Particle Two-Phase Flows

Many terms, definitions and modelling concepts have been qualitatively introduced in Chapter 1. The aim of this chapter is to deepen those (and some additional) in a more comprehensive and sophisticated manner. Reminding that we consider dispersed two-phase flows only, i.e. small portions of one phase are arbitrarily distributed in another, continuous phase, separated flows and corresponding numerical methods are not of any further interest and upcoming statements made do not refer to those unless directly mentioned. With that, this chapter is split into the definition of multiphase specific terms, scales and physical phenomena, followed by the basic operations and assumptions made to derive the system of governing equations. It is closed by the discussion of the state of the art in methods and simulation techniques.

2.1 Definitions and Terminology

In multiphase flows, the term *phase* refers to the thermodynamic state of matter, i.e. solid, liquid or gaseous. That means, that multiphase flows consist of at least two different phases (two-phase flow, multiphase flow), e.g. solid or liquid particles dispersed in a gas, bubbles in liquid, etc. Not to be mistaken with the term *multiphase* is the term *multi-fluid*, which refers to flows consisting of two different fluids, which are, per definition, in the same phase state, e.g. oil in water.

The term *particles* refers in general to small portions of matter dispersed in a continuous phase independent of the thermodynamic state, although

this thesis concentrates on liquid fuel droplets dispersed in air. The terms *continuous* phase, *fluid* phase and *gaseous* phase are used interchangeable. The former two are used to remind that parts of the equations shown are not valid only for droplet-air flows, the latter refers to that specific combination, but the actual usage does not imply strict indication of a certain classification.

The term *polydisperse* usually refers to the local variation of the size of the dispersed particles (rather than only in a global or temporal sense), i.e. the size of the particles is considered with its specific impact on motion, heat and mass exchange between phases and particle-particle collisions. *Monodisperse* in turn, assumes particles to have identical size, at least locally but usually also globally (except some hybrid applications, e.g. vaporising droplets originating from a mono-sized injection). Although usually referring to the particle size only, the term *polydispersity* might be used in general for other particle properties in a similar way.

Furthermore, we consider dispersed phase flows with a particle-continuous phase volume ratio ranging from $\sim 5 \times 10^{-6}$ up to $\sim 5 \times 10^{-4}$, which classifies the dispersed flow as *dilute* (Elghobashi, 1994). If, additionally, the mass loading is small compared to unity as well, the impact of the dispersed phase on the continuous phase can be neglected (*one-way coupling*). Otherwise, a *two-way coupling* is necessary to properly consider the physics, which is the case throughout this thesis. Particle-particle collisions (sometimes called *four-way coupling*) as well as particle-wall collisions are not considered.

2.2 Temporal and Spatial Scales

2.2.1 Levels of Scales

In general, single phase flow structures span over several orders of length and time scales. Often, this aspect complicates even more when considering two-phase or multiphase flows. The range of scales can be enlarged

by the presence of the dispersed phase (usually towards smaller scales) or remains nearly unchanged, depending on the characteristic length scales of the dispersed phase, the interface between the phases and the turbulence scales of the fluid phase. The following example illustrates this issue. Consider a small (fixed) particle in a laminar flow (from left). The characteristic length scale of the particle, e.g. the diameter, shall be smaller than the smallest scales occurring within the undisturbed fluid phase, i.e. in absence of the particle. Consider the relative velocity between the particle and the fluid as such, that the flow behind the particle is within the turbulent regime. Thus, the presence of the particle causes fluid phase flow scales much smaller than in the absence of the particle, as sketched in Fig. 2.1 on the left. Even the fact, that the presence of

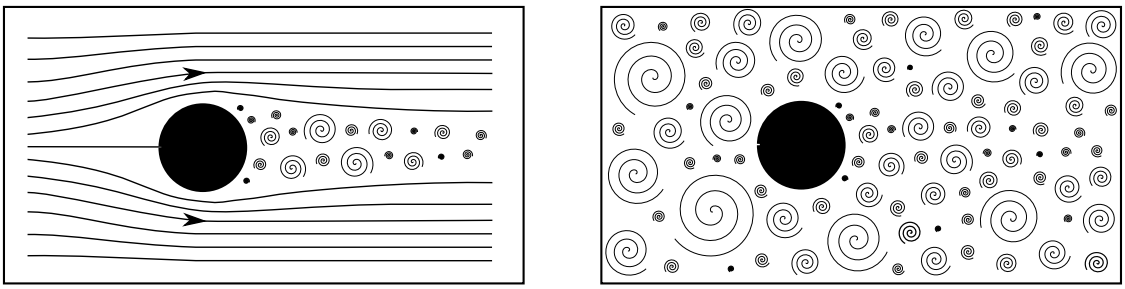

Figure 2.1: Particle with high relative velocity in **Left** laminar flow and in **Right** turbulent flow.

a particle can induce turbulent flow in an otherwise laminar fluid phase, emphasises the added complexity. On the other hand, if the smallest fluid phase scales of turbulence, i.e. the Kolmogorov scales (see Section 2.2.2), are smaller than the particle diameter and considering the flow regime around the particle as Stokes flow, the presence of the particle practically does not change the level of scales present in the fluid flow (Fig. 2.1, right).

In order to classify and describe these different aspects of the two-phase flow regimes, it has been proven to be practical to define the following three levels of scales in dispersed two-phase flows (see also Fox (2012)).

Microscale

In continuous single phase flows, the smallest eddies are considered as the microscale (Fig. 2.2, left), with a continuous transition to the macroscales, i.e. the largest eddies occurring in the given case, which are usually of the order of the geometric length scales. When introducing a second phase, the geometrical shape of the interface between the phases can generates fluid flow structures much smaller than the smallest scales of the undisturbed single phase flow (Fig. 2.2, right). These may arise either in the fluid flow or internal to the second phase and should be considered as the new microscale. Hence, in order to account for the discrepancy between undisturbed fluid flow microscales and microscales induced due to the presence of the second phase, an intermediate scale (termed as *mesoscale*) can be introduced as described below.

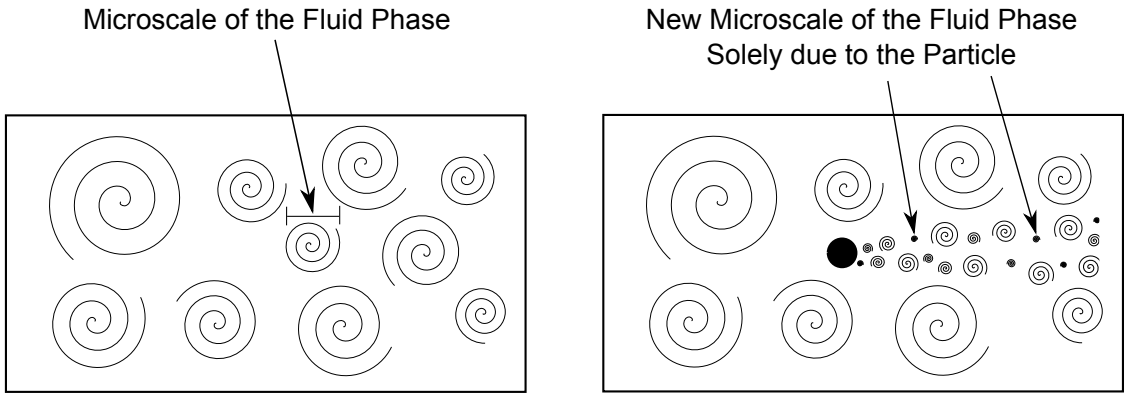

Figure 2.2: Left Microscale in undisturbed single phase flows. **Right** New microscale introduced by the presence of a particle. Fluid flow from left to right.

On the microscale level, particle forces such as drag, lift, etc. are calculated from the given flow field as an integral over the particle surface as a post-processing step. There is no need for a drag model (drag coefficient, etc.) since every scale is resolved.

Mesoscale

The so-called *mesoscale* is defined as a scale between the micro- and the macroscale, accounting for the differentiation of microscales in a disturbed and an undisturbed fluid phase and mainly bred by numerical requirements. Since it is rather unfeasible to resolve the microscales of a two-phase flow for a large number of particles[1], the idea is to reduce the description of the particle state to mean quantities (mesoscopic quantities), e.g. a single particle velocity, temperature, etc. Accordingly, the interaction with the continuous phase is described by 0-dimensional laws for the integral exchange of mass, momentum and heat between phases with the help of the mesoscopic quantities and the fluid properties at the mesoscale. Hence, the drag force, for example, is not computed from the flowfield around the particle a posteriori, but determined by an a priori calculable expression based on analytical or experimental results depending on the mesoscopic quantities.

The mesoscopic quantities of the continuous phase can be defined as the values of the undisturbed field at the particle centre or as mean values gained from an average of the flow field over a length scale comparable to the particle characteristic length scale, especially if the smallest scales of the continuous phase are smaller than the particle length scale. Hence, the particles are still distinguished each by its mesoscopic variables, but the phase interaction is reduced to a point-source approximation. Reducing the fully resolved particle physics to a point source represents the reduction step of the microscopic model to the mesoscopic model (Fox, 2012). Boivin et al. (1998) have shown that the point-mass source is an appropriate approach if the particle characteristic length scale is smaller than the Kolmogorov length scale. Sirignano (2010) stated that current DNS/LES methods are actually inadequate for practical situations, i.e. in combustion chambers and other industrial applications, particle scales are usually comparable to the Kolmogorov scales. Nevertheless this as-

[1] The definition of this scale level has its background in dispersed two-phase flows and is rather difficult to apply in other types of multiphase flow. Hence, the *mesoscale* is defined here with the help of dispersed particle flows to reflect that issue.

sumption is used very often.

Macroscale

Quantities at a *macroscale* represent the averaged behaviour of an ensemble of particles, i.e. integral mean values of the mesoscopic phase space or the resulting quantities of volume averages (see Section 2.5). In some cases, those macroscales can be resolved by the numerical mesh depending on the definition of the underlying NDF/PDF or the size of the averaging volume, e.g. a filtered PDF with the filter size being at least as large as the mesh resolution. In general, this is not automatically the case.

The phase interaction forces are described by macroscopic models, which are either gained by integration of mesoscale models over phase space or expressed in terms of mean quantities gained from the volume or other averages. Hence, the "mean drag", for example, may be expressed in terms of the local mean velocity of the particle cloud and an averaged mean diameter representative for the particle size spectrum.

2.2.2 Typical Multiphase Scales in Comparison

With having characterised the three levels of scales in multiphase flows, we are able to sort out the typical length and time scales of dispersed two-phase flows. The characteristic scales of the fluid phase are categorised first, afterwards those of the dispersed phase, which are the particle relaxation time, the Stokes and Knudsen number, and finally those which are related to the numerics of the simulation, e.g. the mesh resolution.

- In turbulent fluid phases, the Kolmogorov scales describe the smallest scales of the fluid motion, which are characterised and can be calculated by
  - Length scale of smallest eddies $\eta = \left(\nu^3/\varepsilon\right)^{1/4}$ and $\eta/l_0 \sim \mathrm{Re}^{-\frac{3}{4}}$

  - Velocity of smallest eddies $\mathbf{u}_\eta = (\nu\varepsilon)^{1/4}$ and $\mathbf{u}_\eta/\mathbf{u}_0 \sim \mathrm{Re}^{-\frac{1}{4}}$
  - Time scale of smallest eddies $\tau_\eta = (\nu/\varepsilon)^{1/2}$ and $\tau_\eta/\tau_0 \sim \mathrm{Re}^{-\frac{1}{2}}$
  - Length scale where isotropic turbulence starts: $l_c = 1/6\, l_0$ (Pope, 1985)

  Considering particles dispersed in a continuous phase, the following cases may occur: If the Kolmogorov length scale is smaller than the particle size, the smallest scales of the continuous phase can be in fact considered as *microscale*. However, if the Kolmogorov scale of the undisturbed fluid motion, i.e. the same configuration and flow regime but without particles, is larger than the particle length scale, the Kolmogorov scale must be rather termed *mesoscale*, because the flow structures around and/or within the particle which can become much smaller than the Kolmogorov scale. The latter is the case, e.g., when small particles are injected with high velocity in a weakly turbulent or laminar flow field. The actual regime is strongly depending on the configuration and the local situation.

- In typical multiphase applications, the continuous phase is assumed to be statistically continuous - as the name suggests. That means molecular dynamics are not of interest but their averaged characteristics. In dilute dispersed two-phase flows, however, the particle number density can become very low, which result in particle-particle distances comparable to the length scale of the numerical mesh. Furthermore, direct particle-particle interaction reduces to marginal rates and only a weak interaction happens via the continuous phase. Hence, the question arises, whether dispersed particle flows can be described as a continuous phase. The so-called *Knudsen number* $\mathrm{Kn} = \lambda/L$ is a good measure whether a continuum or a statistical mechanics formulation should be used. In continuum phases, i.e. gases and liquids, λ is the mean free path of the molecule and L is a representative physical length scale, e.g. the mesh size or the geometrical dimensions of the given geometry.
  In particle flows, de Chaisemartin et al. (2008) define the Knudsen number as $\mathrm{Kn} = l_0/L$ where l_0 is expressed as $l_0 = 1/n_0\sigma_0$ with n_0 is

the number density and σ_0 is a typical collision cross-section. If the particle phase is dilute and the particles are small, then the Knudsen number is large compared to unity and the effect of collisions becomes small. In this case, treating the dispersed phase as a continuum is questionable and trivially implies problems in defining quantities as pressure or viscosity, as well as speaking of "interpenetrating continua" as often done. Actually, the dispersed phase must be described in a different way using a stochastic description. The resulting equations may describe the development of quantities (e.g. moments), whose fields are indeed "continuous" in space. In contrast, Knudsen numbers small compared to unity are characteristic for granular flows, which are, however, not of further interest at this point.

- The particle relaxation time of particle motion, defined as

$$\tau_p = \frac{\rho_p D^2}{18\eta_c} \,, \tag{2.1}$$

is a measure of how fast a particle adapts to changes in the continuous phase velocity. It can adopt any scale depending on the particle inertia and the fluid phase viscosity. To quantify these regimes, the *Stokes number* St can be used, which is defined as

$$\mathrm{St} = \tau_p/\tau_f \,, \tag{2.2}$$

where τ_f is a fluid phase characteristic time scale. The choice of τ_f depends on the scales the particle motion shall be compared with. When compared to the smallest scales, i.e. $\tau_f = \tau_\eta$, τ_f becomes $\tau(\Delta x) = \left((\Delta x)^2/\varepsilon\right)^{1/3}$. When compared to the mesh resolution Δx or the macroscales with length scale l, $\tau(l) = \left(l^2/\varepsilon\right)^{1/3}$.
If the particles adapt their velocity immediately to that of the continuous phase (tracer particles), the Stokes number is small compared to unity, $\mathrm{St} \ll 1$, whereas the Stokes number is large compared to unity, $\mathrm{St} \gg 1$, for very inert particles. The latter are nearly non-reactive to changes in the continuous phase velocity. Particles with

Stokes numbers around unity, however, can show several phenomena concerning the phase interaction, which are briefly discussed in Section 2.2.3.

- In practical numerical simulations of a large number of particles, it is usually not possible even to resolve the mesoscale, i.e. the particle size is much smaller than the mesh resolution. Therefore, in order to describe the sub-grid scales, one must distinguish between sub-grid scales considering very small scales (the actual microscale), i.e. internal droplet circulation or gas-vapour-film physics, and scales larger than those but still smaller than the mesh resolution, e.g. sub-grid scale gas phase turbulence. The particle-particle distance, however, need not to be smaller than the sub-grid scale gas scales but usually smaller than the mesh resolution. Otherwise, even in a statistical description, one must take care to have proper statistics, due to the very low particle number density.

2.2.3 Phase Interaction Phenomena and Particle Phase "Turbulence" Effects

Dependent on the particle and continuous phase scales, interaction between both can adopt several characteristic phenomena, namely continuous phase turbulence modulation by the particles, dispersion of particles by the turbulent continuous phase flow field, preferential concentration effects and "particle phase turbulence". The term "particle phase turbulence" is used with caution, because chaotic behaviour of particle motion differs from continuous phase turbulence in several aspects.

A recent, detailed review on these topics is given by Balachandar and Eaton (2010). Here, we summarise only some important aspects.

Turbulence Modulation by Particles

The presence of particles can impact the surrounding continuous phase in two ways depending on the particle inertia and the Stokes number. Small particles tend to attenuate turbulence, while large particles augment the fluid phase turbulence (Crowe, 2000, and references therein). This means that small particles act as turbulence dampers, since fluid turbulent energy must be spent to shake these particles crossing the eddy, whereas large particles at large particle Reynolds numbers[2] produce small scale turbulence in their wake. Both cases refer to a certain turbulence scale, for which the characteristic length scale of the "small particles" is actually smaller and that of the "large particles" is larger. In turn, those "large particles" can act in reverse as dampers for even larger turbulence scales as well. Therefore, the terms "small" and "large" are to be compared to the turbulence scale under consideration.

Turbulent Particle-Fluid Interaction/Turbulent Dispersion

Turbulent particle-fluid interaction or turbulent dispersion is the interaction of dispersed particles with a turbulent fluid flow. Turbulent dispersion inherits its chaotic nature solely from the fluid phase turbulence, i.e. different particles injected with exactly the same conditions into a turbulent flow field are most likely to have different trajectories due to the indefinite nature of the fluid phase turbulence. It is not to be mistaken with effects being part of the header "particle phase turbulence" (see the second paragraph below).

Regarding CFD simulations, two cases apply. First, if the particles are smaller than the Kolmogorov length scale, i.e. the fluid flow field is seen by the particles only as shear flow, and the gas phase scales are fully resolved (Direct Numerical Simulation (DNS)), then particle turbulent dispersion is fully resolved even using the point-mass approximation for the particles. Second, if the fluid phase is not fully resolved, i.e. a time or spa-

[2] Defined in Section 3.2.1, Eqn. 3.43

tial average must be applied for proper simulation, the non-resolved part of the interaction between particles and the turbulent flow field must be modelled, independent of the scale comparison between particle size and Kolmogorov length scale. Hence, in Lagrangian particle tracking methods, the immediate fluid velocity at the particle centre is evaluated from the resolved mean and a stochastic component determined by a model. In Eulerian simulations, a model must be found for the sub-grid scale particle-fluid interaction, which is usually more difficult.

The wide spectrum of turbulent dispersion effects can be framed by two cases. On the one hand, if particles are perfect tracers, the resulting particle phase behaviour is similar to that of the fluid phase. Only in this case, the particle dispersion may be unified with the particle phase turbulence and modelled with a turbulent viscosity approach similar to or based on that of the continuous phase. On the other hand, if particles are largely inert to the sub-grid scales of fluid motion, the particle motion can be accurately determined using the resolved component of the fluid velocity.

Preferential Concentration

As turbulent dispersion of particles, preferential concentration is an effect based on the interaction of particles with a turbulent flow field. Other than the turbulent dispersion, which describes the displacement of the actual particle trajectory from its equivalent based on the mean field, the preferential concentration refers to the cloud of the particles, which are sorted and structured in a certain way by the turbulent flow field. Shown in experimental and numerical investigations, particles tend to accumulate in regions of the turbulent field of low vorticity and high strain, respectively (see, e.g., Squires and Eaton, 1991a). This effect depends on the particle Stokes number, where the particles with Stokes numbers around unity are those affected the most. Relaxation times of larger particles are too large to allow a significant reaction on those flow scales which actuate preferential concentration. Tracer particle, on the other hand, follow the fluid phase structure perfectly, which again gives no reason to accu-

mulate the way described before.

Particle Phase "Turbulence"

Effects sometimes termed as "particle phase turbulence" are of different nature[3]. Actually, in dispersed two-phase flow equation systems, a variety of particle velocity correlations can appear depending on the underlying averaging procedures. These correlations, resulting from the convective term (one-point, second order), have a similar appearance as those arising in averaged, turbulent single phase equations. They imply, however, naturally totally different physics as detailed next.

On the one hand, such a correlation may arise due to particle trajectory crossing (PTC) effects, which can occur either due to ensemble average over a large number of particle phase realisations or due to a spatial average, where particle trajectories do not necessarily cross at the given point, but at least within the same volume over which the average is taken from. Even if the curvature of each particle trajectory is resolvable with the given mesh, the difference of the particle velocity between neighbouring trajectories can be large - not to say huge - especially for large particles, e.g. two particles pass nearby each other with high relative velocity as illustrated in Fig. 2.3. When imagine this scenario from an Eulerian view of point, i.e. the particles cross the computational volume (marked as V in Fig. 2.3) at the same time, sub-volume scale structures of the particle velocity field (red vectors) occur. Such effects are of totally different nature as continuous phase turbulence, and need to be modelled correspondingly.

On the other hand, correlations of fluctuating particle velocity components may arise due to the spatial average of a particle velocity field, where the curvature of the particle trajectories is not fully resolved by the numerical mesh. This yields "classical sub-grid stresses" of the particle phase velocity field. However, in dilute dispersed flows, where particle-

[3]Turbulent dispersion of particles is not part of this but stands for another effect as described above.

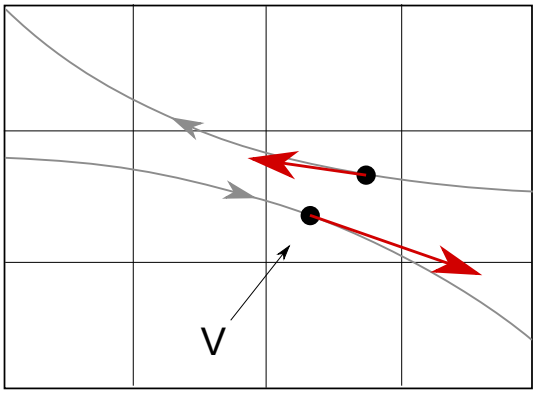

Figure 2.3: Particle phase sub-volume velocity field structures not due to sub-volume scale trajectory curvature.

particle interaction plays only a marginal role, the term “stress” has no evidence, since it is not possible to define a physically motivated viscosity for the dispersed phase. In this case, the use of the general term “particle phase velocity correlation” is more accurate. When the term “particle phase turbulence” or “a turbulence model for the particle phase” is used in the context of volume average based two-phase flow equations, it refers most often to this correlation, since its derivation and its position and notation in the equations is similar to turbulent sub-grid scale stresses or the Reynolds stresses in single phase turbulent flows.

Those and other correlations of particle velocity components appear for each conducted average, i.e. ensemble averages, spatial averages or phase space averages. They will be discussed later on when appearing in the derivation of the two-phase flow equations.

2.3 Types of Average

A fully resolved simulation of a two-phase flow, i.e. considering all scales of the continuous phase flow, all details of the shape of the interface and the internal flow of the particles, is only feasible for a system of a few particles and modest Reynolds number. In any other case, the complexity of the physical scales has to be reduced by a kind of averaging or by

filtering out the smallest scales up to a certain cut-off scale. The numerical method is then able to resolve the remaining scales[4]. Depending on the application and the numerical method used, several types of averaging can be conducted to gain equations for the averaged flow variables of interest, for whose all remaining scales of transport and physical processes can be fully resolved by the given computational mesh, spatially and temporally.

Since we are dealing with two-phase flows where the particle size is fundamentally smaller than the spatial resolution that is possible with present-day computational power, we need several averaging procedures to derive the equations of interest. At this point, the most common averaging procedures will be presented, first, however, without referring to specific two-phase flow applications or numerical methods. The definitions are not given in a rigorous mathematical way, but rather in a phenomenological way of description in the context of fluid dynamics, helping to understand their application to the different two-phase models and their derivation later on.

2.3.1 Time Average

The time average is a pointwise average of the quantity of interest $\psi(\mathbf{x}, t)$ over a certain time period T, which reads

$$\langle \psi \rangle^T = \langle \psi(\mathbf{x}) \rangle^T = \frac{1}{T} \int_T \psi(\mathbf{x}, t) dt \ . \tag{2.3}$$

In CFD, it is applied to obtain Reynolds Averaged Navier-Stokes equations, either for steady state simulations (RANS), i.e. $T \rightarrow \infty$, or transient/unsteady simulations (URANS).

[4] Actually, the more quantitative Nyquist theorem must be applied, which says that the smallest resolved scale is two times the mesh wide (e.g. in Sagaut, 1998, p. 10)

2.3.2 Volume Average

A volume average can be used to reduce the complexity of spatial scales, i.e. it removes all scales which are smaller than the length scale of a certain physical volume V, but approximately[5] preserves the full transient behaviour of the system. Usually it produces the arithmetic (i.e. non-weighted) mean value of all values of a quantity $\psi(\mathbf{x}, t)$ present in the averaging volume for a given flow realisation. It can be written as

$$\langle \psi \rangle^V = \langle \psi(\mathbf{x}, t) \rangle^V = \frac{1}{V} \iiint_V \psi(\boldsymbol{\xi}, t) \mathrm{d}\boldsymbol{\xi} \,, \tag{2.4}$$

where the integration is applied in physical space

$$\mathrm{d}\boldsymbol{\xi} = \mathrm{d}\xi_1 \mathrm{d}\xi_2 \mathrm{d}\xi_3 \tag{2.5}$$

over the averaging volume

$$V = \Delta x_1 \Delta x_2 \Delta x_3 \,. \tag{2.6}$$

2.3.3 Filtering

Usually applied to formulate equations for Large Eddy Simulation, filtering is an operation which removes all scales smaller than a cut-off length scale Δ and time scale τ_c in physical space or, equivalently, in Fourier space corresponding to a cut-off wave number and frequency, respectively. The temporal dimension is not considered here explicitly, although spatial filtering implies usually automatically temporal filtering (Garnier et al., 2009).

Spatial filtering is actually similar to volume averaging in terms of producing a mean value of all samples within a certain volume, however, with the possibility of weighting the contribution of each sample differently. This can be described by a convolution kernel G, which mathematically provides the information about the weighting. G and the spatial

[5] With every spatial average, a time average is implied over a time period corresponding to the largest scales, which are removed by the volume average.

cut-off length scale, or, more colloquially, the filter size/width, are characteristic for the filter used. The convolution or filter kernel G determines with which weight the sample values of a quantity $\psi(\mathbf{x},t)$ in the neighbourhood of point $\mathbf{x}$ are included in the average $\langle\psi(\mathbf{x},t)\rangle^F$. Mathematically this operation can be written as the convolution product

$$\bar{\psi} = \langle\psi\rangle^F = \langle\psi(\mathbf{x},t)\rangle^F = \iiint_{\infty} \psi(\boldsymbol{\xi},t)G(\mathbf{x}-\boldsymbol{\xi})\,\mathrm{d}\boldsymbol{\xi}\,, \tag{2.7}$$

where integration takes place over physical space

$$\mathrm{d}\boldsymbol{\xi} = \mathrm{d}\xi_1\mathrm{d}\xi_2\mathrm{d}\xi_3\,. \tag{2.8}$$

G must have the following characteristics:

- Consistency $\iiint_{\infty} G(\mathbf{x}-\boldsymbol{\xi})\,\mathrm{d}\boldsymbol{\xi} = 1$
- Linearity $\langle\psi+\phi\rangle^F = \bar{\psi}+\bar{\phi}$
- Commutation with differentiation

Furthermore, we restrict ourselves to those cases where G has the following characteristics:

- G is homogeneous (spatially and temporally invariant), isotropic (centred) and localised, i.e. G has always the same shape relative to $\mathbf{x}$, since $\mathbf{x}$ and $\boldsymbol{\xi}$ have the same origin, therefore $\mathbf{x}-\boldsymbol{\xi}$ is a relative position around the given point $\mathbf{x}$.
- In our notation of the sub-grid scale correlation tensors, we make, for the sake of simplicity, but without loss of generality, implicitly the assumption of G being a Reynolds-operator, i.e. $\overline{\bar{\phi}\phi'} = 0$ and $\overline{\bar{\psi}\psi} = \bar{\psi}\bar{\psi}$ (Sagaut, 1998). For example, the top-hat filter is a Reynolds operator. On the other hand the Gauss filter is not: multiple filtering smears out the solution more and more, i.e. $\overline{\bar{\psi}\psi} = \bar{\psi}\bar{\psi}$ is not fulfilled, since it reaches from $-\infty$ to ∞.

- The support of G can be infinite, i.e. G takes in general non-zero values for all $\mathbf{x}$ up to $-\infty$ to ∞ (e.g. Gauss) or compact, i.e. G is zero outside a certain closed interval (e.g. the top-hat filter). Other types of supports are not discussed here.

Calculus rules for gradients and other mathematical operations do not contribute to the matter and will not be presented here, but can be found in Sagaut (1998) and Garnier et al. (2009).

To simplify closure in variable density flows, a density weighted or so-called *Favre average* can be introduced, which reads

$$\langle \rho\psi \rangle^F = \bar{\rho}\tilde{\psi} = \bar{\rho}(\mathbf{x},t)\tilde{\psi}(\mathbf{x},t) = \iiint_{\infty} \rho(\boldsymbol{\xi},t)\psi(\boldsymbol{\xi},t)G(\mathbf{x}-\boldsymbol{\xi})\,\mathrm{d}\boldsymbol{\xi}\,. \tag{2.9}$$

Actually, the volume average as described above can be classified as a special case of spatial filtering. Comparing both definitions, volume average can be interpreted as spatial filtering using a top-hat filter and requiring that the length scale of the averaging volume V is of similar size as the filter length. We will use this interpretation later on for a specific approach to derive two-continua LES equations for dispersed two-phase flows.

2.3.4 Ensemble Average

Ensemble average distinguishes itself from the other types described before in being not associated with any time or spatial scale. In fact, the local and instantaneous average is taken from a large number of different realisations or "virtual copies" of the flow, which deviate from each other in the non-deterministic (chaotic) part of the underlying physics. Hence, the ensemble mean is the mean of all chaotic states that have the same statistics or, in other words, the mean is the expectation value of the quantity considered at the given point in time and space. It can be

defined mathematically as

$$\langle \psi \rangle^E = \lim_{\mathcal{N} \to \infty} \left[\frac{1}{\mathcal{N}} \sum_{\mathcal{N}} \psi(\mathbf{x}, t, \mathcal{H}) \right] , \tag{2.10}$$

where $\psi(\mathbf{x}, t, \mathcal{H})$ is the local and instantaneous value of the property ψ present in realisation $\mathcal{H}$ and $\mathcal{N}$ is the total number of realisations considered.

2.4 Microscale Methods

There are methods developed to resolve every scale occurring in multiphase flows. That means that on a microscale level the interfacial curvature (but not the interfacial transition between phases, i.e. the interface is treated as a jump in phase properties) and all flow structures within each phase are fully resolved. These methods can be seen and referred to as the *(Real) Direct Numerical Simulation* for multiphase flows, where the interface jump condition is the only simplification made, or, per definition, declared as a necessary and legitimate step[6] to separate this kind of method from molecular based simulation techniques. When dealing with those methods, the accurate description of the interface between phases is the main issue. A sub-classification of these methods can be undertaken depending on the mathematical framework. There exist mesh-based methods, usually referred to as *Eulerian* methods and mesh-less methods, usually indicated as of the *Lagrangian* type of framework.

In Eulerian methods, the fluid phases itself are often treated each as a continuous fluid using the Navier-Stokes equations, as done, i.a., in the Volume of Fluid method (VOF) (see Hirt and Nichols, 1981, Youngs, 1982, van Sint Annaland et al., 2005). Even at the smallest scales of continuum mechanics, the interface is a sharp jump of properties, which, however, contributes significantly to the dynamics of the mixture due to the surface tension. Accurate description of the curvature and position of the

[6] and therefore not of simplifying but *direct* nature in the sense of *Direct Numerical Simulation*

interface contributes essentially to the correct prediction of the surface tension. For many decades, numerical methods have been developed to describe the interface, e.g., the front tracking method (Unverdi and Tryggvason, 1992, Tryggvason et al., 2001) or the Level Set method (LS) (Osher and Sethian, 1988, Sussman et al., 1994, Osher and Fedkiw, 2001). Combination of both, the VOF and one of the front tracking methods, gives a method to simulate multiphase flows fully resolved on the microscale (e.g. Sussman and Puckett, 2000, Sussman, 2003).

Originating from astrophysics (Gingold and Monaghan, 1977, Lucy, 1977), the Smoothed Particle Hydrodynamics method (SPH) is a Lagrangian particle tracking method, which describes continuous fluids using a "particle fluid". It has been extended to multiphase applications with the challenge of incorporating the surface tension correctly, see, e.g., Monaghan (1994), Monaghan and Kocharyan (1995), Morris (2000), Colagrossi and Landrini (2003), Hu and Adams (2006, 2009), Höfler et al. (2013), Braun et al. (2013) and comprehensive reviews by Monaghan (2005), Liu and Liu (2010).

Although these methods can be used to resolve all scales of the curvature of the interface, the decisive disadvantage is, that they are only feasible for a few particles or a small physical extend of interfacial curvature with still enormous computational costs. In order to consider more than a very few particles or small details of a separated flow in larger systems of practical applications, the computational costs usually increase tremendously. Therefore, these methods are of restricted use only in academic test cases so far. Moreover, from an engineering point of view, not all scales of the interface are of interest. Simulations of industrial applications using the VOF method for example, are likely conducted for an equation system with a reduced level of scales considered. These can be derived by averaging the two-phase flow, resulting in equations which consider only the large scale curvature and model the non-resolved subgrid scale curvature of the interface. From this point of view, the surface tracking methods mentioned above can be actually of macroscopic type as well.

2.5 Direct Micro- to Macroscale Models

Since microscale methods are notoriously too costly to simulate industrial scale applications, numerous methods have been developed based on the reduction of the flow scales to a level much larger than the characteristic length scale of the particle or even the average particle-particle distance, but which are in general still too small to be resolved with numerical meshes used in industrial-scale applications. This *macroscale* is not to be mistaken as the integral geometric length scale of a given configuration, i.e. the largest scales of the flow. Two possibilities exist to obtain macroscale models, either directly from the microscale, which represent the rather "classical" class of two-fluid or interpenetrating continua models, or from a mesoscale description of the two-phase flow, which is of stochastic nature and is often used in dispersed two-phase flows. To the latter, all kind of methods belong to which consider integral properties of the phases, e.g. moments of the NDF/PDF, or Multi-Fluid methods based on the description of the NDF/PDF with classes, e.g. Quadrature based Method of Moments (QbMM) or methods based on a presumed functional shape of the NDF/PDF. These will be presented in Section 2.6.2, whereas in this section methods derived directly from the microscale are presented and discussed.

2.5.1 Classical Volume Average in Two-Phase Flows

The class of multi-continua methods is constructed such, that at each point in space both, gas phase and dispersed phase quantities, are defined regardless of which phase is actually present at the given time instance. These interpenetrating, continuous phases can be obtained by applying the volume average operation, as defined in Section 2.3.2. To formally derive these equations, the Navier-Stokes equations are multiplied first by a so-called *(phase) indicator function* or *phase function* (Mashayek and Pandya, 2003), $X(\mathbf{x}, t)$, and averaged with help of Eqn. 2.4 after-

wards. This operation can be written as

$$\langle \cdot \rangle^{\mathcal{V}} = \langle X(\mathbf{x}, t) \cdot \rangle^{V} \tag{2.11}$$

where $\langle \cdot \rangle^{\mathcal{V}}$ is the two-phase volume average operator. Note the notation of the single-phase volume average operator $\langle \cdot \rangle^{V}$ and that of the two-phase volume average operator $\langle \cdot \rangle^{\mathcal{V}}$. The latter is introduced to omit writing the multiplication with $X(\mathbf{x}, t)$ for simplicity. For dispersed two-phase flows, the phase indicator function can be defined twofold, either associated to the continuous or the dispersed phase as follows

$$X_{c,d}(\mathbf{x}, t) = \begin{cases} 1 & \text{if } \mathbf{x} \in V_{c,d} \\ 0 & \text{otherwise} \end{cases} \tag{2.12}$$

This means, it adopts unity if the associated phase is present at location $\mathbf{x}$ and is zero elsewhere. When $X(\mathbf{x}, t)$ is written without index, the corresponding relation is equivalently valid for both phases. A phase averaged quantity is obtained by

$$\langle \psi \rangle^{\mathcal{V}} = \langle \psi(\mathbf{x}, t) \rangle^{\mathcal{V}} = \frac{1}{V} \iiint_{V} X(\boldsymbol{\xi}, t) \psi(\boldsymbol{\xi}, t) \mathrm{d}\boldsymbol{\xi} \, . \tag{2.13}$$

By applying the two-phase volume average, equations are obtained for each phase, formally similar to the original Navier-Stokes equations but containing a new quantity α_c or α_d, the so-called *volume fraction* of the continuous and dispersed phase, respectively. These are formally obtained by

$$\langle 1 \rangle^{\mathcal{V}}_{c,d} = \langle X_{c,d}(\mathbf{x}, t) \rangle^{V} = \frac{1}{V} \iiint_{V} X_{c,d}(\boldsymbol{\xi}, t) \, \mathrm{d}\boldsymbol{\xi} = \alpha_{c,d} \, . \tag{2.14}$$

Hence, if only two phases[7] are present, $\alpha_c = 1 - \alpha_d$. If the dispersed phase is gaseous, α_c is also called *void fraction*. The two-fluid equations itself obtained from this procedure are not of interest at this point, although this concept is part of the methodology used below to derive the gas phase equations used in this work (Section 3.1).

[7] In case that one want to distinguish between different fluids per phase, additional fluid volume fractions might be defined.

Normalising the averaged value with the volume occupied only by one phase yields[8]

$$\langle\psi\rangle_{c,d}^{\mathcal{V}_{c,d}} = \langle\psi(\mathbf{x},t)\rangle_{c,d}^{\mathcal{V}_{c,d}} = \frac{1}{V_{c,d}} \iiint_V X_{c,d}(\boldsymbol{\xi},t)\psi(\boldsymbol{\xi},t)\mathrm{d}\boldsymbol{\xi}\ , \tag{2.15}$$

with the relations

$$\langle\psi\rangle_{c,d}^{\mathcal{V}} = \alpha_{c,d}\langle\psi\rangle_{c,d}^{\mathcal{V}_{c,d}}\ . \tag{2.16}$$

In contrast to single phase flows, where the integration over the convolution product is commutative with the spatial derivative, this does not hold in two-phase flows containing the interface described by $X(\mathbf{x},t)$, which is neither homogeneous in time and space nor isotropic or localised (in contrast to G, see Section 2.3.3). Additional calculation rules must be applied. For time derivatives Leibniz' theorem applies, i.e.

$$\left\langle\frac{\partial\psi}{\partial t}\right\rangle^{\mathcal{V}} = \frac{\partial\langle\psi\rangle^{\mathcal{V}}}{\partial t} - \frac{1}{V}\iint_S \mathbf{u}_s(\boldsymbol{\xi}_s,t)\psi(\boldsymbol{\xi}_s,t)\,\mathrm{d}\boldsymbol{\xi}_s\ , \tag{2.17}$$

where S is the interface, $\mathbf{u}_s(\boldsymbol{\xi}_s,t)$ the velocity of the interface relative to the velocity of the gas phase at the interface, $\boldsymbol{\xi}_s$ the subset of $\mathbf{x}$ located at the surface and $\mathrm{d}\boldsymbol{\xi}_s = \mathrm{d}\xi_{s,1}\mathrm{d}\xi_{s,2}\mathrm{d}\xi_{s,3}$. For spatial derivatives, Gauss' theorem applies, which reads

$$\langle\nabla\psi\rangle^{\mathcal{V}} = \nabla\langle\psi\rangle^{\mathcal{V}} + \frac{1}{V}\iint_S \psi(\boldsymbol{\xi}_s,t)\,\mathrm{d}\boldsymbol{\xi}_s\ . \tag{2.18}$$

If one aims for averaged quantities of the particle properties when applying the volume average to a dispersed two-phase flow, the average volume must be much larger than the particle size and even the average particle-particle distance to ensure proper continuum statistics for the dispersed phase, but much smaller than the scale of spatial change

[8] Formally, it is possible to write $\frac{1}{V_{c,d}}\iiint_V X_{c,d}(\boldsymbol{\xi},t)\psi(\boldsymbol{\xi},t)\mathrm{d}\boldsymbol{\xi} = \frac{1}{V_{c,d}}\iiint_{V_{c,d}} \psi(\boldsymbol{\xi},t)\mathrm{d}\boldsymbol{\xi}$, however, this notation implies inaccuracies related to the correct treatment of the interface jump condition and should be therefore avoided.

of the mixture properties[9]. This issue can become challenging and must be verified for each specific case. Discussion on the relation between the size of the averaging volume and the discretised volumes of the computational mesh as well as treatment of the lost information about the sub-volume scales is discussed in Section 2.5.4.

2.5.2 A Variation of the Classical Volume Average Using Point Particles

Actually implying more characteristics of the ensemble average than the volume average, the averaging procedure shown by Crowe et al. (1998) uses elements of both types, but can be applied only to the dispersed phase. Simply said, the ensemble consists of all particles present in the averaging volume V. In contrast to the "classical" volume average as described before, here the particles are treated as 0-dimensional, i.e. having constant properties throughout the volume of each particle. The description, however, keeps the particle volume in order to consider their volume fraction in the continuous phase equations. The ensemble average of the quantity ψ of all particles k present in the averaging volume V reads

$$\langle \psi(\mathbf{x}, t) \rangle^E = \frac{1}{N} \sum_{k=1}^{N} \psi_k(\mathbf{x}_k, t) \,, \tag{2.19}$$

where N is the number of particles in the volume and k is the index of the particles, i.e. $1 \leq k \leq N$. Transport equations of the particle cloud, i.e. all particles present within the averaging volume, result from applying this average on the particle transport equations 3.36 to 3.39 as given in Section 3.2.1 later on. For example, considering only drag and gravity, the application of this volume average to the particle equation of motion reads

$$\frac{1}{N} \sum_{k=1}^{N} \frac{d\mathbf{v}_k}{dt} = \frac{1}{N} \sum_{k=1}^{N} \frac{\mathbf{u}_c|_{\mathbf{x}_k} - \mathbf{v}_k}{\boldsymbol{\tau}_k} + \frac{1}{N} \sum_{k=1}^{N} \mathbf{g} \,, \tag{2.20}$$

[9] In general, the applicability and validity of the volume average is not limited to a certain range of particle size/averaging volume ratios.

which, written in Eulerian framework, yields after some manipulation (see Crowe et al., 1998, Carneiro, 2012):

$$\frac{\partial \alpha_d \mathbf{u}_d}{\partial t} + \nabla \cdot (\alpha_d \mathbf{u}_d \mathbf{u}_d) = \alpha_d \frac{\mathbf{u}_c - \mathbf{u}_d}{\boldsymbol{\tau}} + \alpha_d \mathbf{g} + \frac{1}{\rho_d} \Gamma \mathbf{u}_d \,, \tag{2.21}$$

where α_d is the volume fraction of the particles, $\mathbf{u}_c = \langle \mathbf{u}_c|_{\mathbf{x}_k} \rangle^E = \frac{1}{N} \sum_{k=1}^{N} \mathbf{u}_c|_{\mathbf{x}_k}$ is the mean of the continuous phase velocity at the position of the particle centre $\mathbf{x}_k$, $\mathbf{u}_d = \langle \mathbf{v}_k \rangle^E = \frac{1}{N} \sum_{k=1}^{N} \mathbf{v}_k$ is the mean of all particle velocities $\mathbf{v}_k$ and Γ is the mass exchange rate between the phases, e.g. due to evaporation or condensation.

2.5.3 Unified Volume Average/LES Filtering

In two-phase flows, two-continua equations can be derived by volume average, as described before. This operation yields spatial averaged equations for a given instant in time. In RANS, these equations have to be time averaged subsequently to obtain equations of the time-invariant two-phase flow field. With that, the mesh resolution must be chosen such that this steady state flow field is fully resolved. In LES, two spatial averaging procedures have to be conducted formally: first the volume average to obtain two-continua equations describing both phases, i.e. $\langle \cdot \rangle^{\mathcal{V}}$, and subsequently the filtering operation $\langle \cdot \rangle^F$ separately for each phase to remove the flow scales which cannot be resolved by the chosen mesh. In case, that the averaging volume of the phase-average operation is smaller than the filter size, this fact holds. However, when choosing the averaging volume to be of the same size as the filter width, the idea has been expressed to unify both operations, i.e. applying the volume average to the original two-phase flow field but using directly a variable weighting (Kaufmann, 2004, Sirignano, 2005, Carrara and DesJardin, 2006). A formalism to describe this idea mathematically has been proposed simultaneously by Sirignano (2005) and Carrara and DesJardin (2006).

In order to formulate this idea, we start with the definition of the volume average (Eqn. 2.13)

$$\langle \psi(\mathbf{x},t) \rangle^{\mathcal{V}} = \frac{1}{V} \iiint_V X(\boldsymbol{\xi},t)\psi(\boldsymbol{\xi},t)\,\mathrm{d}\boldsymbol{\xi}\ , \tag{2.22}$$

which, interpreted as filtering with a top hat filter $G_{\mathrm{TH}}(\mathbf{x}-\boldsymbol{\xi})$ having the compact support V, reads

$$\langle \psi(\mathbf{x},t) \rangle^{\mathcal{V}} = \iiint_V G_{\mathrm{TH}}(\mathbf{x}-\boldsymbol{\xi})X(\boldsymbol{\xi},t)\psi(\boldsymbol{\xi},t)\,\mathrm{d}\boldsymbol{\xi}\ , \tag{2.23}$$

$$\tag{2.24}$$

with

$$G_{\mathrm{TH}}(\mathbf{x}-\boldsymbol{\xi}) = \begin{cases} \frac{1}{V} & \text{if } \mathbf{x} \in V \\ 0 & \text{otherwise} \end{cases} \tag{2.25}$$

implying that

$$\iiint_V G_{\mathrm{TH}}(\mathbf{x}-\boldsymbol{\xi})\,\mathrm{d}\boldsymbol{\xi} = 1\ . \tag{2.26}$$

With that, G_{TH} can be replaced by any filter kernel G with compact support $supp(G) = V$ and fulfilling Eqn. 2.26. Including general filters with an infinite support, the combined operation can be finally written as

$$\langle \psi(\mathbf{x},t) \rangle^{\mathcal{VF}} = \iiint_\infty G(\mathbf{x}-\boldsymbol{\xi})X(\boldsymbol{\xi},t)\psi(\boldsymbol{\xi},t)\,\mathrm{d}\boldsymbol{\xi}\ . \tag{2.27}$$

Equation 2.23 results from the fact that the kernel function G is normalised, here consequently with V, wheres the indicator function X is not. Normalisation is achieved in the latter case (classical volume average) by dividing the integral by the average volume, which is not necessary when multiplying with a normalised filter.

Formally, the integration domain can be constrained to the domain occupied by only one of the two phases, i.e. Θ_c or Θ_d, where the explicit

notation of the indicator function can be avoided (e.g. Carrara and Desjardin, 2006). With help of that notation, the following relations can be obtained, here written for the continuous phase[10]

$$\begin{aligned}\langle 1\rangle_c^{\mathcal{VF}} &= \iiint_{\infty} G(\mathbf{x}-\boldsymbol{\xi})X_c(\boldsymbol{\xi},t)\,\mathrm{d}\boldsymbol{\xi} = \iiint_{\Theta_c} G(\mathbf{x}-\boldsymbol{\xi})\,\mathrm{d}\boldsymbol{\xi} \\ &= \langle 1\rangle^{V_cF} = \theta\ , \end{aligned} \tag{2.28}$$

where Θ_c is the space occupied by the continuous phase, θ is the volume fraction of the continuous phase (void fraction) and

$$\begin{aligned}\langle \psi(\mathbf{x},t)\rangle_c^{\mathcal{VF}} &= \iiint_{\infty} G(\mathbf{x}-\boldsymbol{\xi})X_c(\boldsymbol{\xi},t)\psi(\mathbf{x},t)\,\mathrm{d}\boldsymbol{\xi} = \iiint_{\Theta_c} G(\mathbf{x}-\boldsymbol{\xi})\psi(\mathbf{x},t)\,\mathrm{d}\boldsymbol{\xi} \\ &= \langle \psi(\mathbf{x},t)\rangle^{V_cF} = \theta\bar{\psi}(\mathbf{x},t)\ . \end{aligned} \tag{2.29}$$

Using this notation (the integration over Θ_c or Θ_d) helps to obtain the relations above, however, this formulation requires utmost attention to consider the interface jump conditions properly when deriving transport equations for the phases as already mentioned in Section 2.5.1. Since this can be achieved more naturally by keeping the indicator function and the integration over the total volume, the notation for the integration over only the partial volumes is not used from here on.

As in single phase flows, a density weighted average can be used, especially for the continuous phase (since we assume constant liquid/particle density throughout this thesis), which can be written as

$$\begin{aligned}\langle \rho(\mathbf{x},t)\psi(\mathbf{x},t)\rangle_c^{\mathcal{VF}} &= \iiint_{\infty} \rho(\boldsymbol{\xi},t)G(\mathbf{x}-\boldsymbol{\xi})X_c(\boldsymbol{\xi},t)\psi(\boldsymbol{\xi},t)\,\mathrm{d}\boldsymbol{\xi} \\ &= \theta(\mathbf{x},t)\bar{\rho}(\mathbf{x},t)\tilde{\psi}(\mathbf{x},t) = \theta\bar{\rho}\tilde{\psi}\ . \end{aligned} \tag{2.30}$$

The notation $\tilde{\cdot}$ is common in single phase, Favre-averaged fluid equations and is also used here to ease the reading of the equations. Keep in mind, however, it is the continuous phase equation of a two-phase flow,

[10] Since this procedure is used in this work later on for deriving the gas phase equations, all following relations within this section are given for the gas phase only (if not valid for both phases), for simplicity.

where the averaged variables have the same physical behaviour but represent a slightly different average.

For a proper application of this averaging method, the following requirements have to be met (where the first two applies independently for single phase flows as well):

- The size of the average/filter volumes should correspond to the size of the discretised volumes of the computational mesh. Refinement or coarsening of only one is not reasonable, since the resolution of the finer one cannot be kept by the coarser.

- Furthermore, if the averaging volumes are not homogeneous and isotropic (which is usually the case in praxis), averages of spatial derivatives must be handled properly. The larger the change of the volume from a cell to its adjacent cell, the larger the error becomes (see, e.g., Sirignano, 2010).

- As mentioned already in Section 2.5.1, the LES filter kernel is usually time and space invariant. The indicator function X_c, however, is time and space dependent (representing moving particles with different sizes), which requires, in contrast to single-phase filtering, careful treatment of the derivatives (Eqns. 2.17 and 2.18).

2.5.4 Challenges Using Micro- to Macroscale Models

Statistical Noise

A spatial average over a small volume of only a single realisation of the two-phase flow is usually based on only a few particles (especially in dilute dispersed flows, which applies in this work). This means that the convergence of the statistics can become very poor compared to those gained from a large number of dispersed phase realisations implying the same statistics for a given fluid flow realisation. The problem is, that in

averaging volumes, where only a few particles are present, the large gradients subsequently appearing in the particle mean fields may require sophisticated numerical treatment to ensure a stable simulation.

As an example, we consider a particle number density of the order of $1 \times 10^{10}\,\mathrm{m}^{-3}$, which corresponds to ten particles per mm^3 and which is a typical value of the spray inlet conditions of the experiments used to validate the numerical model (see Chapter 7). For computational cells of the size of around $1\,\mathrm{mm}^3$, this value is already marginal. However, in regions where the particle number density tends towards zero, the averaging volumes must be unrealistic large to meet the criteria of sufficient statistics. Significant improvement can be achieved when considering first an ensemble average over a large number of particle phase realisations before averaging over the volume (as discussed in Section 3.2.2).

For the physically continuous gas phase this issue relaxes, since a typical average volume contains a sufficient large number of fluid instances to deliver reasonable statistics (see Section 3.2.2 for references to the filtered density function approach in turbulent and/or reacting single phase flows).

Modelling of Sub-Volume Scales

Closure of the source terms which describe the sub-volume scale dynamics and the interaction of the dispersed phase with the continuous phase is a challenging task. Two-phase closure is a demanding task in general, but becomes excessively difficult when related to macroscale methods derived directly from microscale physics, due to the following reasons. First, applying a direct-micro-to-macro average complicates the identification and attribution of the numerous non-resolved phenomena originating from ensemble and spatial averages (Kaufmann, 2004, p. 50) as well as the phase space average[11], since they hide behind only one or a very few terms. Second, the closure of the sub-volume dispersed phase

[11] i.e. the phase space integration over the NDF transport equation to obtain moment equations, see Chapter 4

velocity correlation tensor(s) is difficult anyway, because the (dilute) dispersed phase is governed by physics significantly different to those of single phase turbulent stresses (see Section 2.2.3). Utmost differentiation of the physics and careful evaluation must be undertaken when aiming to use any kind of viscosity models as used in single-phase continuum flows. Obviously, the liquid itself behaves like a continuum, but this inner-particle flow is not of relevance when discussing the particle phase "stress term", which rather has characteristics of a pressure-less gas[12]. If at all, "any spatial correlation in the dispersed-phase motion is induced via particle interaction with the surrounding fluid motion" (from Février et al., 2005), for which models have to be developed. Further discussion on this topic has been given in Fox (2012) and will be undertaken later on when coming to the derivation of the stochastic equations and the moment closure.

Here again, these issues mainly apply to dispersed phases and relax when coming to proper continuous phases, especially when filtering a single continuous phase realisation only, as it is done here.

2.6 Stochastic Methods (Mesoscale)

As adumbrated in the previous section, physical and mathematical approximations cannot be distinguished in the volume average type models based on only a single dispersed flow realisation. Hence, it is convenient to introduce a mesoscale, which represents the intermediate step to separate the physical and the mathematical approximations. In dispersed multiphase flows, these two steps comprise first, the simplifications of the physics by reducing the full, microscopic flow structure around the particle and the detailed heat and mass transfer to 0-dimensional models, which describe the net effect as point sources for mass, momentum and energy. With that, each particle is described by a set of mesoscopic vari-

[12]To be clear: granular flows are of different nature, which motivates and justifies viscosity models, which have been established in this type of flow.

ables, e.g. particle mass, velocity, temperature, etc. The exchange of mass, momentum and heat is described globally (0-dimensional) for each particle and particle-particle interaction is considered using specific collision models. Subsequently, particles are sorted in phase space and particles with the same mesoscopic variables are counted, which yields a number density function f. The ensemble of particles of which f is built from can be based on at least three concepts:

1. At a given time instant, all particles within a certain volume are taken into account (volume average).

2. All particles flying by a certain point[13] in physical space are taken into account (time average). This is often what is measured in experiments.

3. For a certain point in physical space and for a given time instant, all particles with the same mesoscopic properties but different individual and chaotic residual components (ensemble average or average over realisations of the flow) are considered. Usually this is seen as the most comprehensive choice.

For f, a transport equation ("kinetic equation") can be derived (see Section 3.2.2, where a proper definition of f is given as well), which represents the mesoscopic equation of the particle dynamics. This equation can be solved on a mesoscopic level both, in a Lagrangian manner as well as in an Eulerian framework, or on a macroscopic level, when applying some mathematical simplifications (i.e. the (finite) number of moments considered). The multitude of methods for these approaches is described next for Lagrangian methods in Section 2.6.1 and Eulerian methods in Section 2.6.2.

[13] With typical measurement techniques, this "point" actually extends to a certain measurement volume, which in fact results in a kind of volume-time average.

2.6.1 Lagrangian and Eulerian Solution on the Mesoscopic Level

Lagrangian Methods

Two different Lagrangian methods must be distinguished: the *Discrete Particle Method/Simulation* (DPM/DPS) and the *Lagrangian-Monte-Carlo Approach*. First, the *Discrete Particle Method/Simulation* (DPM/DPS) tracks all physical particles present in the given flow realisation, either each particle individually or by substitutes for particles with identical properties (parcels, numerical particles). Each particle is described by its equations for motion, heat and mass conservation. Second, the *Lagrangian-Monte-Carlo Approach* (e.g. Massot, 2007, with reference to Dukowicz (1980)) or *Direct Simulation Monte Carlo* (DSMC), is a Lagrangian solution method (via statistical particles, i.e. samples) of the kinetic equation (transport equation for f). In contrast to the DPM, the latter considers particles of a large number of realisations. The "parcel" substitute for several similar stochastic particles can be applied here similarly (e.g. Bini and Jones, 2008). Some publications in literature are difficult to definitely relate to one or the other method. Hylkema and Villedieu (1998) and Liu et al. (2002) may be mentioned as examples for the Monte-Carlo approach, for the Discrete Particle Method, e.g., Miller and Bellan (1999, 2000), Okong'o and Bellan (2004), Almeida and Jaberi (2008).

Both methods have most of the notation in common for which the basics will be illustrated here. Either discrete or stochastic particles are transported using the Lagrangian particle transport equations including different levels of physics depending on the specific application. The Lagrangian particle transport equations for dilute spray applications are given later on in Section 3.2.1. To consider the particle dynamics in the gas phase equations, the individual particle contributions to mass, momentum and energy exchange between phases S_k are summed up for all particles N_V in each computational cell V and are introduced as source terms S in the conservation equations of the gas phase (e.g. Okong'o and

Bellan, 2004), here given for mass and momentum as

$$\frac{\partial \rho}{\partial t} + \nabla \cdot (\rho \mathbf{u}) = S_I \ , \tag{2.31}$$

$$\frac{\partial (\rho u)}{\partial t} + \nabla \cdot (\rho \mathbf{u}\mathbf{u}) = -\nabla p + \nabla \cdot \boldsymbol{\tau} + S_{II} \ , \tag{2.32}$$

where the source terms are of the type

$$S = \sum_{N_V} \frac{\omega_k}{V} S_k \ . \tag{2.33}$$

k is the index of the particles. ω_k is a weighting factor to determine the individual contribution of a particle to the different, neighbouring cell centres dependent on the distance in-between (*Particle-Source-In-Cell* method, i.a. in Evans and Harlow, 1957, Crowe et al., 1977, Bini and Jones, 2008).

Lagrangian particle tracking methods are widely used due to their capability to consider different mesoscopic variables, particle crossing and collision naturally and their low artificial dispersion of the trajectories. Research in this area has been started with particle tracking simulations without considering the non-resolved phase interaction. The purpose of these investigations was either to evaluate the physics a priory using Direct Numerical Simulation for the gas phase (e.g. Squires and Eaton, 1990, 1991a,b, Boivin et al., 1998, Mashayek, 1998a,b, Fede and Simonin, 2006, Réveillon et al., 2002, Reveillon and Demoulin, 2007) or to compare fully resolved simulation results with those of an a posteriori filtered DNS or those of a Large Eddy Simulation without considering sub-grid scale interaction (Yeh and Lei, 1991, Simonin et al., 1995, Wang and Squires, 1996a,b, Armenio et al., 1999, Deutsch and Simonin, 1991, Squires and Simonin, 2002, Yang and Lei, 1998, Armenio et al., 1999). Comparison of the performance of several unmodified sub-grid scale models for the gas phase has been carried out by Boivin et al. (2000). Subsequently, models based on modified sub-grid scale models for the gas phase have been proposed (Pannala and Menon, 1999, Mashayek and Jaberi, 1999, Miller and Bellan, 2000, Yuu et al., 2001, Sankaran and Menon, 2002). The state

of the art method, which are nowadays commonly used, is to incorporate a stochastic term in the Lagrangian particle transport equations, which models the instantaneous fluid phase velocity at the location of the individual particle, first proposed by Sommerfeld et al. (1993) and Minier and Peirano (2001), modified, extended and used by Shotorban and Mashayek (2005, 2006a,b), Peirano et al. (2006), Vinkovic et al. (2006), Almeida and Jaberi (2008), Laín and Grillo (2007), Pai and Subramaniam (2007), Bini and Jones (2008), Pozorski and Apte (2009), just to mention a few. A comprehensive overview can be found in Mashayek and Pandya (2003).

Challenges result from the numerical realisation of this method, i.e. load balance between processors, localisation and sorting algorithms, instabilities at high volume fractions, computational costs and statistical noise (see, e.g., Massot, 2007, Bini and Jones, 2008). Minier and Peirano (2001) give a critical discussion on the validity of comparing Lagrangian particle tracking methods with Eulerian macroscopic moment methods, especially concerning computational costs, since Lagrangian methods on the mesoscopic level maintain more information on the underlying physics than Eulerian methods on the macroscopic level (especially moment methods).

Eulerian Methods

Eulerian methods are usually associated with macroscale methods. However, the kinetic equation for f can be solved also on a mesoscopic level in Eulerian framework, although, to the authors knowledge, no application of this kind has been published for two-phase flows. As a relevant method, the stochastic fields approach (Valiño, 1998) can be mentioned, which has been successfully applied, e.g., for solving the PDF transport equation for mixture fraction and progress variable in single phase reacting flows (e.g. Garmory et al., 2006, Mustata et al., 2006, Jones and Navarro-Martinez, 2008, Jones and Prasad, 2009). One could consider the Multi-Fluid method (Laurent and Massot, 2001) as a mesoscopic solution

method of the kinetic equation, at least when using a large number of classes, which, however, is usually not the case due to enormous computational effort. Therefore, when using only a number of classes of the order of 10, the Multi-Fluid method represents rather a piece-wise integration over phase space (directly formulated as such e.g. in Bove et al., 2005). Hence we list this method under the macroscale methods in the next section.

2.6.2 Eulerian Solution on the Macroscopic Level (Moment Methods)

Moment methods owe their name to the mathematical background of "moments of a function". Moments are statistical information about the underlying function, the more moments are known, the more accurate the function can be characterised. Hence, solving transport equations for a certain number of moments of f, an approximate solution of the kinetic equation can be determined. All moment methods distinguish themselves basically by the order of moments considered and the number of mesoscopic variables (phase space).

The range of different types of moment methods is as wide as its multitude of applications. Moment methods may be categorised in "mean and variance" methods and moment methods using moments about zero (see Section 4.1.1 for definitions). In multiphase flow applications the latter type of moments is used more often, due to the easier derivation of transport equations and the characteristics of the moments itself (Section 4.1.2). A large variety of methods is governed by the class of Quadrature based Moment Methods (QbMM), e.g. the *Quadrature Method of Moments* (QMOM) and *Direct Quadrature Method of Moments* (DQMOM).

In order to define basic properties and to deepen this topic, types, structure and the connection between the various model variants are presented, with specific focus on their application in multiphase flows. Since in this work only the particle size-velocity space is of interest, we restrict ourselves on related publications. Therefore the discussion is divided

into mono-variate models (either velocity or size) and multi-variate models (either both, velocity and size, or additionally the continuous phase velocity). Specific moment methods are listed in the following without a description. New-to-the-topic readers might be referred to Section 4.5 and the literature given below. Especially the Quadrature based Moment Methods are discussed in that section in more detail, where some aspects can be clarified better with the knowledge and terminology founded in Chapter 4.

Considering Particle Size Space Only

In these methods, particles can have different sizes, which directly impact motion, vaporisation, condensation, heat transfer rates and collision dynamics, among others. Particle trajectory crossing effects, however, cannot be considered, since particles have the same velocity locally, which is, however, still variable in time and space[14].

- Multi-Fluid: Laurent and Massot (2001), Laurent et al. (2004), Massot (2007) and references therein.
- PMOM: Beck (2000), Beck and Watkins (2002, 2003), Watkins (2007); closure is obtained assuming the shape of the NDF as Rosin Rammler or log-normal distributions. Gharaibah and Polifke (2004); transport of mean and variance of the particle diameter.
- QMOM: McGraw (1997), McGraw and Wright (2003), Marchisio et al. (2003a), Marchisio et al. (2003b), Petitti et al. (2010).
- DQMOM mono-variate: Marchisio and Fox (2005), Zucca et al. (2006), Mazzei et al. (2010), Chan et al. (2010).
- DQMOM bi-variate in volume and surface: Wright Jr. et al. (2001), Marchisio and Fox (2005), Fox (2006).
- Maximum Entropy: Kah et al. (2010), in Gumprich and Sadiki (2012) as post-processing for QMOM.

[14] In contrast, multi-velocity models are often monodisperse in particle size globally.

Considering Particle Velocity Space Only

Models considering the velocity space only, are naturally monodisperse in size, i.e. particles can have different velocities locally but feature the same size (in non-vaprorising flows usually even globally). With that, trajectory crossing effects are possible to describe to an extent, that depends on the number of moments considered.

- Mean and variance: Mesoscopic Eulerian Formalism (MEF) Février et al. (2005).
- MOM: Zhang and Prosperetti (1994, 1997).
- QMOM mono-variate: Le Lostec et al. (2008).
- DQMOM mono-variate: Desjardins et al. (2008), two-node in velocity.

Considering Particle Velocity and Size Space

Considering both, size and velocity space, challenges some of the methods, since available mathematical reconstruction algorithms for the moments or the NDF are not suitable for two-dimensional phase spaces. Therefore, many methods dealing with two property coordinates are either hybrid methods, often Multi-Fluid methods combined with Quadrature based Moment Methods, or make simplifications in order to be able to use the reconstruction algorithms (e.g. the PD-algorithm in QMOM).

- Multi-Fluid in size space, mean and variance in velocity space: Massot (2007), Vié et al. (2010).
- Multi-Fluid in size space, QMOM in velocity space: de Chaisemartin et al. (2008), Kah et al. (2010).
- QMOM in size, Multi-Fluid in velocity space: Fan et al. (2004).
- QMOM bi-variate in volume and velocity: Yoon and McGraw (2004).

- DQMOM size-conditioned-velocity: Fox et al. (2008), DQMOM in size and single node in velocity, i.e. $\mathbf{u}(D)$.
- PMOM size-conditioned-velocity: Bollweg et al. (2007), Carneiro et al. (2010), Dems et al. (2012a,b).

Considering Particle/Fluid Velocity and Particle Size Space

The most comprehensive methods in terms of phase space consider also fluid phase quantities as phase space variables in addition to the dispersed phase quantities.

- Joint particle-fluid-velocity-size-PDF: Minier and Peirano (2001), Carrara and DesJardin (2006).
- Joint particle-fluid-velocity-PDF: Belt and Simonin (2009), Wunsch et al. (2009).

3 Gas and Dispersed Phase Equations

The different approaches to derive two-phase flow equations have been detailed in the last chapter. In this chapter we make use of some of these methods to derive the set of two-phase flow equations which have been utilised in this work. The chapter is split into two parts, first the derivation of the gas phase equations is shown, which is followed by that of the dispersed phase equations. In fact, when deriving the gas phase equations the source terms describing the interaction between both phases remain unclosed in the first instance, but will be closed afterwards from the point of view of the dispersed phase. Furthermore, the actual mathematical treatment of the dispersed phase kinetic transport equation, which will present the final result in this chapter, will be carried out in Chapter 4, where it is integrated over phase space to obtain macroscopic moment equations.

3.1 Gas Phase Equations

Our aim is to derive a closed equation set which can be numerically solved using Large Eddy Simulation. This means that any scale which cannot be resolved by the numerical mesh has to be removed from the equations and be replaced by terms which mimic their impact on the dynamics of the resolved scales. To derive the gas phase equations, we make use of the ideas and the formalism given by Carrara and DesJardin (2006) and Sirignano (2005, 2010) to unify the volume average method and the filtering operation. As discussed in Section 2.5, this approach is a direct micro- to macroscopic model, which is appropriate for continuous phases but shows significant disadvantages for (dilute) dispersed phases.

Hence, we do not apply this method to the dispersed phase, although this has been done accordingly by Sirignano (2010), due to the reasons discussed in Section 2.5.4. An additional aspect to those mentioned there comes into play when considering polydispersity, particle collisions, coalescence and breakup. To include these effects a separate population balance equation must be solved anyway. Using the stochastic approach, they can be included directly into the kinetic equation, which is done in this work (Section 3.2).

In the following, the phase filtering of the instantaneous gas phase field equations is shown, closely following Sirignano (2010). Throughout the following chapters, gas/continuous/fluid phase quantities do not have indices. They cannot be mistaken for phase averaged quantities[1], since the latter do not occur. Applying the $\langle \cdot \rangle^{\mathcal{VF}}$ operator, as defined in Section 2.5.3, to the Navier-Stokes equations yields filtered gas phase equations for the conservation of mass, momentum and energy as follows.

3.1.1 Continuity

$$\langle \frac{\partial \rho}{\partial t} \rangle^{\mathcal{VF}} + \langle \frac{\partial}{\partial x_j}(\rho u_j) \rangle^{\mathcal{VF}} = 0 \,, \tag{3.1}$$

$$\frac{\partial}{\partial t}(\theta \bar{\rho}) + \frac{\partial}{\partial x_j}(\theta \bar{\rho} \tilde{u}_j) = \Gamma \,, \tag{3.2}$$

with the unknown term on the rhs, Γ, given by

$$\Gamma \overset{\text{def.}}{=} \iint_S G(\mathbf{x} - \mathbf{x}_s) \rho(\mathbf{x}_s, t) \left[u_j(\mathbf{x}_s, t) - u_{s,j}(\mathbf{x}_s, t) \right] \, \mathrm{d}S_j \,. \tag{3.3}$$

The interface normal component of the difference between the gas phase velocity at the interface $\mathbf{u}(\mathbf{x}_s, t)$ and the velocity of the interface $\mathbf{u}_s(\mathbf{x}_s, t)$ is the so-called *Stefan velocity*. Therefore, the mass flow rate density Γ gives the mass exchange between phases and can be modelled using, e.g., the

[1] i.e. "mixture quantities" based on a weighted average of gas and dispersed phase quantities, but can represent gas mixtures of different species (also including the vapour fraction as in Section 5.3.2)

D^2 law for vaporising droplets. $\mathbf{x}_s$ is the subset of the coordinate vectors $\mathbf{x}$ and locates the points on the interfaces and $\mathrm{d}S_j$ are the components of the normal interfacial area vector pointing into the gas phase.

3.1.2 Momentum

$$\begin{aligned}\langle\frac{\partial}{\partial t}(\rho u_i)\rangle^{\mathcal{VF}} + \langle\frac{\partial}{\partial x_j}(\rho u_i u_j)\rangle^{\mathcal{VF}} = &-\langle\frac{\partial p}{\partial x_i}\rangle^{\mathcal{VF}} + \langle\frac{\partial \tau_{ij}}{\partial x_j}\rangle^{\mathcal{VF}} \\ &+ \langle\rho g_i\rangle^{\mathcal{VF}}\,, \end{aligned} \tag{3.4}$$

$$\begin{aligned}\frac{\partial}{\partial t}(\theta\bar{\rho}\tilde{u}_i) + \frac{\partial}{\partial x_j}(\theta\bar{\rho}\tilde{u}_i\tilde{u}_j) = &-\theta\frac{\partial \bar{p}}{\partial x_i} + \theta\frac{\partial \bar{\tau}_{ij}}{\partial x_j} + \frac{\partial}{\partial x_j}(\theta\tau^t_{ij}) \\ &- \mathrm{M}_i + \Gamma\,\bar{u}_{d,j} \\ &+ \theta\bar{\rho}g_i\,, \end{aligned} \tag{3.5}$$

implying that

$$\iint_S G(\mathbf{x}-\mathbf{x}_s)\rho(\mathbf{x}_s,t)u_i(\mathbf{x}_s,t)\left[u_j(\mathbf{x}_s,t) - u_{s,j}(\mathbf{x}_s,t)\right]\,\mathrm{d}S_j \approx \Gamma\,\bar{u}_{d,j}(\mathbf{x},t) \tag{3.6}$$

and

$$\begin{aligned}\mathrm{M}_i &\overset{\text{def.}}{=} \iint_S G(\mathbf{x}-\mathbf{x}_s)\tau_{ij}(\mathbf{x}_s,t)\,\mathrm{d}S_j - \iint_S G(\mathbf{x}-\mathbf{x}_s)p(\mathbf{x}_s,t)\,\mathrm{d}S_j + \bar{p}\frac{\partial\theta}{\partial x_i} - \bar{\tau}_{ij}\frac{\partial\theta}{\partial x_j} \\ &= \iint_S G(\mathbf{x}-\mathbf{x}_s)\left(\left[\tau_{ij}(\mathbf{x}_s,t) - \delta_{ij}p(\mathbf{x}_s,t)\right] - \left[\bar{\tau}_{ij}(\mathbf{x}_s,t) - \delta_{ij}\bar{p}(\mathbf{x}_s,t)\right]\right)\,\mathrm{d}S_j\,. \end{aligned} \tag{3.7}$$

The first term approximation can be argued (Sirignano, 2010, p. 211), however, as discussed before, we abstain from a detailed evaluation at this point, since phase interaction source terms are detailed from the particle phase side. The second term M_i represents the aerodynamic force on the particles, which consists of pressure and viscous forces. Finally, the

unknown correlation of sub-grid scale gas phase velocity fluctuations, i.e. the turbulent stresses

$$\tau_{ij}^{t} \overset{\text{def.}}{=} \bar{\rho}\tilde{u}_i\tilde{u}_j - \overline{\rho u_i u_j} \tag{3.8}$$

can be closed by using standard single phase turbulence closures when neglecting turbulence modulation by the particles and assuming that particles are smaller than the Kolmogorov scale.

3.1.3 Species

$$\langle\frac{\partial}{\partial t}(\rho Y_m)\rangle^{\mathcal{VF}} + \langle\frac{\partial}{\partial x_j}(\rho Y_m u_j)\rangle^{\mathcal{VF}} + \langle\frac{\partial}{\partial x_j}(\rho Y_m V_{m,j})\rangle^{\mathcal{VF}} = \langle\rho\dot{\omega}_m\rangle^{\mathcal{VF}} \ , \tag{3.9}$$

$$\frac{\partial}{\partial t}(\theta\bar{\rho}\tilde{Y}_m) + \frac{\partial}{\partial x_j}(\theta\bar{\rho}\tilde{Y}_m\tilde{u}_j) + \frac{\partial}{\partial x_j}(\theta\bar{\rho}\tilde{Y}_m\tilde{V}_{m,j}) = \langle\rho\dot{\omega}_m\rangle^{\mathcal{VF}} + \frac{\partial}{\partial x_j}(\mathrm{j}_{m,j}^{t} + j_{m,j}^{t}) + \Gamma\epsilon_m \ , \tag{3.10}$$

with $\mathrm{j}_{m,j}^{t}$ and $j_{m,j}^{t}$ being the turbulent dispersion and turbulent diffusion flux vectors, respectively,

$$\mathrm{j}_{m,j}^{t} = \theta\bar{\rho}\tilde{Y}_m\tilde{u}_j - \langle\rho Y_m u_j\rangle^{\mathcal{VF}} \ , \tag{3.11}$$

$$j_{m,j}^{t} = \theta\bar{\rho}\tilde{Y}_m\tilde{V}_{m,j} - \langle\rho Y_m V_{m,j}\rangle^{\mathcal{VF}} \ , \tag{3.12}$$

and the fractional mass exchange for each individual species

$$\Gamma\epsilon_m \overset{\text{def.}}{=} \iint_S G(\mathbf{x}-\mathbf{x}_s)\rho(\mathbf{x}_s,t)Y_m(\mathbf{x}_s,t)\left[u_j(\mathbf{x}_s,t) - u_{s,j}(\mathbf{x}_s,t) + V_{m,j}(\mathbf{x}_s,t)\right]\,\mathrm{d}S_j \ , \tag{3.13}$$

where ϵ_m is the fraction of the total mass flow rate density to species m. Clearly, if the droplet consists only of one species (single-component fuel), $\epsilon_{fuel} = 1$, i.e. the full mass flow rate density, Γ, transfers to the fuel vapour species, and $\epsilon_m = 0$ for all other species.

Usually, the diffusion flux $j_j = \rho Y_m V_{m,j}$ of species m is approximated with the spatial gradient of the species mass fraction Y_m times a diffusion coefficient $\mathfrak{D}_m$ of species m into the mixture (Fickian diffusion) as

$$j_j = \rho Y_m V_{m,j} \approx -\rho \mathfrak{D}_m \frac{\partial Y_m}{\partial x_j} \,. \tag{3.14}$$

Often, to simplify the system even more, $\mathfrak{D}_m$ is set equal for all species $\mathfrak{D}_m = \mathfrak{D}$, as long as the given physical phenomenon does not strongly depend on diffusion velocities of individual species significantly different from the others[2]. With that, Eqn. 3.10 can be simplified to

$$\frac{\partial}{\partial t}(\theta\bar{\rho}\tilde{Y}_m) + \frac{\partial}{\partial x_j}(\theta\bar{\rho}\tilde{Y}_m\tilde{u}_j) - \frac{\partial}{\partial x_j}(\theta\bar{\rho}\,\mathfrak{D}\frac{\partial \tilde{Y}_m}{\partial x_j}) = \langle\rho\dot{\omega}_m\rangle^{\mathcal{VF}} + \frac{\partial \mathrm{j}^t_{m,j}}{\partial x_j} + \Gamma^*\epsilon_m \,. \tag{3.15}$$

In turbulent flows, the molecular diffusion term can be arguably neglected entirely compared to the turbulent dispersion

$$\frac{\partial}{\partial x_j}(\theta\bar{\rho}\,\mathfrak{D}\frac{\partial \tilde{Y}_m}{\partial x_j}) \ll \frac{\partial \mathrm{j}^t_{m,j}}{\partial x_j} \tag{3.16}$$

and $\mathrm{j}^t_{m,j}$ can be modelled as

$$\mathrm{j}^t_{m,j} = \theta\bar{\rho}\tilde{Y}_m\tilde{u}_j - \langle\rho Y_m u_j\rangle^{\mathcal{VF}} \approx \theta\bar{\rho}\nu_t\frac{\partial \tilde{Y}_m}{\partial x_j} \overset{\text{or}}{\approx} \theta\bar{\rho}\frac{\nu_t}{\mathrm{Sc}_t}\frac{\partial \tilde{Y}_m}{\partial x_j} \,, \tag{3.17}$$

where the turbulent dispersion of Y_m is actually modelled as an increased diffusion using the turbulent diffusion coefficient ν_t as known from turbulence closure. This turbulent diffusion coefficient can be modified using a turbulent Schmidt number Sc_t to better approximate the physics (see, e.g., Poinsot and Veynante, 2005).

Γ^* is formally different from Γ and reads using the Fickian diffusion ap-

[2] A typical example, where this assumption is not valid, is the case of laminar hydrogen diffusion flames.

proximation

$$\iint_S G(\mathbf{x}-\mathbf{x}_s)\rho(\mathbf{x}_s,t)Y_m(\mathbf{x}_s,t) \left[u_j(\mathbf{x}_s,t)-u_{s,j}(\mathbf{x}_s,t)-\mathfrak{D}\frac{\nabla Y_m(\mathbf{x}_s,t)}{Y_m(\mathbf{x}_s,t)}\right] \mathrm{d}S_j \approx \Gamma^* \epsilon_m \ . \quad (3.18)$$

Finally the species transport equation reads

$$\frac{\partial}{\partial t}(\theta\bar{\rho}\tilde{Y}_m)+\frac{\partial}{\partial x_j}(\theta\bar{\rho}\tilde{Y}_m\tilde{u}_j)-\frac{\partial}{\partial x_j}(\theta\bar{\rho}(\mathfrak{D}+\frac{\nu_t}{\mathrm{Sc}_t})\frac{\partial\tilde{Y}_m}{\partial x_j})=\langle\rho\dot{\omega}_m\rangle^{\mathcal{VF}}+\Gamma^*\epsilon_m \ . \quad (3.19)$$

Summarising the unknowns so far yields the two phase interaction terms Γ and M, whose closure is shown along with the derivation of the dispersed phase equations, and the filtered reaction rate $\langle\rho\dot{\omega}_m\rangle^{\mathcal{VF}}$ of species m, which closure is detailed in Chapter 5. In this work we consider single component fuels only, so $\epsilon_m = 1$ given that m is the fuel vapour species.

3.1.4 Energy

The gas phase energy equation will be developed for the sensible enthalpy[3] h. Its connection with the inner energy e and the total energy (without chemical energy) $E = e + {}^{k}/_{\rho}$, where k is the kinetic energy, can be found in Appendix A.1.1. The balance equation for the sensible enthalpy of the gas phase reads

$$\frac{\partial}{\partial t}(\rho h)+\frac{\partial}{\partial x_j}(\rho h u_j)+\frac{\partial \dot{q}_{\mathrm{rad}}}{\partial x_j}+\frac{\partial}{\partial x_j}\left(\sum_m \rho Y_m V_{m,j} h_m\right) = \frac{dp}{dt}+\frac{\partial}{\partial x_j}\left(\lambda\frac{\partial T}{\partial x_j}\right)+\tau_{ij}\frac{\partial u_i}{\partial x_j}+\sum_m \rho\dot{\omega}_m Q_m \ . \quad (3.20)$$

[3]This choice has been made due to the fact, that the relevant packages of the CFD software OpenFOAM, which has been used for the simulations, are based on the sensible enthalpy.

Simplifying by using Fickian diffusion and neglecting radiation yields after applying the phase filtering

$$\begin{aligned}\langle\frac{\partial}{\partial t}(\rho h)\rangle^{\mathcal{VF}} + \langle\frac{\partial}{\partial x_j}(\rho h u_j)\rangle^{\mathcal{VF}} - \langle\frac{\partial}{\partial x_j}\left(\sum_m \rho\mathfrak{D}_m(\frac{\partial Y_m}{\partial x_j})h_m\right)\rangle^{\mathcal{VF}} \\ = \langle\frac{dp}{dt}\rangle^{\mathcal{VF}} + \langle\frac{\partial}{\partial x_j}\left(\lambda\frac{\partial T}{\partial x_j}\right)\rangle^{\mathcal{VF}} + \langle\tau_{ij}\frac{\partial u_i}{\partial x_j}\rangle^{\mathcal{VF}} + \langle\sum_m \rho\dot{\omega}_m Q_m\rangle^{\mathcal{VF}}\ , \quad (3.21)\end{aligned}$$

where the result will be dealt with term by term:

Temporal Derivative

$$\langle\frac{\partial}{\partial t}(\rho h)\rangle^{\mathcal{VF}} = \frac{\partial}{\partial t}(\theta\bar{\rho}\tilde{h}) + \iint_S G(\mathbf{x}-\boldsymbol{\xi})\rho(\boldsymbol{\xi},t)h(\boldsymbol{\xi},t)u_{s,j}(\boldsymbol{\xi},t)\,\mathrm{d}S_j \quad (3.22)$$

The unknown surface integral will be dealt with later on, along with further surface integrals stemming from the other terms.

Convective Term

$$\begin{aligned}\langle\frac{\partial}{\partial x_j}(\rho h u_j)\rangle^{\mathcal{VF}} &= \frac{\partial}{\partial x_j}(\langle\rho h u_j\rangle^{\mathcal{VF}}) - \iint_S G(\mathbf{x}-\boldsymbol{\xi})\rho(\boldsymbol{\xi},t)h(\boldsymbol{\xi},t)u_j(\boldsymbol{\xi},t)\,\mathrm{d}S_j \\ &= \frac{\partial}{\partial x_j}(\theta\bar{\rho}\tilde{h}\tilde{u}_j) - \iint_S G(\mathbf{x}-\boldsymbol{\xi})\rho(\boldsymbol{\xi},t)h(\boldsymbol{\xi},t)u_j(\boldsymbol{\xi},t)\,\mathrm{d}S_j \\ &\quad + \frac{\partial}{\partial x_j}(\langle\rho h u_j\rangle^{\mathcal{VF}} - \theta\bar{\rho}\tilde{h}\tilde{u}_j)\ , \quad (3.23)\end{aligned}$$

where the divergence of the turbulent energy flux $\frac{\partial}{\partial x_j}(\langle \rho h u_j \rangle^{\mathcal{VF}} - \theta \bar{\rho} \tilde{h} \tilde{u}_j)$ is a purely single phase correlation, which can be modelled as

$$\frac{\partial}{\partial x_j}(\langle \rho h u_j \rangle^{\mathcal{VF}} - \theta \bar{\rho} \tilde{h} \tilde{u}_j) \approx \frac{\partial}{\partial x_j} \left(\frac{\bar{\rho} \nu_t}{\mathrm{Pr}_t} \left(\frac{\partial}{\partial x_j}(\theta \tilde{h}) - \underbrace{\iint_S G h \, \mathrm{d}S_j}_{\text{assumed to be = 0}} \right) \right) , \tag{3.24}$$

where η_t is the turbulent viscosity provided by the turbulence model and the turbulent Prandtl number Pr_t is a model constant, usually with a value close to Pr.

Species Diffusion

The heat transport due to molecular diffusion (Dufour effect) would yield

$$\begin{aligned} \langle \frac{\partial}{\partial x_j} \left(\sum_m \rho \mathfrak{D}_m (\frac{\partial Y_m}{\partial x_j}) h_m \right) \rangle^{\mathcal{VF}} = \frac{\partial}{\partial x_j} \left(\sum_m \langle \rho \mathfrak{D}_m (\frac{\partial Y_m}{\partial x_j}) h_m \rangle^{\mathcal{VF}} \right) \\ - \iint_S G(\mathbf{x} - \boldsymbol{\xi}) \sum_m \left(\rho \mathfrak{D}_m (\frac{\partial Y_m}{\partial x_j}) h_m \right) \mathrm{d}S_j , \end{aligned} \tag{3.25}$$

but can be usually neglected (Gerlinger, 2005, p. 23), which is done here for simplicity, i.e.

$$\frac{\partial}{\partial x_j} \left(\sum_m \langle \rho \mathfrak{D}_m (\frac{\partial Y_m}{\partial x_j}) h_m \rangle^{\mathcal{VF}} \right) \approx 0 . \tag{3.26}$$

Pressure Term

The phase space average of the pressure term has been developed by Sirignano (2010) as

$$\begin{aligned}\langle\frac{dp}{dt}\rangle^{\mathcal{VF}} &= \langle\frac{\partial p}{\partial t} + u_j\frac{\partial p}{\partial x_j}\rangle^{\mathcal{VF}} \\ &= \theta\left(\frac{\partial \bar{p}}{\partial t} + \tilde{u}_j\frac{\partial \bar{p}}{\partial x_j}\right) - \underbrace{\left(\theta\tilde{u}_j\frac{\partial \bar{p}}{\partial x_j} - \langle u_j\frac{\partial p}{\partial x_j}\rangle^{\mathcal{VF}}\right)}_{\stackrel{\text{def.}}{=}\Delta_g} \\ &\quad + \underbrace{\bar{p}\frac{\partial \theta}{\partial t} + \iint\limits_S G(\mathbf{x}-\boldsymbol{\xi})p(\boldsymbol{\xi},t)u_{s,j}(\boldsymbol{\xi},t)\,\mathrm{d}S_j}_{S_* \stackrel{\text{def.}}{=} \iint\limits_S G(\mathbf{x}-\boldsymbol{\xi})(p(\boldsymbol{\xi},t)-\bar{p}(\mathbf{x},t))u_{s,j}(\boldsymbol{\xi},t)\,\mathrm{d}S_j}\,,\end{aligned} \tag{3.27}$$

where the first term on the rhs is the total derivative of the filtered pressure

$$\theta\left(\frac{\partial \bar{p}}{\partial t} + \tilde{u}_j\frac{\partial \bar{p}}{\partial x_j}\right) = \theta\frac{d\bar{p}}{dt}\,. \tag{3.28}$$

S_* is the pressure work done by the particle on the gas or vice versa in case of mass exchange, i.e. a regressing or advancing interface. Otherwise $S_* = 0$ either. Following the argumentation of Sirignano (2010), Δ_g is proportional to the Mach number up to the power of 2 and S_* to the square of the Mach number as well, hence both can be neglected for low Mach number flow.

Heat Transfer

The energy transfer due to conduction can be simplified to (Gerlinger, 2005, Poinsot and Veynante, 2005):

$$\frac{\partial}{\partial x_j}\langle\lambda\frac{\partial T}{\partial x_j}\rangle^{\mathcal{VF}} = \frac{\partial}{\partial x_j}\langle\frac{\rho\nu}{\mathrm{Pr}}\frac{\partial h}{\partial x_j}\rangle^{\mathcal{VF}} \approx \frac{\partial}{\partial x_j}\left(\frac{\bar{\rho}\bar{\nu}}{\mathrm{Pr}}\left(\frac{\partial}{\partial x_j}(\theta\tilde{h}) - \iint\limits_S Gh\,\mathrm{d}S_j\right)\right)\,, \tag{3.29}$$

where the surface integral is approximately zero and the sub-grid scale fluctuation of the viscosity is neglected.

Viscous Dissipation

The viscous work is neglected (Gerlinger, 2005, Sirignano, 2010), i.e.

$$\langle \tau_{ij} \frac{\partial u_i}{\partial x_j} \rangle^{\mathcal{VF}} \approx 0 \; . \tag{3.30}$$

Chemical Heat Source

The standard enthalpy of formation Q_m is a constant, which yields

$$\langle \sum_m \rho \dot{\omega}_m Q_m \rangle^{\mathcal{VF}} = \sum_m \langle \rho \dot{\omega}_m \rangle^{\mathcal{VF}} Q_m \; . \tag{3.31}$$

Finally the surface integrals are added and modelled as

$$\iint_S G \left(\rho h \left(u_j - u_{s,j} \right) - \lambda \frac{\partial T}{\partial x_j} - \sum_m \left(\rho \mathfrak{D}_m \frac{\partial Y_m}{\partial x_j} h_m \right) \right) \approx \Gamma (\bar{h}_s - q_{gl}) \; , \tag{3.32}$$

where $\bar{h}_s$ is the filtered specific gas enthalpy at the droplet surface and q_{gl} is the total specific heat transferred to the droplet, from which a part is used for droplet heat up and the remaining for vaporising liquid, i.e. $q_{gl} = \Delta h_v + q_{\text{heatup}}$. Δh_v is the latent heat of vaporisation.

The molecular heat conduction term and the turbulent heat diffusion term can be combined using $\eta_{\text{eff}} = \eta + \eta_t$ and $\text{Pr}_{\text{eff}} = \text{Pr} + \text{Pr}_t$ (or neglecting the molecular term entirely in turbulent flows), which gives the equation for the sensible enthalpy of the gas phase as

$$\begin{aligned} &\frac{\partial}{\partial t}(\theta \bar{\rho} \tilde{h}) + \frac{\partial}{\partial x_j}(\theta \bar{\rho} \tilde{h} \tilde{u}_j) - \frac{\partial}{\partial x_j} \left(\frac{\bar{\rho} \nu_{\text{eff}}}{\text{Pr}_{\text{eff}}} \frac{\partial}{\partial x_j}(\theta \tilde{h}) \right) \\ &\qquad = \theta \left(\frac{\partial \bar{p}}{\partial t} + \tilde{u}_j \frac{\partial \bar{p}}{\partial x_j} \right) + \Gamma (\bar{h}_s - q_{gl}) + \sum_m \langle \rho \dot{\omega}_m \rangle^{\mathcal{VF}} Q_m \; . \end{aligned} \tag{3.33}$$

In order to calculate the filtered gas phase density, the ideal gas law has to be phase filtered, which is trivial for a single component flow, but becomes the opposite when dealing with gas mixtures:

$$\begin{aligned} \langle p \rangle^{\mathcal{VF}} &= \langle \rho R \sum_m \frac{Y_m}{W_m} T \rangle^{\mathcal{VF}} \,, \\ \theta \bar{p} &= \theta \bar{\rho} R \sum_m \frac{\widetilde{Y_m T}}{W_m} \,, \\ \bar{p} &= \bar{\rho} R \sum_m \frac{\widetilde{Y_m T}}{W_m} \,, \end{aligned} \tag{3.34}$$

which becomes for mono-molecular gases

$$\bar{p} \approx \bar{\rho} \frac{R}{W} \tilde{T} \,, \tag{3.35}$$

but must be closed (or trivially approximated) for multi-component gases.

3.2 Dispersed Phase Equations

As a short reminder, within this work we exclusively deal with dispersed, dilute two-phase flows, with mass loadings large enough to make two-way coupling mandatory. Furthermore, we make the assumption that the particle size is smaller than the Kolmogorov scale of the fluid, i.e. particles can be treated as point sources without major loss of accuracy, which is widely done in this kind of two-phase flows, although the fulfilment of this condition is often questionable in highly turbulent industrial flows. These point source particles are often described in a Lagrangian frame of reference, which we describe in the next section and which we use as a starting point to derive a statistical model in the following section.

3.2.1 Lagrangian Particle Transport Equations

The (theoretically) easiest and at the same time most accurate way to describe particle motion including thermal physics is the Lagrangian framework, provided that the point source approximation applies. Assuming spherical particles, i.e. no particle orientation must be considered, the equations describing the individual particle position $\mathbf{x}_p^{(n)}$, velocity $\mathbf{v}_p^{(n)}$, temperature $T_p^{(n)}$ and change of particle mass $m_p^{(n)}$ read

$$\frac{d\mathbf{x}_p^{(n)}(t)}{dt} = \mathbf{v}_p^{(n)} \,, \tag{3.36}$$

$$\frac{d\mathbf{v}_p^{(n)}(t)}{dt} = \frac{1}{m_p^{(n)}}\mathbf{F}^{(n)} - \frac{1}{\rho_p}(\nabla p)^{@\mathbf{x}_p^{(n)}} + \frac{1}{\rho_p}(\nabla \boldsymbol{\tau})^{@\mathbf{x}_p^{(n)}} + \left(1 - \frac{\rho^{@\mathbf{x}_p^{(n)}}}{\rho_p}\right)\mathbf{g} \,, \tag{3.37}$$

$$\frac{dT_p^{(n)}(t)}{dt} = \frac{\dot{Q}_{l,\,\mathrm{eff}}^{(n)}}{m_p^{(n)} c_{\mathrm{p}l}} \,, \tag{3.38}$$

$$\frac{dm_p^{(n)}(t)}{dt} = -\dot{m}^{(n)} \,, \tag{3.39}$$

where the superscript (n) is the individual particle marker, ρ_p the particle mass density, p and $\boldsymbol{\tau}$ the continuous phase pressure and shear stress tensor, respectively, $\mathbf{g}$ the gravitational acceleration, $c_{\mathrm{p}l}$ the heat capacity of the particle material, here with index l for "liquid", and Δh_v is the latent heat. Pressure forces (pressure gradient and buoyancy force) will be neglected, since the ratio of densities is small ($<1 \times 10^{-3}$). Already neglected are the Saffman and extended lift forces (slip-shear lift force, slip-rotation lift force (Magnus force)), torque (resulting from the continuous-phase stress tensor), added mass and external body forces other than gravity, near-wall effects concerning the drag force, compressibility effects and rarefaction effects.

Properties with the superscript $@\mathbf{x}_p^{(n)}$ represent gas phase properties in the immediate (but hypothetically undisturbed) vicinity of the particle. Those are relevant for the integral (mesoscopic or macroscopic) models

of drag, heat and mass transfer, when dropping the full resolution of the droplet and using the point source approximation instead. $\mathbf{F}^{(n)}$ represents such an integral law for the drag force acting on a particle, which depends on the particle relaxation time $\boldsymbol{\tau}_p^{(n)}$, the relative velocity $\mathbf{u}^{@\mathbf{x}_p^{(n)}} - \mathbf{v}_p^{(n)}$ between the particle and the continuous phase at the particle location:

$$\mathbf{F}^{(n)} = \frac{m_p^{(n)}}{\boldsymbol{\tau}_p^{(n)}} f_1 (\mathbf{u}^{@\mathbf{x}_p^{(n)}} - \mathbf{v}_p^{(n)}) \,, \tag{3.40}$$

where f_1 is a function of various properties and parameters depending on the flow regime. $f_1 = 1$ for Stokes flow around rigid spheres and

$$f_1 = (1 + 0.15\,\mathrm{Re}_p^{0.687}) \tag{3.41}$$

including non-Stokes flow, here using the law of Schiller and Nauman (1935)[4]. The particle relaxation time

$$\boldsymbol{\tau}_p^{(n)} = \frac{\rho_p {D^{(n)}}^2}{18 \eta^{@\mathbf{x}_p^{(n)}}} \tag{3.42}$$

describes how fast the particle adapts its motion on changes in the continuous phase velocity. The particle Reynolds number

$$\mathrm{Re}_p = \frac{(\mathbf{u}^{@\mathbf{x}_p^{(n)}} - \mathbf{v}_p^{(n)}) D^{(n)}}{\nu^{@\mathbf{x}_p^{(n)}}} \,, \tag{3.43}$$

where $\nu^{@\mathbf{x}_p^{(n)}}$ is the continuous phase kinematic viscosity and $D^{(n)}$ the particle diameter, is primarily used as a classification measure for the different flow regimes around a particle, i.e. creeping flow, laminar (un)steady/(non)symmetric flow, turbulent flow, etc. It appears in many drag laws, since the drag force depends significantly on the flow regime in most cases.

$\dot{Q}_{l,\,\mathrm{eff}}^{(n)}$ is the net heat transfer rate to or from the droplet due to convection, mass transfer or radiation, which is effectly used to heat up or cool

[4] Vaporisation can significantly influence the drag, e.g. Fendell et al. (1966), but is not considered here and must be left for future work.

down the droplet. As already seen for the momentum exchange between phases, heat exchange is described with the help of integral laws as well, which distinguish between cases for heat transfer only and coupled heat and mass transfer (i.a. vaporisation and condensation). Considering heat transfer only, the total heat convectively transferred from the continuous phase to the droplet is

$$\dot{Q}_l^{(n)} = \mathrm{Nu}\pi D^{(n)} \lambda^{@\mathbf{x}_p^{(n)}} (T^{@\mathbf{x}_p^{(n)}} - T_p^{(n)}) \,, \tag{3.44}$$

with $\mathrm{Nu} = 2$ for Stokes flow.

The heat loss/gain due to vaporisation/condensation could be incorporated just by adding the product of the mass transfer rate and the latent heat, i.e. $\dot{Q}_{l,\,\mathrm{eff}}^{(n)} = \dot{Q}_l^{(n)} - \dot{m}_M^{(n)} \Delta h_v^{(n)}$. This approach, however, does neither consider the coupled behaviour of both processes nor the impacts of the presence of vapour in the vicinity of the droplet. A more comprehensive model of coupled heat and mass exchange in droplet vaporisation is the well known law given for spherical, liquid droplets by Abramzon and Sirignano (1989), which basic equations for heat and mass exchange rate read

$$\dot{Q}_{l,\,\mathrm{eff}}^{(n)} = \dot{m}_T^{(n)} \frac{c_{\mathrm{p}v}^{@\mathbf{x}_p^{(n)}} (T^{@\mathbf{x}_p^{(n)}} - T_p^{(n)})}{\mathrm{B}_\mathrm{T}^{@\mathbf{x}_p^{(n)}}} - \dot{m}_M^{(n)} \Delta h_v^{(n)} \,, \tag{3.45}$$

$$\dot{m}_T^{(n)} = \mathrm{Nu}^* \pi \frac{\lambda^{@\mathbf{x}_p^{(n)}}}{c_{\mathrm{p}v}} D^{(n)} \ln(1 + \mathrm{B}_\mathrm{T}^{@\mathbf{x}_p^{(n)}}) \,, \tag{3.46}$$

$$\dot{m}_M^{(n)} = \mathrm{Sh}^* \pi \rho^{@\mathbf{x}_p^{(n)}} \mathfrak{D} D^{(n)} \ln(1 + \mathrm{B}_\mathrm{M}^{@\mathbf{x}_p^{(n)}}) \,, \tag{3.47}$$

where the mass exchange rate $\dot{m}^{(n)}$ is defined to be positive when pointing from the liquid state towards the vapour state and can be derived either from heat conduction physics (Eqn. 3.46) or from species diffusion physics (Eqn. 3.47). Both must be the same in a real, coupled heat and mass transfer problem, i.e. $\dot{m}_T^{(n)} = \dot{m}_M^{(n)}$. The logarithmic terms $\ln(1 + \mathrm{B}_\mathrm{M}^{@\mathbf{x}_p^{(n)}})$ and $\ln(1 + \mathrm{B}_\mathrm{T}^{@\mathbf{x}_p^{(n)}})$ indicate that Stefan flux is considered (instead of $\mathrm{B}_\mathrm{M}^{@\mathbf{x}_p^{(n)}}$ and $\mathrm{B}_\mathrm{T}^{@\mathbf{x}_p^{(n)}}$ solely in case of neglecting Stefan flux).

B_M is the Spalding mass transfer number

$$B_M = \frac{Y_{F,s} - Y_{F,\infty}^{@\mathbf{x}_p^{(n)}}}{1 - Y_{F,s}}$$

and B_T the Spalding heat transfer number

$$B_T = \frac{c_{pv}^{@\mathbf{x}_p^{(n)}} \left(T^{@\mathbf{x}_p^{(n)}} - T_{d,s}\right)}{\Delta h_v^{(n)} + \dot{Q}_{l,\,\mathrm{eff}}^{(n)} / \dot{m}_T^{(n)}} \,,$$

where the surface fuel fraction can be calculated with the help of

$$Y_{F,s} = \left[1 + \frac{W_{AIR}}{W_F}\left(\frac{p^{@\mathbf{x}_p^{(n)}}}{p_{F,s}} - 1\right)\right]^{-1}$$

and the surface vapour pressure using the Clausius Clapeyron law

$$p_{F,s} = p_{ref} \exp\left[-\frac{\Delta h_v}{R}\left(\frac{1}{T_{F,s}} - \frac{1}{T_{ref}}\right)\right] \,,$$

which states, that the vapour pressure of a liquid at a given temperature can be related to the known vapour pressure at a reference temperature.

Again, setting $\mathrm{Nu}^* = 2$ and $\mathrm{Sh}^* = 2$ is valid only for Stokes[5] flow (S). For non-Stokes flow (nS) the iterative procedure of Abramzon and Sirignano (1989) using the Frossling correlations has been applied in this work, which consists of modifying the Nusselt and Sherwood number, Nu^* and Sh^*, respectively, as

$$\mathrm{Nu}^* = 2 + \frac{\mathrm{Nu}_0 - 2}{F_T^{@\mathbf{x}_p^{(n)}}} \quad \text{with } \mathrm{Nu}_0 = 2 + 0.552\,\mathrm{Re}_p^{1/2}\mathrm{Pr}^{1/3} \,, \tag{3.48}$$

$$\mathrm{Sh}^* = 2 + \frac{\mathrm{Sh}_0 - 2}{F_M^{@\mathbf{x}_p^{(n)}}} \quad \text{with } \mathrm{Sh}_0 = 2 + 0.552\,\mathrm{Re}_p^{1/2}\,\mathrm{Sc}^{1/3} \,. \tag{3.49}$$

[5] Throughout the thesis, the splitting of source terms into two terms corresponding to *Stokes flow*, termed *Stokes part* (S), and flow with higher particle Reynolds numbers, termed *non-Stokes part* (nS), does not strictly refer to the actual Stokes flow or *creeping flow* around a sphere, i.e. $\mathrm{Re} \ll 1$, but more generally for a splitting around particle Reynolds numbers of the order of unity. In many correlations, however, the additional term compared to that given for pure Stokes flow does contribute asymtotically most often. Hence, a clear separational Reynolds number cannot be given anyway. Contributions due to free convection are not considered.

Besides the Frossling correlation

$$\mathrm{Sh}_0 = 2 + 0.552\,\mathrm{Re}^{1/2}\,\mathrm{Sc}^{1/3}\,, \tag{3.50}$$

the Ranz-Marshall correlation is widely used, which reads

$$\mathrm{Sh}_0 = 2 + 0.6\,\mathrm{Re}^{1/2}\,\mathrm{Sc}^{1/3}\,. \tag{3.51}$$

Other correlations exist, but they are not of further interest here. A summary can be found in Kolaitis and Founti (2006). For completeness the Prandtl and Schmidt number are given by

$$\mathrm{Pr} = \left.\frac{\nu\rho c_\mathrm{p}}{\lambda}\right|^{@\mathbf{x}_p^{(n)}} \approx \text{const.} \qquad \text{and} \qquad \mathrm{Sc} = \frac{\nu^{@\mathbf{x}_p^{(n)}}}{\mathfrak{D}} = \text{const.}\,, \tag{3.52}$$

respectively, assuming temperature independence of both[6]. Simplifying yields

$$\begin{aligned}
\mathrm{Nu}^* &= 2 + 0.552\,\mathrm{Re}^{1/2}\mathrm{Pr}^{1/3}\frac{1}{F_\mathrm{T}^{@\mathbf{x}_p^{(n)}}} \\
&= 2 + 0.552\left(\frac{(\mathbf{u}^{@\mathbf{x}_p^{(n)}} - \mathbf{v}_p^{(n)})D^{(n)}}{\nu^{@\mathbf{x}_p^{(n)}}}\right)^{1/2}\mathrm{Pr}^{1/3}\frac{1}{F_\mathrm{T}^{@\mathbf{x}_p^{(n)}}}\,, \qquad (3.53)\\
\mathrm{Sh}^* &= 2 + 0.552\,\mathrm{Re}^{1/2}\,\mathrm{Sc}^{1/3}\frac{1}{F_\mathrm{M}^{@\mathbf{x}_p^{(n)}}} \\
&= 2 + 0.552\left(\frac{(\mathbf{u}^{@\mathbf{x}_p^{(n)}} - \mathbf{v}_p^{(n)})D^{(n)}}{\nu^{@\mathbf{x}_p^{(n)}}}\right)^{1/2}\mathrm{Sc}^{1/3}\frac{1}{F_\mathrm{M}^{@\mathbf{x}_p^{(n)}}}\,, \qquad (3.54)
\end{aligned}$$

where $F_{\mathrm{T,M}}$ are the correction factors for the film thickness

$$F_{\mathrm{T,M}}^{@\mathbf{x}_p^{(n)}} = (1 + \mathrm{B}_{\mathrm{T,M}}^{@\mathbf{x}_p^{(n)}})^{0.7}\frac{\ln(1 + \mathrm{B}_{\mathrm{T,M}}^{@\mathbf{x}_p^{(n)}})}{\mathrm{B}_{\mathrm{T,M}}^{@\mathbf{x}_p^{(n)}}}\,. \tag{3.55}$$

[6]That does not mean, that the gas phase quantities ν, ρ, c_p and λ are considered as temperature independent. In fact, however, this will be the case as shown later on, except the density and heat capacity

For a given $\mathrm{B_M}^{@\mathbf{x}_p^{(n)}}$, $\mathrm{B_T}^{@\mathbf{x}_p^{(n)}}$ is iteratively corrected with help of Nu^* and Sh^* until the desired accuracy is reached in terms of equality of mass flow rate densities, $\dot{m}_T^{(n)} \approx \dot{m}_M^{(n)}$ (see Abramzon and Sirignano, 1989, for further details). With the help of the corrected heat transfer number $\mathrm{B_T}^{@\mathbf{x}_p^{(n)}}$ and Eqn. 3.45, the part of the heat transfer rate into the droplet which is completely used for heating the droplet, i.e. $\dot{Q}_{l,\,\mathrm{eff}}^{(n)}$, can be calculated.

Finally, the Lagrangian particle equations for particle velocity and temperature development read

$$\begin{aligned}\frac{d\mathbf{v}_p^{(n)}}{dt} &= \frac{1}{\boldsymbol{\tau}_p^{(n)}}(1+0.15\,\mathrm{Re}^{0.687})(\mathbf{u}^{@\mathbf{x}_p^{(n)}} - \mathbf{v}_p^{(n)}) + \mathbf{g} \\ &= \frac{18\eta^{@\mathbf{x}_p^{(n)}}}{\rho_p D^{(n)^2}}(1+0.15\left(\frac{|\mathbf{u}^{@\mathbf{x}_p^{(n)}} - \mathbf{v}_p^{(n)}|D^{(n)}}{\nu^{@\mathbf{x}_p^{(n)}}}\right)^{0.687})(\mathbf{u}^{@\mathbf{x}_p^{(n)}} - \mathbf{v}_p^{(n)}) + \mathbf{g}\end{aligned} \tag{3.56}$$

$$\frac{dT_p^{(n)}}{dt} = \frac{1}{m_p^{(n)}}\frac{c_{\mathrm{p}v}^{@\mathbf{x}_p^{(n)}}}{c_{\mathrm{p}l}}\left(\dot{m}_T^{(n)}\frac{T^{@\mathbf{x}_p^{(n)}} - T_p^{(n)}}{\mathrm{B_T}^{@\mathbf{x}_p^{(n)}}} - \dot{m}_M^{(n)}\Delta h_v^{(n)}\right) . \tag{3.57}$$

Discussion of non-equilibrium vaporisation rate models, e.g. based on the Langmuir-Knudsen law (Bellan and Summerfield, 1978, Bellan and Harstad, 1987), which might give better results in certain circumstances is given in Miller et al. (1998). Further literature on droplet vaporisation aspects can be found, e.g., in Hubbard et al. (1975), Sirignano (1983), Sazhin (2006), Birouk and Gökalp (2006).

3.2.2 (Filtered) Number Density Function and its Transport Equation

Dispersed two-phase flows using point-source particles could be directly simulated by solving the Lagrangian particle equations shown above in-

dividually for each physical particle present in the configuration considered. This would represent a complete description of the dispersed phase, however, only of a single realisation. Since the interest is usually not on the individual particle motion of one realisation, but on the statistically most probable[7] flow field, effort has been undertaken to find a formalism and method to describe particle motion and development in a statistical sense. On the one hand, a statistical description improves the statistical noise, on the other hand it can reduce the computational cost significantly, since for practical simulations, physical particle numbers of 1×10^6 - 1×10^9 and higher have to be handled, which can become quite expensive if not impracticable otherwise.

To derive a statistical formalism, a kind of indicator function must be defined first, which indicates - spoken in terms of two-phase flows - particles depending on their location and physical properties (the so-called *phase space* in multiphase flows and *sample space* in single phase flows). In case of the point-source particle formulation, this indicator function can be formulated with help of delta functions and is usually called *fine-grained density* (see Pope, 1985, p. 127), O'Brian (1980), Hyland et al. (1999) or *(fine grained) phase space density* especially in two-phase flow applications (Hyland et al., 1999, Mashayek and Pandya, 2003).

Considering the mesoscopic quantities, size (diameter) D, velocity $\mathbf{c}_p$ and temperature ζ_p of particles, that is the phase space $\boldsymbol{\mathcal{I}} = D, \mathbf{c}_p, \zeta_p$, the fine-grained density function, including the obvious variation in physical and time space $\mathbf{x}, t$, reads

$$W_p^{(n)}(D, \mathbf{c}_p, \zeta_p; \mathbf{x}, t) = \delta(\mathbf{x} - \mathbf{x}_p^{(n)}(t))\delta(D - D_p^{(n)}(t))\delta(\mathbf{c}_p - \mathbf{v}_p^{(n)}(t))\delta(\zeta - T_p^{(n)}(t)) \ , \quad (3.58)$$

[7] Here, "most probable" still refers to an instantaneous and local state. Obviously, the interest goes further into (spatially and/or temporally) averaged statistics/fields.

with

$$\delta(\mathbf{x} - \mathbf{x}_p^{(n)}(t)) = \prod_{i=1}^{3} \delta(x_i - x_{p,i}^{(n)}(t)) \,, \tag{3.59}$$

$$\delta(\mathbf{c}_p - \mathbf{v}_p^{(n)}(t)) = \prod_{j=1}^{3} \delta(c_{p,j} - v_{p,j}^{(n)}(t)) \,. \tag{3.60}$$

This fine grained density function is a summarising formulation for all particles, which, still distinguishes each particle, i.e. there has been no averaging process or statistical simplification done so far.

To obtain a kind of probability density function, one has to gather a large number of particles described by the fine-grained PDF, sort them by the phase space coordinates and count identical particles in terms of the phase space. Two methods basically exist to conduct this procedure.

First, commonly applied in single phase flows (O'Brian, 1980, Pope, 1981, Zhou and Pereira, 2000, Gicquel et al., 2002, Sheikhi et al., 2003), single phase reacting flows (Pope, 1985, Gao, 1993, Colucci et al., 1998, Jaberi et al., 1999) and two-phase flows (Hyland et al., 1999, Mashayek and Pandya, 2003, Carrara and DesJardin, 2005, 2006, 2008), a spatial summation (or counting) process of phase space points (concrete particles) yields a probability density function on the phase space considered, the so-called *filtered density function* (FDF).

Second, in dispersed particle flows, a pointwise, phase space conditioned summation over a large number of two-phase flow realisations $\mathcal{H}_{f\&p}$ is usually conducted, mainly to overcome the issue, that the statistics may become very poor for dilute dispersed phase flows when using a spatial summation only. In single phase flows, this might be statistically sufficient, since in a typical LES cell there are enough different samples present for each sample space coordinate. In two-phase flows, especially in dilute dispersed flows, spatially based statistics from a single particle phase realisation $\mathcal{H}_p$ might become very poor, since the particle number can become very low for a volume of the size order of a computational cell. Therefore, it is meaningful to perform a collection over a large number of particle phase flow realisations for a given single phase realisation

$\mathcal{H}_f$ or, most general, for a large number of two-phase flow realisations $\mathcal{H}_{f\&p}$.

Both approaches, for single and two phase flows, are briefly sketched using two concrete examples. First, using the notation of Colucci et al. (1998), who considered turbulent reacting single phase flows, the filtered density function $P_L(\mathbf{\Psi}; \mathbf{x}, t)$ for a species mass fraction array $\mathbf{\Phi}$ can be defined, which is a spatial average over the fine grained PDF, therein named $\varrho(\mathbf{\Psi}, \mathbf{\Phi}(\mathbf{x}, t)) = \delta(\mathbf{\Psi} - \mathbf{\Phi}(\mathbf{x}, t))$.

$$P_L(\mathbf{\Psi}; \mathbf{x}, t) = \iiint_{\infty} G(\mathbf{x} - \boldsymbol{\xi}) \varrho(\mathbf{\Psi}; \boldsymbol{\xi}, t) \, \mathrm{d}\boldsymbol{\xi} \, , \tag{3.61}$$

with $\mathbf{\Psi}$ is the mass fraction sample space, i.e. all possible values of $\mathbf{\Phi}$. As a second example, now given for dispersed phase flows with the notation of Février et al. (2005), an ensemble average over a very large number $\mathcal{N}_{f\&p}$ of two-phase realisations $\mathcal{H}_{f\&p}$ is conducted, which gives the one-particle, *ensemble based number density function*[8] (EbNDF) $f_p^{(1)}(\mathbf{c}_p; \mathbf{x}, t)$ "defining the local probable number of particle centres at the position $\mathbf{x}$, with a given translation velocity $\mathbf{v}_p = \mathbf{c}_p$, at time t" (formulation taken from Février et al., 2005):

$$f_p^{(1)}(\mathbf{c}_p; \mathbf{x}, t) = \lim_{\mathcal{N}_{f\&p} \to \infty} \left[\frac{1}{\mathcal{N}_{f\&p}} \sum_{\mathcal{H}_{f\&p}} \sum_{n=1}^{N_p} W_p^{(n)}(\mathbf{c}_p; \mathbf{x}, t, \mathcal{H}_{f\&p}) \right] . \tag{3.62}$$

$f_p^{(1)}(\mathbf{c}_p; \mathbf{x}, t)$ is constructed pointwise, this means that for Eulerian computations the corresponding (meso- or macroscopic) equations have to be averaged or filtered to be resolved by the computational mesh, i.e. either $f_p^{(1)}$ is filtered before taking phase space averages (FDF approach) and hence the moment fields are smooth at the filter scale level (Bini and Jones, 2008, Pandya and Mashayek, 2002) or the macroscopic moment equations obtained from the phase space integration are filtered afterwards. The latter has been done, e.g., by Riber et al. (2005, 2006).

[8] We use this term to distinguish the different NDFs properly. Usually, solely the term NDF is used for ensemble average based density functions.

In this work, we follow the approach by filtering first the ensemble of fine grained density functions and afterwards integrating over phase space (as Fox (2012) suggests as the more rigorous option). Details on filtering of a PDF can be found in Bini and Jones (2008) for example.

The fine-grained density function conditioned on a single continuous phase realisation $\mathcal{H}_f$ (Février et al., 2005, Sec. 3.1) reads

$$\begin{aligned} &W_p^{(n)}(D, \mathbf{c}_p, \zeta_p; \mathbf{x}, t, \mathcal{H}_p | \mathcal{H}_f) \\ &\quad = \delta(\mathbf{x} - \mathbf{x}_p^{(n)}(t))\delta(D - D_p^{(n)}(t))\delta(\mathbf{c}_p - \mathbf{v}_p^{(n)}(t))\delta(\zeta_p - T_p^{(n)}(t)) \ . \end{aligned} \tag{3.63}$$

Applying a sample accumulation[9] over a large number of particle phase realisations and a spatial filtering on the fine-grained density function yields

$$\begin{aligned} &\breve{\breve{f}}(D, \mathbf{c}_p, \zeta_p; \mathbf{x}, t | \mathcal{H}_f) \\ &\quad = \iiint_{\infty} G(\mathbf{x} - \boldsymbol{\xi}) \lim_{\mathcal{N}_p \to \infty} \left[\frac{1}{\mathcal{N}_p} \sum_{\mathcal{H}_p} \sum_{n=1}^{N_p} W_p^{(n)}(D, \mathbf{c}_p, \zeta_p; \boldsymbol{\xi}, t, \mathcal{H}_p | \mathcal{H}_f) \right] \mathrm{d}\boldsymbol{\xi} \ , \end{aligned} \tag{3.64}$$

where we refer to $\breve{\breve{f}}(D, \mathbf{c}_p, \zeta_p; \mathbf{x}, t | \mathcal{H}_f)$ as a *filtered, ensemble based number density function* (FEbNDF). The notation $\breve{f}$ we use here instead of $f^{(1)}$ is the more used in publications after Février et al. (2005) but refers to the same quantity. Since the dispersed phase density is usually approximately constant for single-component liquid fuels, no Favre average is needed. $\breve{\breve{f}}(D, \mathbf{c}_p, \zeta_p; \mathbf{x}, t | \mathcal{H}_f)$ is a one-point NDF, which is, as shown by Février et al. (2005), completely sufficient at least for cases without particle-particle collisions, since particle motion is only correlated via the fluid flow field.

This operation may be defined as an operator consisting of sample accu-

[9] We use the term *sample accumulation* instead of "ensemble average" when concerned with creating the NDF to account for the fact, that actually no average is conducted but only a summarising description for a large number of samples is used.

mulation

$$\langle \cdot | D, \mathbf{c}_p, \zeta_p, \mathcal{H}_f \rangle^{\mathcal{E}} = \frac{\lim_{\mathcal{N}_p \to \infty} \left[\frac{1}{\mathcal{N}_p} \sum_{\mathcal{H}_p} \sum_{n=1}^{N_p} \cdot W_p^{(n)}(D, \mathbf{c}_p, \zeta_p; \mathbf{x}, t, \mathcal{H}_p | \mathcal{H}_f) \right]}{\breve{f}(D, \mathbf{c}_p, \zeta_p; \mathbf{x}, t | \mathcal{H}_f)} \tag{3.65}$$

and phase space conditioned, spatial filtering (Eqn. 2.27)

$$\langle \cdot | D, \mathbf{c}_p, \zeta_p \rangle^{\mathcal{F}} = \iiint_{\infty} G(\mathbf{x} - \boldsymbol{\xi}) \cdot \, \mathrm{d}\boldsymbol{\xi} \, , \tag{3.66}$$

which yields

$$\langle \cdot | D, \mathbf{c}_p, \zeta_p, \mathcal{H}_f \rangle^{\mathcal{E}\mathcal{F}} = \langle \langle \cdot | D, \mathbf{c}_p, \zeta_p, \mathcal{H}_f \rangle^{\mathcal{E}} | D, \mathbf{c}_p, \zeta_p, \rangle^{\mathcal{F}} \, , \tag{3.67}$$

where $\cdot$ can be any variable or function. A value obtained from this operation is noted with $\breve{\cdot}$ as

$$\breve{\breve{\psi}}(D, \mathbf{c}_p, \zeta_p; \mathbf{x}, t, \mathcal{H}_f) = \langle \psi(D, \mathbf{c}_p, \zeta_p; \boldsymbol{\xi}, t, \mathcal{H}_f) | D, \mathbf{c}_p, \zeta_p; \mathbf{x}, t, \mathcal{H}_f \rangle^{\mathcal{E}\mathcal{F}} \, . \tag{3.68}$$

With help of this operation a transport equation for $\breve{\breve{f}}(D, \mathbf{c}_p, \zeta_p; \mathbf{x}, t | \mathcal{H}_f)$ can be derived (see Appendix A.1.3), where the Lagrangian derivatives $\frac{d}{dt}$ are to be replaced using the Lagrangian particle transport equations 3.36 to 3.39. It reads

$$\begin{aligned}
&\frac{\partial}{\partial t} \breve{\breve{f}}(D, \mathbf{c}_p, \zeta_p; \mathbf{x}, t | \mathcal{H}_f) + \frac{\partial}{\partial x_j} (c_{p,j} \breve{\breve{f}}(D, \mathbf{c}_p, \zeta_p; \mathbf{x}, t | \mathcal{H}_f)) \\
&= - \frac{\partial}{\partial c_{p,j}} \left(\langle \langle \frac{dv_{p,j}^{(n)}}{dt} | D, \mathbf{c}_p, \zeta_p, \mathcal{H}_f \rangle^{\mathcal{E}} \breve{f}(D, \mathbf{c}_p, \zeta_p; \mathbf{x}, t | \mathcal{H}_f) | D, \mathbf{c}_p, \zeta_p, \mathcal{H}_f \rangle^{\mathcal{F}} \right) \\
&\quad - \frac{\partial}{\partial \zeta_p} \left(\langle \langle \frac{dT_p^{(n)}}{dt} | D, \mathbf{c}_p, \zeta_p, \mathcal{H}_f \rangle^{\mathcal{E}} \breve{f}(D, \mathbf{c}_p, \zeta_p; \mathbf{x}, t | \mathcal{H}_f) | D, \mathbf{c}_p, \zeta_p, \mathcal{H}_f \rangle^{\mathcal{F}} \right) \\
&\quad - \frac{\partial}{\partial D} \left(\langle \langle \frac{dD^{(n)}}{dt} | D, \mathbf{c}_p, \zeta_p, \mathcal{H}_f \rangle^{\mathcal{E}} \breve{f}(D, \mathbf{c}_p, \zeta_p; \mathbf{x}, t | \mathcal{H}_f) | D, \mathbf{c}_p, \zeta_p, \mathcal{H}_f \rangle^{\mathcal{F}} \right) \, .
\end{aligned} \tag{3.69}$$

Finally by simplifying the notation using $D, \mathbf{c}_p, \zeta_p = \boldsymbol{\mathcal{I}}$, i.e. $\boldsymbol{\mathcal{I}}$ is the set of phase space variables (or internal variables), dropping the explicit notation of the dependence on $(;\mathbf{x}, t)$ and neglecting the notation for the conditioning on $\mathcal{H}_f$, Eqn. 3.69 becomes

$$\begin{aligned}\frac{\partial}{\partial t}\breve{\breve{f}}(\boldsymbol{\mathcal{I}}) + \frac{\partial}{\partial x_j}(c_{p,j}\breve{\breve{f}}(\boldsymbol{\mathcal{I}})) = &- \frac{\partial}{\partial D}\left(\langle\breve{f}\langle\frac{dD^{(n)}}{dt}|\boldsymbol{\mathcal{I}}\rangle^{\mathcal{E}}|\boldsymbol{\mathcal{I}}\rangle^{\mathcal{F}}\right) \\ &- \frac{\partial}{\partial c_{p,j}}\left(\langle\breve{f}\langle\frac{dv_{p,j}^{(n)}}{dt}|\boldsymbol{\mathcal{I}}\rangle^{\mathcal{E}}|\boldsymbol{\mathcal{I}}\rangle^{\mathcal{F}}\right) \\ &- \frac{\partial}{\partial \zeta_p}\left(\langle\breve{f}\langle\frac{dT_p^{(n)}}{dt}|\boldsymbol{\mathcal{I}}\rangle^{\mathcal{E}}|\boldsymbol{\mathcal{I}}\rangle^{\mathcal{F}}\right), \end{aligned} \tag{3.70}$$

where Einstein summation applies for index j.

To keep things clear, we explicitly remind that

1. $\mathbf{v}_p^{(n)} = \mathbf{v}_p^{(n)}(x,t)$ is the individual, physical particle velocity. In general, variables with superscript $^{(n)}$ represent properties of individual particle, whereas

2. $\mathbf{c}_p$ is the internal variable or phase space coordinate of the particle velocity, i.e. $\mathbf{v}_p^{(n)}$ are concrete values (samples) of the phase space $\mathbf{c}_p$. The same applies to $D^{(n)}$ and D, $T_p^{(n)}$ and ζ_p as well as $\mathbf{x}_p^{(n)}$ and $\mathbf{x}$, although the latter is only a "pseudo" phase space variable.

3. Actually, $\langle\frac{\partial \mathbf{x}_p^{(n)}}{\partial t}|D, \mathbf{c}_p, \zeta_p\rangle^{\mathcal{EF}} \overset{(3.36)}{=} \langle\mathbf{v}_p^{(n)}|D, \mathbf{c}_p, \zeta_p\rangle^{\mathcal{EF}} = \mathbf{c}_p$.

3.2.3 Solution Methods and Closure of the RHS Terms

In order to solve Eqn. 3.70, two different types of methods are usually applied. First, the NDF can be represented and transported by a sufficiently large number of stochastic particles in a Lagrangian way (which must not

be mistaken with the real physical particles), or second, by solving transport equations for the moments of the NDF up to a certain order usually implying further closure assumptions (i.e. the different kind of moment methods). Dependent on the type of solution method applied, several approaches have been proposed for the closure of unknown terms due to the ensemble average or the LES filtering, which will be dealt with in the following sorted by Lagrangian and Eulerian methods.

Lagrangian Simulations

In the Lagrangian particle tracking methods, the phase space considered remains fully resolved, i.e. the full NDF is kept and represented by a sufficient large number of stochastic particles, as such that the actual shape of the NDF can be reconstructed appropriately throughout the phase space from the ensemble of particles at any physical location in the given domain. The only closure needed is that due to particle-fluid interaction either on sub-grid scale level when using Large Eddy Simulation or on the non-resolved spatial and temporal interaction in RANS-type simulations. The closure in Lagrangian two-phase LES reduces actually to the determination of the sub-grid scale fluid phase velocity at the physical position of the particle (the particle trajectory is then fully resolved by using sufficient small time steps for solving the Lagrangian particle transport equations and simultaneously updated fluid phase velocity). Further details and examples have been given in Section 2.6.1.

Eulerian Simulations

Eulerian solution of the NDF transport equation is usually based on the moments of the NDF. This is however not yet the topic here, but will be discussed in detail in Chapter 4. In this paragraph, a precurser step is shown, which is necessary to be able to integrate over the phase space to obtain moment transport equations. This step focuses on the evaluation of the right hand side terms of Eqn. 3.70, i.e. $\langle \check{f} \langle \frac{dv_{p,j}^{(n)}}{dt} | \boldsymbol{\mathcal{I}} \rangle^{\mathcal{E}} | \boldsymbol{\mathcal{I}} \rangle^{\mathcal{F}}$,

$\langle \check{f} \langle \frac{dT_p^{(n)}}{dt} | \boldsymbol{\mathcal{I}} \rangle^{\mathcal{E}} | \boldsymbol{\mathcal{I}} \rangle^{\mathcal{F}}$ and $\langle \check{f} \langle \frac{dD^{(n)}}{dt} | \boldsymbol{\mathcal{I}} \rangle^{\mathcal{E}} | \boldsymbol{\mathcal{I}} \rangle^{\mathcal{F}}$. They consist of the combined operation of phase space conditioned sample accumulation and spatially filtering acting on the Lagrangian derivatives, i.e. the derivative following the particle (Balachandar and Eaton, 2010). To handle this operation correctly, we evaluate the different aspects in detail.

It must be first emphasised, that we still keep the full phase space, i.e. we do not undertake any averaging procedure on particle velocity, size or temperature at this point, since we sum up only particles with identical phase space position, but from different realisations or spatial locations. This means that the phase space variables are invariant to both operations, because both are conditioned on phase space. However, that does not necessarily mean that the derivatives of the phase space variables are invariant for identical particles in phase space as well. Fortunately, when replacing the Lagrangian derivatives with help of the Lagrangian particle transport equations 3.37 to 3.39, only phase space variables and gas phase quantities remain, which in turn implies that both operations affect only the gas phase quantities being implicitely contained in the derivatives.

Let us consider now the gas phase quantities. As mentioned before, we consider the case of an ensemble of a large number of particle phase realisation for a given gas phase realisation. This means that the gas phase properties are locally invariant to the sample accumulation operation, i.e. there is no variation to be considered locally. Undergoing the spatial filtering, however, gas phase quantities (with superscript $^{@\mathbf{x}_p^{(n)}}$), although conditioned on the same phase space point, are gathered from different locations in physical space, i.e. identical particles in terms of phase space can be surrounded by different gas phase conditions. This means that the gas phase sub-grid scale fluctuations must be incorporated at this point.

With that, the source terms can be generally split into an averaged derivative and a residual component referring to each particle:

$$\langle \check{f} \langle \frac{d}{dt} | \boldsymbol{\mathcal{I}} \rangle^{\mathcal{E}} | \boldsymbol{\mathcal{I}} \rangle^{\mathcal{F}} = \check{\bar{f}} \langle \frac{d}{dt} | \boldsymbol{\mathcal{I}} \rangle^{\mathcal{E}\mathcal{F}} + (\langle \check{f} \langle \frac{d}{dt} | \boldsymbol{\mathcal{I}} \rangle^{\mathcal{E}} | \boldsymbol{\mathcal{I}} \rangle^{\mathcal{F}} - \check{\bar{f}} \langle \frac{d}{dt} | \boldsymbol{\mathcal{I}} \rangle^{\mathcal{E}\mathcal{F}}) \, , \quad (3.71)$$

or using a "prime component" notation, here the fluctuation of the derivative, which is known as *phase space diffusion current*

$$\langle \check{f} \langle \frac{d}{dt} | \boldsymbol{\mathcal{I}} \rangle^{\mathcal{E}} | \boldsymbol{\mathcal{I}} \rangle^{\mathcal{F}} = \check{\check{f}} \langle \frac{d}{dt} | \boldsymbol{\mathcal{I}} \rangle^{\mathcal{E}\mathcal{F}} + \langle \check{f} \langle (\frac{d}{dt} | \boldsymbol{\mathcal{I}} \rangle^{\mathcal{E}})' | \boldsymbol{\mathcal{I}} \rangle^{\mathcal{F}} \, . \tag{3.72}$$

The prime refers to the gas phase quantities varying within the support of the filter kernel, i.e. the physical space.

Development of closure for these type of terms has a long history. Originally concerned with ensemble averages over two-phase flow realisations (actually only the gas phase realisations, since phase space conditioned ensemble average over particle phase realisations does not contribute any randomness), and without any further average or filtering operation, sophisticated closure methods for the phase space diffusion current are

- Kraichnan's *Direct Interaction Approximation* (DIA) (Kraichnan, 1958, 1959). Applied by Reeks (1980) to Stokes drag and higher particle Reynolds numbers based on a correlation by Serafini (1954).
- Kraichnan's *Lagrangian History Direct Interaction* (LHDI) (Kraichnan, 1965, 1977). Applied by Reeks (1983) to Stokes drag and other mesoscopic particle-fluid interaction forces (Reeks, 1992). Pandya and Mashayek (2003b) proposed an extension to non-isothermal flows, i.e. adding the droplet temperature to the phase space and correspondingly a closure for heat transfer between the droplet and the fluid phase.
- the Novikov-Furutsu-Donsker formula (Novikov, 1965, Furutsu, 1963, Donsker, 1964). Applied by Derevich (2000) and Hyland et al. (1999) to Stokes drag, by Zaichik (1999) for general drag and heat transfer and by Pandya and Mashayek (2003a) to non-isothermal flows as described in the previous item.
- Van Kampen's method (van Kampen, 1997). Applied by Pandya and Mashayek (2001, 2003a,b) to non-isothermal flows.

When considering an ensemble average over a large number of particle phase and(!) continuous phase realisations as well as an additionally average or filtering needed due to the numerical method, as a result the gas phase properties would have to be split into three components, a mean and two residual components, first the pointwise deviation of the individual gas phase realisation value to that of the mean of all gas phase realisations and the deviation of the local realisation mean values to their spatial mean counterparts. To the author's knowledge, this has not been attempted so far. However, if one considers only a large number of particle phase realisations conditioned on a single fluid phase realisation, LES filtering remains (in our case) the only operation producing unknown residual component correlations. Using the idea of a certain similarity between ensemble average over realisations and ensemble average over a spatial volume, Pandya and Mashayek (2002) took Reeks' ensemble closure (Reeks, 1992) and developed a similar closure for the phase space diffusion current based on an "ensemble of spatial distributed samples". This closure, however, is for a single two-phase flow realisation only.

When using a large number of particle phase realisations for a given fluid phase realisation, which is our case, the same closure as proposed by Pandya and Mashayek (2002) could be adapted. All of these closure methods, however, are neither straightforward to integrate over phase space, nor to implement in CFD codes (due to the time integrals in the closure). Details on the former issue are given, e.g., in Mashayek and Pandya (2003) and references therein (Zaichik, 1999, Derevich, 2000). Considering one of these closures was out of the scope of the current work. Therefore, we follow the strategy to validate the implemented models without considering the phase space diffusion current[10]. This means that, instead of a particle number weighted mean of the individual gas phase contributions, an arithmetic mean of the gas phase quantities is used. As we will see in the following, the term $\left\langle \frac{d}{dt} | \boldsymbol{\mathcal{I}} \right\rangle^{\mathcal{EF}}$ itself, implies challenging difficulties of proper closure, nevertheless.

[10]Following the strategy to integrate first over phase space (for a given fluid phase realisation) and filtering afterwards the moment equations (e.g. done by Riber et al., 2006, Boileau et al., 2008, Masi et al., 2008, Riber et al., 2009), the phase space diffusion current does not appear in the previously presented form but other unknown correlations appear, which needs closure. The problem just relocates.

Hence, for the remaining term $\langle \frac{d}{dt} | \boldsymbol{\mathcal{I}} \rangle^{\mathcal{EF}}$, non-filtered quantities can be decomposed into a spatial mean and a residual component, as usually done in single phase LES simulations, and using the Favre average when applicable. Some macroscopic closures have been proposed for some of the unknowns, but since we are at the mesoscopic level, appropriate closures must be found. Tenneti et al. (2010), for example, proposed a mesoscopic drag model. A brief discussion on mesoscopic models for collision can be found in Fox (2012).

The source terms will be dealt with one by one starting with the source term $\langle \frac{dv_{p,j}^{(n)}}{dt} | \boldsymbol{\mathcal{I}} \rangle^{\mathcal{EF}}$, in our case representing the drag between phases and the gravity. When starting with the Stokes part only

$$\begin{aligned} \langle \frac{dv_{p,j,S}^{(n)}}{dt} | \boldsymbol{\mathcal{I}} \rangle^{\mathcal{EF}} &= \langle \frac{18\eta^{@\mathbf{x}_p^{(n)}}}{\rho_p D^{(n)^2}} (u_j^{@\mathbf{x}_p^{(n)}} - v_{p,j}^{(n)}) | \boldsymbol{\mathcal{I}} \rangle^{\mathcal{EF}} + \langle g_j | \boldsymbol{\mathcal{I}} \rangle^{\mathcal{EF}} \\ &= \frac{18}{\rho_d D^2} \langle \eta^{@\mathbf{x}_p^{(n)}} (u_j^{@\mathbf{x}_p^{(n)}} - v_{p,j}^{(n)}) | \boldsymbol{\mathcal{I}} \rangle^{\mathcal{EF}} + g_j \,, \end{aligned}$$

we directly see that it is evident to drop correlations containing the gas phase viscosity (and all other gas phase quantities except the velocity), otherwise the chance to be able to close the term vanishes rapidly. Thus, this term becomes

$$\approx \frac{18\bar{\nu}\bar{\rho}}{\rho_d D^2} (\tilde{u}_j - c_{p,j}) + g_j \,, \tag{3.73}$$

where Favre average applies to the velocity, i.e.

$$\langle \eta^{@\mathbf{x}_p^{(n)}} u_j^{@\mathbf{x}_p^{(n)}} | \boldsymbol{\mathcal{I}} \rangle^{\mathcal{EF}} = \langle \nu^{@\mathbf{x}_p^{(n)}} \rho^{@\mathbf{x}_p^{(n)}} u_j^{@\mathbf{x}_p^{(n)}} | \boldsymbol{\mathcal{I}} \rangle^{\mathcal{EF}} \approx \bar{\nu}\bar{\rho}\tilde{u}_j \,. \tag{3.74}$$

Note that the averaged gas phase quantities are still conditioned on phase space $\psi_g(\boldsymbol{\mathcal{I}})$. In line with neglecting the residual component due to spatial filtering conditioned on phase space, we neglect also the dependence on phase space. That means we assume the gas phase quantities to be the same for all droplet classes (i.e. invariant to the phase space integration): $\langle \mathbf{u}^{@\mathbf{x}_p^{(n)}} | \boldsymbol{\mathcal{I}} \rangle^{\mathcal{EF}} \approx \bar{\mathbf{u}}(\boldsymbol{\mathcal{I}}; \mathbf{x}, t) \approx \bar{\mathbf{u}}(\mathbf{x}, t)$. The same applies to Favre averaged

quantities. Hence, the notation using $\bar{\psi}_g$ and $\tilde{\psi}_g$, respectively, implies this simplification.

The non-Stokes extension for the drag force (Schiller and Nauman, 1935) is a non-linear term in gas phase velocity

$$\begin{aligned}\langle \frac{dv_{p,j,nS}^{(n)}}{dt} | \boldsymbol{\mathcal{I}} \rangle^{\mathcal{EF}} &= \langle 0.15 \frac{18\eta^{@\mathbf{x}_p^{(n)}}}{\rho_p D^{(n)^2}} \left(\frac{|u_j^{@\mathbf{x}_p^{(n)}} - v_{p,j}^{(n)}| D^{(n)}}{\nu^{@\mathbf{x}_p^{(n)}}} \right)^{0.687} (u_j^{@\mathbf{x}_p^{(n)}} - v_{p,j}^{(n)}) | \boldsymbol{\mathcal{I}} \rangle^{\mathcal{EF}} \\ &= 0.15 \frac{18 D^{0.687}}{\rho_d D^2} \langle \eta^{@\mathbf{x}_p^{(n)}} \left(\frac{|u_j^{@\mathbf{x}_p^{(n)}} - v_{p,j}^{(n)}|}{\nu^{@\mathbf{x}_p^{(n)}}} \right)^{0.687} (u_j^{@\mathbf{x}_p^{(n)}} - v_{p,j}^{(n)}) | \boldsymbol{\mathcal{I}} \rangle^{\mathcal{EF}} ,\end{aligned}$$

where we replace non-filtered with filtered quantities[11], yielding

$$\approx 0.15 \frac{18 \bar{\nu} \bar{\rho}}{\rho_d D^2} \left(\frac{|\tilde{u}_j - c_{p,j}| D}{\bar{\nu}} \right)^{0.687} (\tilde{u}_j - c_{p,j}) \, . \tag{3.75}$$

Keeping the full decomposition of the fluid velocity is outlined in Appendix Eqn. A.28.

The combination of both parts yields the filtered expression for the drag term

$$\langle \frac{dv_{p,j}^{(n)}}{dt} | \boldsymbol{\mathcal{I}} \rangle^{\mathcal{EF}} \approx \frac{18 \bar{\nu} \bar{\rho}}{\rho_d D^2} (1 + 0.15 \left(\frac{|\tilde{u}_j - c_{p,j}| D}{\bar{\nu}} \right)^{0.687}) (\tilde{u}_j - c_{p,j}) + g_j \, . \tag{3.76}$$

When dealing with the drag term, we have seen that keeping each local variation of the gas phase quantities is virtually impossible. Thus, we do not make any further attempt to keep and model gas phase quantity correlations in the subsequent source terms for heat and mass transfer. Non-filtered quantities are replaced simply by filtered quantities. The few

[11] Considering that we will solve an equation for the $M^{(3)}$ flux only, which represents the momentum of the particles, i.e. mainly that of the large, inert particles, this assumption relaxes to a certain amount since the inertia of large particles effectively filters out the small scale fluid eddies.

intermediate steps from $\langle \check{f} \langle \frac{dT_p^{(n)}}{dt} | \boldsymbol{\mathcal{I}} \rangle^{\mathcal{E}} | \boldsymbol{\mathcal{I}} \rangle^{\mathcal{F}}$ and $\langle \check{f} \langle \frac{dD^{(n)}}{dt} | \boldsymbol{\mathcal{I}} \rangle^{\mathcal{E}} | \boldsymbol{\mathcal{I}} \rangle^{\mathcal{F}}$ to the final terms shown below are given in Appendix A.1.4. The approximated source terms, with considering higher particle Reynolds numbers, read for the heat transfer

$$\begin{aligned}\langle \frac{dT_p^{(n)}}{dt} | \boldsymbol{\mathcal{I}} \rangle^{\mathcal{EF}} \approx & \frac{12\bar{\lambda}}{\rho_d D^2 c_{\mathrm{Pl}}} (\bar{T} - \zeta_p) \frac{\ln(1+\bar{\mathrm{B}}_\mathrm{T})}{\bar{\mathrm{B}}_\mathrm{T}} \\ & + 0.552 \cdot 6 \frac{\bar{\lambda} \mathrm{Pr}^{1/3}}{D^{3/2} \rho_d c_{\mathrm{Pl}}} \left(\frac{(\bar{\mathbf{u}} - \mathbf{c}_p)}{\bar{\nu}} \right)^{1/2} (\bar{T} - \zeta_p) \frac{1}{(1+\bar{\mathrm{B}}_\mathrm{T})^{0.7}} \\ & - \frac{12 \bar{\rho} \mathfrak{D}}{\rho_d D^2 c_{\mathrm{Pl}}} \Delta h_v(\zeta_p) \ln(1+\tilde{\mathrm{B}}_\mathrm{M}) \\ & - 0.552 \cdot 6 \frac{\bar{\rho} \mathfrak{D} \, \mathrm{Sc}^{1/3}}{D^{3/2} \rho_d c_{\mathrm{Pl}}} \left(\frac{(\tilde{\mathbf{u}} - \mathbf{c}_p)}{\bar{\nu}} \right)^{1/2} \Delta h_v(\zeta_p) \frac{\tilde{\mathrm{B}}_\mathrm{M}}{(1+\tilde{\mathrm{B}}_\mathrm{M})^{0.7}}\end{aligned} \tag{3.77}$$

and the mass transfer

$$\begin{aligned}\langle \frac{dD^{(n)}}{dt} | \boldsymbol{\mathcal{I}} \rangle^{\mathcal{EF}} \approx & -4 \frac{\bar{\rho} \mathfrak{D}}{\rho_d D} \ln(1+\tilde{\mathrm{B}}_\mathrm{M}) \\ & - 0.552 \cdot 2 \frac{\bar{\rho}}{\rho_d} \mathfrak{D} \frac{\mathrm{Sc}^{1/3}}{D^{1/2}} \left(\frac{(\tilde{\mathbf{u}} - \mathbf{c}_p)}{\bar{\nu}} \right)^{1/2} \frac{\tilde{\mathrm{B}}_\mathrm{M}}{(1+\tilde{\mathrm{B}}_\mathrm{M})^{0.7}} \, .\end{aligned} \tag{3.78}$$

If at all, despite the complex models mentioned above, only global models might be practical in the form of, e.g., $\dot{m}' = ...$, where the author is not aware of a proposal for such a model.

To summarise, in this chapter the derivation and closure of the gas phase equations has been shown, where the closure of the phase interaction terms was skipped. Their closure will be achieved based on the dispersed phase equations. The latter were derived from a stochastic approach up to the point of formulating the transport equation of the particle number densitiy function. Its integration and further treatment is shown in the next chapter.

4 Moments Model

Solving a partial differential equation for a function, as Eqn. 3.70, is not a trivial task for which various methods have been developed. Besides direct (mathematical) solvers, evaluating the NDF transport equations in practical CFD is either done by solving for several discrete realisations in Lagrangian or Eulerian framework, both on the mesoscopic level of modelling, as described in Section 2.6.1, or on the macroscopic level by transporting certain information about the NDF (see Section 2.6.2). To be clear, the term *Eulerian* refers only to a mathematical framework independent of any model or scale. That means, there exist mesoscopic models whose equations are written and solved in an Eulerian frame of reference and there are macroscopic models, e.g. the moment methods, where the quantities are treated as Eulerian fields and are solved for in Eulerian framework. In this chapter, the macroscopic Eulerian moment methods are the object of further interest.

4.1 Introduction to the Moment Formalism

First, we give the basic definitions, concepts and operations to derive a macroscopic model from the mesoscopic kinetic equation of the NDF (Eqn. 3.70). This is done by integrating this equation over phase space, which yields quantities commonly referred to as *moments*. The macroscopic model consists of transport equations for these moments, describing their evolution in time, physical and phase space, and closures for several (mathematical) closure problems. As stated before, the step from the mesoscopic to the macroscopic model does (theoretically) not require physical modelling, but is a mathematical closure problem. To overcome

this closure problem, however, further physical simplifications in addition to those made in the step from the microscopic to the mesoscopic model are required, which, mathematically formulated, allow the closure of the unknown terms. These connections between the mathematical closure problem and corresponding physical simplifications will be highlighted in the following derivations.

4.1.1 General Moment Definitions

Moments are characteristic properties of a distribution function, which in turn is entirely specified in case that an infinite number of moments of the distribution is known. Reconstruction of a distribution from a given (finite) set of moments is called the *moment problem*. In the literature three types of the moment problem are distinguished, depending on the underlying support of the distribution. The moment problem in its most general version with an infinite support of the distribution is called *Hamburger* moment problem, when constrained to a non-negative support only, *Stieltjes* moment problem (in Stieltjes, 1894, p. 48), and in case of a certain interval, *Hausdorff* moment problem. For our purposes this classification is not of importance, although a classification would be interesting since in multiphase flows, the underlying variables would require all three types of support due to their physical correspondence, i.e. particle sizes are always non-negative, velocities both positive and negative, etc.

A more relevant classification can be conducted concerning the moments itself. Of common concern are moments *about zero* or *about the origin* (sometimes also called *raw* or *crude* moments or *Stieltjes* moments (Wright Jr., 2007)) and *central* moments or moments *about the mean*. Since there is no established agreement how to refer to the former one, the general expression "moments about zero/the origin" (as used, e.g., in Kenney, 1939) will be used from here on in conjunction with the term "central moments" for the latter type.

Mono-variate moments about zero, i.e. based on a single sample property x, are defined as

$$M^{(k)} = \int_{-\infty}^{\infty} x^k f(x) \mathrm{d}x \ , \tag{4.1}$$

with the first order moment ($k = 1$) is the so-called *mean* or *expectation value* usually noted μ with $\mu = \mu^{(1)} = M^{(1)}$, given that $f(x)$ is a probability density function, i.e. it has the characteristic that $\int_{-\infty}^{\infty} f(x) \mathrm{d}x = 1$. Commonly known moments about the mean are the variance ($k = 2$), skewness ($k = 3$) and kurtosis ($k = 4$), etc., defined by

$$\mu^{(k)} = \int_{-\infty}^{\infty} (x - \mu)^k f(x) \mathrm{d}x \ . \tag{4.2}$$

The different moment definitions are associated with certain advantages and disadvantages. Central moments are widely used in all kind of statistical description, whereas especially in multi-phase flows, the use of central moments can be advantageous as it will be discussed in the next section. Both types of moments are equivalent in terms of information about the distribution and can be related to each other, e.g. the variance σ^2 can be expressed in terms of moments about zero by

$$\sigma^2 = \mu^{(2)} = \frac{M^{(0)} M^{(2)} - (M^{(1)})^2}{(M^{(0)})^2} = \frac{M^{(2)}}{M^{(0)}} - \left(\frac{M^{(1)}}{M^{(0)}} \right)^2 \ . \tag{4.3}$$

Joint moments or multivariate moments, i.e. moments of multi-dimensional functions $f(\mathbf{x})$, feature a weighting with powers of each coordinate $\mathbf{x} = (x_1, x_2, x_3, ...)^\top$:

$$M^{(k,l,m,...)} = \int \cdots \int x_1^k x_2^l x_3^m ... f(\mathbf{x}) \mathrm{d}\mathbf{x} \ . \tag{4.4}$$

The term *co-variance* commonly used usually refers to the bi-variate moment of first order $M^{(1,1)}$.

4.1.2 Moments in Multiphase Flow Framework

Central moments are widely used in PDF methods for combustion modelling, turbulence modelling and multiphase modelling. The mean and variance of a sample of values are moments commonly known, since they are often applied when considering statistics of a given problem. Especially in two-phase flows, however, the use of moments about zero is significantly advantageous, mainly due to two reasons. First, moments based on a phase space which does not include the particle velocity must be naturally transported with different velocities. It is much easier to define these velocities and to derive moment transport equations analytically using moments about zero. In continuous, single phase flows, this problem does not occur. The often used mean and variance of mixture fraction or progress variable in PDF-based combustion models can be naturally convected with the gas phase velocity, since the underlying distribution refers to gas phase properties. In two-phase flows this holds only for perfect tracers ($\mathrm{St} \ll 1$), i.e. particles which follow perfectly the continuous phase. As soon as the distribution is based on particles having a non-vanishing, locally non-uniform slip velocity to the continuous phase (mainly due to their size dependent inertia), each moment must be convected with its own so-called *moment transport velocity*. Second, considerably advantageous is the fact that in dispersed phase flows the one-dimensional low order moments about zero based on the particles diameter[1] only,

$$M^{(k)} = \int_0^\infty D^k f^*(D) \mathrm{d}D \ , \tag{4.5}$$

can be assigned to physical properties of the particle population:

$M^{(0)}$: total number of particles per unit volume
or the total particle number density

$M^{(1)}$: sum of particle diameter

[1] Here it is implicitely assumed that the particles are spherical.

$\pi M^{(2)}$: total surface area per unit volume
or the total particle surface density

$\frac{\pi}{6} M^{(3)}$: total particle volume per unit volume
or the local volume fraction of particles

This allows a direct assessment of the plausibility of the experimental or numerical data and often a straightforward comparison. In definition 4.5, the support can be constrained to non-negative values, i.e. the lower integration boundary can be set to zero, since particles with negative diameter have no physical correspondence. Hence it makes no sense to define a function $f^*(D)$ for negative values of D. The same applies for other so-called *internal* variables (i.e. physical properties which vary from particle to particle), e.g. velocity, temperature, shape, etc., where the support of the distribution should be adjusted to the interval physically possible, e.g. temperatures must be larger than 0 K. The explicit notation of these limits are omitted from here on. Other internal variables describing the size of a particle are in general equally usable, e.g. particle surface or particle volume.

Using the diameter space as an example, the difference between moments about zero and moments about the mean (central moments) is exemplified next. The moments about zero are obtained from the basic integral by definition, the central moments by a decomposition into a mean D_{10} and a residual component D', i.e. $D = D_{10} + D'$. For the first moment about zero, which is the mean, the two different approaches read

$$\underbrace{M^{(1)}}_{\substack{\text{First moment}\\ \text{about zero}}} \leftarrow \int D f(D) \mathrm{d}D \rightarrow \underbrace{D_{10} M^{(0)}}_{\substack{\text{First central moment}\\ \text{(Mean)}}} , \tag{4.6}$$

whereas for the second moment about zero, which corresponds to the

variance, they become

$$\underbrace{M^{(2)}}_{\substack{\text{Second moment}\\ \text{about zero}}} \leftarrow \int D^2 f(D)\mathrm{d}D \rightarrow \underbrace{D_{10}D_{10}M^{(0)}}_{\text{Mean component}} + \underbrace{\int D'^{(n)}D'^{(n)}f(D)\mathrm{d}D}_{\substack{\text{Second central moment}\\ \text{(variance)}}} . \tag{4.7}$$

Reformulating the variance using $D' = D - D_{10}$, its nature as a central moment becomes more clear:

$$\int D'D' f(D)\mathrm{d}D = \int \left(D - D_{10}\right)^2 f(D)\mathrm{d}D . \tag{4.8}$$

In the previous relations, the quantity D_{10} is used, which is a specific *mean diameter* of the particle size distribution. Mean diameters can be defined in general using the moments about zero as

$$D_{ab} = \left(\frac{M^{(a)}}{M^{(b)}}\right)^{\frac{1}{a-b}} . \tag{4.9}$$

Dependent on the physical particle shape or the specific application, different variations of these mean diameters are used, e.g. the arithmetic mean diameter D_{10}, which is equal to the expectation value $\mu = D_{10}$, or, especially for non-spherical particles, the ratio between particle volume and particle surface can be of interest, which is the so-called *Sauter mean diameter* $D_{32} = M^{(3)}/M^{(2)}$.

Besides the particle mass or size, other particle properties can have a significant impact on the physical behaviour of the particles, e.g. the temperature on vaporisation rates or the reflectivity on the droplet heat-up via radiation. In these cases, considering several particle properties as internal variables simultaneously, can become inevitable to capture the desired physics properly. Considering spray combustion as the background of this work, we consider the particle size, here in terms of the diameter D (valid for spherical droplets), the particle velocity $\mathbf{c}_p$ and the particle temperature ζ_p. With this set of internal variables, the joint moments are defined as:

$$M^{(k,l,m)} = \iiint D^k \mathbf{c}_p^l \zeta_p^m f(D, \mathbf{c}_p, \zeta_p)\, \mathrm{d}\zeta_p \mathrm{d}\mathbf{c}_p \mathrm{d}D . \tag{4.10}$$

If the NDFs in each phase space dimension are independent, this relation simplifies to

$$M_D^{(k)} M_{\mathbf{c}_p}^{(l)} M_{\zeta_p}^{(m)} = \int D^k f_D(D)\mathrm{d}D \int \mathbf{c}_p^l f_{\mathbf{c}_p}(\mathbf{c}_p)\mathrm{d}\mathbf{c}_p \int \zeta_p^m f_{\zeta_p}(\zeta_p)\mathrm{d}\zeta_p \ . \quad (4.11)$$

4.2 The Ansatz for the Particle NDF

In the scope of this work, we consider moments of $f(D, \mathbf{c}_p, \zeta_p)$ up to an order for each phase space coordinate as specified next. First, the particle size space is described using moments about zero up to third order, i.e. $M^{(1)}$-$M^{(3)}$ and $M^{(0)}$-$M^{(3)}$ depending on the application (see Section 4.5.1). Second, the phase space of the particle velocity is considered by the first central moment, which is the size conditioned expectation value $\breve{\mathbf{u}}(D)$, i.e. it is assumed that particles with the same diameter have locally the same velocity. Hence the particle velocity can vary only with diameter (and time obviously) for a given position. Actually, velocity moments up to second order are formally kept, but only for analytical purposes to discuss the different proposals in the literature to close these. Finally, the particle temperature is considered by its overall expectation value, which means, that the temperature is locally uniform for all particles. These restrictions can be formulated *a priori* by choosing the following ansatz for the NDF:

$$\breve{\breve{f}}(D, \mathbf{c}_p, \zeta_p) = \breve{\breve{f}}^*(D)\delta(\mathbf{c}_p - \breve{\mathbf{u}}(D))\delta(\zeta_p - \breve{\breve{T}}_p) \ , \quad (4.12)$$

where $\breve{\breve{f}}^*(D)$ is continuous over D, the first Dirac delta allows particles of a certain diameter D to have locally the same (averaged) velocity $\breve{\mathbf{u}}(D)$ conditioned on size D only and the second Dirac delta implies that all particles of any size or velocity have locally the same (time-varying) temperature, i.e. the expectation value of $\breve{\breve{f}}(D, \mathbf{c}_p, \zeta_p)$. A similar notation can be found in de Chaisemartin et al. (2008) for a bi-variate case including particle surface and velocity. Therein this ansatz for the NDF is accurately referred to as "a single node quadrature method of moments in velocity space conditioned by size" with the background of QbMMs in mind. The

closure $\breve{\mathbf{u}}(D)$ does not allow non-equilibrium velocity distribution effects far from the Maxwellian distribution for the individual particle size (i.e. particle trajectory crossing of equal sized particles is not possible, which would be, in the simplest case a bi-modal distribution representing two crossing, monodisperse particle jets).

4.3 Phase Space Integration - Where the Particle Velocity Components Come Into Play

At this point some aspects of the integration of Eqn. 3.70 are described and discussed, with emphasis on the information kept of the FEbNDF and those which are not.

So far, the full phase space has been kept and the filtering operation has affected only the gas phase quantities. Now, the phase space integration will be carried out to obtain moment equations from the kinetic equation. At this point the particle velocity components[2] become important. In order to evaluate the integrals properly, one must keep in mind on which (conditioned) averages the phase space is actually based on. Here, these are ensemble average and spatial filtering. Therefore, before formally conducting the integration over the entire phase space, we describe the components for each phase space dimension separately except the particle temperature. Since it will be only considered by its overall expectation value, the temperature space is not considered in the following, but again when deriving the actual equations.

4.3.1 Velocity Space Integration

Formally, the integration over velocity space gives first, the mean velocity for a specific diameter, i.e. the size conditioned expectation value of

[2] i.e. residual components between an averaged value and the actual value, not the components of the velocity vector.

the particle velocity, and second, higher order moments. As shown in Eqn. 4.7, a decomposition of the particle velocity in a mean and residual components is evident to explicitly separate the mean component from the unknown residual component correlation. Hence, central moments are used for the velocity space to be able to identify and model the correlation terms of the residual components of the particle velocity. Since the NDF over phase space is based on two averaging procedures, we separately describe these two contributions before the combined decomposition is given.

First Contribution: The Ensemble Average

With dropping the explicit notation of the conditioning of the ensemble average on the gas phase realisation, $|\mathcal{H}_f$, the particle velocity can be expressed as

$$\mathbf{v}_p^{(n)} = \mathbf{v}_p^{(n)}(t, \mathcal{H}_p|D) = \breve{\mathbf{u}}(D; \mathbf{x}, t) + \breve{\mathbf{u}}'^{(n)}(D, \mathbf{c}_p; \mathbf{x}, t, \mathcal{H}_p) \,, \tag{4.13}$$

where $\breve{\mathbf{u}}(D; \mathbf{x}, t)$ is the pointwise (i.e. based on the non-filtered f) mean or expectation value of the velocity distribution conditioned on particle size D over particle phase realisations. Correspondingly, $\breve{\mathbf{u}}'^{(n)}(D, \mathbf{c}_p; \mathbf{x}, t, \mathcal{H}_p)$ is the residual component between the mean and the actual particle velocity $\mathbf{v}_p^{(n)}$.

Modelling for correlations containing this residual component of the particle velocity due to ensemble average has been conducted, e.g., by Simonin et al. (2002), Kaufmann et al. (2004)[3] or Reeks (1992). Application of the phase space integration when considering only this contribution, i.e. an NDF solely based on the ensemble average (EbNDF), is shown in the Appendix A.2.2.

[3] Incorporation of the size conditioned first central moment of the velocity distribution, known under the term *Random Uncorrelated Velocity* tensor (Riber et al., 2006), is governed by the term *Random Uncorrelated Motion* (Kaufmann et al., 2004).

Second Contribution: The Spatial Filtering

Solely spatial filtering for a given two-phase flow realisation yields similarly

$$\mathbf{v}_p^{(n)} = \mathbf{v}_p^{(n)}(t|D) = \bar{\mathbf{u}}(D;\mathbf{x},t) + \bar{\mathbf{u}}'^{(n)}(D,\mathbf{c}_p;\mathbf{x},t) \ , \tag{4.14}$$

where $\bar{\mathbf{u}}'^{(n)}(D,\mathbf{c}_p;\mathbf{x},t)$ is the deviation of the actual particle velocity $\mathbf{v}_p^{(n)}$ from the particle size conditioned spatial mean $\bar{\mathbf{u}}(D;\mathbf{x},t)$.

The co-variance of this component, often named *particle stress tensor*[4] has been topic of closure research especially in volume average based macroscopic models , but rather less in macroscopic models based on the mesoscopic kinetic equation of the NDF, e.g. Pandya and Mashayek (2002). The result of phase space integration considering only the sub-filter particle velocity fluctuations is detailed in Appendix A.2.1.

Combined Decomposition of Velocity Space

As a result, the particle velocity can be decomposed into a mean and two residual components due to ensemble average and spatial filtering, respectively, as

$$\mathbf{v}_p^{(n)} = \breve{\mathbf{u}}(D;\mathbf{x},t) + \breve{\mathbf{u}}'(D,\mathbf{c}_p;\mathbf{x},t) + \breve{\mathbf{u}}'^{(n)}(D,\mathbf{c}_p;\mathbf{x},t,\mathcal{H}_p) \ , \tag{4.15}$$

where $\breve{\mathbf{u}}'(D,\mathbf{c}_p;\mathbf{x},t)$ is the residual component between the spatial average of the mean ensemble values $\breve{\mathbf{u}}(D;\mathbf{x},t)$ and the individual, pointwise ensemble mean values $\breve{\mathbf{u}}(D;\mathbf{x},t)$, and $\breve{\mathbf{u}}'^{(n)}(D,\mathbf{c}_p;\mathbf{x},t,\mathcal{H}_p)$ is the residual component between an individual pointwise ensemble mean $\breve{\mathbf{u}}(D;\mathbf{x},t)$ and the individual particle velocity $\mathbf{v}_p^{(n)}$. Despite the two residual component correlations shown before, an additional unknown cross correlation between the ensemble average residual component and the filtering residual component appears. The derivation of that correlation is shown in Appendix A.2.3, however, whether a closure has been proposed in literature so far eludes the authors knowledge.

[4] Discussion on this terminology is given in Section 2.2.3 and Section 2.5.4, second paragraph.

4.3.2 Size Space Integration

Similarly, the particle diameter can vary locally between realisations and in physical space. Since the size space is integrated using moments about zero, no fluctuating component explicitly occurs. Hence with

$$M^{(k)} = \int D^k \breve{\breve{f}}(D)\mathrm{d}D \,, \tag{4.16}$$

ensemble average and filtering residual components hide behind the moments without being able to distinguish both contributions. Nevertheless, closure of higher order moments must be conducted, see Section 4.5.1.

Third Contribution to the Particle Velocity

Along with the integration over size space, a further average is built from the size conditioned mean velocities, which produces a third residual component for the particle velocity due to its integration over the size spectrum:

$$\begin{aligned} \mathbf{v}_p^{(n)}(t, \mathcal{H}_p|D) = \breve{\mathbf{u}}^{(k)}(\mathbf{x}, t) &+ \breve{\mathbf{u}}^{(k)\prime}(D; \mathbf{x}, t) \\ &+ \breve{\mathbf{u}}'(D, \mathbf{c}_p; \mathbf{x}, t) \\ &+ \breve{\mathbf{u}}'^{(n)}(D, \mathbf{c}_p; \mathbf{x}, t, \mathcal{H}_p) \,, \end{aligned} \tag{4.17}$$

where $\breve{\mathbf{u}}^{(k)\prime}(D; \mathbf{x}, t)$ is the deviation of $\breve{\mathbf{u}}(D; \mathbf{x}, t)$ from the size weighted mean of order k, $\breve{\mathbf{u}}^{(k)}(\mathbf{x}, t)$, i.e. $\breve{\mathbf{u}}(D; \mathbf{x}, t) = \breve{\mathbf{u}}^{(k)}(\mathbf{x}, t) + \breve{\mathbf{u}}^{(k)\prime}(D; \mathbf{x}, t)$

Modelling of this component has been proposed, e.g., by Carneiro (2012) in general or by Pandya and Mashayek (2002) for $k = 0$. Phase space integration using this triple decomposition has already been discussed in Appendix A.2.3.

4.3.3 A few Notes on Dispersed Phase "Turbulence" Modelling

As we have seen in the previous two sections 4.3.1 and 4.3.2 and especially in the Appendix A.2.1 to A.2.4, several unknown correlations appear in Eulerian mesoscopic-based models, which origin from different physical aspects. Gas phase correlations can be closed on the mesoscopic level (LHDI, etc.). Definition and some closures for the dispersed phase correlations have been shown above. Summarising, three dispersed phase velocity correlations appear:

- the tensor of mesoscopic particle velocity correlations of second order, resulting from the velocity space integration due to the ensemble average,
- the tensor of mesoscopic particle velocity correlations of second order, resulting from the velocity space integration due to spatial filtering
- and the correlations of the residual component between size conditioned mean velocities and moment transport velocities.

In volume average based models (VAbM), the unknown particle phase stress due to RANS average or LES filtering corresponds to the second point. Different two-phase flow realisations are usually not considered. VAbM closure for RANS has been reported for example by Issa and Oliveira (1997) based on Wang and Stock (1993), Oliveira and Issa (1998), Rizk and Elghobashi (1989), Elghobashi and Abou Arab (1989), Elghobashi et al. (1984), Mostafa and Elghobashi (1985), Deutsch and Simonin (1991), Simonin et al. (1993), Simonin et al. (1995), Zhou (2009) and for LES, e.g., by Zhou (2009), Liu et al. (2010), Mimouni et al. (2009). However, Eulerian volume average based models are often of rather empirical nature than rigorously derived from particle phase physics. This issue must attract more attention in future research.

4.4 Derivation of Moment Equations

This section is concerned with the derivation of the macroscopic equations for the transport of the moments, the particle momentum and the particle energy by integration of Eqn. 3.70 over the particle phase space, i.e.

$$\iiint \dots \mathrm{d}\zeta_p \mathrm{d}\mathbf{c}_p \mathrm{d}D \; . \tag{4.18}$$

4.4.1 Preliminary Steps

In order to derive the moment equations, we will evaluate the typical integrals appearing for the specific choice of the NDF (4.12) beforehand. For linear and non-linear terms in D only, the phase space integration basically yields

$$\begin{aligned}
&\iiint D^k \breve{\breve{f}}(D, \mathbf{c}_p, \zeta_p)\, \mathrm{d}\zeta_p \mathrm{d}\mathbf{c}_p \mathrm{d}D \\
&= \iiint D^k \breve{\breve{f}}^*(D) \delta(\mathbf{c}_p - \breve{\mathbf{u}}(D)) \delta(\zeta_p - \breve{\breve{T}}_p)\, \mathrm{d}\zeta_p \mathrm{d}\mathbf{c}_p \mathrm{d}D \\
&= \int D^k \breve{\breve{f}}^*(D) \left(\underbrace{\int \delta(\mathbf{c}_p - \breve{\mathbf{u}}(D)) \left(\underbrace{\int \delta(\zeta_p - \breve{\breve{T}}_p) \mathrm{d}\zeta_p}_{=1} \right) \mathrm{d}\mathbf{c}_p}_{=1} \right) \mathrm{d}D \\
&= \int D^k \breve{\breve{f}}^*(D)\, \mathrm{d}D \\
&= \breve{\breve{M}}^{(k)} \; .
\end{aligned} \tag{4.19}$$

Terms which are linear in particle velocity, do not give bi-variate moments of the type $M^{(k,l)}$ in our case, but the already mentioned moment

transport velocities for the size moments.

$$
\begin{aligned}
&\iiint D^k \mathbf{c}_p \breve{\breve{f}}(D, \mathbf{c}_p, \zeta_p)\, \mathrm{d}\zeta_p \mathrm{d}\mathbf{c}_p \mathrm{d}D \\
&= \iiint D^k \breve{\breve{f}}^*(D) \delta(\mathbf{c}_p - \breve{\mathbf{u}}(D)) \delta(\zeta_p - \breve{\breve{T}}_p) \mathbf{c}_p\, \mathrm{d}\zeta_p \mathrm{d}\mathbf{c}_p \mathrm{d}D \\
&= \int D^k \breve{\breve{f}}^*(D) \left(\underbrace{\int \delta(\mathbf{c}_p - \breve{\mathbf{u}}(D)) \mathbf{c}_p \left(\underbrace{\int \delta(\zeta_p - \breve{\breve{T}}_p) \mathrm{d}\zeta_p}_{=1} \right) \mathrm{d}\mathbf{c}_p}_{=\breve{\mathbf{u}}(D)} \right) \mathrm{d}D \\
&= \int D^k \breve{\mathbf{u}}(D) \breve{\breve{f}}^*(D)\, \mathrm{d}D \\
&\overset{\text{def.}}{=} \breve{\breve{M}}^{(k)} \breve{\mathbf{u}}^{(k)} \,,
\end{aligned}
\tag{4.20}
$$

whereas for terms of second order in particle velocity, e.g. the moment flux convection terms occurring in the moment flux transport equations, read

$$
\begin{aligned}
&\iiint D^k \mathbf{c}_p \mathbf{c}_p \breve{\breve{f}}(D, \mathbf{c}_p, \zeta_p)\, \mathrm{d}\zeta_p \mathrm{d}\mathbf{c}_p \mathrm{d}D \\
&= \iiint D^k \breve{\breve{f}}^*(D) \delta(\mathbf{c}_p - \breve{\mathbf{u}}(D)) \delta(\zeta_p - \breve{\breve{T}}_p) \mathbf{c}_p \mathbf{c}_p\, \mathrm{d}\zeta_p \mathrm{d}\mathbf{c}_p \mathrm{d}D \\
&= \int D^k \breve{\breve{f}}^*(D) \left(\underbrace{\int \delta(\mathbf{c}_p - \breve{\mathbf{u}}(D)) \mathbf{c}_p \mathbf{c}_p \left(\underbrace{\int \delta(\zeta_p - \breve{\breve{T}}_p) \mathrm{d}\zeta_p}_{=1} \right) \mathrm{d}\mathbf{c}_p}_{=\breve{\mathbf{u}}(D)\breve{\mathbf{u}}(D)} \right) \mathrm{d}D \\
&= \int D^k \breve{\mathbf{u}}(D) \breve{\mathbf{u}}(D) \breve{\breve{f}}^*(D)\, \mathrm{d}D \\
&= \breve{\breve{M}}^{(k)} (\breve{\mathbf{u}}\breve{\mathbf{u}})^{(k)} \\
&\overset{\text{def.}}{=} \breve{\breve{M}}^{(k)} \breve{\mathbf{u}}^{(k)} \breve{\mathbf{u}}^{(k)} + \int D^k \breve{\mathbf{u}}'(D) \breve{\mathbf{u}}'(D) \breve{\breve{f}}^*(D)\, \mathrm{d}D \,.
\end{aligned}
\tag{4.21}
$$

The last term on the rhs is the correlation of the "third" contribution

of the particle velocity (Section 4.3.2) and requires closure. It cannot be closed without any assumption for the particle velocities. These assumptions imply (as discussed briefly before) a physical correspondence. As done split the particle velocity into a weighted mean velocity $\breve{\mathbf{u}}^{(k)}$ and its deviation to the size conditioned velocity mean $\breve{\mathbf{u}}(D)$, written as $\breve{\mathbf{u}}'(D) = \breve{\mathbf{u}}^{(k)\prime}(D) = \breve{\mathbf{u}}(D) - \breve{\mathbf{u}}^{(k)}$. $\breve{\mathbf{u}}'$ is the "third contribution" mentioned before in Section 4.3.2. Modelling of $\int D^k \breve{\mathbf{u}}' \breve{\mathbf{u}}' \breve{\breve{f}}^*(D)\,\mathrm{d}D$ is not trivial and it is of different nature compared to the particle phase stress arising from the spatial filtering (Appendix A.2.1). With the background of ansatz 4.12 and the relaxation approach closure (see Section 4.5.3) we refer to Carneiro (2012, p.81) for a closure suggestion.

Summarising the relations outlined before gives (for notation supposes the abbreviations $\boldsymbol{\mathcal{I}}$ and $\mathrm{d}\boldsymbol{\mathcal{I}}$ are used from here on, which stand for $\boldsymbol{\mathcal{I}} = (D, \mathbf{c}_p, \zeta_p)^\top$ and $\mathrm{d}\boldsymbol{\mathcal{I}} = \mathrm{d}\zeta_p \mathrm{d}\mathbf{c}_p \mathrm{d}D$, respectively):

$$\breve{M}^{(0)} = \iiint \breve{\breve{f}}(\boldsymbol{\mathcal{I}}; \mathbf{x}, t)\,\mathrm{d}\boldsymbol{\mathcal{I}}\,, \tag{4.22}$$

$$\breve{M}^{(1)} = \iiint D \breve{\breve{f}}(\boldsymbol{\mathcal{I}}; \mathbf{x}, t)\,\mathrm{d}\boldsymbol{\mathcal{I}}\,, \tag{4.23}$$

$$\vdots$$

$$\breve{M}^{(k)} = \iiint D^k \breve{\breve{f}}(\boldsymbol{\mathcal{I}}; \mathbf{x}, t)\,\mathrm{d}\boldsymbol{\mathcal{I}}\,, \tag{4.24}$$

$$\breve{M}^{(k)} \breve{\mathbf{u}}^{(k)} \overset{\text{def.}}{=} \iiint \mathbf{c}_p D^k \breve{\breve{f}}(\boldsymbol{\mathcal{I}}; \mathbf{x}, t)\,\mathrm{d}\boldsymbol{\mathcal{I}}\,, \tag{4.25}$$

$$\breve{M}^{(k)} \phi \overset{\text{def.}}{=} \iiint \left(\phi | \phi \neq \phi(D, \mathbf{c}_p)\right) D^k \breve{\breve{f}}(\boldsymbol{\mathcal{I}}; \mathbf{x}, t)\,\mathrm{d}\boldsymbol{\mathcal{I}}\,. \tag{4.26}$$

ϕ is a general replacement for any property which might arise in the moment equations, but which is not a function of the internal variables, i.e. filtered gas phase quantities $\phi = \bar{\phi}_g$ or constant dispersed phase quantities $\phi = \phi_d$. Hence it is not affected by the integration and can be treated as a constant. Note, that the order of the superscript automatically implies the type of weighting, e.g. volume weighted properties (or equivalently mass weighted for constant particle density) comprise the super-

script $^{(3)}$. For the moment transport velocities this means that

$$\breve{\breve{\mathbf{u}}}^{(3)} = \frac{1}{\breve{\breve{M}}^{(3)}} \iiint \mathbf{c}_p D^3 \breve{\breve{f}}(\boldsymbol{\mathcal{I}}; \mathbf{x}, t)\, \mathrm{d}\boldsymbol{\mathcal{I}} \tag{4.27}$$

is the mass weighted particle mean velocity and

$$\breve{\breve{\mathbf{u}}}^{(0)} = \frac{1}{\breve{\breve{M}}^{(0)}} \iiint \mathbf{c}_p \breve{\breve{f}}(\boldsymbol{\mathcal{I}}; \mathbf{x}, t)\, \mathrm{d}\boldsymbol{\mathcal{I}} \tag{4.28}$$

is the arithmetic particle mean velocity. In general, i.e. everything in-between and beyond, the moment transport velocities are defined such that

$$\breve{\breve{\mathbf{u}}}^{(k)} = \frac{1}{\breve{\breve{M}}^{(k)}} \iiint \mathbf{c}_p D^k \breve{\breve{f}}(\boldsymbol{\mathcal{I}}; \mathbf{x}, t)\, \mathrm{d}\boldsymbol{\mathcal{I}}\ . \tag{4.29}$$

Non-linear terms marked with the superscript $^{(k)}$, e.g. expression like $(\mathbf{c}_p \mathbf{c}_p)^{(k)}$, are not meant as an already weighted property but a term for which the weighting still has to be applied, i.e. it is an abbreviation for the whole integration. This notation is used, however, only very few times in the following, where its meaning remains clear.

Note that the notation $\breve{\breve{\cdot}}$ over macroscopic variables acts as a reminder to distinguish between the moments shown in previous publications of the authors group (Carneiro et al., 2008, 2009, 2010, Dems et al., 2012a,b) and the ensemble averaged and LES-filtered type of moments defined in this work. Up to this point this notation has been kept but will be omitted from here on for simplicity. Gas phase properties, however, will be subsequently still marked, either filtered $\bar{\cdot}$ or Favre-filtered $\tilde{\cdot}$. The ensemble average $\breve{\cdot}$ does not apply as we use a single gas phase realisation only.

The derivation of the equations follows in its fundamental structure Mossa (2005), except the difference, that we avoid, shortly said, notations like $\iiint \frac{D^3}{D} f(\boldsymbol{\mathcal{I}})\, \mathrm{d}\boldsymbol{\mathcal{I}} = \frac{M^{(3)}}{M^{(1)}}$, which are transformed subsequently into $M^{(2)}$ in Mossa (2005). Instead, we directly formulate $\iiint \frac{D^3}{D} f(\boldsymbol{\mathcal{I}})\, \mathrm{d}\boldsymbol{\mathcal{I}} = \iiint D^2 f(\boldsymbol{\mathcal{I}})\, \mathrm{d}\boldsymbol{\mathcal{I}} = M^{(2)}$.

4.4.2 Mass-Averaged Equations, i.e. Equations for $M^{(3)}$

Mass averaged equations can be obtained by multiplying Eqn. 3.70 with $\rho_p D^3$. Additionally, Eqn. 3.70 will be formally multiplied with $\psi(\boldsymbol{\mathcal{I}})$, which is a placeholder to be replaced subsequently by D,$\mathbf{c}_p$ or ζ_p to obtain the corresponding mass weighted transport equations for volume fraction, momentum and energy, respectively. $\psi(\boldsymbol{\mathcal{I}})$ is solely a placeholder for the internal variables $D, \mathbf{c}_p, \zeta_p$ (or combinations of them), but not a function of spatial coordinates or time as well as another scalar s or vector $\mathbf{v}$, i.e. $\psi \neq \psi(s, \mathbf{v}; \mathbf{x}, t)$. With that, it follows that

$$\frac{\partial \psi(\boldsymbol{\mathcal{I}})}{\partial s, \mathbf{v}; \mathbf{x}, t} = 0 \quad \text{and} \quad \frac{\partial \psi = D}{\partial D} = \frac{\partial \psi = \mathbf{c}_p}{\partial \mathbf{c}_p} = \frac{\partial \psi = \zeta_p}{\partial \zeta_p} = 1 \,. \tag{4.30}$$

To keep the derivation clearly structured, it is done on a term by term basis. Using the placeholder $\psi(\boldsymbol{\mathcal{I}})$, each term will be integrated in a general manner and subsequently specified for the different types of conservation equations.

Time Derivative (Eqn. 3.70)

$$\begin{aligned}
&\iiint \frac{\partial f(\boldsymbol{\mathcal{I}})}{\partial t} \psi(\boldsymbol{\mathcal{I}}) \rho_p D^3 \, \mathrm{d}\boldsymbol{\mathcal{I}} \\
&= \frac{\partial}{\partial t} \iiint \psi(\boldsymbol{\mathcal{I}}) \rho_p D^3 f(\boldsymbol{\mathcal{I}}) \, \mathrm{d}\boldsymbol{\mathcal{I}} - \iiint f(\boldsymbol{\mathcal{I}}) \underbrace{\frac{\partial \psi(\boldsymbol{\mathcal{I}}) \rho_p D^3}{\partial t}}_{\overset{(4.30)}{=} 0} \mathrm{d}\boldsymbol{\mathcal{I}} \\
&= \frac{\partial}{\partial t} \iiint \psi(\boldsymbol{\mathcal{I}}) \rho_p D^3 f(\boldsymbol{\mathcal{I}}) \, \mathrm{d}\boldsymbol{\mathcal{I}} \,.
\end{aligned} \tag{4.31}$$

Setting $\psi(\boldsymbol{\mathcal{I}}) = 1$ gives the time derivative for the third moment transport equation

$$\frac{\partial}{\partial t} \iiint 1 \rho_p D^3 f(\boldsymbol{\mathcal{I}}) \, \mathrm{d}\boldsymbol{\mathcal{I}} = \frac{\partial \rho_d M^{(3)}}{\partial t} \,. \tag{4.32}$$

The temporal change of the particle phase momentum is obtained setting $\psi(\boldsymbol{\mathcal{I}}) = \mathbf{c}_p$

$$\frac{\partial}{\partial t} \iiint \mathbf{c}_p \rho_p D^3 f(\boldsymbol{\mathcal{I}}) \, \mathrm{d}\boldsymbol{\mathcal{I}} = \frac{\partial \rho_d M^{(3)} \mathbf{u}^{(3)}}{\partial t} \, . \tag{4.33}$$

The change of particle phase temperature with time is given with $\psi(\boldsymbol{\mathcal{I}}) = \zeta_p$ by

$$\frac{\partial}{\partial t} \iiint \zeta_p \rho_p D^3 f(\boldsymbol{\mathcal{I}}) \, \mathrm{d}\boldsymbol{\mathcal{I}} = \frac{\partial \rho_d M^{(3)} T_d}{\partial t} \, . \tag{4.34}$$

Convective Term (Eqn. 3.70)

$$\begin{aligned}
&\iiint \nabla \cdot (\mathbf{c}_p f(\boldsymbol{\mathcal{I}})) \psi(\boldsymbol{\mathcal{I}}) \rho_p D^3 \, \mathrm{d}\boldsymbol{\mathcal{I}} \\
&= \nabla \cdot \iiint \psi(\boldsymbol{\mathcal{I}}) \mathbf{c}_p \rho_p D^3 f(\boldsymbol{\mathcal{I}}) \, \mathrm{d}\boldsymbol{\mathcal{I}} - \iiint \mathbf{c}_p f(\boldsymbol{\mathcal{I}}) \rho_p \underbrace{\nabla \cdot (\psi(\boldsymbol{\mathcal{I}}) D^3)}_{\overset{(4.30)}{=} 0} \, \mathrm{d}\boldsymbol{\mathcal{I}} \\
&= \nabla \cdot \iiint \psi(\boldsymbol{\mathcal{I}}) \mathbf{c}_p \rho_p D^3 f(\boldsymbol{\mathcal{I}}) \, \mathrm{d}\boldsymbol{\mathcal{I}} \, .
\end{aligned} \tag{4.35}$$

Similar to the temporal derivative we get the three convective terms for mass, momentum and energy as

$$\nabla \cdot \iiint 1 \mathbf{c}_p \rho_p D^3 f(\boldsymbol{\mathcal{I}}) \, \mathrm{d}\boldsymbol{\mathcal{I}} = \nabla \cdot (\rho_d M^{(3)} \mathbf{u}^{(3)}) \, , \tag{4.36}$$

$$\nabla \cdot \iiint \mathbf{c}_p \mathbf{c}_p \rho_p D^3 f(\boldsymbol{\mathcal{I}}) \, \mathrm{d}\boldsymbol{\mathcal{I}} = \nabla \cdot (\rho_d M^{(3)} (\mathbf{u}\mathbf{u})^{(3)}) \, , \tag{4.37}$$

$$\nabla \cdot \iiint \zeta_p \mathbf{c}_p \rho_p D^3 f(\boldsymbol{\mathcal{I}}) \, \mathrm{d}\boldsymbol{\mathcal{I}} = \nabla \cdot (\rho_d M^{(3)} T_d \mathbf{u}^{(3)}) \, . \tag{4.38}$$

Momentum Exchange Source Term Due to Drag (Eqn. 3.70)

$$
\begin{aligned}
&- \iiint \frac{\partial}{\partial c_{p,j}} \left(\langle \frac{dv_{p,j}^{(n)}}{dt} | \boldsymbol{\mathcal{I}} \rangle^{\mathcal{VF}} f(\boldsymbol{\mathcal{I}}) \right) \psi(\boldsymbol{\mathcal{I}}) \rho_p D^3 \, \mathrm{d}\boldsymbol{\mathcal{I}} \\
&= \underbrace{- \iiint \frac{\partial}{\partial c_{p,j}} \left(\langle \frac{dv_{p,j}^{(n)}}{dt} | \boldsymbol{\mathcal{I}} \rangle^{\mathcal{VF}} \psi(\boldsymbol{\mathcal{I}}) \rho_p D^3 f(\boldsymbol{\mathcal{I}}) \right) \mathrm{d}\boldsymbol{\mathcal{I}}}_{=0 \text{ in line with Mossa (2005)}} \\
&\quad + \iiint \langle \frac{dv_{p,j}^{(n)}}{dt} | \boldsymbol{\mathcal{I}} \rangle^{\mathcal{VF}} f(\boldsymbol{\mathcal{I}}) \rho_p \left(D^3 \frac{\partial \psi(\boldsymbol{\mathcal{I}})}{\partial c_{p,j}} + \psi(\boldsymbol{\mathcal{I}}) \underbrace{\frac{\partial D^3}{\partial c_{p,j}}}_{=0} \right) \mathrm{d}\boldsymbol{\mathcal{I}} \\
&= \iiint \langle \frac{dv_{p,j}^{(n)}}{dt} | \boldsymbol{\mathcal{I}} \rangle^{\mathcal{VF}} f(\boldsymbol{\mathcal{I}}) \rho_p D^3 \frac{\partial \psi(\boldsymbol{\mathcal{I}})}{\partial c_{p,j}} \, \mathrm{d}\boldsymbol{\mathcal{I}} \, .
\end{aligned} \tag{4.39}
$$

The mass conservation is not affected by momentum exchange between phases ($\psi(\boldsymbol{\mathcal{I}}) = 1$), which is in line with the mathematical derivation:

$$
= \iiint \langle \frac{dv_{p,j}^{(n)}}{dt} | \boldsymbol{\mathcal{I}} \rangle^{\mathcal{VF}} f(\boldsymbol{\mathcal{I}}) \rho_p D^3 \underbrace{\frac{\partial 1}{\partial c_{p,j}}}_{=0} \mathrm{d}\boldsymbol{\mathcal{I}} = 0 \, . \tag{4.40}
$$

Considering the drag coefficient correlation by Schiller and Naumann we develop the Stokes and non-Stokes part separately using Eqn. 3.73 and Eqn. 3.75, respectively. With $\psi(\boldsymbol{\mathcal{I}}) = \mathbf{c}_p$ we obtain for Stokes drag and the body force due to gravitation the closed[5] expression

$$
= \iiint \langle \frac{dv_{p,j}^{(n)}}{dt} | \boldsymbol{\mathcal{I}} \rangle^{\mathcal{VF}} f(\boldsymbol{\mathcal{I}}) \rho_p D^3 \frac{\partial \mathbf{c}_p}{\partial c_{p,j}} \, \mathrm{d}\boldsymbol{\mathcal{I}} \, ,
$$

[5] In fact, in classical volume averaged based two-phase equations, a closure problem arises already for Stokes drag at this point. This issue is detailed in Appendix A.2.5

$$\text{with} \quad \frac{\partial \mathbf{c}_p}{\partial c_{p,j}} = \underbrace{\frac{\partial c_{p,j}}{\partial c_{p,j}}}_{=1} \mathbf{e}_j \quad \text{and} \quad \mathbf{e}_{j=1} = \begin{pmatrix} 1 \\ 0 \\ 0 \end{pmatrix}, \mathbf{e}_{j=2} = \begin{pmatrix} 0 \\ 1 \\ 0 \end{pmatrix}, \mathbf{e}_{j=3} = \begin{pmatrix} 0 \\ 0 \\ 1 \end{pmatrix},$$

where Einstein summation applies to obtain a vectorial source term

$$\begin{aligned} &\overset{(3.73)}{=} \iiint \left(\frac{18\bar{\nu}\bar{\rho}}{\rho_p D^2} (\tilde{\mathbf{u}} - \mathbf{c}_p) + \mathbf{g} \right) f(\boldsymbol{\mathcal{I}}) \rho_p D^3 \, \mathrm{d}\boldsymbol{\mathcal{I}} \\ &= \iiint \left(18\bar{\nu}\bar{\rho} D (\tilde{\mathbf{u}} - \mathbf{c}_p) + \mathbf{g} D^3 \rho_p \right) f(\boldsymbol{\mathcal{I}}) \, \mathrm{d}\boldsymbol{\mathcal{I}} \\ &\overset{(4.20)}{=} 18\bar{\eta} M^{(1)} (\tilde{\mathbf{u}} - \mathbf{u}^{(1)}) + \mathbf{g} M^{(3)} \rho_d \, . \end{aligned} \tag{4.41}$$

Similarly, using the empirical correction for particle Reynolds numbers beyond Stokes flow,

$$\begin{aligned} &= \iiint \langle \frac{dv_{p,j}^{(n)}}{dt} | \boldsymbol{\mathcal{I}} \rangle^{\mathcal{VF}} f(\boldsymbol{\mathcal{I}}) \rho_p D^3 \underbrace{\frac{\partial \mathbf{c}_p}{\partial c_{p,j}}}_{=\text{see above}} \mathrm{d}\boldsymbol{\mathcal{I}} \\ &\overset{(3.75)}{=} \iiint \left(\frac{18\bar{\nu}\bar{\rho}}{\rho_p D^2} 0.15 \left(\frac{|\tilde{\mathbf{u}} - \mathbf{c}_p| D}{\bar{\nu}} \right)^{0.687} (\tilde{\mathbf{u}} - \mathbf{c}_p) \right) f(\boldsymbol{\mathcal{I}}) \rho_p D^3 \, \mathrm{d}\boldsymbol{\mathcal{I}} \\ &= \iiint 18\bar{\nu}\bar{\rho} 0.15 \left(\frac{|\tilde{\mathbf{u}} - \mathbf{c}_p|}{\bar{\nu}} \right)^{0.687} (\tilde{\mathbf{u}} - \mathbf{c}_p) D^{1.687} f(\boldsymbol{\mathcal{I}}) \, \mathrm{d}\boldsymbol{\mathcal{I}} \, , \end{aligned}$$

with approximately closing $|\tilde{\mathbf{u}} - \mathbf{c}_p| = |\tilde{\mathbf{u}} - \mathbf{u}^{(1)}|^*$, which yields

$$\approx 18\bar{\nu}\bar{\rho} 0.15 \left(\frac{|\tilde{\mathbf{u}} - \mathbf{u}^{(1)}|}{\bar{\nu}} \right)^{0.687} (\tilde{\mathbf{u}} - \mathbf{u}^{(1.687)}) M^{(1.687)} \, . \tag{4.42}$$

The approximation * is arbitrarily chosen in line with the transport velocity $\mathbf{u}^{(1)}$ valid for Stokes flow. It is not clear whether, e.g., $\mathbf{u}^{(1.687)}$ might be closer to the correct solution. The combination of both contributions

to the drag term (abbreviated as **M**) and the gravity force reads

$$
\begin{aligned}
&= 18\bar{\eta}\Bigg(M^{(1)}(\tilde{\mathbf{u}} - \mathbf{u}^{(1)}) \\
&\qquad + 0.15\left(\frac{|\tilde{\mathbf{u}} - \mathbf{u}^{(1)}|}{\bar{\nu}}\right)^{0.687} (\tilde{\mathbf{u}} - \mathbf{u}^{(1.687)}) M^{(1.687)}\Bigg) + \mathbf{g}M^{(3)}\rho_d \\
&\overset{\text{def.}}{=} \mathbf{M}^{(3)} + \mathbf{g}M^{(3)}\rho_d \,. \qquad (4.43)
\end{aligned}
$$

Momentum exchange acts only in a kinetic way and does not contribute to temperature and sensible enthalpy, respectively, since the kinetic energy of the particle phase is not considered in the energy balance.

Setting $\psi(\boldsymbol{\mathcal{I}}) = \zeta_p$ yields

$$
= \iiint \langle \frac{dv_{p,j}^{(n)}}{dt} | \boldsymbol{\mathcal{I}} \rangle^{\mathcal{VF}} f(\boldsymbol{\mathcal{I}}) \rho_p D^3 \underbrace{\frac{\partial \zeta_p}{\partial c_{p,j}}}_{=0} \, \mathrm{d}\boldsymbol{\mathcal{I}} = 0 \,. \qquad (4.44)
$$

Mass Exchange Source Term Due to Vaporisation (Eqn. 3.70)

Here, each conservation equation comprises a source term, first the mass transfer from liquid to vapour in the mass conservation equation, second, the implied momentum transfer due to mass transfer and finally, the transferred energy contained in the transferred mass. Since the vaporisation rate depends significantly on the slip velocity between the phases, we split the vaporisation rate in the part for Stokes flow conditions and the additional contribution due to higher relative velocities. Concerning this separation and terminology, some comments are given in Footnote 5 on page 61. This separation holds for all three source terms as presented below. Contributions due to free convection are not considered. Replace-

ment of the placeholder $\psi(\boldsymbol{\mathcal{I}})$ in the general expression

$$
\begin{aligned}
&- \iiint \frac{\partial}{\partial D} \left(\langle \frac{dD^{(n)}}{dt} | \boldsymbol{\mathcal{I}} \rangle^{\mathcal{VF}} f(\boldsymbol{\mathcal{I}}) \right) \psi(\boldsymbol{\mathcal{I}}) \rho_p D^3 \, \mathrm{d}\boldsymbol{\mathcal{I}} \\
&= \text{... similarly to Eqn. 4.39 the first term becomes zero} \\
&\qquad + \iiint \langle \frac{dD^{(n)}}{dt} | \boldsymbol{\mathcal{I}} \rangle^{\mathcal{VF}} f(\boldsymbol{\mathcal{I}}) \rho_p \left(\psi(\boldsymbol{\mathcal{I}}) \underbrace{\frac{\partial D^3}{\partial D}}_{3D^2} + D^3 \frac{\partial \psi(\boldsymbol{\mathcal{I}})}{\partial D} \right) \mathrm{d}\boldsymbol{\mathcal{I}} \\
&= \iiint \langle \frac{dD^{(n)}}{dt} | \boldsymbol{\mathcal{I}} \rangle^{\mathcal{VF}} f(\boldsymbol{\mathcal{I}}) \rho_p \left(\psi(\boldsymbol{\mathcal{I}}) 3D^2 + D^3 \frac{\partial \psi(\boldsymbol{\mathcal{I}})}{\partial D} \right) \mathrm{d}\boldsymbol{\mathcal{I}} \qquad (4.45)
\end{aligned}
$$

by $\psi(\boldsymbol{\mathcal{I}}) = 1$, $\psi(\boldsymbol{\mathcal{I}}) = \mathbf{c}_p$ and $\psi(\boldsymbol{\mathcal{I}}) = \zeta_p$ yields the expressions for the mass, momentum and temperature equation, respectively.

First, setting $\psi(\boldsymbol{\mathcal{I}}) = 1$,

$$
= \iiint \langle \frac{dD^{(n)}}{dt} | \boldsymbol{\mathcal{I}} \rangle^{\mathcal{VF}} f(\boldsymbol{\mathcal{I}}) \rho_p \left(3D^2 + D^3 \underbrace{\frac{\partial 1}{\partial D}}_{=0} \right) \mathrm{d}\boldsymbol{\mathcal{I}} \, ,
$$

gives the Stokes part (S)

$$
\begin{aligned}
&\overset{(A.32)}{=} - \iiint 4 \frac{\bar{\rho}\mathfrak{D}}{\rho_p D} \ln(1 + \tilde{\mathrm{B}}_{\mathrm{M}}) f(\boldsymbol{\mathcal{I}}) \rho_p 3D^2 \, \mathrm{d}\boldsymbol{\mathcal{I}} \\
&= - \iiint 12 \bar{\rho}\mathfrak{D} \ln(1 + \tilde{\mathrm{B}}_{\mathrm{M}}) D f(\boldsymbol{\mathcal{I}}) \, \mathrm{d}\boldsymbol{\mathcal{I}} \\
&= \underbrace{-12 \bar{\rho}\mathfrak{D} \ln(1 + \tilde{\mathrm{B}}_{\mathrm{M}}) M^{(1)}}_{\equiv -\Gamma^{\mathrm{S}}_{M^{(3)}}} \qquad (4.46)
\end{aligned}
$$

and the additional part due to higher Reynolds numbers (nS)

$$
\begin{aligned}
&\overset{(A.33)}{=} -\iiint 0.552 \cdot 2\frac{\bar{\rho}}{\rho_p}\mathfrak{D}\frac{\mathrm{Sc}^{1/3}}{D^{1/2}}\left(\frac{(\tilde{\mathbf{u}}-\mathbf{c}_p)}{\bar{v}}\right)^{1/2}\frac{\tilde{\mathrm{B}}_\mathrm{M}}{(1+\tilde{\mathrm{B}}_\mathrm{M})^{0.7}}f(\boldsymbol{\mathcal{I}})\rho_p 3D^2\,\mathrm{d}\boldsymbol{\mathcal{I}} \\
&= -0.552\cdot 6\bar{\rho}\mathfrak{D}\frac{\mathrm{Sc}^{1/3}}{\bar{v}^{1/2}}\iiint(\tilde{\mathbf{u}}-\mathbf{c}_p)^{1/2}\frac{\tilde{\mathrm{B}}_\mathrm{M}}{(1+\tilde{\mathrm{B}}_\mathrm{M})^{0.7}}f(\boldsymbol{\mathcal{I}})D^{3/2}\,\mathrm{d}\boldsymbol{\mathcal{I}} \\
&= \underbrace{-0.552\cdot 6\bar{\rho}\mathfrak{D}\,\mathrm{Sc}^{1/3}\left(\frac{(\tilde{\mathbf{u}}-\mathbf{u}^{(1.5)})}{\bar{v}}\right)^{1/2}\frac{\tilde{\mathrm{B}}_\mathrm{M}}{(1+\tilde{\mathrm{B}}_\mathrm{M})^{0.7}}M^{(1.5)}}_{\equiv -\Gamma^{\mathrm{nS}}_{M^{(3)}}}\,. \qquad (4.47)
\end{aligned}
$$

The sum of both is noted as

$$
\Gamma_{M^{(3)}} = \Gamma^{\mathrm{S}}_{M^{(3)}} + \Gamma^{\mathrm{nS}}_{M^{(3)}}\,. \qquad (4.48)
$$

Second, setting $\psi(\boldsymbol{\mathcal{I}}) = \mathbf{c}_p$,

$$
= \iiint \langle\frac{dD^{(n)}}{dt}|\boldsymbol{\mathcal{I}}\rangle^{\mathcal{VF}} f(\boldsymbol{\mathcal{I}})\rho_p\left(\mathbf{c}_p 3D^2 + D^3\underbrace{\frac{\partial \mathbf{c}_p}{\partial D}}_{=0}\right)\mathrm{d}\boldsymbol{\mathcal{I}}\,,
$$

gives the Stokes part (S)

$$
\begin{aligned}
&\overset{(A.32)}{=} -\iiint 4\frac{\bar{\rho}\mathfrak{D}}{\rho_p D}\ln(1+\tilde{\mathrm{B}}_\mathrm{M})f(\boldsymbol{\mathcal{I}})\mathbf{c}_p\rho_p 3D^2\,\mathrm{d}\boldsymbol{\mathcal{I}} \\
&= -\iiint 12\bar{\rho}\mathfrak{D}\ln(1+\tilde{\mathrm{B}}_\mathrm{M})D\mathbf{c}_p f(\boldsymbol{\mathcal{I}})\,\mathrm{d}\boldsymbol{\mathcal{I}} \\
&= -12\bar{\rho}\mathfrak{D}\ln(1+\tilde{\mathrm{B}}_\mathrm{M})M^{(1)}\mathbf{u}^{(1)} \\
&= -\Gamma^{\mathrm{S}}_{M^{(3)}}\mathbf{u}^{(1)} \qquad (4.49)
\end{aligned}
$$

and the additional part due to higher Reynolds numbers (nS)

$$
\begin{aligned}
&\overset{(A.33)}{=} -\iiint 0.552 \cdot 2\frac{\bar{\rho}}{\rho_p}\mathfrak{D}\frac{\mathrm{Sc}^{1/3}}{D^{1/2}}\left(\frac{(\tilde{\mathbf{u}}-\mathbf{c}_p)}{\bar{v}}\right)^{1/2}\frac{\tilde{\mathrm{B}}_\mathrm{M}}{(1+\tilde{\mathrm{B}}_\mathrm{M})^{0.7}}f(\boldsymbol{\mathcal{I}})\mathbf{c}_p\rho_p 3D^2\,\mathrm{d}\boldsymbol{\mathcal{I}}\\
&= -0.552\cdot 6\bar{\rho}\mathfrak{D}\frac{\mathrm{Sc}^{1/3}}{\bar{v}^{1/2}}\iiint(\tilde{\mathbf{u}}-\mathbf{c}_p)^{1/2}\frac{\tilde{\mathrm{B}}_\mathrm{M}}{(1+\tilde{\mathrm{B}}_\mathrm{M})^{0.7}}f(\boldsymbol{\mathcal{I}})\mathbf{c}_p D^{3/2}\,\mathrm{d}\boldsymbol{\mathcal{I}}\\
&= -0.552\cdot 6\bar{\rho}\mathfrak{D}\,\mathrm{Sc}^{1/3}\left(\frac{(\tilde{\mathbf{u}}-\mathbf{u}^{(1.5)})}{\bar{v}}\right)^{1/2}\frac{\tilde{\mathrm{B}}_\mathrm{M}}{(1+\tilde{\mathrm{B}}_\mathrm{M})^{0.7}}M^{(1.5)}\mathbf{u}^{(1.5)}\\
&= -\Gamma^{\mathrm{nS}}_{M^{(3)}}\mathbf{u}^{(1.5)}\,. \qquad (4.50)
\end{aligned}
$$

The sum of both is approximated as

$$
\Gamma^{\mathrm{S}}_{M^{(3)}}\mathbf{u}^{(1)}+\Gamma^{\mathrm{nS}}_{M^{(3)}}\mathbf{u}^{(1.5)}\approx\Gamma_{M^{(3)}}\mathbf{u}^{(1)}\,. \qquad (4.51)
$$

Third, setting $\psi(\boldsymbol{\mathcal{I}})=\zeta_p$,

$$
= \iiint\langle\frac{dD^{(n)}}{dt}|\boldsymbol{\mathcal{I}}\rangle^{\mathcal{VF}}f(\boldsymbol{\mathcal{I}})\rho_p\left(\zeta_p 3D^2+D^3\underbrace{\frac{\partial\zeta_p}{\partial D}}_{=0}\right)\mathrm{d}\boldsymbol{\mathcal{I}}\,,
$$

gives the Stokes part (S)

$$
\begin{aligned}
&\overset{(A.32)}{=} -\iiint 4\frac{\bar{\rho}\mathfrak{D}}{\rho_p D}\ln(1+\tilde{\mathrm{B}}_\mathrm{M})f(\boldsymbol{\mathcal{I}})\zeta_p\rho_p 3D^2\,\mathrm{d}\boldsymbol{\mathcal{I}}\\
&= -\iiint 12\bar{\rho}\mathfrak{D}\ln(1+\tilde{\mathrm{B}}_\mathrm{M})D\zeta_p f(\boldsymbol{\mathcal{I}})\,\mathrm{d}\boldsymbol{\mathcal{I}}\\
&= -12\bar{\rho}\mathfrak{D}\ln(1+\tilde{\mathrm{B}}_\mathrm{M})M^{(1)}T_d\\
&= -\Gamma^{\mathrm{S}}_{M^{(3)}}T_d \qquad (4.52)
\end{aligned}
$$

and the additional part due to higher Reynolds numbers (nS)

$$
\begin{aligned}
&\overset{(A.33)}{=} -\iiint 0.552 \cdot 2\frac{\bar{\rho}}{\rho_p}\mathfrak{D}\frac{\mathrm{Sc}^{1/3}}{D^{1/2}}\left(\frac{(\tilde{\mathbf{u}}-\mathbf{c}_p)}{\bar{\nu}}\right)^{1/2}\frac{\tilde{\mathrm{B}}_\mathrm{M}}{(1+\tilde{\mathrm{B}}_\mathrm{M})^{0.7}} f(\boldsymbol{\mathcal{I}})\zeta_p\rho_p 3D^2\,\mathrm{d}\boldsymbol{\mathcal{I}} \\
&= -0.552\cdot 6\bar{\rho}\mathfrak{D}\frac{\mathrm{Sc}^{1/3}}{\bar{\nu}^{1/2}}\iiint(\tilde{\mathbf{u}}-\mathbf{c}_p)^{1/2}\frac{\tilde{\mathrm{B}}_\mathrm{M}}{(1+\tilde{\mathrm{B}}_\mathrm{M})^{0.7}} f(\boldsymbol{\mathcal{I}})\zeta_p D^{3/2}\,\mathrm{d}\boldsymbol{\mathcal{I}} \\
&= -0.552\cdot 6\bar{\rho}\mathfrak{D}\,\mathrm{Sc}^{1/3}\left(\frac{(\tilde{\mathbf{u}}-\mathbf{u}^{(1.5)})}{\bar{\nu}}\right)^{1/2}\frac{\tilde{\mathrm{B}}_\mathrm{M}}{(1+\tilde{\mathrm{B}}_\mathrm{M})^{0.7}} M^{(1.5)}T_d \\
&= -\Gamma^{\mathrm{nS}}_{M^{(3)}}T_d\,. \qquad (4.53)
\end{aligned}
$$

The sum of both yields

$$
\left(\Gamma^{\mathrm{S}}_{M^{(3)}}+\Gamma^{\mathrm{nS}}_{M^{(3)}}\right)T_d = \Gamma_{M^{(3)}}T_d\,. \qquad (4.54)
$$

Energy Exchange Source Term Due to Heat Conduction and Energy Transfer Through Vaporisation (Eqn. 3.70)

The general expression reads

$$
\begin{aligned}
&-\iiint\frac{\partial}{\partial\zeta_p}\left(\langle\frac{dT_p^{(n)}}{dt}|\boldsymbol{\mathcal{I}}\rangle^{\mathcal{VF}}f(\boldsymbol{\mathcal{I}})\right)\psi(\boldsymbol{\mathcal{I}})\rho_p D^3\,\mathrm{d}\boldsymbol{\mathcal{I}} \\
&= \text{... similarly to Eqn. 4.39 the first term becomes zero} \\
&\quad +\iiint\langle\frac{dT_p^{(n)}}{dt}|\boldsymbol{\mathcal{I}}\rangle^{\mathcal{VF}}f(\boldsymbol{\mathcal{I}})\rho_p\left(\psi(\boldsymbol{\mathcal{I}})\underbrace{\frac{\partial D^3}{\partial\zeta_p}}_{=0}+D^3\frac{\partial\psi(\boldsymbol{\mathcal{I}})}{\partial\zeta_p}\right)\mathrm{d}\boldsymbol{\mathcal{I}} \\
&= \iiint\langle\frac{dT_p^{(n)}}{dt}|\boldsymbol{\mathcal{I}}\rangle^{\mathcal{VF}}f(\boldsymbol{\mathcal{I}})\rho_p D^3\frac{\partial\psi(\boldsymbol{\mathcal{I}})}{\partial\zeta_p}\,\mathrm{d}\boldsymbol{\mathcal{I}}\,. \qquad (4.55)
\end{aligned}
$$

Mass continuity ($\psi(\boldsymbol{\mathcal{I}})=1$) and momentum conservation ($\psi(\boldsymbol{\mathcal{I}})=\mathbf{c}_p$),

i.e.

$$\iiint \langle \frac{dT_p^{(n)}}{dt} | \boldsymbol{\mathcal{I}} \rangle^{\mathcal{VF}} f(\boldsymbol{\mathcal{I}}) \rho_p D^3 \underbrace{\frac{\partial 1}{\partial \zeta_p}}_{=0} \, \mathrm{d}\boldsymbol{\mathcal{I}} = 0 \,, \tag{4.56}$$

$$\iiint \langle \frac{dT_p^{(n)}}{dt} | \boldsymbol{\mathcal{I}} \rangle^{\mathcal{VF}} f(\boldsymbol{\mathcal{I}}) \rho_p D^3 \underbrace{\frac{\partial \mathbf{c}_p}{\partial \zeta_p}}_{=0} \, \mathrm{d}\boldsymbol{\mathcal{I}} = 0 \,, \tag{4.57}$$

are not affected by heat conduction and the latent enthalpy consumption. The source term for the temperature equation will be spit into two parts. The first part considers only heat transfer for forced flow in the Stokes regime, whereas the second part incorporates the increase of heat conduction due to forced convection at higher Reynolds numbers, i.e. particle and gas flow have different velocities. Here again, contributions of free convection are not considered. The net heat transferred to the particle is determined by first transferring all conductive heat to the droplet, as it would be without vaporisation, and afterwards subtracting all the heat which the particle looses due to the heat needed to transfer the liquid into vapour. Setting $\psi(\boldsymbol{\mathcal{I}}) = \zeta_p$ yields

$$\iiint \langle \frac{dT_p^{(n)}}{dt} | \boldsymbol{\mathcal{I}} \rangle^{\mathcal{VF}} f(\boldsymbol{\mathcal{I}}) \rho_p D^3 \underbrace{\frac{\partial \zeta_p}{\partial \zeta_p}}_{=1} \, \mathrm{d}\boldsymbol{\mathcal{I}}$$

and with introducing the part for low Reynolds numbers (Stokes flow, (S)), it becomes

$$\begin{aligned}
&\overset{(A.30)}{=} \iiint \left[\frac{12}{c_{\mathrm{p}d}} \bar{\lambda} (T - \zeta_p) \frac{\ln(1 + \bar{\mathrm{B}}_\mathrm{T})}{\bar{\mathrm{B}}_\mathrm{T}} - \frac{12}{c_{\mathrm{p}d}} \bar{\rho} \mathfrak{D} \ln(1 + \tilde{\mathrm{B}}_\mathrm{M}) \Delta h_v(\zeta_p) \right] D f(\boldsymbol{\mathcal{I}}) \, \mathrm{d}\boldsymbol{\mathcal{I}} \\
&= 12 \frac{\bar{\lambda}}{c_{\mathrm{p}d}} (T - T_d) M^{(1)} \frac{\ln(1 + \bar{\mathrm{B}}_\mathrm{T})}{\bar{\mathrm{B}}_\mathrm{T}} - 12 \bar{\rho} \mathfrak{D} \frac{\Delta h_v(T_d)}{c_{\mathrm{p}d}} \ln(1 + \bar{\mathrm{B}}_\mathrm{M}) M^{(1)} \\
&= 12 \frac{\bar{\lambda}}{c_{\mathrm{p}d}} (T - T_d) M^{(1)} \frac{\ln(1 + \bar{\mathrm{B}}_\mathrm{T})}{\bar{\mathrm{B}}_\mathrm{T}} - \Gamma^{\mathrm{S}}_{M^{(3)}} \frac{\Delta h_v(T_d)}{c_{\mathrm{p}d}} \,,
\end{aligned} \tag{4.58}$$

where $\Delta h_v(T_d)$ is the expectation value of $\Delta h_v(\zeta_p)$. Actually, since $\dot{m}_T \overset{!}{=} \dot{m}_M$, one can write using $12\bar{\lambda}/c_{\mathrm{P}v} \ln(1+\bar{\mathrm{B}}_\mathrm{T}) M^{(1)} = \Gamma^{\mathrm{S}}_{M^{(3)}}$:

$$= -\Gamma^{\mathrm{S}}_{M^{(3)}} \frac{1}{c_{\mathrm{P}d}} \left(\Delta h_v(T_d) - c_{\mathrm{P}v} \frac{(T - T_d)}{\bar{\mathrm{B}}_\mathrm{T}} \right) . \tag{4.59}$$

The additional part due to higher Reynolds numbers (nS) develops as

$$\begin{aligned} &\overset{(A.31)}{=} \iiint 0.552 \cdot 6 \frac{\bar{\lambda} \mathrm{Pr}^{1/3}}{D^{3/2} \rho_p c_{\mathrm{P}l}} \left(\frac{\mathbf{u} - \mathbf{c}_p}{\bar{\nu}} \right)^{1/2} \frac{(T - \zeta_p)}{(1+\bar{\mathrm{B}}_\mathrm{T})^{0.7}} f(\boldsymbol{\mathcal{I}}) \rho_p D^3 \, \mathrm{d}\boldsymbol{\mathcal{I}} \\ &\quad - \iiint 0.552 \cdot 6 \frac{\bar{\rho} \mathfrak{D} \, \mathrm{Sc}^{1/3}}{D^{3/2} \rho_p c_{\mathrm{P}l}} \left(\frac{\tilde{\mathbf{u}} - \mathbf{c}_p}{\bar{\nu}} \right)^{1/2} \frac{\Delta h_v(\zeta_p) \tilde{\mathrm{B}}_\mathrm{M}}{(1+\tilde{\mathrm{B}}_\mathrm{M})^{0.7}} f(\boldsymbol{\mathcal{I}}) \rho_p D^3 \, \mathrm{d}\boldsymbol{\mathcal{I}} \end{aligned}$$

$$\begin{aligned} &= 0.552 \cdot 6 \frac{\bar{\lambda} \mathrm{Pr}^{1/3}}{c_{\mathrm{P}l} \bar{\nu}^{1/2}} \iiint (\mathbf{u} - \mathbf{c}_p)^{1/2} \frac{(T - \zeta_p)}{(1+\bar{\mathrm{B}}_\mathrm{T})^{0.7}} f(\boldsymbol{\mathcal{I}}) D^{3/2} \, \mathrm{d}\boldsymbol{\mathcal{I}} \\ &\quad - 0.552 \cdot 6 \frac{\bar{\rho} \mathfrak{D} \, \mathrm{Sc}^{1/3}}{c_{\mathrm{P}l} \bar{\nu}^{1/2}} \iiint (\tilde{\mathbf{u}} - \mathbf{c}_p)^{1/2} \frac{\Delta h_v(\zeta_p) \tilde{\mathrm{B}}_\mathrm{M}}{(1+\tilde{\mathrm{B}}_\mathrm{M})^{0.7}} f(\boldsymbol{\mathcal{I}}) D^{3/2} \, \mathrm{d}\boldsymbol{\mathcal{I}} . \end{aligned}$$

Here, some simplification must be done in order to gain closed equations, i.e. the particle temperature and size dependent quantities $\bar{\mathrm{B}}_\mathrm{T}$ and $\bar{\mathrm{B}}_\mathrm{M}$ are replaced a priori by their expectation values concerning size (temperature is mono-valued per definition, Eqn. 4.12), $\bar{\mathrm{B}}^{(0)}_\mathrm{T}$ and $\bar{\mathrm{B}}^{(0)}_\mathrm{M}$, but this specific notation is forgotten in the following. Furthermore, for $\Delta h_v(\zeta_p)$, the same applies as mentioned before. Additionally the velocity term is approximated as follows:

$$\begin{aligned} &\approx 0.552 \cdot 6 \frac{\bar{\lambda} \mathrm{Pr}^{1/3}}{c_{\mathrm{P}l}} \left(\frac{\tilde{\mathbf{u}} - \mathbf{u}^{(1.5)}}{\bar{\nu}} \right)^{1/2} \frac{(T - T_d)}{(1+\bar{\mathrm{B}}_\mathrm{T})^{0.7}} M^{(1.5)} \\ &\quad - 0.552 \cdot 6 \frac{\bar{\rho} \mathfrak{D} \, \mathrm{Sc}^{1/3}}{c_{\mathrm{P}l}} \left(\frac{\tilde{\mathbf{u}} - \mathbf{u}^{(1.5)}}{\bar{\nu}} \right)^{1/2} \frac{\Delta h_v(T_d) \tilde{\mathrm{B}}_\mathrm{M}}{(1+\tilde{\mathrm{B}}_\mathrm{M})^{0.7}} M^{(1.5)} . \end{aligned} \tag{4.60}$$

Combining both and using the abbreviation for the mass transfer rate density Γ, the final source term reads

$$= \quad -\left(\Gamma^{\mathrm{S}}_{M^{(3)}} + \Gamma^{\mathrm{nS}}_{M^{(3)}}\right) \frac{1}{c_{\mathrm{p}d}} \left(\Delta h_v(T_d) - c_{\mathrm{p}v} \frac{(T - T_d)}{\bar{\mathrm{B}}_{\mathrm{T}}}\right) \ . \tag{4.61}$$

Third Moment $M^{(3)}$ Conservation Equations

Gathering all terms together results in the macroscopic equations of the moment model, which read for the convection of $M^{(3)}$

$$\frac{\partial}{\partial t}(\rho_d M^{(3)}) + \nabla \cdot (\rho_d M^{(3)} \mathbf{u}^{(3)}) = -\Gamma_{M^{(3)}} \ , \tag{4.62}$$

the conservation of the third moment flux $M^{(3)}\mathbf{u}^{(3)}$ (which is the momentum equation of the dispersed phase)

$$\frac{\partial}{\partial t}(\rho_d M^{(3)} \mathbf{u}^{(3)}) + \nabla \cdot (\rho_d M^{(3)} (\mathbf{u}\mathbf{u})^{(3)}) = \mathbf{M}^{(3)} + \mathbf{g} M^{(3)} \rho_d - \Gamma_{M^{(3)}} \mathbf{u}^{(1)} \tag{4.63}$$

where it is assumed that $(\mathbf{u}\mathbf{u})^{(3)} \approx \mathbf{u}^{(3)}\mathbf{u}^{(3)}$ (Eqn. 4.21), and the transport equation for the dispersed phase temperature T_d

$$\frac{\partial}{\partial t}(\rho_d M^{(3)} T_d) + \nabla \cdot (\rho_d M^{(3)} T_d \mathbf{u}^{(3)}) = -\Gamma_{M^{(3)}} \left(T_d + \frac{\Delta h_v(T_d)}{c_{\mathrm{p}d}} - \frac{c_{\mathrm{p}v}}{c_{\mathrm{p}d}} \frac{(T - T_d)}{\bar{\mathrm{B}}_{\mathrm{T}}}\right) \ . \tag{4.64}$$

When the sensible enthalpy h_d is used instead of the temperature, one obtains by setting $h_d = c_{\mathrm{p}d} T_d$

$$\frac{\partial}{\partial t}(\rho_d M^{(3)} h_d) + \nabla \cdot (\rho_d M^{(3)} \mathbf{u}^{(3)} h_d) = -\Gamma_{M^{(3)}} \left(h_d + \Delta h_v(T_d) - c_{\mathrm{p}v} \frac{(T - T_d)}{\bar{\mathrm{B}}_{\mathrm{T}}}\right) \ . \tag{4.65}$$

Those set of equations can require a special solver due to its hyperbolic character, especially the momentum equation. This equation behaves similar to phenomena found in pressure-less gas dynamics, which would collapse to the Burger's equation without any source terms (no drag, etc.). Even in its presented form it can produce shock like gradients in the particle volume fraction, when not properly treated, which is not physical. However, in practical simulations, the strong coupling to the gas phase through drag impedes such structures and numerical dissipation contributes on its own. For further reading on this topic, see, e.g., LeVeque (2002) on hyperbolic problems and Bouchut (1994) or Bouchut et al. (2003) on pressure-less gas dynamics and its numerical treatment (Massot, 2007).

4.4.3 Equations for $M^{(2)}$, $M^{(2)}$ and $M^{(2)}$

If an infinite number of moments is known, the distribution is fully characterised. Obviously, it is not even feasible to solve a huge number of moment equations. Using quadrature based methods, presumed shape methods or the maximum entropy formalism, it is possible to reconstruct a distribution from only a few low order moments. In presumed shape methods usually two (Gauss, Rosin-Rammler, i.a.), three (Gamma, clipped Beta, i.a.) or four moments (e.g. Beta) are sufficient to fully reconstruct the distribution. In quadrature based methods, the number of transported moments (prognostic moments) depends on the desired accuracy of the reconstruction. In each case, additional moment transport equations to the third moment transport equation are needed. All moment transport equations are similar in structure, which makes a general derivation possible. Source terms can be expressed in a general manner as well, however we will restrict ourselves to the formulations for the moments $M^{(2)}$, $M^{(1)}$ and $M^{(0)}$, since no other prognostic moments are used throughout this work. To determine the moment transport velocities occurring in these equations, additional moment flux transport equations could be solved, which implies, however, a significant additional computational effort. Instead, as presented in Section 4.5.3 in more detail, a

relaxation time approach is used to determine the moment transport velocities $\mathbf{u}^{(2)}$, $\mathbf{u}^{(1)}$ and $\mathbf{u}^{(0)}$. Therefore only the moment transport equations will be derived in the following.

The derivation of the equations is similar to the one for the mass weighted equations. Hence, only the essential steps will be shown. The derivation for the time derivative and the convection term can be handled in a general manner using the moment order $k = 0, 1, 2, ...$, yielding for the

Time Derivative (Eqn. 3.70)

$$\iiint \frac{\partial f(\boldsymbol{\mathcal{I}})}{\partial t}\psi(\boldsymbol{\mathcal{I}})\rho_p D^k \,\mathrm{d}\boldsymbol{\mathcal{I}} = \frac{\partial}{\partial t}\iiint \psi(\boldsymbol{\mathcal{I}})\rho_p D^k f(\boldsymbol{\mathcal{I}}) \,\mathrm{d}\boldsymbol{\mathcal{I}}$$
$$\overset{\psi(\boldsymbol{\mathcal{I}})=1}{=} \frac{\partial}{\partial t}\iiint 1\rho_p D^k f(\boldsymbol{\mathcal{I}}) \,\mathrm{d}\boldsymbol{\mathcal{I}} = \frac{\partial}{\partial t}(\rho_d M^{(k)}) \tag{4.66}$$

and the

Convective Term (Eqn. 3.70)

$$\iiint \nabla\cdot(\mathbf{c}_p f(\boldsymbol{\mathcal{I}}))\psi(\boldsymbol{\mathcal{I}})\rho_p D^k \,\mathrm{d}\boldsymbol{\mathcal{I}} = \nabla\cdot\iiint \psi(\boldsymbol{\mathcal{I}})\mathbf{c}_p\rho_p D^k f(\boldsymbol{\mathcal{I}}) \,\mathrm{d}\boldsymbol{\mathcal{I}}$$
$$\overset{\psi(\boldsymbol{\mathcal{I}})=1}{=} \nabla\cdot\iiint 1\mathbf{c}_p\rho_p D^k f(\boldsymbol{\mathcal{I}}) \,\mathrm{d}\boldsymbol{\mathcal{I}} = \frac{\partial}{\partial t}(\rho_d M^{(k)}\mathbf{u}^{(k)}) \,. \tag{4.67}$$

Right Hand Side Source Terms (Eqn. 3.70)

Except the source term due to mass variation, which consequently affects surface or diameter variation of the particles as well, all other source terms becomes zero for any order of k as already shown in Eqn. 4.56 and Eqn. 4.40.

Since the mass transfer between phases affects the change of surface, diameter and droplet number density differently, the source terms must be

handled separately. First, for the second moment $M^{(2)}$ the term reads in general

$$
\begin{aligned}
&-\iiint \frac{\partial}{\partial D}\left(\langle\frac{dD^{(n)}}{dt}|\boldsymbol{\mathcal{I}}\rangle^{\mathcal{VF}} f(\boldsymbol{\mathcal{I}})\right)\psi(\boldsymbol{\mathcal{I}})\rho_p D^2\,\mathrm{d}\boldsymbol{\mathcal{I}}\\
&=\iiint \langle\frac{dD^{(n)}}{dt}|\boldsymbol{\mathcal{I}}\rangle^{\mathcal{VF}} f(\boldsymbol{\mathcal{I}})\rho_p\left(\psi(\boldsymbol{\mathcal{I}})\underbrace{\frac{\partial D^2}{\partial D}}_{2D}+D^2\frac{\partial\psi(\boldsymbol{\mathcal{I}})}{\partial D}\right)\mathrm{d}\boldsymbol{\mathcal{I}}\\
&=\iiint \langle\frac{dD^{(n)}}{dt}|\boldsymbol{\mathcal{I}}\rangle^{\mathcal{VF}} f(\boldsymbol{\mathcal{I}})\rho_p\left(\psi(\boldsymbol{\mathcal{I}})2D+D^2\frac{\partial\psi(\boldsymbol{\mathcal{I}})}{\partial D}\right)\mathrm{d}\boldsymbol{\mathcal{I}}\,. \qquad (4.68)
\end{aligned}
$$

For $\psi(\boldsymbol{\mathcal{I}}) = 1$ it follows for the low particle Reynolds number flow (Stokes flow, (S))

$$
\begin{aligned}
&\iiint \langle\frac{dD^{(n)}}{dt}|\boldsymbol{\mathcal{I}}\rangle^{\mathcal{VF}} f(\boldsymbol{\mathcal{I}})\rho_p\left(2D+D^2\underbrace{\frac{\partial 1}{\partial D}}_{=0}\right)\mathrm{d}\boldsymbol{\mathcal{I}}\\
&\overset{(A.32)}{=} -\iiint 4\frac{\bar{\rho}\mathfrak{D}}{\rho_p D}\ln(1+\tilde{\mathrm{B}}_{\mathrm{M}})f(\boldsymbol{\mathcal{I}})\rho_p 2D\,\mathrm{d}\boldsymbol{\mathcal{I}}\\
&= -\iiint 8\bar{\rho}\mathfrak{D}\ln(1+\tilde{\mathrm{B}}_{\mathrm{M}})f(\boldsymbol{\mathcal{I}})\,\mathrm{d}\boldsymbol{\mathcal{I}}\\
&= \underbrace{-8M^{(0)}\bar{\rho}\mathfrak{D}\ln(1+\tilde{\mathrm{B}}_{\mathrm{M}})}_{\equiv -\Gamma^{\mathrm{S}}_{M^{(2)}}} \qquad (4.69)
\end{aligned}
$$

and accordingly for higher Reynolds numbers (nS)

$$
\overset{(A.33)}{=} \underbrace{-0.552\cdot 4\bar{\rho}\mathfrak{D}\,\mathrm{Sc}^{1/3}\left(\frac{(\tilde{\mathbf{u}}-\mathbf{u}^{(0.5)})}{\bar{\nu}}\right)^{1/2}\frac{\tilde{\mathrm{B}}_{\mathrm{M}}}{(1+\tilde{\mathrm{B}}_{\mathrm{M}})^{0.7}}M^{(0.5)}}_{\equiv -\Gamma^{\mathrm{nS}}_{M^{(2)}}}\,. \qquad (4.70)
$$

Similarly, the general term develops for the transport equation of $M^{(1)}$ as

$$
\begin{aligned}
&- \iiint \frac{\partial}{\partial D} \left(\langle \frac{dD^{(n)}}{dt} | \boldsymbol{\mathcal{I}} \rangle^{\mathcal{VF}} f(\boldsymbol{\mathcal{I}}) \right) \psi(\boldsymbol{\mathcal{I}}) \rho_p D \, \mathrm{d}\boldsymbol{\mathcal{I}} \\
&= \iiint \langle \frac{dD^{(n)}}{dt} | \boldsymbol{\mathcal{I}} \rangle^{\mathcal{VF}} f(\boldsymbol{\mathcal{I}}) \rho_p \left(\psi(\boldsymbol{\mathcal{I}}) \underbrace{\frac{\partial D}{\partial D}}_{1} + D \frac{\partial \psi(\boldsymbol{\mathcal{I}})}{\partial D} \right) \mathrm{d}\boldsymbol{\mathcal{I}} \\
&= \iiint \langle \frac{dD^{(n)}}{dt} | \boldsymbol{\mathcal{I}} \rangle^{\mathcal{VF}} f(\boldsymbol{\mathcal{I}}) \rho_p \left(\psi(\boldsymbol{\mathcal{I}}) + D \frac{\partial \psi(\boldsymbol{\mathcal{I}})}{\partial D} \right) \mathrm{d}\boldsymbol{\mathcal{I}}
\end{aligned} \tag{4.71}
$$

and by setting $\psi(\boldsymbol{\mathcal{I}}) = 1$

$$
\begin{aligned}
&\iiint \langle \frac{dD^{(n)}}{dt} | \boldsymbol{\mathcal{I}} \rangle^{\mathcal{VF}} f(\boldsymbol{\mathcal{I}}) \rho_p \left(1 + D \underbrace{\frac{\partial 1}{\partial D}}_{=0} \right) \mathrm{d}\boldsymbol{\mathcal{I}} \\
&\overset{(A.32)}{=} - \iiint 4 \frac{\bar{\rho} \mathfrak{D}}{\rho_p D} \ln(1 + \tilde{\mathrm{B}}_{\mathrm{M}}) f(\boldsymbol{\mathcal{I}}) \rho_p \, \mathrm{d}\boldsymbol{\mathcal{I}} \\
&= - \iiint 4 \frac{\bar{\rho} \mathfrak{D}}{D} \ln(1 + \tilde{\mathrm{B}}_{\mathrm{M}}) f(\boldsymbol{\mathcal{I}}) \, \mathrm{d}\boldsymbol{\mathcal{I}} \\
&= \underbrace{-4 M^{(-1)} \bar{\rho} \mathfrak{D} \ln(1 + \tilde{\mathrm{B}}_{\mathrm{M}})}_{\equiv -\Gamma^{\mathrm{S}}_{M^{(1)}}} .
\end{aligned} \tag{4.72}
$$

and

$$
\overset{(A.33)}{=} \underbrace{-0.552 \cdot 2 \bar{\rho} \mathfrak{D} \, \mathrm{Sc}^{1/3} \left(\frac{(\tilde{\mathbf{u}} - \mathbf{u}^{(-1.5)})}{\bar{v}} \right)^{1/2} \frac{\tilde{\mathrm{B}}_{\mathrm{M}}}{(1 + \tilde{\mathrm{B}}_{\mathrm{M}})^{0.7}} M^{(-1.5)}}_{\equiv -\Gamma^{\mathrm{nS}}_{M^{(1)}}} . \tag{4.73}
$$

The derivation of a source term for $M^{(0)}$ is not a trivial task since the framework presented above simply yields $\Gamma_{M^{(0)}} = 0$. This is clearly non-physical, since vaporising droplets vanish at a certain point when becoming small enough. This problem occurs also for QbMMs, and is discussed

in detail by Fox et al. (2008). A solution to that problem is presented in Massot et al. (2010) and used later on in Kah et al. (2010, 2012). It is, however, not directly applicable in our framework. We avoid this problem by solving for the moments $M^{(1)}$ to $M^{(3)}$ only in vaporising flow simulations.

Transport Equations for $M^{(2)}$, $M^{(1)}$ and $M^{(0)}$

Bringing all the different terms together yields the moment transport equations including vaporisation for the moment order $k = 0 - 2$

$$\frac{\partial}{\partial t}(\rho_d M^{(2)}) + \nabla \cdot (\rho_d M^{(2)} \mathbf{u}^{(2)}) = -\Gamma^{\mathrm{S}}_{M^{(2)}} - \Gamma^{\mathrm{nS}}_{M^{(2)}} = -\Gamma_{M^{(2)}} \,, \tag{4.74}$$

$$\frac{\partial}{\partial t}(\rho_d M^{(1)}) + \nabla \cdot (\rho_d M^{(1)} \mathbf{u}^{(1)}) = -\Gamma^{\mathrm{S}}_{M^{(1)}} - \Gamma^{\mathrm{nS}}_{M^{(1)}} = -\Gamma_{M^{(1)}} \,, \tag{4.75}$$

$$\frac{\partial}{\partial t}(\rho_d M^{(0)}) + \nabla \cdot (\rho_d M^{(0)} \mathbf{u}^{(0)}) = 0 \,. \tag{4.76}$$

4.4.4 Connection to the Gas Phase

The gas phase interacts with the dispersed phase via the mass averaged equations for the moment of third order $M^{(3)}$. To use the source terms derived for the dispersed phase equations of $M^{(3)}$ in the corresponding gas phase equations, they have to be multiplied with the factor $\pi/6$ since the gas phase equations are expressed in terms of the volume fraction. Therefore, with $\alpha_c = (1 - \alpha_d)$ and $\alpha_d = \pi/6\, M^{(3)}$ we have

$$\Gamma = \Gamma^* = \frac{\pi}{6} \Gamma_{M^{(3)}} \,. \tag{4.77}$$

The same applies for the momentum and energy exchange rates. The total heat conducted from the gas phase to the droplet, q_{gl}, can be now specified as

$$q_{gl} = c_{\mathrm{P}v} \frac{(T - T_d)}{\bar{\mathrm{B}}_{\mathrm{T}}} \,. \tag{4.78}$$

4.5 Moment Model Closures

Similar to the single phase turbulence close problem, moment equations usually contain unknown correlations due to the particle velocity fluctuations. Additionally, however, moment equations can feature, besides the moments of higher order, also moments of lower, negative or non-integer valued order. The derivation of equations for the unknown moments to solve the problem is in neither case a final solution, since these equations usually imply unknown moments of even higher or different order. Actually, this problem reflects the fact, that a distribution is not fully characterised until an infinite number of moments is known. Hence, to solve the problem with only a few moments known, e.g. where equations are solved for (so-called *prognostic* moments), one assumes a functional form of the distribution. As result, with help of the prognostic moments, the distribution can be fully characterised and from that any associated moment (so-called *diagnostic* moments) can be calculated. A variety of methods are available to solve the moment problem with only a few prognostic moments, which are detailed next.

In contrast to Section 2.6.2, here the classical moment methods are discussed. The range of different types of moment methods is as wide as its multitude of applications. Most of these models can be categorised in a rather qualitative manner by classifying them via the type of the assumed shape for the NDF. The main mechanism in moment methods is the closure for terms, where moments of a certain order arise, which are not solved for via a transport equation. To solve this issue, some assumptions have to be made to calculate unknown moments from known (transported) moments. This can be accomplished by

- presuming a mathematical functional form for the distribution, i.e. a geometrical shape. Common functional shapes are, i.a., Gauss, log-Normal, Rosin Rammler, Gamma/Beta. This method is usually simply referred to as *Method of Moments* (MOM), sometimes as *Presumed Method of Moments* (PMOM). By assuming a functional form of the NDF, only a few moments must be known to be able to recon-

struct the NDF. If the NDF is determined from the set of known moments, any unknown moment can be calculated. Widely used in single phase, (reacting) flows with central moments (i.a. mean and variance), it has been extensively used in multiphase flows with closures of second order (Gauss, log-Normal, RR) and sometimes with higher order closure (Beck, 2000, Beck and Watkins, 2002, 2003, Carneiro et al., 2009, 2010).

- approximating the NDF as a sum of Dirac deltas. This category can be summarised under the term *Quadrature based Moment Methods* (QbMMs). Various variants extist, e.g. the two main methods the *Quadrature Method of Moments* (QMOM) (McGraw, 1997)) and the *Direct Quadrature Method of Moments* (DQMOM) (Marchisio and Fox, 2005) as well as sub-variants as *Sectional QMOM* (SQMOM) (Gumprich and Sadiki, 2012), *Extended QMOM* (EQMOM) (Yuan et al., 2012), *Method of Moments with Interpolative Closure* (MOMIC) (Frenklach and Harris, 1987, 1994, Frenklach, 2002) or hybrid methods combining for example DQMOM and MOMIC by Mueller et al. (2009).

- conducting the phase space integration only over very small intervals. Within each interval the variation of the NDF is small and moments of higher order than the mean can be neglected. The accuracy of this approximation obviously depends on the size of the intervals, i.e. the number of intervals used to approximate the NDF. This method is usually called *Multi-Fluid* method (MF) (Laurent and Massot, 2001), which is actually similar to DQMOM but with fixed classes. Care must be taken with the term "Multi-Fluid" since volume average based methods where the volume average is conditioned on the given phase space (classes), are often named equally. Both methods are obviously very similar, however, with subtle differences. Variations have been proposed, e.g. the *Parallel Parent and Daughter Classes Method* by Bove et al. (2005) and hybrid methods incorporating the QbMMs especially for multi-dimensional phase spaces, where the classical reconstruction methods are not devel-

oped for.

- making no assumption of the shape at all. A very promising method is the Maximum Entropy method based on the work of Shannon (1948), Jaynes (1957), Mead and Papanicolaou (1984) and recently applied, e.g., by Kah et al. (2010) or Gumprich and Sadiki (2012). Actually, in this method, no shape is presumed but other assumptions must be made concerning the characteristics of the NDF, here the property that the NDF is that with the maximum entropy for the given moments.

In this work, we use the first approach assuming a certain mathematical functional form of the NDF to overcome the closure problem. Since we consider the infinite Knudsen number regime only (collision between particles can be neglected), the presumed function method of moments is quite applicable in the sense of implementation and computational cost, because the numerical integration of the collision kernels does not apply. For finite Knudsen number regimes, QbMMs are much more applicable since the numerical integration reduces to a summation of only a few values. Also bi- or multi-modal distributions are unlikely to occur in the test cases considered in this work, for which presumed shape methods can be difficult to use due to the lack of appropriate shape functions.

4.5.1 Moment Closure: Presumed Distribution Function

Presuming a functional form of the distribution is very common in a wide range of applications. To match the requirements of the specific application, a multitude of distributions have been developed to capture the characteristics of the specific physical distribution present in the given flow configuration. In this work we restrict ourselves to the Gamma and Beta distribution. The Gamma distribution is usually appropriate to represent typical initial particle size spectra of polydispersed two-phase experiments with the advantage of requiring only three moments. The Beta distribution is more flexible, which is especially beneficial when particle

populations develop to shapes far from the Gamma distribution shape. Both distributions are based on the Gamma function, defined as

$$\Gamma(x) = \int_0^\infty t^{x-1} e^{-t} \mathrm{d}t \ . \tag{4.79}$$

The basics of the Gamma and the Beta distribution are given next.

Gamma Distribution

Gamma (and Beta) distribution function formulations exist in a variety of versions, either differing in the definition and arrangement of the parameters or their number. The latter depends on the assumptions made, e.g., about the support (compact, infinite, etc.). Furthermore, one must distinguish whether the specific distribution formulation refers to a number density function or a probability density function. Equivalent formulations for both distinguish themselves by the scaling parameter which the NDF implies, whereas the PDF does not. Throughout this work, distribution functions refer to number density functions, therefore the definition of $f^*(D)$ as Gamma distribution implies the scaling parameter C_0 as

$$f^*(D) = C_0 \frac{D^{q-1} e^{-\frac{D}{p}}}{p^q \Gamma(q)} \ . \tag{4.80}$$

The gamma distribution can be reconstructed from three prognostic, consecutive moments, e.g. $M^{(0)}$-$M^{(2)}$, by

$$p = \frac{M^{(0)} M^{(2)} - (M^{(1)})^2}{M^{(0)} M^{(1)}} \ , \tag{4.81}$$

$$q = \frac{(M^{(1)})^2}{M^{(0)} M^{(2)} - (M^{(1)})^2} \ , \tag{4.82}$$

$$C_0 = M^{(0)}. \tag{4.83}$$

where the scaling parameter is given directly as the total particle number density $M^{(0)}$. Using the set $M^{(1)}$-$M^{(3)}$, the formulations read

$$p = \frac{M^{(1)}M^{(3)} - (M^{(2)})^2}{M^{(1)}M^{(2)}}\,, \tag{4.84}$$

$$q = \frac{2(M^{(2)})^2 - M^{(1)}M^{(3)}}{M^{(1)}M^{(3)} - (M^{(2)})^2}\,, \tag{4.85}$$

$$C_0 = \frac{M^{(1)}}{pq}. \tag{4.86}$$

In general ($M^{(k)}$-$M^{(k+2)}$), the following formulas apply

$$p = \frac{M^{(k)}M^{(k+2)} - (M^{(k+1)})^2}{M^{(k)}M^{(k+1)}}\,, \tag{4.87}$$

$$q = \frac{(k+1)(M^{(k+1)})^2 - kM^{(k)}M^{(k+2)}}{M^{(k)}M^{(k+2)} - (M^{(k+1)})^2}\,, \tag{4.88}$$

$$C_0 = \frac{M^{(k)}}{p^k \Pi_{l=0}^{k-1}(q+l)} \quad \text{for } k > 0. \tag{4.89}$$

In turn, diagnostic moments can be calculated with help of the parameters p, q and C_0 by

$$M^{(k)} = C_0 \frac{\Gamma(q+k)p^k}{\Gamma(q)}\,. \tag{4.90}$$

Beta Distribution

The Beta distribution is based on the Gamma function as well, but allows more flexible shapes, e.g. both, positively and negatively skewed. The increased flexibility, however, requires in case of the NDF version at least four consecutive moments for its reconstruction including the constraints that the minimum value is set to zero and the maximum value is fixed (but not nessecarily unity). Two moment PDF versions, commonly known from, e.g., combustion modelling, additionally imply a maximum value of unity (applicable e.g. for the mixture fraction, which always lies

in the interval [0,1]) and the use as a probability density function, i.e. the scaling parameter drops. Additionally, in conjunction with the additional prognostic moment needed for the reconstruction compared to the Gamma distribution, the validity of the moment set might be more easily violated (see the next section for a discussion on that issue). Including $M^{(0)}$ to the prognostic set of moments in order to have four moments available is often preferred to the fourth moment. In case of mass exchange between phases, however, the transport equation for $M^{(0)}$ requires a corresponding source term. Especially in the case of considering vaporisation with help of the D^2-law, this source term is not trivial to derive, describe and to close. This issue is discussed in Section 4.4.3. Finally, the beta distribution reads (in the form we used in this work)

$$f^*(D) = \frac{C_0}{B(p,q)} \frac{D^{p-1}\left(D_{\max} - D\right)^{q-1}}{D_{\max}^{p+q-1}} , \tag{4.91}$$

where $B(p,q)$ is the Beta function and the parameters C_0, $D_{\max}$, p and q can be determined using the first four moments by

$$D_{\max} = \frac{\Delta_{1,1} M^{(1)} - \Delta_{0,1} M^{(3)}}{\Delta_{1,1} M^{(0)} - \Delta_{0,1} M^{(2)}} , \tag{4.92}$$

$$p = \frac{M^{(1)}\left(D_{\max} M^{(1)} - M^{(2)}\right)}{D_{\max} \Delta_{0,1}} , \tag{4.93}$$

$$q = \frac{\left(D_{\max} M^{(0)} - M^{(1)}\right)\left(D_{\max} M^{(1)} - M^{(2)}\right)}{D_{\max} \Delta_{0,1}} , \tag{4.94}$$

$$C_0 = M^{(0)} , \tag{4.95}$$

where the so-called *Hankel-Hadamard determinants* $\Delta_{0,1}$ and $\Delta_{1,1}$ are defined in the next section. Diagnostic moments of the Beta distribution can be calculated with help of

$$M^{(k)} = C_0 D_{\max}^k \frac{B(p+k,q)}{B(p,q)} . \tag{4.96}$$

4.5.2 Validity of Moment Sets

General Conditions

Independent of the specific choice of the moment closure, a set of moments must fulfil certain conditions to be *valid*. That means on the one hand, that only from a valid set of moments a realisable distribution can be reconstructed, and on the other hand, that moment sets calculated from a given distribution are always valid moment sets. These conditions qualifying a set of moments to be valid or not are given mathematically by the so-called *Hankel-Hadamard determinants* (see Shohat and Tamarkin, 1943). For each moment set, the corresponding determinants, given by the following condition, must be satisfied.

$$\Delta_{k,l} = \begin{vmatrix} M^{(k)} & M^{(k+1)} & \dots & M^{(k+l)} \\ M^{(k+1)} & M^{(k+2)} & \dots & M^{(k+l+1)} \\ \vdots & \vdots & \ddots & \vdots \\ M^{(k+l)} & M^{(k+l+1)} & \dots & M^{(k+2l)} \end{vmatrix} \geq 0 \,, \tag{4.97}$$

for all combinations of k, l with the constraints $l \geq 0$ and $k = 0, 1, 2, ..., k_{\max}$, with $k_{\max} = 2l$ for an even number of prognostic moments and $k_{\max} = 2l + 1$ for an odd number. In our case, where the moment sets $M^{(0)}$ to $M^{(2)}$ and $M^{(1)}$ to $M^{(3)}$ are used as prognostic moments, these conditions reduce for $k = 0, 1$ and $l = 1$ to the following two conditions:

$$\Delta_{0,1} = M^{(0)} M^{(2)} - (M^{(1)})^2 \geq 0 \,, \tag{4.98}$$

$$\Delta_{1,1} = M^{(1)} M^{(3)} - (M^{(2)})^2 \geq 0 \,, \tag{4.99}$$

which are the Hankel-Hadamard determinant $\Delta_{0,1}$ and $\Delta_{1,1}$, respectively. They constitute a necessary and sufficient condition that a distribution function exists for the given set of moments. In this case the given conditions (and, more generally, all 2x2 determinants) equal the corresponding *convexity conditions* (or Schwarz's Inequalities). This condition can be formulated also as non-negative curvature of $\ln M^{(k)}$ (Feller, 1971, Chapter 8, p.155). Note that the convexity conditions are a necessary but not sufficient condition for a valid set of moments, especially when it comes to

higher order moment sets, where the Hankel-Hadamard determinants present the more restrictive conditions (3x3 and higher determinants). Equations 4.98 and 4.99 can be rearranged and generalised to (general convexity condition):

$$... \geq \frac{M^{(k+1)}}{M^{(k)}} ... \geq \frac{M^{(3)}}{M^{(2)}} \geq \frac{M^{(2)}}{M^{(1)}} \geq \frac{M^{(1)}}{M^{(0)}} \tag{4.100}$$

They can be reformulated in terms of mean diameters as typically used in spray applications as

$$... \geq D_{32} \geq D_{21} \geq D_{10} \, . \tag{4.101}$$

Another general conclusion from the Hankel-Hadamard determinants is, that the moments have to be positive, which results from the Hankel-Hadamard determinants of order 1x1, i.e. $M^{(k)} \geq 0$, which is in line with their special physical meaning in the context of a particle size distribution function.

Worth to note here is that, as mentioned for example in Kah et al. (2010), so-called *canonical* moments (see e.g. Dette and Studden, 1997) are advantageous in handling validity issues since - due to their definition - each canonical moment of a valid moment set independently lies within the interval]0,1[and vice verca. Hence it can be easily checked whether a moment set is valid or not (see also Kah et al., 2012, p.398f). The applicability of canonical moments with the presumed shape moment method has not been tested within the scope of this work but can be considered as a task for future investigations.

Additional Constraints due to Specific Distributions

With a specific choice of the functional form of the distribution function, further conditions can arise due to the characteristics of the underlying mathematical function or the reconstruction algorithm. We restrict ourselves on the consideration of the Beta distribution, which has been in-

vestigated in this regard due to its implicit[6] use in the present simulations. When using the Beta distribution as given above, it is obvious that both shape parameters, p and q consist of only known conditions, i.e. the Hankel-Hadamard determinant $\Delta_{0,1}$ in the denominator and the convexity conditions in the numerator. Therefore, these shape parameters imply no additional restrictions. Considering, however, the formula for $D_{\max}$, two additional conditions can be derived, which might stricter than those given by the Hankel-Hadamard determinants.

It can be shown, that both, enumerator and denominator of the $D_{\max}$ term as formulated in Eqn. 4.92, have to be negative, which yields the following restrictions:

$$M^{(3)}\Delta_{0,1} \geq M^{(1)}\Delta_{1,1} \qquad \text{and} \qquad M^{(2)}\Delta_{0,1} \geq M^{(0)}\Delta_{1,1}\,. \tag{4.102}$$

Whether these conditions are more restrictive than the Hankel-Hadamard determinants will be shown next.

Moment Space Validity Maps

For practical purposes and in order to be able to create algorithms to handle non-valid moment sets, it is helpful to plot these conditions in moment space maps. First, one can determine whether a condition is automatically fulfilled by another condition and which are the most restrictive ones framing the space of valid moment sets. Since the moment space is multidimensional (the dimension of the moment space is obviously the number of moments considered), it is reasonable to plot the map for two moments only and keeping all other moments constant. With a specific moment correction algorithm in mind (as described in the next paragraph), we use $M^{(1)} - M^{(2)}$ plots for given $M^{(0)}$ and $M^{(3)}$. We made

[6] Actually, the Beta distribution was not used to determine diagnostic moments. In all cases presented, the Gamma distribution was reconstructed from the moments $M^{(1)}$ to $M^{(3)}$. However, in each case, an equation for $M^{(0)}$ was solved. As long as $M^{(0)}$ matched the other moments, i.e. built a valid set of four moments, it was used in subsequent terms when needed. If $M^{(0)}$ did not match, it was corrected according to the conditions due to the Beta distribution. This has no straightforward reasoning, but remained from accompanying simulations using the Beta distribution. Since the conditions due to the Beta distribution are slightly stricter than those of the Gamma distribution, it does not present a problem.

this specific choice due to the chosen bounding procedure, where $M^{(1)}$ and $M^{(2)}$ are modified - if necessary - and holding $M^{(0)}$ and $M^{(3)}$ constant since they represent total particle number and volume (mass) per unit volume. Both properties are conservative in non-vaporising sprays without coalescence and break-up. Therefore, the conditions 4.102 are recasted to have $M^{(2)}$ as a function of the other moments, yielding

$$M^{(2)} \geq -\frac{M^{(0)}M^{(3)}}{2M^{(1)}} + \sqrt{\frac{{M^{(0)}}^2{M^{(3)}}^2}{4{M^{(1)}}^2} + 2M^{(1)}M^{(3)}} \tag{4.103}$$

and

$$M^{(2)} \geq \frac{{M^{(1)}}^2}{4M^{(0)}} + \sqrt{\frac{{M^{(1)}}^4}{16{M^{(0)}}^2} + \frac{M^{(1)}M^{(3)}}{2}}\,, \tag{4.104}$$

respectively. To be able to determine the final range of valid $\left(M^{(1)}, M^{(2)}\right)$ combinations for given $M^{(0)}$ and $M^{(3)}$, all constraints are plotted in a $M^{(2)}$ over $M^{(1)}$ graph. The map shown in Fig. 4.1 is normalised with the coordinates of the critical point $\left(M^{(1)}_{\text{max}}, M^{(2)}_{\text{max}}\right)$. It marks the maximum valid values of $M^{(1)}$ and $M^{(2)}$ for given $M^{(0)}$ and $M^{(3)}$. It is characterised as the intersection of several conditions, from which it can be derived that

$$M^{(1)}_{\text{max}} = \sqrt[3]{{M^{(0)}}^2M^{(3)}} \quad \text{and} \quad M^{(2)}_{\text{max}} = \sqrt[3]{M^{(0)}{M^{(3)}}^2}\,. \tag{4.105}$$

Correction Schemes and Moment Space Preserving Transport Schemes

In practical simulations, it is extremely difficult to guarantee the validity of moment sets throughout the whole computational domain and time, even if the initial and boundary moment sets fulfil these conditions (see e.g. Watkins, 2005, Petitti et al., 2010). Valid moment sets for every cell at every time is a crucial requirement for a stable simulation. Invalid moment sets occurring during the simulation must be corrected to guarantee a realisable reconstruction of the distribution throughout the domain. This can be accomplished either using correction schemes of more

[8] Using canonical moments, these plots comprise the characteristic that these zones are rectangular (see e.g. Vié et al., 2013)

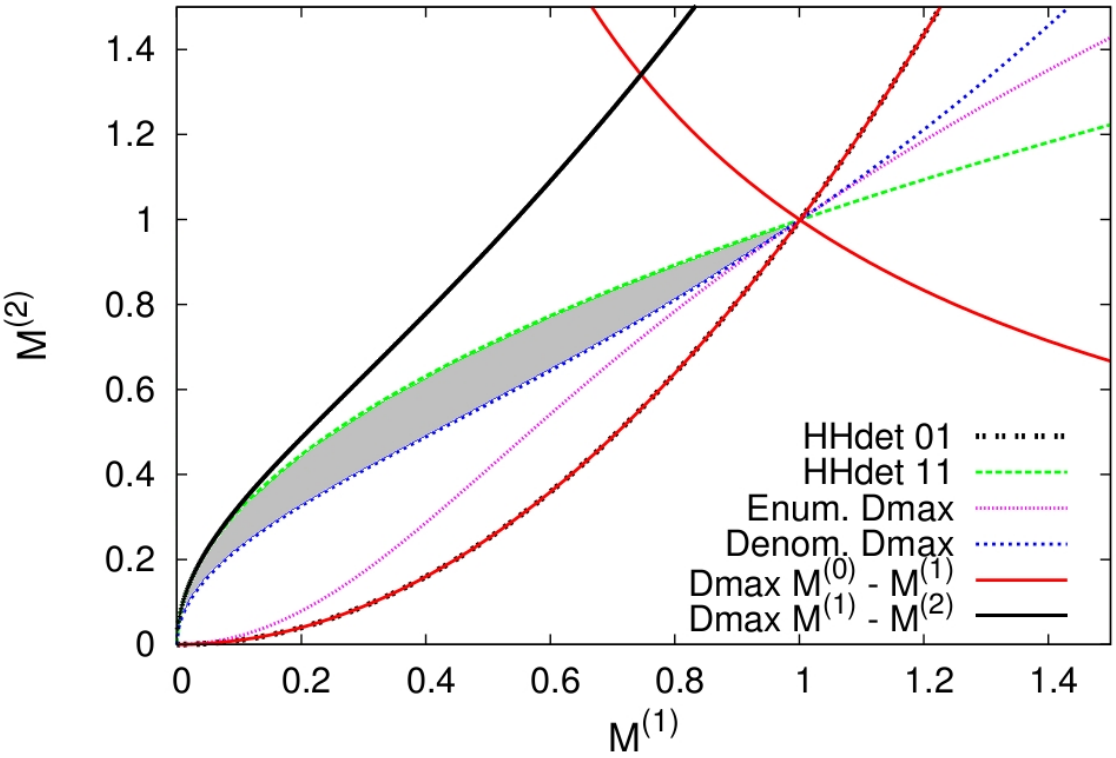

Figure 4.1: Resulting zone[8] for valid $M^{(1)}$-$M^{(2)}$ combinations (grey zone) for given $M^{(0)}$ and $M^{(3)}$. Each line represents the individual border between valid and invalid moment combination for a certain condition.

or less good quality (ranging from mathematically elegant to crude work around) or using moment space preserving discretisation schemes, where the latter is much preferable. First we will discuss the former solution, afterwards a few words on the latter one.

Beck (2000) reported problems with invalid moment sets using three prognostic moments. In this early work, this problem was bypassed by using a log-normal distribution instead of applying a correction algorithm or appropriate schemes. McGraw (2006) proposed an algorithm to detect and correct individual moments deviating from a valid sequence of moments. This algorithm is shown for the application on six transported moments, however, it cannot be applied to only four moments directly. Throughout this work we use a rather crude correction algo-

rithm based in the correction of $M^{(1)}$ and $M^{(2)}$, as already adumbrated in the paragraph before. For the practical implementation, conditions 4.103 and 4.104 were used to limit the moments in such a way that the conditions are surely fulfilled with a minimal change in the moment values. As resulting bounding algorithm the following procedure has been proven to be a practical solution (concerning code stability and unconditioned validity of moment sets). First $M^{(1)}$ is bounded due to the maximal valid value according to Eqn. 4.105 and afterwards $M^{(2)}$ due to either the condition for $D_{\max}$, i.e. Eqn. 4.104, or $\Delta_{1,1}$. However, the parameters p and q as well as $D_{\max}$ can still become very large, which results in abnormal distribution shapes. This can be avoided by keeping an appropriate distance to the invalid moment phase space limits or with additional constraints, which are demonstrated e.g. by Watkins (2005). Throughout the presented results[9], the former has been applied by forcing $0.01 \leq q \leq 20$ for iso-thermal and $1.01 \leq q \leq 20$ for non-isothermal flows, respectively. The parameter p needs no artificial limitation since it is covered by $\Delta_{1,1}$.

Very recently, an effort has been made to avoid such procedures by further developing and implementing moment advection schemes in practical simulations, which naturally preserve the valid moment space. Generally spoken, only first order schemes in space have this characteristic, but not necessarily in any case. Wright Jr. (2007) provides a good start to tackle this topic, with references therein pointing to related work with other background and first attempts to apply these schemes in CFD. Further discussion has been recently published by Desjardins et al. (2008), Vikas et al. (2010, 2011) and Kah et al. (2012).

4.5.3 Moment Transport Velocity Closure: Relaxation Time Approach

When using the full bi-variate size-velocity phase space for integration, one obtains combined size-velocity moments, which imply naturally a moment transport velocity. However, when reducing the bi-variate size-velocity phase space to a continuous size dependency and a size-

[9] For those, only the Gamma distribution has been used.

conditioned mean particle velocity $\mathbf{u}(D)$, the size dependent moments require to be transported with appropriate moment transport velocities, which were defined as (see Eqn. 4.29)

$$\mathbf{u}^{(k)} = \frac{1}{M^{(k)}} \int D^k \mathbf{u}(D) f^*(D) \, \mathrm{d}D \, . \tag{4.106}$$

In practice, this means that, e.g. the third moment $M^{(3)}$ has to be transported with a mass weighted particle velocity or the zeroth moment $M^{(0)}$ with an arithmetic mean of the size-conditioned particle velocity. To determine these moment transport velocities occurring in the moment transport equations 4.62 and 4.74 to 4.76, one could solve a moment flux transport equation for each order k of the prognostic moments (see e.g. Beck and Watkins, 2003). Solving for these additional transport equations can become costly even when considering only a few moments to be transported, e.g. three or four. This clearly reduces the benefits of using Eulerian moment methods in terms of computational time reduction (compared to e.g. Lagrangian methods). Only in two special cases, one can use only a single moment transport equation without significant loss of accuracy. First, when considering aerosol-like dispersed particle flows, where the particles behave like tracers (almost) perfectly following the gas phase, moments can be transported with the gas phase velocity. Second, when the particle size distribution tends to be rather monodisperse locally (but not necessarily temporally or globally), the moments can be convected with a common particle phase velocity. Polydispersed sprays usually do not behave as such, either. Another alternative is to model these transport velocities. We use a so-called *relaxation time approach* outlined in detail by Carneiro (2012), Carneiro et al. (2010). We restrict ourselves to a short summary of the main aspects.

The relaxation time approach is based on the idea of the "Equilibrium Eulerian Method" by Ferry and Balachandar (2001, 2002) where particle velocities are determined by a linear expansion around the continuous phase velocity in terms of the particle relaxation time. A similar expression can be found in Shih and Lumley (1986). Bollweg et al. (2007) extended this idea in terms of using a linear interpolation between the

continuous phase velocity and a reference particle velocity to determine intermediate particle velocities. Using the mass weighted particle velocity $\mathbf{u}^{(3)}$ as reference velocity, the intermediate moment transport velocities, i.e. velocities "between" the gas phase velocity and $\mathbf{u}^{(3)}$, are covered and can be determined using the integral version formulated by Carneiro et al. (2010) as

$$\mathbf{u}^{(k)} \approx \mathbf{u}_c + \frac{\tau^{(k)}}{\tau^{(3)}} \left(\mathbf{u}^{(3)} - \mathbf{u}_c \right) . \tag{4.107}$$

When considering Stokes flow only, the unknown integral relaxation time $\tau^{(k)}$ generally depends on a moment of the same order and one of two orders higher,

$$\tau^{(k)} \propto \frac{M^{(k+2)}}{M^{(k)}} , \tag{4.108}$$

which can be closed by the presumption of the functional form of the distribution as outlined above. Eqn. 4.107 implies a dependency of $\mathbf{u}(D)$ on D of $\mathbf{u}(D) \propto D^2$. For large particles this dependency becomes invalid. This issue has been discussed, e.g. in Carneiro (2012) and Mossa (2005). Another brief discussion can be found in Vié et al. (2013). For simplicity, we formally keep the assumption of Stokes particles for all simulations presented in this work, even when not being strictly valid.

5 Combustion Closure

In liquid fuelled combustion, the fuel is fed into the combustion device in liquid phase. Combustion, however, takes always place as a chemical reaction between gases (exceptions may exist, e.g., some solid-gas reaction, but these are not of interest here). Nevertheless, combustion of liquid fuels can be categorised into two main types, *homogeneous* and *heterogeneous* combustion. To distinguish between those types, the intensity of the interaction of the liquid fuel and the flame can be used as an adequate measure. Hence, in homogeneous combustion the liquid fuel is neither surrounded by the flame nor its vaporisation rate is determined by the flame (at the most by radiation or hot products through recirculation). In turn, if the liquid and flame dynamics directly rely on each other, or, in other words, if the flame is in the direct vicinity of the liquid, the combustion type is called heterogeneous. Actually most of the spray combustion applications belong to the latter, nevertheless most of the spray combustion models are based on the assumption of the former. This issue will be discussed in more detail in the corresponding sections.

Characteristics and modelling of both types are considered separately in Section 5.2 and Section 5.3, respectively. In practice, the clear classification of a given flame into one of the two types is sometimes not possible. In order to give an overview of academical investigations of spray flames as provided in the next Section 5.1, it is more appropriate to categorise the experimental work along different lines. Hence, it is sorted according to its specific type of configuration, i.e. counterflow spray flames, cone spray flames and spray jet flames. Additionally, only stationary flames are considered, instationary diesel injection like configurations (i.e. with relevant terms as *penetration depth*, *ignition delay*, etc.) are out of the scope and not of further interest here. References leading into that topic can be

found in the comprehensive review on spray flames given by Jenny et al. (2012).

5.1 Configurations and Experimental Investigations of Spray Flames

Investigations of liquid fuelled combustion range from fundamental experiments of single droplets, patterned and unstructured droplet arrangements and small and large droplet groups up to industrial scale fuel atomiser nozzles and combustion devices. Of our interest are configurations for which comprehensive data of the particle population are available, but which does not imply complicated geometries or the need for large mesh sizes, for example. Hence, this overview focuses on fundamental research experiments, which are appropriate to validate the solver, numerical schemes, reaction mechanisms, etc., either in a fundamental way and on more complex flow configurations. As an essential feature, a sufficiently detailed database for validation and accurate determination of the boundary conditions must be available in either case.

Besides arrangements of individual droplets, counterflow spray flames represent one of the basic configurations for model validation, i.e. the validation of vaporisation rates, combustion models, chemical mechanisms, etc. An overview of available experiments and simulations is given, e.g., in Greenberg and Sarig (1993, 1996) or Gutheil and Sirignano (1998). Often referenced counter flow flame databases have been published by Chen and Gomez (1992), Darabiha et al. (1992) and Gao et al. (1996). In principle similar to counterflow flames are stagnation point flames, investigated, e.g. , by Chen et al. (1988), Li (1997) and Lin and Lin (2005).

Of wide interest is the investigation of spray flames where the spray is generated by liquid atomisers. There exist a variety of techniques, which are not of specific interest here. A classification of these configurations can be undertaken into air-coflow assisted hollow cone spray flames as reported, e.g., in Chen and Gomez (1997), Friedman and Renksizbulut

(1999), Cabra et al. (2000), Marley et al. (2004a), Marley et al. (2004b) and Düwel et al. (2007), or similarly with a swirling coflow. The latter is often combined with an area expansion like geometry to achieve a recirculation zone in order to ensure continuous flame ignition, e.g. in lean flames, or aerodynamic flame stabilisation, e.g. in swirling flows. Some relevant experiments have been conducted in the groups of

- Presser et al. (1992, 1994), Widmann and Presser (2002), which features a simple geometry and provides comprehensive data on methanol spray combustion.
- Cai et al. (2005), Fu et al. (2005a), who investigated the Lean Direct Injection (LDI) combustion concept, and whose database is often used for validation, e.g., by Kirtaş et al. (2006), Patel and Menon (2008), Iannetti et al. (2008), Knudsen and Pitsch (2010), Dewanji et al. (2012) and is also used in this work, see Section 7.3.
- Allouis et al. (2008) applying Lean Premixed Prevaporised (LPP) combustion for gas turbine burners.
- or the MERCATO experiment (Lecourt et al., 2011), for gas turbine combustion as well, simulated, e.g., by Franzelli et al. (2013).

Spray jet flames are also often investigated, which usually feature homogeneously mixed droplet-air pipe flows injected into a quiescent environment or a slow coflow. Besides their industrial relevance, these configurations facilitate the measurement of particle population quantities more accurately than in the dense spray regions present at the exit of atomiser nozzles. This is of significant benefit for numerical simulations, for which accurate inlet conditions for the spray can be set based on the measured data. Due to the upstream mixing, however, the droplets usually underlie a certain degree of prevaporisation, which might be of advantage or not, depending of the aim of the investigation or application. If the spray is fully prevaporised, homogeneous combustion clearly occurs, e.g., as in Hwang et al. (2007), but most often, heterogeneous combustion modes develop depending on the degree of prevaporisation, the vaporisation

rate compared to the jet velocity, the particle loading, the size distribution, etc. Some relevant publications in this area are

- Karpetis and Gomez (1998, 1999), Mikami et al. (2005), where the different flame types are explained, e.g. triple flames.
- configurations of the University of Sydney (Chen et al., 2002, Stårner et al., 2005, Gounder et al., 2007, Masri and Gounder, 2010), which have been simulated, i.a. in Chrigui et al. (2013) and this work for validation of the polydisperse vaporisation modelling (see Section 7.2).
- several others, e.g., Pichard et al. (2002), Nomura et al. (2007), Baessler et al. (2007) with simulations reported in Chrigui et al. (2010a), or the experiments by Chrigui et al. (2009) and related simulations published in Chrigui et al. (2010b).
- An experimental confined jet configuration with separate fuel vapour assistance is reported in Richards et al. (1988).
- Specific discussion of the triple flame type is given in Muñiz and Mungal (1997), Marley et al. (2004a,b).

In the following two sections, both homogeneous and heterogeneous combustion are described separately in more detail, each with a discussion on modelling approaches and related numerical work. The combustion modelling developed and used in this work is described and the verification of its implementation is shown using simple 1D cases.

5.2 Homogeneous Combustion

To put it simply, homogeneous spray combustion is nothing but single phase combustion based on a fuel-oxidiser mixture determined by the vaporising spray. There does not take place any direct interaction between

the spray and the flame. That means that the flame dynamics does not depend on the vaporisation rate of the fuel droplets, but only on the same quantities as single phase combustion does, e.g., mixture characteristics, convective flow velocity vs. flame speed or chemical kinetics. However, these quantities are usually influenced and modified significantly by the spray, depending on the residence time and characteristics of the flow between the vaporised spray and the flame. Especially the degree of mixing of fuel vapour and air is initially rather low within the spray due to the large pointwise supply of pure fuel vapour, but improves downstream, depending on the time before reaching the flame front. This means that the mixture fraction PDF initially features a large variance, which becomes smaller with an increasing residence time of a given fluid volume between the vaporisation of the droplets and the flame front. Hence, homogeneous combustion, i.e. prevaporised from the point of view of the flame, ranges from premixed to nearly unmixed.

In consequence, practical application and experimental investigation possess a large number of different flame types, configurations and phenomena. In the following, some relevant experiments are listed, which have been used to validate theoretical models and numerical simulation results. The listing is far from complete, but primarily provides some practical configurations which act as specific examples to demonstrate the different approaches in modelling and simulation.

5.2.1 Models for Spray Combustion and Applications in Literature

In most numerical simulations, spray combustion is treated as homogeneous combustion. However, especially the spray flamelet models are often applied to configurations where an envelope flame burns around the entire spray. In this case, it can be difficult to distinguish clearly between heterogeneous combustion, i.e. external sheath/group combustion already applies (case I in Fig. 5.1, see also Section 5.3), and homogeneous combustion, i.e. the flame does not directly interact with the outer droplets of the spray (case II and III in Fig. 5.1). The spray combustion

models can be basically classified into those which consider the specific characteristics of the high variance of the mixture fraction field due to the pointwise vaporisation of the fuel (case II) and those which directly incorporate the droplets in the vicinity of the flame (spray flamelets, case I). The latter should rather be classified as heterogeneous combustion models, but to retain the discussion of the spray combustion models compact, even those are discussed here. In the section about heterogeneous combustion (Section 5.3), only models for single droplet combustion and those explicitly modelling group combustion are discussed. General overviews can be found in Faeth (1996), Gutheil (2011) and Jenny et al. (2012). In the following, some of the available models are discussed.

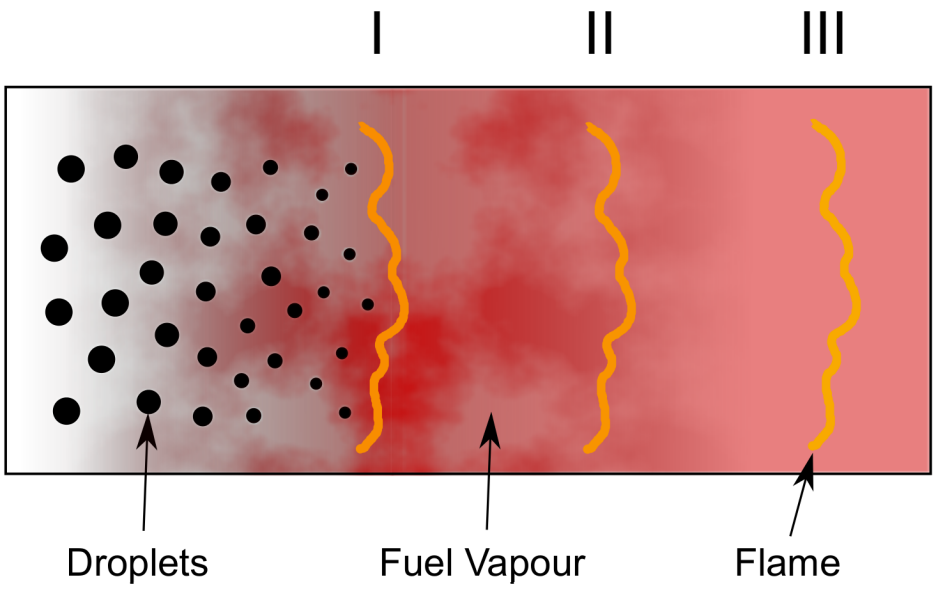

Figure 5.1: (Indefinite) Transition between heterogeneous (I) and homogeneous (III) spray combustion.

Almost all spray combustion models refer to partially or non-premixed combustion. This is consistent, when ignoring those special cases, where a perfectly premixed mixture of fuel-vapour/air is burnt, but which still carries droplets, which interact with the resulting premixed flame. In any other "premixed spray combustion" case, the spray must be clearly separated from the flame zone to ensure a residence time between spray and

flame long enough to allow perfect mixing of fuel vapour and oxidiser. In this case, standard single phase models can be simply applied.

Spray combustion methods and models are sorted considering the averaging method used for the equation system. Hence, the models are categorised into laminar flows (no averaging needed), RANS simulations, filtered equations (LES) and DNS, the latter including those conducted to develop sub-grid scale submodels for LES. The work of specific research groups is summarised and if applicable, the publications of experimental data are referenced which have been used for validation.

Laminar

Most laminar cases are concerned with the investigation of spray counterflow diffusion flames, with spray and carrier gas from one side and the oxidiser (mixture) from the other side. Dependent on the vaporisation rate, droplets are either vaporised before reaching the flame front (Fig. 5.2) or pass the flame front, eventually with a subsequent reversal of the flow direction within the opposite stream (Fig. 5.3). In the former, no direct droplet-flame interaction occurs, only the grade of mixing with the inert carrier gas impacts the flame dynamics, whereas in the latter case, heterogeneous combustion plays a role, depending on the remaining liquid fuel mass. With these counterflow configurations, a whole set of different states can be precalculated, tabulated and used for the simulation. This is done either to reduce the cost or to increase the accuracy (by using a sophisticated external chemistry solver) in laminar cases, or to incorporate the sub-grid PDF of the mixture and droplet quantities to account for the non-resolved scales in turbulent flows.

Fundamental analytical work forms the basis of spray counterflow flames, which imply usually reduced physics. Equation systems including more comprehensive physics, are typically solved numerically, where related work can be found for a 1-dimensional description, e.g., in Seshadri et al. (1989), Continillo and Sirignano (1990), Chen et al. (1992), Darabiha et al. (1992), Gao et al. (1996), Massot et al. (1998). In Gutheil and

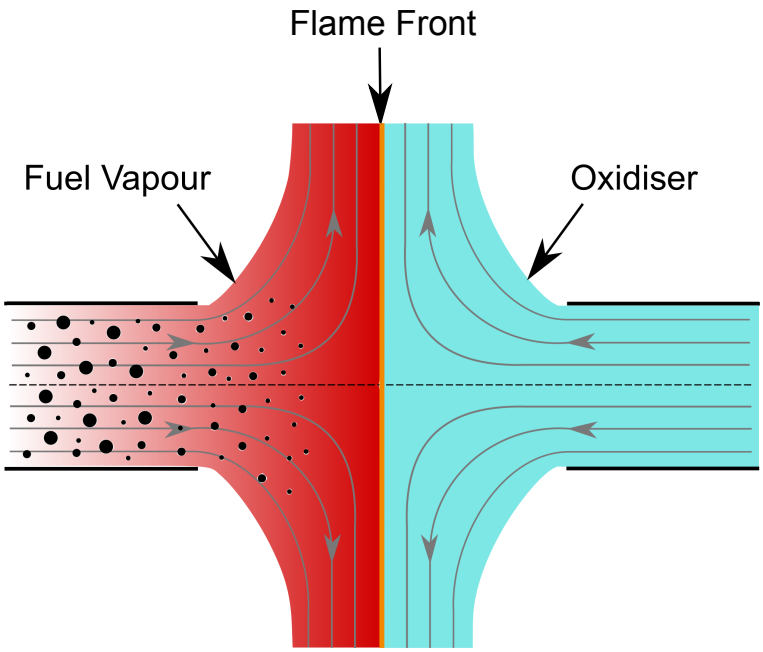

Figure 5.2: Laminar, prevaporised, homogeneous spray counter flow flame.

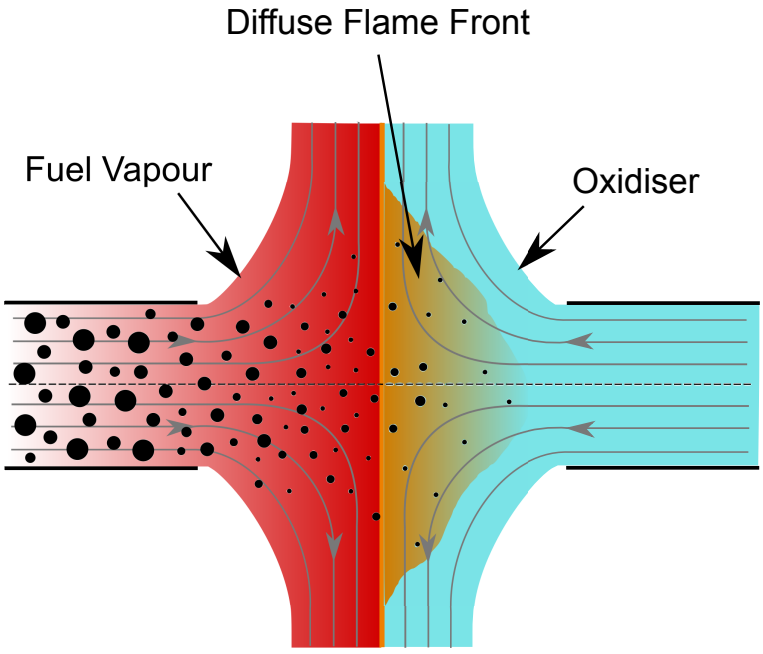

Figure 5.3: Laminar, partially prevaporised, heterogeneous spray counter flow flame.

Sirignano (1998), a comprehensive overview and comparison with spray counterflow experiments is given. Recent work considers two dimensions, e.g., Schlotz and Gutheil (2000), Watanabe et al. (2007), Franzelli et al. (2012).

RANS

Along with the popular and often applied RANS simulation for industrial scale applications, numerous attempts have been made to modify single phase combustion models or to develop specific two-phase models for the use in two-phase combustion. A choice is listed in Tab. 5.1. Those

Table 5.1: Spray combustion models used in RANS

Model name	References
Gas flamelet (accounting for point-wise fuel sources due to vaporisation)	Chang et al. (1996), Hollmann and Gutheil (1996)
Spray flamelet (counterflow spray flames)	Hollmann and Gutheil (1998), Gutheil and Sirignano (1998), Demoulin and Borghi (2000), Gutheil (2001)
Eddy Breakup model (EBU)	Guo et al. (2002), Dhuchakallaya and Watkins (2010), Wang et al. (2011)
Conditional Moment Closure (CMC)	Wright et al. (2005)
Modified Bray-Moss-Libby (BML)	Chrigui et al. (2010a,b)
Flamelet Generated Manifolds (FGM)	Bekdemir et al. (2009, 2010, 2011), Egüz et al. (2012, 2013)
Partially Stirred Reactor (PaSR) (with PDF transport of species and IEM mixing)	Sabel'nikov et al. (2006)

examples are only a few among many others. Hence, a clear trend of how to model heterogeneous combustion in spray applications cannot be figured out. More or less, these methods give adequate agreement with the experimental results, but still lack on a conclusive approach of considering spray combustion modes as discussed in Section 5.3. Although these

refer to heterogeneous combustion modes whereas the given examples have been listed under the key word homogeneous combustion, it is actually the fact, that many of these examples feature at least one of the heterogeneous modes. As discussed before, clear homogeneous combustion in two-phase flames is actually a very specific case, which does not often occur and does not have much in common with spray combustion. However, in most of the numerical simulations this assumption is used.

LES

The same is valid for LES simulations of two-phase flames. Here, single phase combustion models are usually used unaltered or adapted, e.g., a single phase flamelet model in Moriai et al. (2013) and Franzelli et al. (2013), FGM in Chrigui et al. (2012, 2013) and direct tabulated chemistry in Tillou et al. (2014). A two-phase Thickened Flame model has been proposed by Kaufmann (2004), which is strictly valid only for laminar or DNS flows. For its use in RANS and LES, sub-grid scale models must be incorporated as done for the single phase counterpart.

DNS and DNS for Developing SGS-Models

To investigate and to develop sophisticated two-phase combustion models for the different combustion modes, DNS can be a very helpful tool, escpecially used with the Lagrangian description of the particles (Direct Simulation Monte Carlo, DSMC). So far, these attempts have been restricted to the droplet and vapour dynamics, e.g., the droplet sub-grid scale model for mixture fraction and variance by Réveillon and Vervisch (1998). Other DNS simulations focused on the applicability and phenomenological investigation of a given problem. Examples are: Neophytou and Mastorakos (2009) and Neophytou et al. (2011), which used detailed chemistry for droplet mists and droplet clusters; laminar and weakly turbulent spray jet flames in Réveillon and Vervisch (2005); a 2D flamelet/progress variable approach in Baba and Kurose (2008), Fujita

et al. (2013) and Kitano et al. (2013); or Smith et al. (2000) using a two-phase CMC approach developed in Mortensen and Bilger (2009).

A brief conclusion can be made as follows. For homogeneous combustion, single phase models may be used, which are modified to account for the altered fuel vapour field due to the heterogeneous, pointwise vaporisation of the dispersed droplets. Considering that, especially for flamelet models, this fact proves as a challenge, because the fuel vapour source does not represent a simple change in mixture fraction (because only the fuel species increases!), but represents a continuous change in the boundary conditions, which should be accounted for as an additional dimension of the flamelet tabulation. The proposed two-phase flame models as referred to before, does not account for that issue (to the author's understanding). Dealing with that issue is the main problem for most of the approaches, where a detailed and direct (tabulated) chemistry PDF approach seems to be not only the best approach (which is trivial) but rather the only appropriate one, especially if the droplets interact directly with the flame or the combustion products.

In this work, we make use of direct Arrhenius chemistry using the single phase, standard PaSR and an adapted Thickened Flame Model (TFM). This model, however, does not account for two-phase combustion modes, but properly treats the interaction of the droplet dynamics with the thickened gas phase zone, i.e. reduced vaporisation rates, drag coefficients, residence times, etc. Both approaches are not sophisticated, but act as a first step for developing and implementing a spray combustion CFD solver. As mentioned before, the PaSR is used in its standard, single phase version as implemented in OpenFOAM. Its formulation can be found in the literature (Vulis, 1961, Nordin, 2001). Here we only present the adapted Thickened Flame Model for dispersed flows, which is done in the next section.

5.2.2 A Two-Phase Thickened Flame Model (TFM)

In premixed combustion, the flame thickness δ_l^0 is about 0.1 to 1 mm. With the resolution of a typical LES mesh for industrial scale and most academical applications, the flame front cannot be resolved. Hence, the intermediate species concentrations cannot be resolved and the accurate description of the physics within the flame is not possible. To overcome this issue, a method has been developed which artificially thickens the flame. This happens in a way that the flame is thickened by a factor **F** but keeping the laminar flame speed s_l^0 unchanged. Considering that s_l^0 is a function of the molecular diffusion coefficient $\mathfrak{D}$ and the reaction rate $\dot{\omega}$ and that the flame thickness δ_l^0 is proportional to the ratio of $\mathfrak{D}$ and s_l^0 according to

$$s_l^0 \propto \sqrt{\mathfrak{D}\dot{\omega}} \qquad \delta_l^0 \propto \frac{\mathfrak{D}}{s_l^0}\,, \tag{5.1}$$

multiplying $\mathfrak{D}$ with the thickening factor **F** and dividing $\dot{\omega}$ by **F** does not alter the flame speed but enlarges the flame thickness by the factor **F**. As long as the smallest turbulent scales and the smallest wrinkling structures are resolved by the mesh (laminar flows, DNS), this constitutes an accurate method to simulate the full flame physics on a mesh which is not able to resolve the flame front. However, such a combination of mesh and flow scales is almost never the case. Therefore, as soon as some structures of the flame wrinkling are lost due to the thickening, or when the smallest turbulent eddies of the flow, which alter the flame front, cannot be resolved by the mesh anymore (LES, RANS), the non-resolved effects must be modelled.

Meneveau and Poinsot (1991) introduced an efficiency factor **E**, which has been adapted to the Thickened Flame model by Angelberger et al. (1998), Colin et al. (2000). The efficiency factor gives the ratio of the wrinkling of the physical flame and that of the thickened flame. The wrinkling factor itself is the ratio between the sub-grid scale turbulent flame speed and the laminar flame speed. With that the following transformations

have to be conducted

$$\mathfrak{D} \rightarrow \mathbf{EF}\mathfrak{D} \ , \ \dot{\omega} \rightarrow \frac{\mathbf{E}\dot{\omega}}{\mathbf{F}} \ , \ s_l^0 \rightarrow \mathbf{E}s_l^0 \ , \ \delta_l^0 \rightarrow \mathbf{F}\delta_l^0 \ . \tag{5.2}$$

Additionally, the turbulence-flame interaction is altered in another way, which can be expressed in terms of the Damköhler number Da, which becomes $\mathrm{Da} \rightarrow \mathrm{Da}/\mathbf{F}$ (see Colin et al., 2000). That means that the thickened flame becomes less sensitive to turbulence, but more sensitive to strain (Poinsot et al., 1991).

In order to use the Thickened Flame model towards partially and non-premixed combustion as well, Legier et al. (2000) introduced a local thickening algorithm, which modifies only the flame and its vicinity, but preserves mixing and diffusion dynamics everywhere else. Furthermore, in LES of partially and non-premixed combustion, where the sub-grid scale turbulence is not resolved, a sub-grid PDF of the mixture fraction must be considered to correctly describe turbulence-chemistry interaction. The influence of considering the PDF on the results depends on the configuration and the grade of unmixedness. This issue relaxes for the temporal variation of the sub-grid scales, since the flame is thickened, hence the small temporal variations are slowed down to a time scale which is resolved.

Legier et al. (2000) stated, that the TFM is appropriate for cases where premixed and non-premixed flames coexist, since it does not presume a flame structure. In partially prevaporised spray flames as we will investigate later on, the flame structure varies between those extremes, therefore the TFM qualifies as a reasonable choice. In a first step, the sub-grid PDF has not been incorporated.

So far, the description of the TFM has been concerned about single phase flows only. In homogeneously combusting two-phase flows, the combustion is not altered compared to single phase combustion, but the interaction of the thickened flame with the droplets must be considered properly. Thickening the flame results in an enlarged hot zone the droplets must travel through. Consequently, to preserve the amount of liquid, which is vaporised during the time the droplet needs to pass the thick-

ened flame, the vaporisation rate must be reduced by the factor $\mathbf{F}$ to ensure slower vaporisation, i.e. $\Gamma \rightarrow \frac{1}{\mathbf{F}}\Gamma$.

With that, the gas phase and dispersed phase equations can be finally given.

Gas Phase

The gas phase mass continuity reads

$$\frac{\partial}{\partial t}(\theta\bar{\rho}) + \nabla \cdot (\theta\bar{\rho}\tilde{\mathbf{u}}) = \frac{1}{\mathbf{F}}\Gamma \tag{5.3}$$

and the species transport

$$\begin{aligned}\frac{\partial}{\partial t}(\theta\bar{\rho}\tilde{Y}_m) + \nabla \cdot (\theta\bar{\rho}\tilde{Y}_m\tilde{\mathbf{u}}) - \nabla \cdot (\theta\bar{\rho}(\mathfrak{D} + \frac{\nu_t}{\mathrm{Sc}_t})\mathbf{E}\,\mathbf{F}\nabla\tilde{Y}_m) \\ = \frac{\mathbf{E}}{\mathbf{F}}\langle\rho\dot{\omega}_m\rangle^{\mathcal{VF}} + \frac{1}{\mathbf{F}}\Gamma^*\epsilon_m\,.\end{aligned} \tag{5.4}$$

The gas phase momentum conservation becomes

$$\begin{aligned}\frac{\partial}{\partial t}(\theta\bar{\rho}\tilde{\mathbf{u}}) + \nabla \cdot (\theta\bar{\rho}\tilde{\mathbf{u}}\tilde{\mathbf{u}}) = &- \theta\nabla\bar{p} + \theta\nabla\cdot\bar{\boldsymbol{\tau}} + \nabla\cdot(\theta\boldsymbol{\tau}^t) \\ &- \mathbf{M} + \frac{1}{\mathbf{F}}\Gamma\bar{\mathbf{u}}_d \\ &+ \theta\bar{\rho}\mathbf{g}\end{aligned} \tag{5.5}$$

and the sensible enthalpy equation

$$\begin{aligned}\frac{\partial}{\partial t}(\theta\bar{\rho}\tilde{h}) + \nabla \cdot (\theta\bar{\rho}\tilde{h}\tilde{\mathbf{u}}) + \nabla \cdot \left(\frac{\bar{\rho}\nu_{\mathrm{eff}}}{\mathrm{Pr}_{\mathrm{eff}}}\mathbf{E}\mathbf{F}\nabla(\theta\bar{h})\right) \\ = \theta\left(\frac{\partial\bar{p}}{\partial t} + \tilde{\mathbf{u}}\nabla\bar{p}\right) + \frac{1}{\mathbf{F}}\Gamma(\bar{h}_s - q_{gl}) + \frac{\mathbf{E}}{\mathbf{F}}\sum_m\langle\rho\dot{\omega}_m\rangle^{\mathcal{VF}}Q_m\,.\end{aligned} \tag{5.6}$$

Particle Phase

As discussed before, the droplet phase equations must be modified accordingly. For the $M^{(k)}$ transport equation, the modified vaporisation rate

yields

$$\frac{\partial}{\partial t}(\rho_d M^{(k)}) + \nabla \cdot (\rho_d M^{(k)} \mathbf{u}^{(k)}) = -\frac{1}{\mathbf{F}} \Gamma_{M^{(k)}} \tag{5.7}$$

and for the dispersed phase momentum or $\mathbf{u}^{(3)}$ transport equation

$$\frac{\partial}{\partial t}(\rho_d M^{(3)} \mathbf{u}^{(3)}) + \nabla \cdot (\rho_d M^{(3)} (\mathbf{u}\mathbf{u})^{(3)}) = \mathbf{M}^{(3)} + \mathbf{g} M^{(3)} \rho_d - \frac{1}{\mathbf{F}} \Gamma_{M^{(3)}} \mathbf{u}^{(1)} \,. \tag{5.8}$$

The droplet sensible enthalpy equation $h_d = c_{\mathrm{P}d} T_d$ is given by

$$\frac{\partial}{\partial t}(\rho_d M^{(3)} h_d) + \nabla \cdot (\rho_d M^{(3)} \mathbf{u}^{(3)} h_d) = -\frac{1}{\mathbf{F}} \Gamma_{M^{(3)}} \left(h_d + \Delta h_v(T_d) - c_{\mathrm{P}v} \frac{(T - T_d)}{\bar{\mathrm{B}}_{\mathrm{T}}} \right) \,. \tag{5.9}$$

Verification

The implementation of the dynamic thickening into OpenFOAM has been verified using a simple 1D non-prevaporised methanol flame in a homogeneous droplet-air flow, with initially equal velocities of 0.4 m/s for both phases and temperatures for gas and droplets of 393 K and 273 K, respectively. The values of the droplet population are arbitrarily chosen, with the droplet volume fraction being $\alpha_d = 0.0023$ and an initial mean diameter $D_{10} = 1.977\,23 \times 10^{-5}$ m. The boiling temperature of methanol is set to 337.75 K. The domain length of 0.02 m is discretised into 300 points, i.e. each cell size is about $\Delta x = 66.67\,\mu$m, which is fine enough to resolve the unthickened flame properly. The 3-step methanol mechanism of Westbrook and Dryer (1981) has been used. Fig. 5.4 shows the dynamic thickening factor over the domain length. Its maximum value has been set to 8.

The graphs in Fig. 5.5 show several quantities of the gas and dispersed phase plotted over the domain length as indicated in Fig. 5.4. Each plot

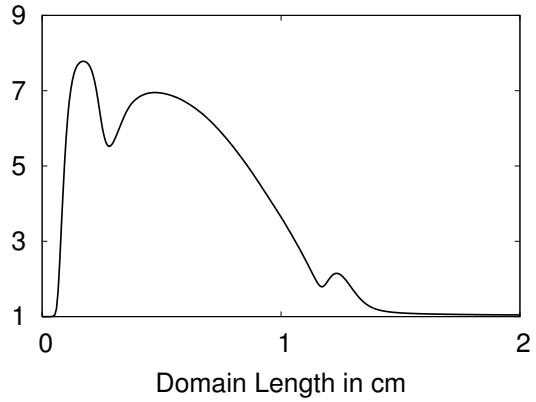

Figure 5.4: Profile of the dynamic thickening factor.

shows the results of the original, unchanged flame, the result of the thickened flame calculation and its rescaled values accordingly to the local thickening value. For this study, the absolute values are not of specific interest. Hence, the values are normalised with the maximum value. In general, the shape and slope of the original and rescaled flame front agree very well for most of the variables. Considerable deviations can be observed for the heat transfer rate between gas and droplets and the methanol vapour mass fraction[1]. The latter might results from the fact that the gas phase velocity is slightly lower in the thickened case at the positions more downstream, which accordingly absorbs more vapour per volume and time interval. The mechanism which is responsible for the higher heat transfer rate from the air to the droplets is not clear.

[1]To be clear, both quantities are shown in their full strength for the thickened case, but are reduced by the thickening factor accordingly when acting as source terms in the corresponding equations. Otherwise the overall balances would obviously not be fulfilled.

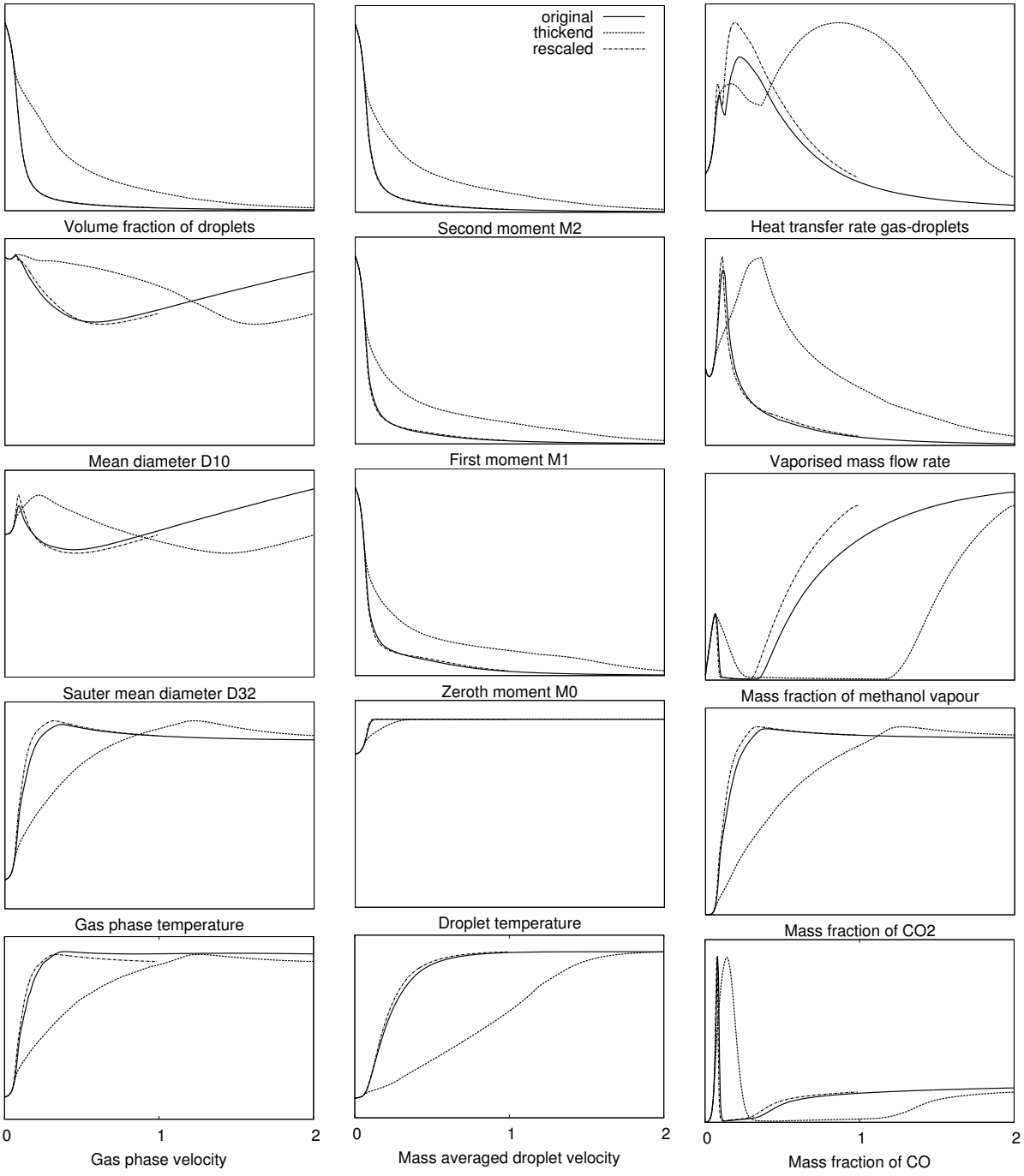

Figure 5.5: Original, thickened and rescaled flame simulation results.

5.3 Heterogeneous Combustion

The general term *heterogeneous combustion* stands for all types of flames in multiphase combustion, which directly interact or depend on the dynamics of the fuel[2] droplets. That means, that the reaction occurs in the immediate vicinity of the vaporising droplets and depends strongly on the vaporisation rate, the mass diffusion velocity of fuel vapour to the flame and the droplet Reynolds and Peclet number, which determine the shape and position of the flame relative to the droplet(s). Chiu and Liu (1977) and Chiu et al. (1996) investigated the different types of heterogeneous combustion and observed the following four modes. Each mode is exemplified using a spray jet flame configuration consisting of an air jet laden with fuel droplets.

- *Single droplet combustion* (SDC) is a mode, where an individual flame establishes at each droplet. Fig. 5.6 shows a very dilute fuel spray dispersed in an oxidising gas jet. Due to the partial prevaporisation, a premixed flame establishes first. The droplets ignite when crossing this flame and burn individually downstream.

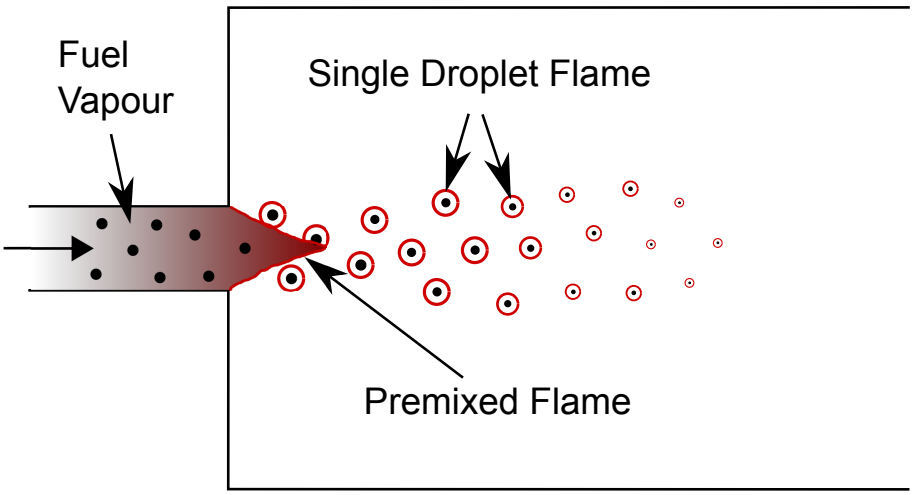

Figure 5.6: Example for Single Droplet Combustion.

[2] In specific cases, the particles or droplets may provide the oxidiser, but we do not consider this case in the further description.

- *Internal group combustion* describes a combustion mode where a single flame surrounds a small cluster of droplets, which feed this flame with fuel vapour and the outer droplets (or the droplets inbetween the clusters) are burning in single droplet combustion mode.

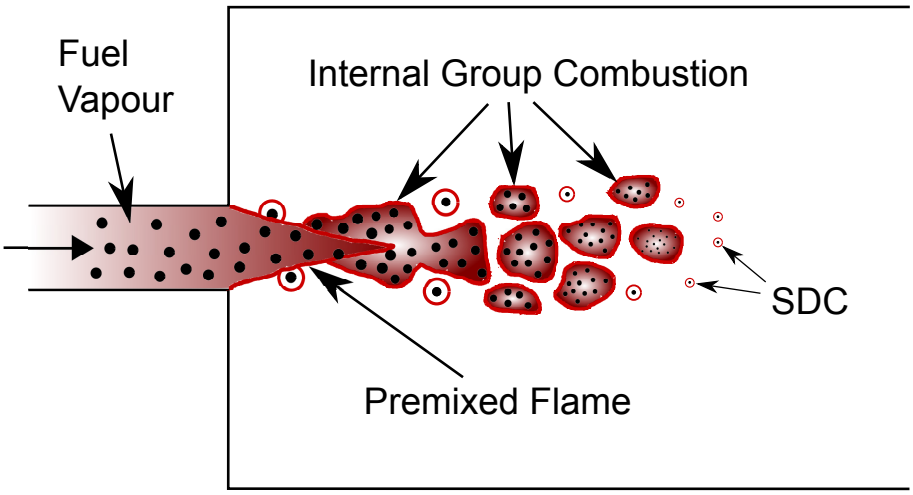

Figure 5.7: Example for Internal Group Combustion.

- In the *external group combustion* mode, the flame surrounds the entire group of droplets, i.e. the large structures of the spray. All droplets are vaporising and contributing fuel vapour to the reaction.

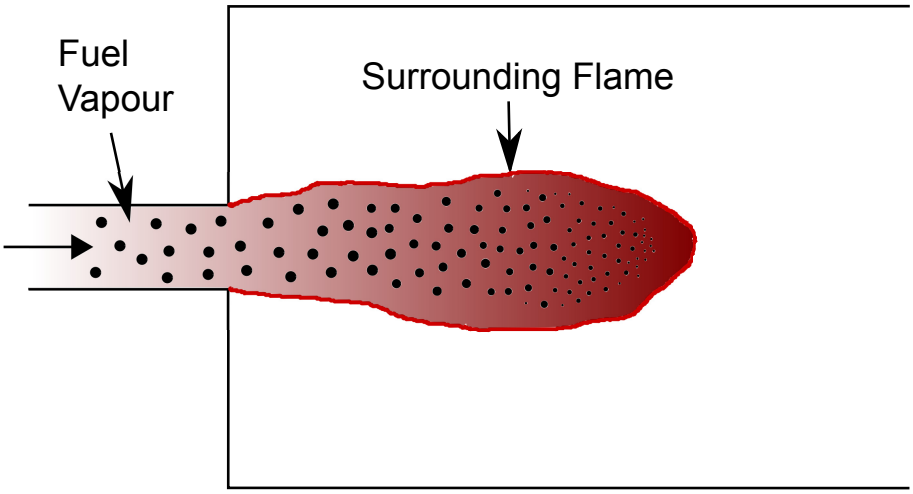

Figure 5.8: Example for External Group Combustion.

- *External sheath combustion* is a special case of the external group combustion mode, which implies the same structure and arrangement of the droplets and the flame but contains a core region, where the droplets are surrounded by cold gas, which suppresses vaporisation of the droplets. Only the droplets closer to the flame are vaporising and feeding the flame.

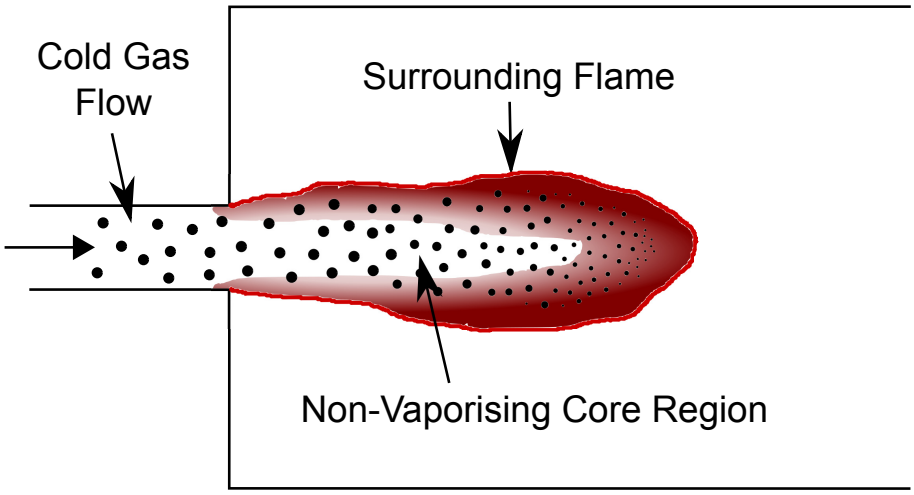

Figure 5.9: Example for External Sheath Combustion.

The occurrence of those modes depend on the droplet number density, droplet group size, droplet diameter, fuel volatility and the ambient conditions. All these effects have been observed experimentally, although a clear separation is sometimes difficult. Attempts to establish regime maps and discussions on them have been given by Chiu and Liu (1977), Chiu et al. (1996), Chigier (1983), Kuo (1986), Borghi (1995), Réveillon and Vervisch (2005), Urzay (2011) and Kuo and Acharya (2012). A listing of further relevant experimental work is not given here but can be found, e.g., in Jenny et al. (2012) or Sirignano (2010). Theoretical and numerical work has been focused strongly on the single droplet combustion mode, which is given below in Section 5.3.1, but less on group combustion modes. This results from the fact that even single droplet combustion is quite difficult to handle mathematically and to find a solution for comprehensive physics, not to mention the complexity of droplet

array and group combustion. With modern CFD methods and the available computational power, resolved simulations of combusting droplet pairs, droplet arrays and droplet groups can be conducted to investigate these modes in more detail. For realistic droplet numbers, however, resolving the individual droplets and flames is far from feasible. Therefore, statistical and macroscopic models must be developed, which consider those combustion modes in an effective way. Literature on both, single droplet and group combustion simulation in realistic/large scale applications are rare due to the complexity and the lack of affordable models. The nearby approach to simulate external group combustion and external sheath combustion, is to use spray flamelets where the droplets considerably approach the flame front or even cross it.

In this work a single droplet combustion model for polydispersed moment methods is proposed, which is based on net rates of vaporisation, species reaction and heat release as shown in the next section. Besides that, no further attempt has been made to consider any type of heterogeneous combustion mode and must be left for future work.

5.3.1 Single Droplet Combustion

To observe single droplet combustion, the following requirements must be met. First, and most essential, the droplet-droplet spacing must be large enough to avoid flame interaction of neighbouring droplets. Second, a lean or purely oxidising/inert gas mixture must be present to allow a sufficient transport of oxygen to the individual flames. If the droplets are surrounded by a high amount of fuel vapour or reaction products and too less oxygen, individual flames cannot establish, but only a flame surrounding the droplet group at a position where enough oxidiser is available. Furthermore, the position and shape of the individual flame around the droplet depends on the flow and the ambient conditions of the gas phase. Starting from a quiescent surrounding, the following flame shapes can be observed with increasing droplet Reynolds number: spherical flame, envelope flame, side (or boundary layer an-

chored) flame and wake flame (Chiu and Huang, 1996). If the Reynolds number becomes too large, the flame extinguishes and pure evaporation remains. The dependence on the droplet Reynolds number, however, is not unique, but depends on the history of the flow. That means, that the switching point between flame types is not singular, but depends on whether coming from high Reynolds numbers or from low Reynolds numbers (hysteresis loop). In fact, there exists a certain "inertia" of the current flame type regarding its change to another type. Details can be found in (Chiu and Huang, 1996).

Literature

All SDC flame types additionally differ from each other in mass vaporisation rates and heat release. These quantities are of specific interest when aiming for evaporation and single droplet combustion models describing the physics in a 0-dimensional but time dependent manner. Besides these models, a large effort has been undertaken to find 1-dimensional and 2-dimensional solutions for all single droplet combustion modes. Early analytical work is reported, i.a., by Godsave (1954), Spalding (1954), Goldsmith and Penner (1954), Fendell et al. (1966), Fendell (1968) and Kassoy and Williams (1968), in which an increasing amount of physics has been taken into account with time, i.e. steady state, spherical, transient, convective flows, etc. More recent work, e.g., Gogos et al. (1986), Fachini Filho (1999), Dwyer (1989), Ackermann and Williams (2005) and Ulzama and Specht (2007) still aims for accurate analytical solutions, but due to the complexity of the equations, an increasing amount is solved numerically. Reviews on the topic can be found in Williams (1973), Law (1982), Faeth (1977, 1983), Sirignano (1983, 1993), Borghi (1996), King (1996) and Chiu (2000).

With increasing complexity of the physics considered, the analytical solutions become notoriously complex and the equation systems too costly to include into numerical simulations. In order to be able to consider single droplet combustion for a large number of droplets in CFD simulations of

spray flames, we consider a 0-dimensional, spherically symmetric model similarly to the vaporisation modelling. The chosen model and the modifications done to be used in the moment equations are shown next.

5.3.2 A Single Droplet Combustion Model for Moment Methods

In this section, an Eulerian Single Droplet Combustion model (ESDCM) is proposed based on an available model for 0-dimensional, spherical, time dependent droplet combustion. Many models exist that provide time dependent mass vaporisation and heat transfer rates for combusting droplets. Here we chose the one from Ulzama and Specht (2007), because it is quite convenient to be used in the moment model framework. It provides the vaporisation rate and the heat release for a combusting droplet under the following assumptions and simplifications:

- 1D spherical (micro-gravity, quiescent air)
- unity Lewis number in the gas phase
- spatially uniform but transient droplet temperature
- c_p of gas and liquid are constant
- no temperature dependence of the gas phase properties
- combustion products do not affect the process
- 1-step, irreversible thin flame
- radiation is neglected
- the droplets persist at their initial temperature T_0; only the amount of liquid which will be vaporised, $\dot{m}_v$, is heated up.

The mathematical details and equations of the model are given next and prepared to be able to carry out the ensemble average, the filtering and the phase space integration in order to obtain appropriate source terms for the moment equations.

Vaporisation Rate

The vaporisation rate will be developed similarly to Section 3.2.1 using the effective or net heat transfer rate to the droplet $\dot{Q}_{l,\text{eff}}^{(n),\text{SDC}}$. It is the difference between the total heat conducted from the flame to the droplet, termed q in line with the original article (Ulzama and Specht, 2007), and the latent heat, which must be spent to vaporise the liquid, and is given by

$$\dot{Q}_{l,\text{eff}}^{(n),\text{SDC}} = \underbrace{4\pi\lambda^{@\mathbf{x}_p^{(n)}} \frac{T_f^{(n)} - T_s^{(n)}}{\frac{2}{D^{(n)}} - \frac{1}{r_f^{(n)}}}}_{=q} - \dot{m}_v \Delta h_v^{(n)} \,, \tag{5.10}$$

where $T_f^{(n)}$ is the temperature of the flame around the droplet n, $T_s^{(n)}$ is the vapour temperature at the droplet surface, i.e. T_boil, and r_f is the radius of the spherical, thin flame. For the ease of reading, the notation $@\mathbf{x}_p^{(n)}$ indicating the gas phase quantities at the droplet location, i.e. for $\lambda^{@\mathbf{x}_p^{(n)}}$, $T^{@\mathbf{x}_p^{(n)}}$, $\text{B}_{\text{T,M}}^{@\mathbf{x}_p^{(n)}}$, $\nu^{@\mathbf{x}_p^{(n)}}$, and the individual droplet identifier, the superscript $^{(n)}$, i.e. for $\dot{Q}_{l,\text{eff}}^{(n),\text{SDC}}$, $T_f^{(n)}$, $T_s^{(n)}$, $T_p^{(n)}$, $D^{(n)}$, $\Delta h_v^{(n)}$, are omitted in the following. Rearrangement of q yields

$$\dot{Q}_{l,\text{eff}}^{\text{SDC}} = 2\pi\lambda D(T_f - T_s) \underbrace{\frac{1}{1 - \frac{D}{2r_f}}}_{\text{correction factor}} - \dot{m}_v \Delta h_v \,. \tag{5.11}$$

The equivalent expression for pure evaporation, i.e. inserting Eqn. 3.46 into Eqn. 3.45 with considering Stokes flow only, $\text{Nu}^* = 2$, reads

$$\dot{Q}_{l,\text{eff}} = 2\pi\lambda D(T - T_p) \underbrace{\frac{\ln(1 + \text{B}_\text{T})}{\text{B}_\text{T}}}_{\text{correction factor}} - \dot{m}_M \Delta h_v \,. \tag{5.12}$$

Comparing both, it becomes clear that in the latter expression the correction factor accounts for the Stefan flux and that of the former for the physics between the droplet surface and the flame, i.e. $(1 - {}^{D}/_{2r_f})^{-1}$.

In the evaporative case, $\dot{Q}_{l,\text{eff}}$ can be completely used to heat up the droplet, since the heat up of the vapour from T_p to T is not taken into account at that point but in the energy equation Eqn. 3.33. In case of the single droplet combustion model presented by Ulzama and Specht (2007), the heat up of the vapour from T_s to T_f is considered directly in the heat balance of the model. This implies two reasonable points. First, as pointed out by the authors, the heat up of the vapour consumes the highest amount of the combustion heat compared to the liquid heat up and the latent heat. Second, it occurs between the droplet surface and the flame, independent of the state of the gas phase around the burning droplet. Hence, in contrast to Eqn. 3.33, here the vapour heat up is considered directly in the model. This will have an impact on the corresponding source terms in the gas and dispersed phase equations as shown later on.

Consequently, the remaining heat $\dot{Q}^{\text{SDC}}_{l,\text{eff}}$ must be spent to heat up the liquid[3] from T_0 to T_s and the vapour from T_s to T_f. The latent heat has already been considered in Eqn. 5.10. Hence,

$$\dot{Q}^{\text{SDC}}_{l,\text{eff}} = \dot{m}_v \left[c_{\text{p}l}(T_s - T_0) + c_{\text{p}v}(T_f - T_s) \right] \ . \tag{5.13}$$

Setting Eqn. 5.10 equal to Eqn. 5.13 yields the amount of liquid mass $\dot{m}_v$, which can be vaporised with the given heat, as

$$\dot{m}_v = \frac{4\pi\lambda_g(T_f - T_s)}{\left(\frac{2}{D} - \frac{1}{r_f}\right)\left[c_{\text{p}l}(T_s - T_p) + \Delta h_v + c_{\text{p}v}(T_f - T_s)\right]} \ . \tag{5.14}$$

The mass flow rate is defined to be positive when pointing from liquid to vapour. Replacing r_f by the expression given by Sirignano (2010)

$$r_f = \frac{D}{2}\frac{\ln(1 + \text{B}_\text{M})}{\ln(1 + \nu Y_{\text{ox},\infty})} \tag{5.15}$$

[3] As stated before, the model of Ulzama and Specht (2007) implies, that the initial droplet temperature T_0 remains constant, and only the amount of liquid which will be vaporised at the given time instant $\dot{m}_v$ is heated up from the initial droplet temperature T_0 to T_s.

yields

$$\dot{m}_v = \underbrace{\frac{2\pi\lambda_g(T_f - T_s)D}{\left(1 - \frac{\ln(1+\nu Y_{\mathrm{ox},\infty})}{\ln(1+B_T)}\right)\left[c_{\mathrm{p}l}(T_s - T_p) + \Delta h_v + c_{\mathrm{p}v}(T_f - T_s)\right]}}_{\equiv \frac{\pi}{4}\rho_p D K} . \tag{5.16}$$

Although a formulation of r_f is given in the original article, the one of Sirignano (2010) is used instead, because the original formulation is more complicated and requires an iterative solution procedure. It might be more accurate, since it is the original term for the model. K is the SDC-specific gasification rate as similarly defined in the D^2 law as (see Appendix A.3.1)

$$D^2(t) = D_0^2 - Kt . \tag{5.17}$$

Source Terms for the Gas Phase and Moment Equations

In order to obtain source and sink terms for the gas and dispersed phase equations, the ensemble average, spatial filtering and phase space integration is done accordingly to the evaporation source terms regarding the treatment of unknown correlations.

The source term for the dispersed phase mass continuity equation ($M^{(3)}$ equation) is obtained by

$$\Gamma^{\mathrm{SDC}}_{M^{(3)}} = \frac{6}{\pi}\iiint \dot{m}_v \,\mathrm{d}\boldsymbol{\mathcal{I}} = \frac{6}{\pi}\iiint \frac{\pi}{4}\rho_p D K \,\mathrm{d}\boldsymbol{\mathcal{I}} \approx \frac{3}{2}\rho_d K M^{(1)} , \tag{5.18}$$

where K is assumed to be invariant to the filtering. For general moment order it becomes

$$\Gamma^{\mathrm{SDC}}_{M^{(k)}} = \frac{k}{2}\rho_d K M^{(k-2)} . \tag{5.19}$$

With Eqn. 4.77 the source term for the gas phase mass continuity equation becomes

$$\Gamma^{\mathrm{SDC}} = \frac{\pi}{6}\Gamma^{\mathrm{SDC}}_{M^{(3)}} = \frac{\pi}{4}\rho_d K M^{(1)} \tag{5.20}$$

and the momentum sources for the dispersed and gas phase momentum equations

$$\Gamma^{\mathrm{SDC}}_{M^{(3)}}\mathbf{u}^{(1)} = \frac{3}{2}\rho_d K M^{(1)}\mathbf{u}^{(1)} \ , \tag{5.21}$$

$$\Gamma^{\mathrm{SDC}}\mathbf{u}^{(1)} = \frac{\pi}{4}\rho_d K M^{(1)}\mathbf{u}^{(1)} \ . \tag{5.22}$$

The source terms for the droplet and gas phase enthalpy differ from those given for the evaporation due to the different arrangement of the vapour heat up term in both cases. Here, the heat balance is constructed such, that the droplets persist at the temperature they actually had, when the single droplet combustion mode started (i.e. switched on in the numerical simulation as $T_s = T_d(t = \mathrm{SDC}{\rightarrow}\mathrm{on})$). Consequently, the droplet temperature is not changed as long the combustion remains in single droplet combustion mode and only the enthalpy which is lost due to mass loss must be considered, i.e. the source for the droplet enthalpy equation is

$$\Gamma^{\mathrm{SDC}}_{M^{(3)}} h_d \ . \tag{5.23}$$

To evaluate the source term for the gas phase, a simple balance can be made considering the chemical heat release from the droplet combustion $\dot{Q}_{\mathrm{comb}}$ and the heat needed for the droplet physics. As a result, the amount of the chemical heat release, which contributes to the gas phase temperature around the burning droplet, becomes

$$\dot{Q}_{\mathrm{comb}} - q \quad \Leftrightarrow \quad \dot{m}_v \frac{\Delta h_{\mathrm{comb}}}{W_v} - q \ , \tag{5.24}$$

where h_{comb} is the molar heat of reaction and W_v is the molar mass of the liquid.

In the numerical simulation, either the source terms due to pure evaporation or due to single droplet combustion are switched to be active. A simultaneous consideration of both modes locally is not possible and rather unlikely in reality. The switch is denoted as

$$\mathbf{S} = \mathbf{S}(\mathbf{x}, t) = \begin{cases} 1 & \text{if SDC applies} \\ 0 & \text{otherwise} \end{cases} \ , \tag{5.25}$$

which simply activates single droplet combustion when multiplying the corresponding terms by $\mathbf{S}$ and activates the pure evaporation with homogeneous combustion (thickened flame model) when multiplying the source terms by $1-\mathbf{S}$. With that the equations for the droplet and gas phase can be given.

Particle Phase Equations

Moment transport

$$\frac{\partial}{\partial t}(\rho_d M^{(k)}) + \nabla \cdot \left(\rho_d M^{(k)} \mathbf{u}^{(k)}\right) = -\left[(1-\mathbf{S})\frac{1}{\mathbf{F}}\Gamma_{M^{(k)}} + \mathbf{S}\,\Gamma^{\mathrm{SDC}}_{M^{(k)}}\right] \tag{5.26}$$

Momentum

$$\begin{aligned}\frac{\partial}{\partial t}(\rho_d M^{(3)} \mathbf{u}^{(3)}) + \nabla \cdot \left(\rho_d M^{(3)} \mathbf{u}^{(3)} \mathbf{u}^{(3)}\right) \\ = \mathbf{M}^{(3)} + \mathbf{g} M^{(3)} \rho_d - (1-\mathbf{S})\frac{1}{\mathbf{F}}\Gamma_{M^{(3)}}\mathbf{u}^{(1)} - \mathbf{S}\,\Gamma^{\mathrm{SDC}}_{M^{(3)}}\mathbf{u}^{(1)}\end{aligned} \tag{5.27}$$

Sensible enthalpy

$$\begin{aligned}\frac{\partial}{\partial t}(\rho_d M^{(3)} h_d) + \nabla \cdot \left(\rho_d M^{(3)} \mathbf{u}^{(3)} h_d\right) \\ = -(1-\mathbf{S})\frac{1}{\mathbf{F}}\Gamma_{M^{(3)}}\left[h_d + \Delta h_v(T_d) - c_{\mathrm{p}v}\frac{(T-T_d)}{\bar{\mathrm{B}}_{\mathrm{T}}}\right] \\ - \mathbf{S}\Gamma^{\mathrm{SDC}}_{M^{(3)}} h_d\end{aligned} \tag{5.28}$$

Gas Phase Equations

The gas mass continuity equation reads

$$\frac{\partial \rho}{\partial t} + \nabla \cdot (\rho \mathbf{u}) = -\frac{\pi}{6}\left[(1-\mathbf{S})\frac{1}{\mathbf{F}}\Gamma_{M^{(3)}} + \mathbf{S}\,\Gamma^{\mathrm{SDC}}_{M^{(3)}}\right] . \tag{5.29}$$

Special attention must be paid to the species equations. Up to now, no comment has been given of how the actual combustion will be taken into account. As outlined in the introduction of this section (5.3.2), the reaction is assumed to be infinitely fast compared to the diffusion of fuel vapour and oxidiser and can be described by a one-step reaction mechanism. That means that fuel vapour and oxidiser directly transform to the final products. Here, we consider a reaction mechanism in the form of

$$\nu_v \mathrm{F} + \nu_{\mathrm{O2}} \mathrm{O_2} \rightarrow \nu_{\mathrm{CO2}} \mathrm{CO_2} + \nu_{\mathrm{H2O}} \mathrm{H_2O} \tag{5.30}$$

With that, the ansatz *vaporised equals burnt* can be made. Hence, the vaporised mass flow rate is proportionally distributed to the product species CO_2 and H_2O directly and taken from the oxidiser species O_2 by the specific amount determined by the stoichiometric coefficients in Eqn. 5.30. The fuel vapour species F remains unchanged. As the result, the gas phase equations for the species read

Fuel species

$$\frac{\partial}{\partial t}(\rho Y_{v,\infty}) + \nabla \cdot (\rho Y_{v,\infty} \mathbf{u}) - \nabla \cdot (\eta_{\mathrm{eff}} \mathbf{E}\,\mathbf{F}\,\nabla Y_{v,\infty}) = \frac{\mathbf{E}}{\mathbf{F}} \dot{\omega} + \frac{\pi}{6}(1 - \mathbf{S}) \frac{1}{\mathbf{F}} \Gamma_{M^{(3)}} \,, \tag{5.31}$$

O_2 species

$$\frac{\partial}{\partial t}(\rho Y_{\mathrm{ox},\infty}) + \nabla \cdot (\rho Y_{\mathrm{O2},\infty} \mathbf{u}) - \nabla \cdot (\eta_{\mathrm{eff}} \mathbf{E}\,\mathbf{F}\,\nabla Y_{\mathrm{O2},\infty}) = \frac{\mathbf{E}}{\mathbf{F}} \dot{\omega} - \frac{\pi}{6} \mathbf{S} \frac{1}{\mathbf{F}} \frac{\nu_{\mathrm{O2}} W_{\mathrm{O2}}}{\nu_v W_v} \Gamma^{\mathrm{SDC}}_{M^{(3)}} \,, \tag{5.32}$$

CO_2 species

$$\frac{\partial}{\partial t}(\rho Y_{\mathrm{CO2},\infty}) + \nabla \cdot (\rho Y_{\mathrm{CO2},\infty} \mathbf{u}) - \nabla \cdot (\eta_{\mathrm{eff}} \mathbf{E}\,\mathbf{F}\,\nabla Y_{\mathrm{CO2},\infty}) = \frac{\mathbf{E}}{\mathbf{F}} \dot{\omega} + \frac{\pi}{6} \mathbf{S} \frac{1}{\mathbf{F}} \frac{\nu_{\mathrm{CO2}} W_{\mathrm{CO2}}}{\nu_v W_v} \Gamma^{\mathrm{SDC}}_{M^{(3)}} \,, \tag{5.33}$$

H_2O species

$$\frac{\partial}{\partial t}(\rho Y_{\text{H2O},\infty}) + \nabla \cdot (\rho Y_{\text{H2O},\infty}\mathbf{u}) - \nabla \cdot (\eta_{\text{eff}}\mathbf{E}\,\mathbf{F}\,\nabla Y_{\text{H2O},\infty}) = \frac{\mathbf{E}}{\mathbf{F}}\dot{\omega} + \frac{\pi}{6}\mathbf{S}\frac{1}{\mathbf{F}}\frac{\nu_{\text{H2O}}W_{\text{H2O}}}{\nu_v W_v}\Gamma^{\text{SDC}}_{M^{(3)}} \ , \quad (5.34)$$

where W_{O2}, W_{CO2} and W_{H2O} are the molar masses of the oxygen, carbon dioxide and water, respectively.

The vapour momentum is transferred to the gas phase at the status after vaporisation. The contribution of momentum due to the volume expansion of the vapour and product species due to the heat up to the flame temperature, respectively, is accounted for implicitly by the reaction heat source term in the energy equation.

$$\frac{\partial}{\partial t}(\rho\mathbf{u}) + \nabla \cdot (\rho\mathbf{u}\mathbf{u}) = -\nabla p + \nabla \cdot \boldsymbol{\tau} + \frac{\pi}{6}\mathbf{M}^{(3)} + \rho\mathbf{g} + \frac{\pi}{6}(1-\mathbf{S})\frac{1}{\mathbf{F}}\Gamma_{M^{(3)}}\mathbf{u}^{(1)} + \frac{\pi}{6}\mathbf{S}\,\Gamma^{\text{SDC}}_{M^{(3)}}\mathbf{u}^{(1)} \ . \quad (5.35)$$

The gas phase sensible enthalpy equation finally becomes

$$\begin{aligned}\frac{\partial}{\partial t}(\rho h) + \nabla \cdot (\rho\mathbf{u}h) - \nabla \cdot (\eta_{\text{eff}}\mathbf{E}\,\mathbf{F}\,\nabla T) &= -\frac{dp}{dt} + \frac{\mathbf{E}}{\mathbf{F}}\dot{\omega} \\ &\quad + (1-\mathbf{S})\left[-\frac{\pi}{6}\frac{1}{\mathbf{F}}\Gamma_{M^{(3)}}c_{\text{p}v}T_d + \frac{1}{\mathbf{F}}\pi\ \text{Nu}\,kM^{(1)}\left(T_d - T\right)\right] \\ &\quad + \mathbf{S}(\dot{m}_v\frac{\Delta h_{\text{comb}}}{W_v} - q) \ . \end{aligned} \quad (5.36)$$

When Does Single Droplet Combustion Occur?

The following criteria must be met:

1. The droplet must be ignited, i.e. pass a hot gas zone with a residence time therein at least as long as the ignition delay time. Here, it is simply assumed that $\mathbf{S} = 1$ if $T > T_{\text{ign}}$ without considering the ignition delay time.

2. The droplet must have appropriate conditions around it, i.e. oxidiser.

3. There must be enough space to the next droplet, otherwise SDC switches to a kind of group combustion mode. Twardus and Brzustowski (1977) and Brzustowski et al. (1979) found that the droplet-droplet spacing (dds) to diameter ratio $\mathcal{R} = dds/D$ must be at least $\mathcal{R} \geq 8.5$ for heptane, for less-volatile fuels Umemura and Takamori (2005) give a value of around 10.

The last criterion can be formulated as follows. The mean droplet-droplet spacing dds can be given in terms of the number density $M^{(0)}$ as $dds = 1/\sqrt[3]{M^{(0)}}$. If the mean diameter $D_{10} = M^{(1)}/M^{(0)}$ is used for D, $\mathcal{R}$ can be written as

$$\mathcal{R} = \frac{dds}{D_{10}} = \frac{\sqrt[3]{M^{(0)^2}}}{M^{(1)}} \,. \tag{5.37}$$

For practical simulations, we choose $\mathcal{R} \geq 10$. SDC is switched off if $\mathcal{R} \leq 10$ or when the oxidiser mass fraction becomes marginal.

Validation

The proposed Eulerian Single Droplet Combustion model (ESDCM) has been implemented into the existing solver for homogeneous spray combustion. Which of both combustion models locally applies during the simulation has been discussed in the paragraph before. Here, a rough comparison is shown between results obtained from the homogeneous combustion and those from the ESDCM. The same 1D non-premixed two-phase flame has been used as discussed in the last paragraph of Section 5.2.2, where the two-phase thickened flame model has been verified in a similar way. In the case of the ESDCM simulation, the model has been

switch on from the very beginning (not considering an appropriate ignition temperature) and switched of when no oxidiser is left, which is the case after a certain length as indicated in Fig. 5.10. The value used for the heat of combustion of methanol is $\Delta h_{\text{comb, CH3OH}} = -735\,\text{kJ/mol}$. The PaSR simulation has been conducted using the 1-step scheme for methanol of Westbrook and Dryer (1981).

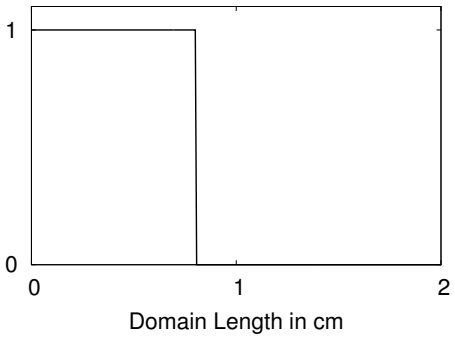

Figure 5.10: Domain where the ESDCM applies.

As Fig. 5.11 shows, the overall behaviour of the ESDCM is in the same range as that of the homogeneous combustion using the PaSR. The main difference is the speed of reaction. As the gas phase temperature and the species concentrations indicate by their maximum value at approximately 4 mm, all the oxygen is consumed at that point and the remaining liquid mass is still vaporising, which results in an increase of the fuel vapour species and a decrease in the mass fraction of the other species. In the ESDCM model results, oxygen is left up to 8 mm. Since the ESDCM does not imply any mechanism to recognise the vanishing oxygen concentration, it must be switched off explicitly. Otherwise, the SDC would continue as long as droplets exist. Although the reaction happens faster in the PaSR simulation, the overall decrease in liquid volume fraction and the moments is faster applying the ESDCM. However, the liquid velocity is increasing faster as well at the very beginning, which contributes to an increase of those values independent of the vaporisation rate.

Considering these first results, it is clear that a comprehensive verification and validation of the model is needed, which could be undertaken

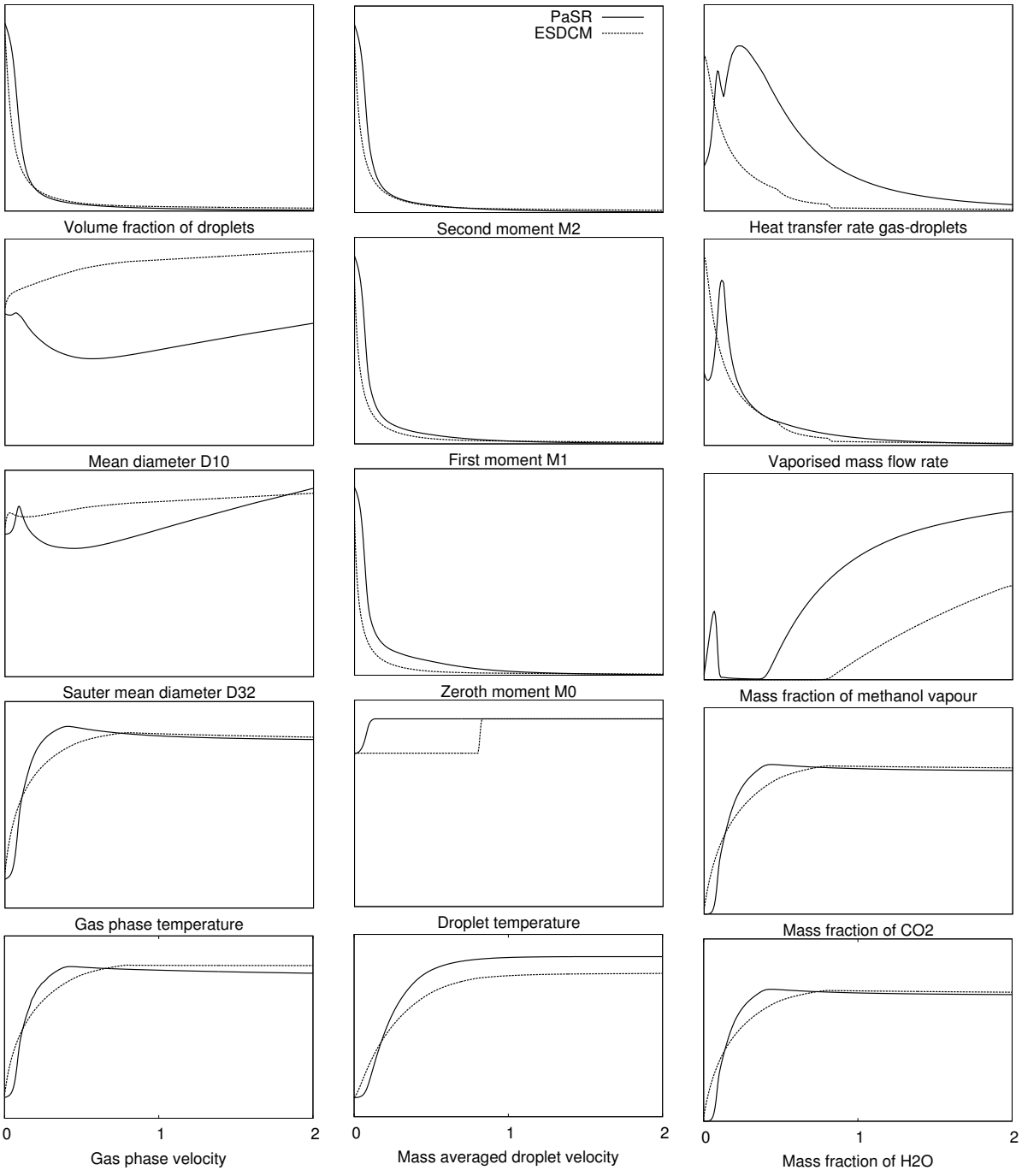

Figure 5.11: Simulation results for methanol combustion using PaSR compared to ESDCM.

using a spectral or analytical solution for each droplet size class and experiments where single droplet combustion explicitly occurs or domi-

nates the combustion. Tests carried out on a 3D case are too preliminary to be presented and discussed here, but must be left for future work.

6 Numerical Issues

Discussing the fundamentals of CFD in general is out of the scope of this work. Even the presentation of the specific characteristics of two-phase equation systems or (pressure-less) dispersed phase equations including their requirements on the solver exceeds the present framework. In fact, the focus of this work does not coincide with developing, evaluating or implementing sophisticated methods, which serve the characteristics of the equations in a comprehensive way. Instead, rather standard solvers and discretisation have been used as applied commonly in single phase, (weakly) compressible flows. Nevertheless, some specific issues deviate from these methods, which will be discussed here in order to clarify the details of the solver and the numerical setup which has been used to obtain the results presented in Chapter 7. The structure of the solvers, the implementation of the equations and some other issues are discussed in the next section, whereas details on the discretisation, the boundary conditions, etc. are given in Section 6.3. Some remarks concerning dispersed phase equation solution methods, pressure-less fluid equations or moment space preserving discretisation schemes have been already given in the previous chapters.

6.1 Implementation in OpenFOAM

The derived equation system for the gas phase and the dispersed phase have been implemented into the CFD software package OpenFOAM using different versions ranging from version 1.5 up to 2.1.x. The presented results, however, are solely produced by solvers compiled with either version 2.1.x or 2.1.1. OpenFOAM is a modularly built open-source code

for various CFD applications and it is a convenient tool for the implementation and testing of new submodels and solvers. The original two-phase formulation of the model (Carneiro et al., 2008, Dems et al., 2012a) is based on the OpenFOAM solver `twoPhaseEulerFoam`, which provides the framework for an Eulerian-Eulerian two-phase solver and features a common pressure equation for both phases. The recent formulation of the model as shown in the previous chapters implies a phase coupling solely by the source terms for mass, momentum and energy exchange. Still, the continuous phase momentum equation is not solved directly but with the help of a pressure equation. In contrast, the dispersed phase momentum equation is solved directly to obtain the dispersed phase velocity field. This topic is detailed in Section 6.1.3. Besides the governing structure of the solvers, many details contribute to the final versions used to produce the results. Some of the most important features are described next.

6.1.1 Phase-Intensive Formulation of the Transport Equations

Solving the dispersed phase moment equations 4.62, 4.74 to 4.76 and especially equations 4.63 and 4.65 can become notoriously difficult, if the moments tend towards zero. This happens in all regions where physically no spray is present[1]. Actually, the same applies for the continuous phase equations if θ becomes very small, which is the case when the volume fractions of the dispersed phase becomes large, e.g. in separated flow simulations or when phase inversion occurs. Both does usually not happen in dispersed two-phase flows with a clearly distinguished dispersed phase, except when combined with phenomena like free surfaces, e.g. in bubble columns. Since the numerical results presented refer to clearly dispersed two-phase flows with a small volume fraction of the dispersed phase, this issue of vanishing volume fraction, respective moments, is relevant only for the dispersed phase equations. Hence, only the dispersed phase equations must be treated appropriately.

[1] Due to the Eulerian field constraint, spray quantities must be defined and the equations are solved for nevertheless, which raises this problem.

As reported in Weller (2005), solving Eqn. 4.63 directly and applying artificial modifications on vanishing α_d is not productive, e.g. using limiters or setting the dispersed phase velocity to a certain fixed value or even equal to the continuous phase velocity[2] for vanishing α_d. Neither of them was satisfactory. Hence a more comprehensive way of tackling this problem has been discussed therein as briefly recapitulated and applied to our set of equations.

In general, conservation equations of momentum and energy for both phases can be formulated either in a conservative or a phase-intensive (or non-conservative) way. In line with the work of Weller (2005) and Rusche (2002), phase-intensive versions of the dispersed phase momentum and enthalpy equation were derived. This was done by factoring out the time and convective term on the left hand side and including the mass conservation equation as detailed in Appendix A.4.1.

As a result, the phase intensive formulations of the momentum and enthalpy equation of the dispersed phase read

$$\frac{\partial \mathbf{u}^{(3)}}{\partial t} + \mathbf{u}^{(3)} \nabla \cdot \mathbf{u}^{(3)} = \frac{\mathbf{M}^{(3)}}{\rho_d M^{(3)}} + \mathbf{g} - \frac{1}{\rho_d M^{(3)}} \Gamma_{M^{(3)}} (\mathbf{u}^{(1)} - \mathbf{u}^{(3)}) \,, \tag{6.1}$$

$$\frac{\partial h_d}{\partial t} + \mathbf{u}^{(3)} \nabla h_d = -\frac{1}{\rho_d M^{(3)}} \Gamma_{M^{(3)}} \left(\Delta h_v(T_d) - c_{\mathrm{p}v} \frac{(T - T_d)}{\bar{\mathrm{B}}_{\mathrm{T}}} \right) \,. \tag{6.2}$$

The phase intensive formulation is more stable, especially concerning the aforementioned problem of having marginal values for the volume fractions and moments. However it may become less accurate since velocity instead of momentum is transported. In two-phase flows this issue can become much more important than in variable density single phase flows (highly compressible or non-isothermal), since the phase-averaged mass density (i.e. particle mass to the total volume) can vary more than the density in the aforementioned types of single phase flow. In case of the

[2]The dispersed phase velocity $\mathbf{u}^{(3)}$ represents a mass weighted particle velocity even if there is virtually no particle present. Although having a marginal number density, the NFD is defined nevertheless and does not necessarily contain only tracer particles. Hence, the mass averaged particle velocity can be still significantly different from the continuous phase velocity. Test simulations have shown that using this approach dis-balances the velocity equations crudely.

phase-intensive formulation, simply spoken, the velocities are arithmetically averaged, whereas in the conservative equation, a mass weighted average is conducted, which is significantly more physical. A simple, 2-dimensional example of this issue is given in Appendix Section A.4.2.

Due to the lack of alternative solutions, the phase intensive formulation has been kept for the dispersed phase to solve the problem of vanishing volume fraction values when solving the momentum and enthalpy equation. Especially the temperature equation is very unstable when using the conservative equation, probably due to the less damping effect through the continuous phase via heat exchange than compared to the momentum exchange via drag. The continuous phase has been simulated using the conservative formulation. Here, this issue relaxes, since the volume fraction is always close to unity.

6.1.2 Treatment of Implicit and Explicit Source Terms

Besides the phase-intensive formulation of the dispersed phase equations, an additional step has been undertaken to stabilise the numerical solution of both, the gas and dispersed phase equations. The toolbox of OpenFOAM provides a command `fvm::Sp()`, which allows to add specific terms into the main matrix, which are otherwise treated as explicit sources. These are those terms which are a function of the variable the equation is solved for, but which are not preceded by a temporal or spatial derivative as for example `fvm::ddt()`, `fvm:div()` or `fvm::laplacian()`. This procedure has been applied in all cases, i.e. those parts of the phase interaction source terms on the right hand side of the momentum and the enthalpy equations, which contain the variable which is solved for. The explicit parts usually remain in their original notation. An exception for that are the moment transport equations, where $\Gamma_{M^{(k)}}$ has been additionally divided by the corresponding moment $M^{(k)}$ and directly multiplied again, which is noted in the code, e.g. for $M^{(2)}$ as

```
- fvm::Sp(-Gamma_m2/m2,m2)
```

This trick may improve the stability, since the otherwise explicit source becomes a sort of implicit, i.e. Γ is divided by the old value, but multiplied by the one which is implicitly solved for in the current time step. This procedure does not work, however, for the species equations due to some unknown reason. `fvm::Sp()` should be always preceded by a negative sign, hence, the double negative sign here.

To be able to make use of this tool for those source terms of the dispersed phase equations, where the order of the moment transport velocity is not equal to the order of those the moment flux transport equation is solved for, the "foreign" moment transport velocities are replaced by the "correct" transport velocity using the relaxation approach and the related moments occurring in the relaxation times. This has been applied for the drag source terms in Eqn. 4.63. For example $\mathbf{u}^{(1)}$ has been replaced by

$$\mathbf{u}^{(1)} = \frac{{M^{(3)}}^2}{M^{(1)}M^{(5)}}\mathbf{u}^{(3)} \; . \tag{6.3}$$

With that, the drag force source term in the third moment flux equation becomes implicit.

6.1.3 The Pressure Poisson Equation for Two-Phase Flows

In pressure-based CFD solvers for incompressible and weakly compressible single phase flows, a pressure equation is typically solved instead of the mass continuity and momentum equation. This so-called *Poisson*[3] *pressure equation* takes the general form

$$-\Delta p = f(\nu, \mathbf{u}) \; , \tag{6.4}$$

with the fluid pressure p is the unknown variable and f is a function of the fluid viscosity ν and the velocity $\mathbf{u}$. That means f represents the momentum equation without the pressure gradient and simplified by inserting the mass continuity.

[3] If $f = 0$, then it is called *Laplace equation*.

This procedure has a number of advantages, which are not discussed here, but can be found in any text book about numerical methods for CFD. For two-phase flows, one has to consider three issues when deriving the corresponding pressure equation. They are related to the "new" quantities occurring in the momentum equations of the different phases, i.e. the volume fractions, the phase interaction source terms as for example the drag and the mass exchange between the phases. Depending on the underlying averaging method used to derive the equations, one must distinguish between two types of pressure equations.

First, as the outcome of volume averaging, both the continuous and dispersed phase momentum equation contain the pressure gradient term. Usually the pressure is assumed to be equal for both phases, which means that the effect of the surface tension force acting as a pressure jump for curved interfaces is neglected. Using this type of momentum equation, a combined mass continuity equation including all phases can be constructed, from which, with the help of the momentum equations, a common pressure equation can be derived. This procedure has been shown in Weller (2005) in detail for the OpenFOAM solver `twoPhaseEulerFoam` for incompressible and compressible flows including the phase interaction forces due to drag, lift and virtual mass. Mass exchange, however, is not considered.

Second, if the dispersed phase equations are based on the kinetic approach, no pressure occurs in the momentum equation of the dispersed phase. Hence, the former method cannot be applied. As in Lagrangian simulations of dispersed two-phase flows, we choose to solve directly the dispersed phase momentum equation and use a modified pressure equation for the continuous phase separately. Compared to the pressure equation for single-phase flows, this pressure equation must incorporate the volume fractions, the drag force and the mass source due to evaporation. Since we neglect the volume fraction of the droplets in the gas phase equations, only the two source terms must be considered.

Let us discuss both terms separately. The drag force acts similar as a body force, which occurs only at the right hand side of the momentum equa-

tion. When creating the discretised form of the pressure equation, this term is stored together with the left hand side in the main matrix and treated correspondingly in the implementation of the solver as done in OpenFOAM. The mass exchange source term, however, contributes to the momentum equation and additionally occurs in the mass balance equation. Hence, its appearance in the pressure equation is twofold. First, it must be treated similar to the drag force in the momentum equation, but must be included in the pressure equation a second time due to its appearance on the right hand side of the mass balance equation. As shown here for the compressible case, it becomes an additional term in the pressure equation compared to the single phase case (e.g. `rhoPimpleFoam`) as:

```
fvScalarMatrix pEqn
(
    fvm::ddt(psi, p)
  + fvc::div(phi)
  - fvm::laplacian(rho*rAU, p)
  - Gamma_alphaD
);
```

The drag is already included in the flux `phi`.

This modification[4] ensures that the impact of the introduced gas/vapour mass per volume on the pressure and/or the velocities is considered properly. This means that in case of an isochoric change of state the pressure is raised and in case of an isobaric process the amount of the additionally introduced volume due to the expansion from liquid to gaseous state is forced to leave the domain somewhere else. The latter results in a fluid motion, even if the original state is quiescent.

The results[5] shown in Chapter 7 are based on the equation structure as presented in the previous chapters, hence featuring a single phase pres-

[4] In the actual implementation, Γ is defined and coded throughout the solvers with opposite sign compared to the notation in this thesis. Hence this term occurs in the actual code with positive sign.

[5] The results presented in Section 7.1 for the case of Sommerfeld and Qiu (1991) are also based on the recent approach and differ therefore from those published in Dems et al. (2012a), which have been calculated with a common, incompressible pressure equation.

sure equation for the continuous phase and a direct solution of the dispersed phase momentum equation, which is reformulated into a phase-intensive form as shown in Section 6.1.1. The coupling of the dispersed phase to the continuous phase only via the drag provides a sufficient stabilisation to prevent problems with shock-like solutions for the dispersed phase momentum equation. The numerical diffusion due to `upwind` discretisation obviously contribute to that fact on its own.

6.2 Monodisperse Solvers

For the numerical simulations of the experiment of Sommerfeld and Qiu (1991) (see Section 7.1) and the Sydney spray burner (see Section 7.2), monodispersed simulations have been carried out for comparison with the polydispersed results. The simulations of the former experiment are based on the arithmetic mean diameter D_{10}, since profiles of this quantity are explicitly given in the database. Those of the latter are based on the Sauter mean diameter D_{32}. In both cases, the corresponding moments are transported instead of the mean diameter according to $D_{10} = M^{(1)}/M^{(0)}$ and $D_{32} = M^{(3)}/M^{(2)}$. All moments are convected with the same velocity $\mathbf{u}_d$, which is chosen to be equal to the mass averaged velocity $\mathbf{u}^{(3)}$ from the polydispersed cases. This does not represent any specific constraint, since in both experiments all particles travel approximately with the same velocity at the inlet. In the case of using D_{10}, α_d is calculated via $\alpha_d = \pi/6\, M^{(0)} D_{10}^3$, which is required for the dispersed phase momentum equation. Corresponding to Eqn. 4.43, a formulation of the drag coefficient has been chosen using D_{10} and D_{32}, respectively, as

$$\stackrel{\text{def.}}{=} 18\bar{\eta} M^{(1)}(\tilde{\mathbf{u}} - \mathbf{u}^{(3)}) \left(1 + 0.15 \left(\frac{D_{10}|\tilde{\mathbf{u}} - \mathbf{u}^{(3)}|}{\bar{\nu}}\right)^{0.687}\right) \tag{6.5}$$

and

$$\stackrel{\text{def.}}{=} 18\bar{\eta}\frac{\frac{6}{\pi}\alpha_d}{D_{32}^2}(\tilde{\mathbf{u}}-\mathbf{u}^{(3)})\left(1+0.15\left(\frac{D_{32}|\tilde{\mathbf{u}}-\mathbf{u}^{(3)}|}{\bar{\nu}}\right)^{0.687}\right) . \tag{6.6}$$

The source terms for mass and heat exchange between the phases, which are required for the simulation of the evaporation, are formulated similar to the drag using the Sauter mean diameter (Eqn. 6.6). The case of Sommerfeld and Qiu (1991) is an isothermal case using glass beads, hence it does not require the consideration of mass or heat exchange. Therefore, the presented drag term is the only subject of modification. Obviously, deriving these terms strictly from a corresponding formulation of the NDF would probably yield formally different terms.

6.3 Numerical Setup

6.3.1 Boundary Conditions

Finding appropriate boundary conditions for the dispersed phase quantities is not trivial. Many tests have been conducted, from which the following set has been proved to work adequately well with the current solver. The overview of all the conditions is given in Tab. 6.1. The conditions are quite standard. There are only a few specific choices to be mentioned. The dispersed phase velocity $\mathbf{u}^{(3)}$ is set to a slip condition at the walls due the physical fact, that droplets which travel parallel to the wall does not recognise it independent of the distance until they touch the wall. Clearly, when considering the presence of the gas phase, they are obviously affected by its boundary layer. Such effects, however, are not considered here. Additionally, this choice helps a bit to avoid accumulation of droplet mass in the wall adjacent cells, due to the arising low dispersed phase velocity when using a non-slip boundary condition.

The gas phase velocity is usually neither homogeneous nor stationary at the inlets, due to the upstream development of the flow. Hence, some

Table 6.1: Boundary conditions used in OpenFOAM.

	inlets	**spray inlets**	**air inlets**
	type	value	value
gas velocity	`fixedValue`	in-house bc	
particle velocity	`fixedValue`	same as gas phase	
moments	`fixedValue`	as given in the corresponding result section	spray inlet values times 1×10^{-7}
pressure	`zeroGradient`	-	-
nuSgs	`zeroGradient`	-	-

	walls		**outlet**	
	type	value	type	value
gas velocity	`fixedValue`	0 m/s	`zeroGradient`	-
particle velocity	`slip`	-	`zeroGradient`	-
moments	`zeroGradient`	-	`zeroGradient`	-
pressure	`zeroGradient`	-	`fixedValue`	101 325 Pa
nuSgs	`zeroGradient`	-	`zeroGradient`	-

specific boundary conditions have been implemented in OpenFOAM, which allow to specify certain profiles for each velocity component independently and if desired with imposed turbulent fluctuations. When necessary, the `waveTransmissive` boundary condition has been used at the inlets and outlets to avoid the development of nonphysical acoustics, which probably arise from the initial pressure field (often shock-like).

6.3.2 Discretisation and Solution Methods

Choosing appropriate discretisation schemes for the dispersed phase is even more challenging. Fortunately, the choice for the moment transport equations is rather limited naturally. This results from the specific characteristics of the moment set, which must be valid throughout the domain to ensure a meaningful reconstruction of the distribution (see Section 4.5.2, last paragraph). Hence, `upwind` is used for moment transport and the $\mathbf{u}^{(3)}$ transport equation. Since `upwind` is strongly dissipative, this contributes unintentionally to the dispersion of the particles, which

might compensating the neglected dispersed velocity and cross correlations to a certain amount (Section 3.2.3 and Chapter 4). The specific choice made for the discretisation and the solution methods is given for each presented case separately in Appendix A.5.

7 Results

Three cases will be investigated comparing numerical and experimental results: an isothermal, non-evaporating, swirling, particle laden flow (Sommerfeld and Qiu, 1991), a vaporising droplet-laden air jet (Chen et al., 2002, 2006) and a combusting spray (Cai et al., 2005, Fu et al., 2005a,b). Each case implies polydisperse effects. The first focuses on the kinematic dynamics of the particles depending on particle size, the second is more concerned with the size dependent vaporisation rate and the aim of the reacting spray is to show the applicability of the moments model in such a configuration, but represents only the first step into this direction.

7.1 Sommerfeld and Qiu (1991)

7.1.1 Description and Setup

Validation of polydisperse particle behaviour requires a flow configuration which clearly features particle size dependent motion dynamics. Hence, the simulations for polydisperse and monodisperse distributions are expected to give different results. Furthermore, in order to validate the moments model in combination with LES, the flow field should be significantly better represented using LES than using RANS. The experimental setup of Sommerfeld and Qiu (1991) meets these criteria. The main geometry consists of a cylindrical confinement of 1 m length and approximately 200 mm of diameter. A sketch of the geometrical dimensions and the positions of the measurement planes is given in Fig. 7.1 and Fig. 7.2. Two flow streams are injected, a non-swirling air jet laden

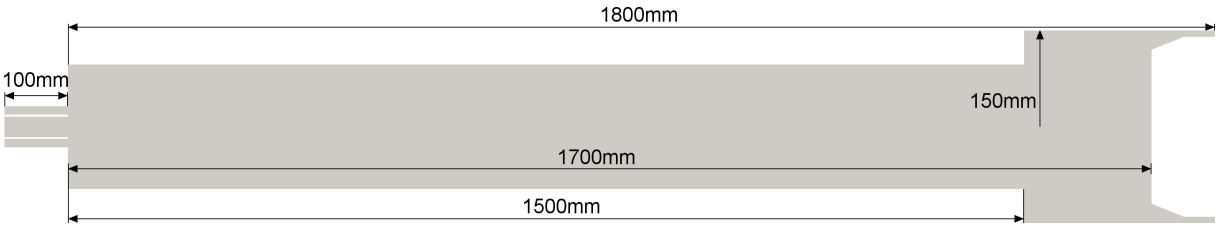

Figure 7.1: Geometrical dimensions and arrangement of the numerical domain.

Figure 7.2: Details of the geometrical dimensions and position of the measurement planes.

with small glass beads and a coaxial swirling air flow, which surrounds the inner jet. Combined with an essential area expansion, this configuration results in a vortex breakdown and a central recirculation zone. The central particle laden jet and the recirculation zone form a counterflow situation, which perfectly serves as a segregation of small and large particle dynamics. Depending on their inertia, the particles travel beyond the stagnation point into the reverse air flow up to a certain distance until they are entirely decelerated and follow the air flow outwards. Besides these physical criteria, measurement data of particle quantities as particle sizes and velocities must be available to allow a detailed validation of the numerical results. The published data provide a sufficient data base for our purposes.

Validation of the polydisperse model implies two aspects. First, the gen-

eral applicability of the presented LES formulation (including the numerous simplifications) must be verified, both, regarding the gas flow and the particle flow. This is done by comparison with experimental data to evaluate the "absolut accuracy" and by comparison of numerical results which differ in certain sub-models or terms in the equations, i.e. a simpler against a more sophisticated model. However, since closure for many terms is yet not known or proposed models are rather complex and difficult to implement, in the present work the simplified LES formulation has been validated only by comparison with the experimental data. With that, a conclusion can be drawn only in the sense, up to which accuracy the model is able to predict the measured fields. It cannot be concluded, which simplification is the most significant and which can be made anyway because its impact is marginal. Additionally, the quality of the results depends on the question, whether one is interested in mean fields and averaged first order deviations, or in high order accuracy of each specific correlation and particle-flow interaction. In the scope of this work, the validation is restricted to the comparison of mean and rms values of gas phase and particle velocities as well as moment fields, mean diameters and particle mass fluxes if available.

Second, the difference of the polydisperse model compared to a monodisperse simulation (see Section 6.2) is of specific interest, in order to show whether the effort of considering size and velocity space is worth and essential to represent the flow features, or if the monodisperse model results in rather similar predictions.

The case of Sommerfeld and Qiu (1991) has been used for validation by numerous researchers, whose publications can be used to draw further conclusions on the accuracy of present numerical methods for polydispersed two-phase flows. Apte et al. (2003) and Oefelein (2006), among others, simulated this case using 3-dimensional LES and a Lagrangian formulation for the particle motion, whereas an Eulerian formulation of the dispersed phase has been used by Boileau et al. (2008) and Cuenot et al. (2006). A 2-dimensional, Eulerian-Eulerian simulation has been conducted by Zhou and Liu (2010), which used a standard turbulence model

for the dispersed phase.

In Fig. 7.3, the experimentally measured size distribution of the glass beads is shown, overlain by the mathematical approximation using a Gamma distribution. Its parameters are $p = 5.85 \times 10^{-6}\,\mathrm{m}$, $q = 2.39453$ and $C_0 = 7.182\,467 \times 10^{8}\,\mathrm{m}^{-3}$, which correspond to the moments $M^{(1)} = 10\,061.2\,\mathrm{m}^{-2}$, $M^{(2)} = 5.258\,31 \times 10^{-1}\,\mathrm{m}^{-1}$ and $M^{(3)} = 3.055\,774\,9 \times 10^{-5}$. To obtain the same injected mass flux for the monodispersed simulation, the values for $M^{(1)}$ and $M^{(0)}$ become $15\,090.25\,\mathrm{m}^{-2}$ and $3.353\,388 \times 10^{8}$, respectively. Hence, the arithmetic mean diameter $D_{10} = M^{(1)}/M^{(0)} = 45\,\mu\mathrm{m}$ according to the value given in Sommerfeld and Qiu (1991).

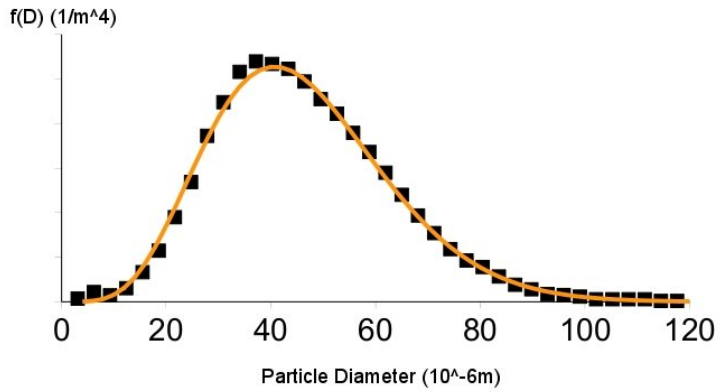

Figure 7.3: Experimental size distribution of the glass beads and its mathematical approximation using the Gamma distribution.

Initially, inlet pipes have been considered up to 200 mm upstream from the area expansion, but omitted in the present results due to problems with non-physically growing acoustics using the compressible solver. The cubic stagnation chamber at the end of the cylindrical confinement has been considered approximately by using a cylindrical geometry with the same axial length and total volume and with a strongly narrowed, coaxial outlet positioned at the largest diameter of the stagnation chamber. In Fig. 7.4 the numerical mesh is shown for the interesting region of the simulation domain. The block-structured, hexahedral mesh consists of 1 223 922 computational volumes.

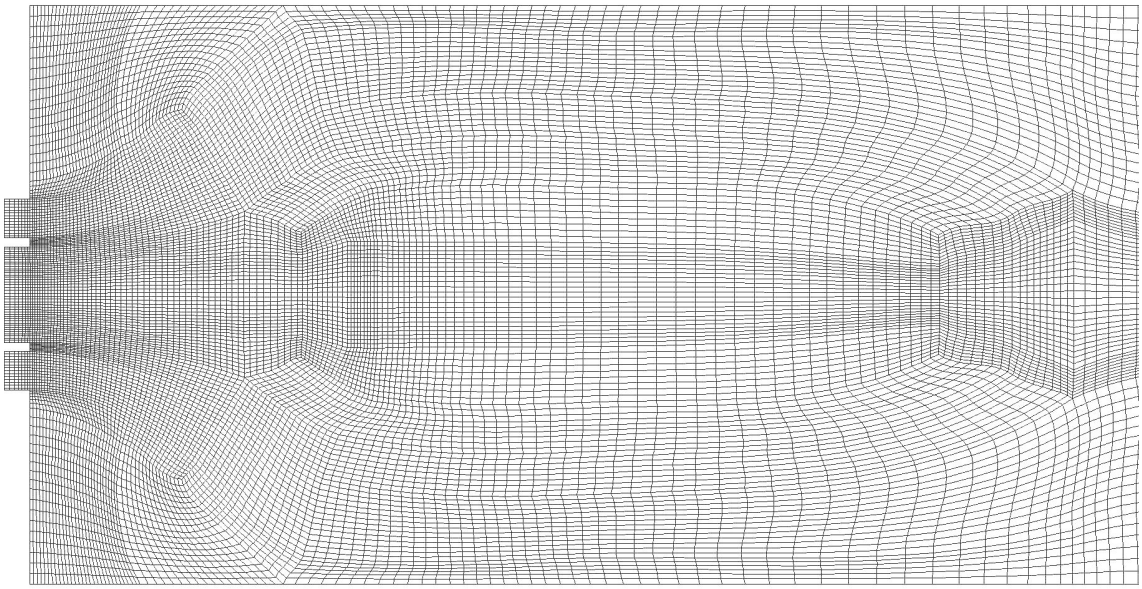

Figure 7.4: The numerical mesh, consisting of 1 223 922 cells. Inlet and downstream pipes are cut in this visualisation. The present results are actually calculated without considering the inlet pipes, but which are shown here to indicate their position.

The numerical boundary conditions correspond to those listed in the tables 6.1, with specified values as follows. Mean velocity profiles have been imposed on the inlets, which are adapted on the experimental data at the measurement plane $z = 3\,\mathrm{mm}$. The peak value of the axial velocity component at the air inlet is around $18\,\mathrm{m/s}$, that of the azimuthal component around $13\,\mathrm{m/s}$. The peak value of the gas phase velocity at the mixture inlet is around $12\,\mathrm{m/s}$ in axial direction for the non-swirling pipe flow. As discretisation schemes, those given in Appendix A.5.1 have been used. The WALE model (Nicoud and Ducros, 1999) was used to close the gas phase subgrid turbulent stresses (Eqn. 3.8). The same is true for all other turbulent simulations presented in this work.

7.1.2 Results

The history of the simulation results is as follows, both for the polydisperse and the monodisperse simulation. The first second in physical time, only the single phase flow was simulated. The following two seconds, the dispersed phase flow developed and the time average was evaluated over another two seconds of physical time. The plots in Fig. 7.5 show instantaneous contours of the gas and dispersed phase velocity magnitude, the arithmetic mean diameter D_{10}, as well as the moments $M^{(3)}$, $M^{(1)}$ and $M^{(0)}$. Although the turbulent gas phase shows small flow struc-

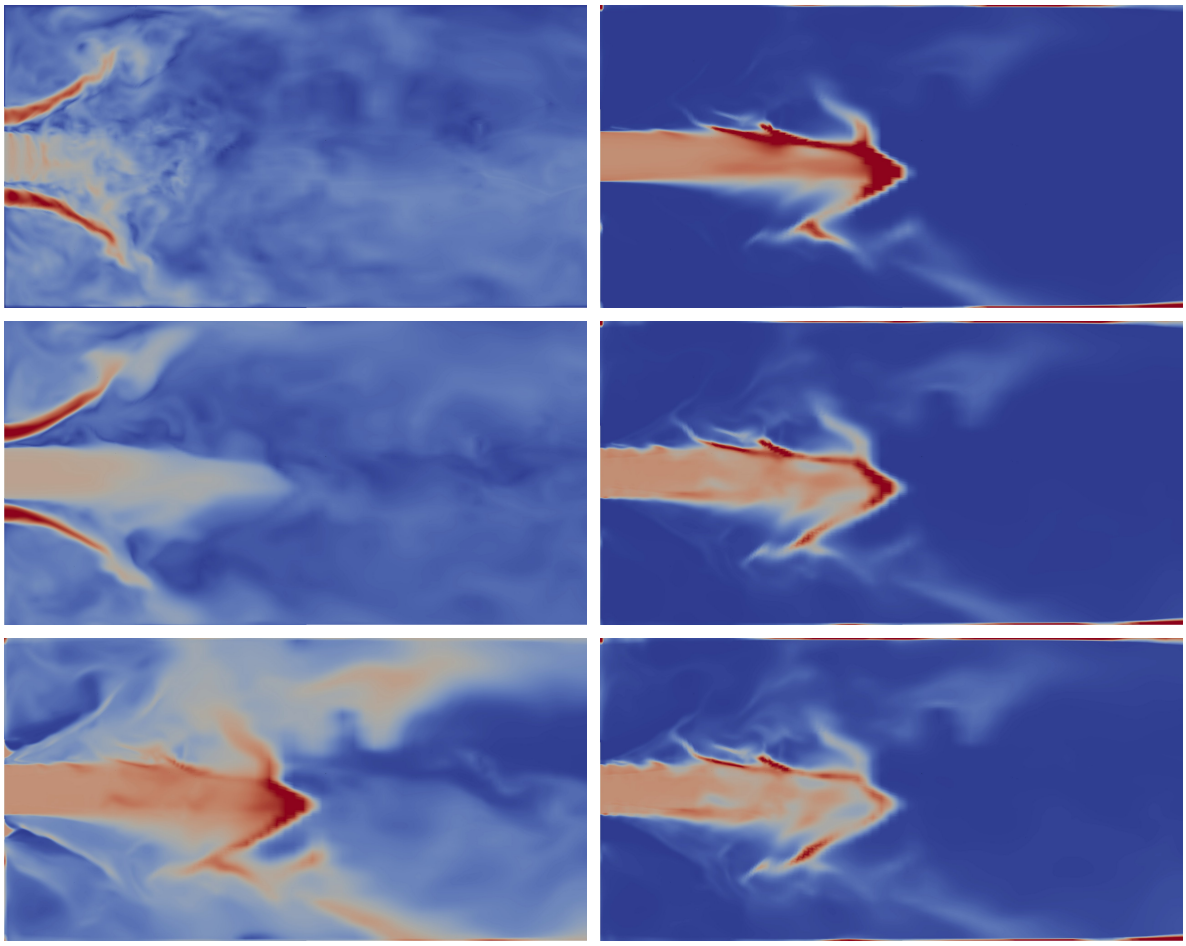

Figure 7.5: Instantaneous contour plots of **Left** $\mathbf{u}$ $(0 - 25\,\mathrm{m/s})$, $\mathbf{u}^{(3)}$ $(0 - 22\,\mathrm{m/s})$ and D_{10} $(0 - 70\,\mu\mathrm{m})$ **Right** $M^{(3)}$, $M^{(1)}$, $M^{(0)}$. The maximum value of the moment plots is 1.5x the inlet value.

tures and turbulent eddies, the mass averaged dispersed phase velocity implies only large flow scales due to the inert motion of the large particles, which characterise this quantity. The mass averaged particle velocity follows the swirling air outwards, but effectively filters out small turbulent structures. Furthermore, it becomes clear at this specific point (as discussed in Section 6.1.1), that $\mathbf{u}^{(3)}$ is in general different from the gas phase velocity even for the case of vanishing particle number density, which is the case in the coaxial air flow.

The mean diameter D_{10} increases with increasing penetration depth into the recirculation zone. This is physical, because smaller droplets are decelerated much faster than the large droplets and are not present anymore in the size distribution downstream. D_{10} abruptly tends towards zero after a certain distance downstream. This is where the largest droplets are finally stopped and accumulated by the reversed gas flow. This fact is confirmed by the moment fields shown on the right hand column in Fig. 7.5. Additionally, they indicate that the very small droplets are able to follow the swirling flow outwards around the recirculation zone much better than the larger droplets. Hence, $M^{(0)}$ is the moment which is dispersed the most in radial direction.

A quantitative comparison with the experimental data is given for the gas and dispersed phase mean and rms velocity components in Fig. 7.6 and Fig. 7.7 (axial), Fig. 7.8 and Fig. 7.9 (radial) and Fig. 7.10 and Fig. 7.11 (azimuthal). All velocity components match with the experimental data well, with only small differences between the mono- and the polydisperse simulation. These differences concentrate on the centre line jet into the recirculation zone. In the polydisperse simulation, the axial velocity of the particles remain higher for a longer time compared to the monodisperse simulation. This is due to the larger droplets considered in the polydisperse simulation, whose velocity is altered slower by the gas phase due to their large relaxation times, whereas in the monodisperse simulation only mid-sized particles of $D_{10} = 45\mu m$ are considered.

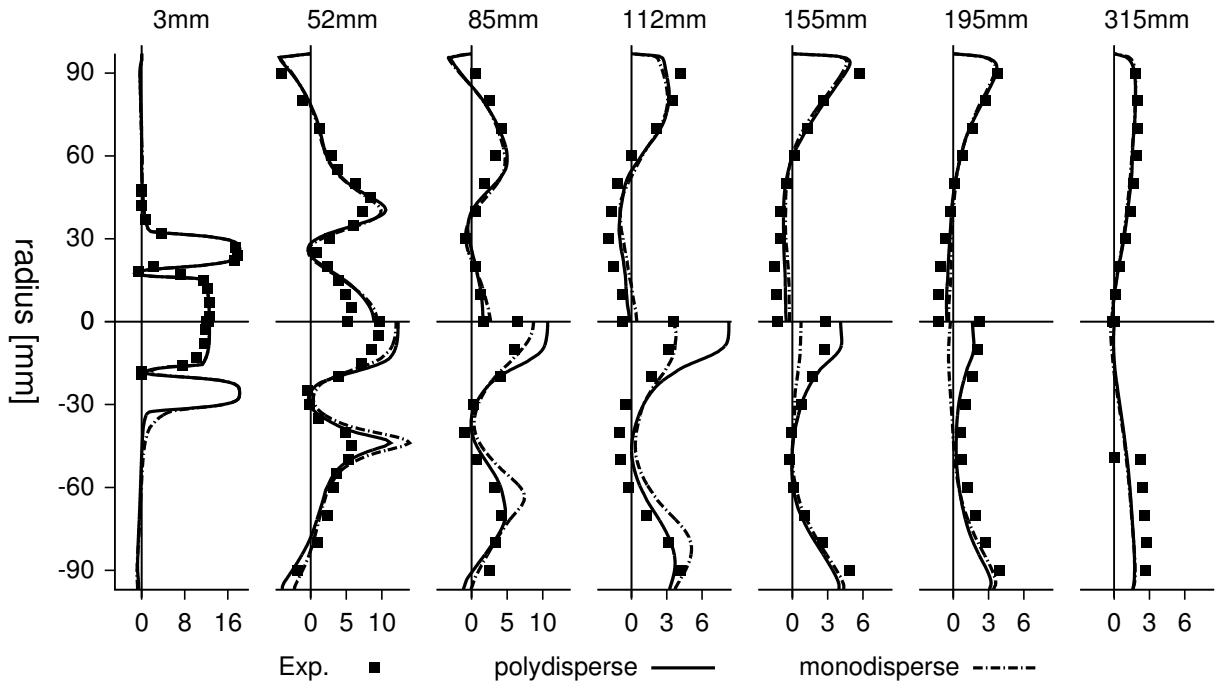

Figure 7.6: Axial mean velocity component (m/s) of **Upper Half** gas phase **Lower Half** dispersed phase.

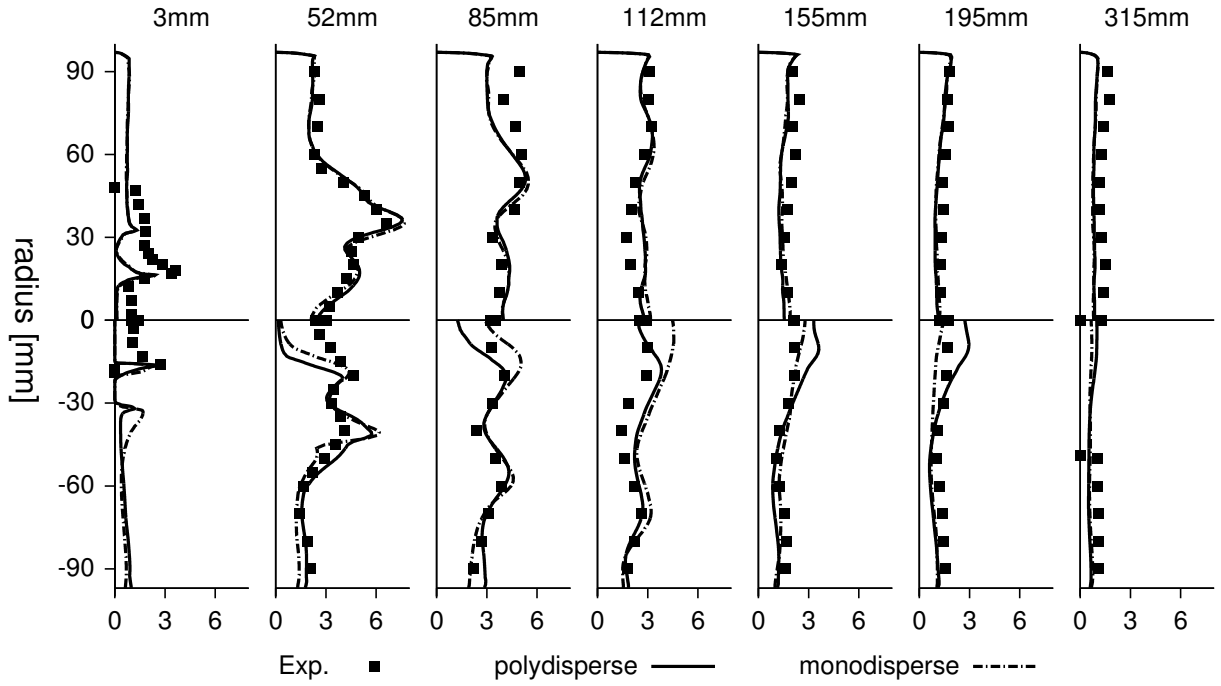

Figure 7.7: Axial RMS velocity component (m/s) of **Upper Half** gas phase **Lower Half** dispersed phase.

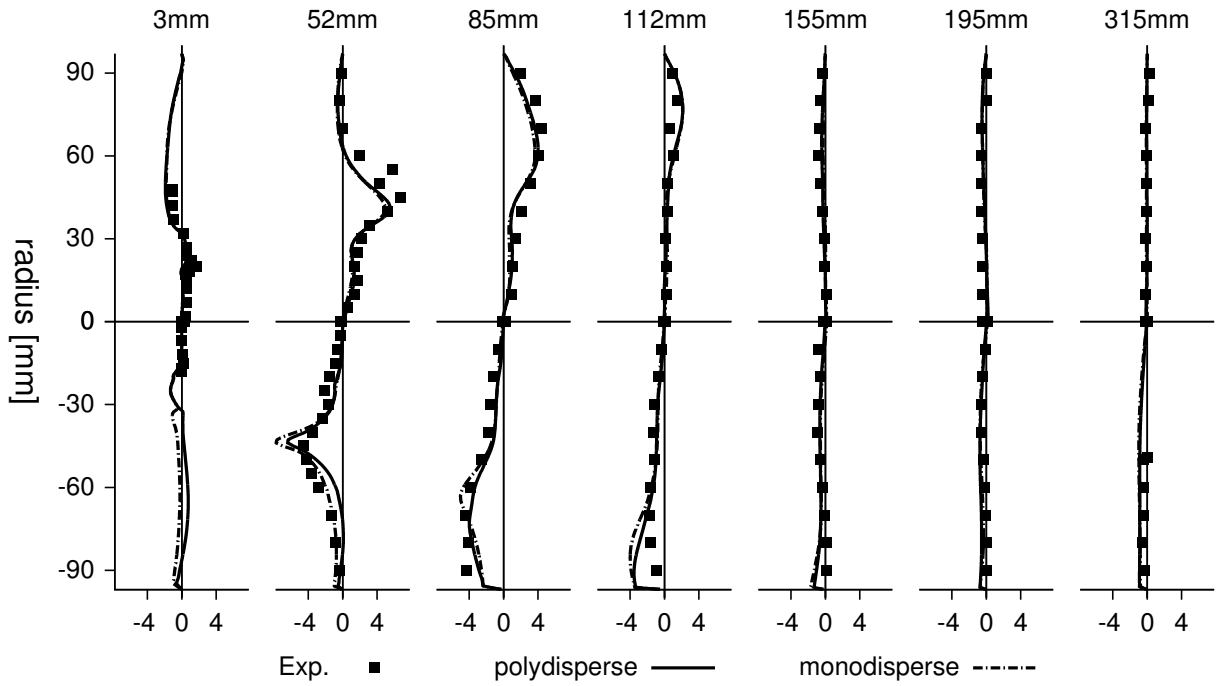

Figure 7.8: Radial mean velocity component (m/s) of **Upper Half** gas phase **Lower Half** dispersed phase.

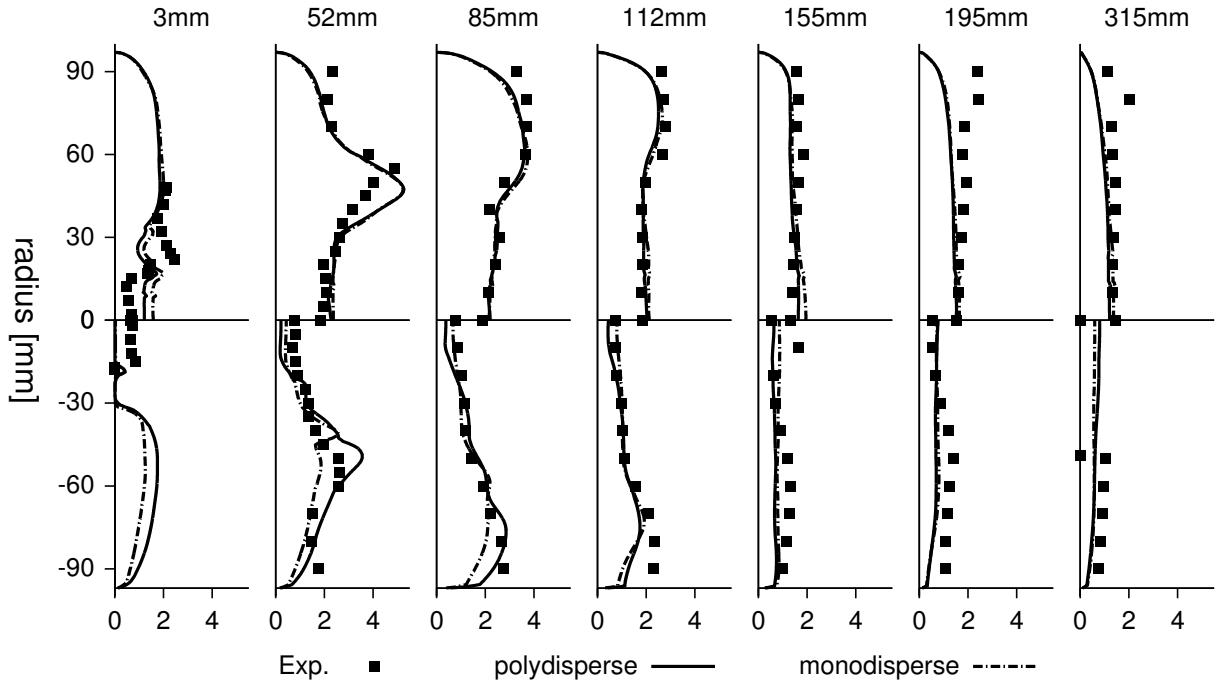

Figure 7.9: Radial RMS velocity component (m/s) of **Upper Half** gas phase **Lower Half** dispersed phase.

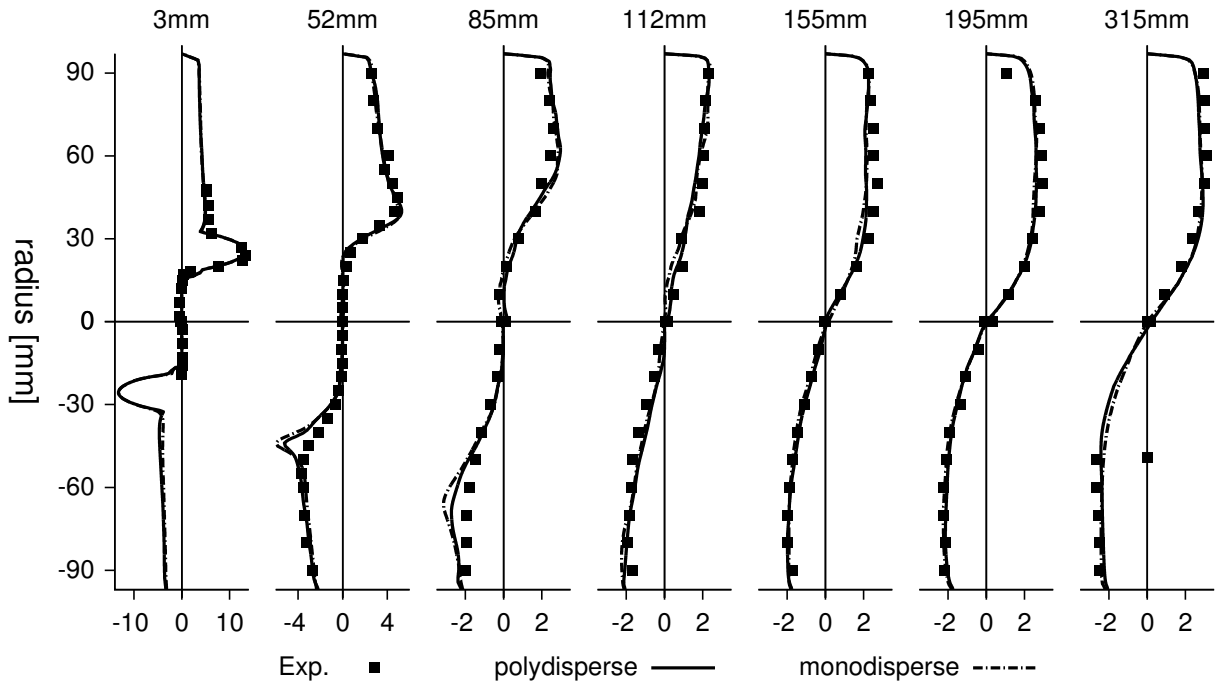

Figure 7.10: Tangential mean velocity component (m/s) of **Upper Half** gas phase **Lower Half** dispersed phase.

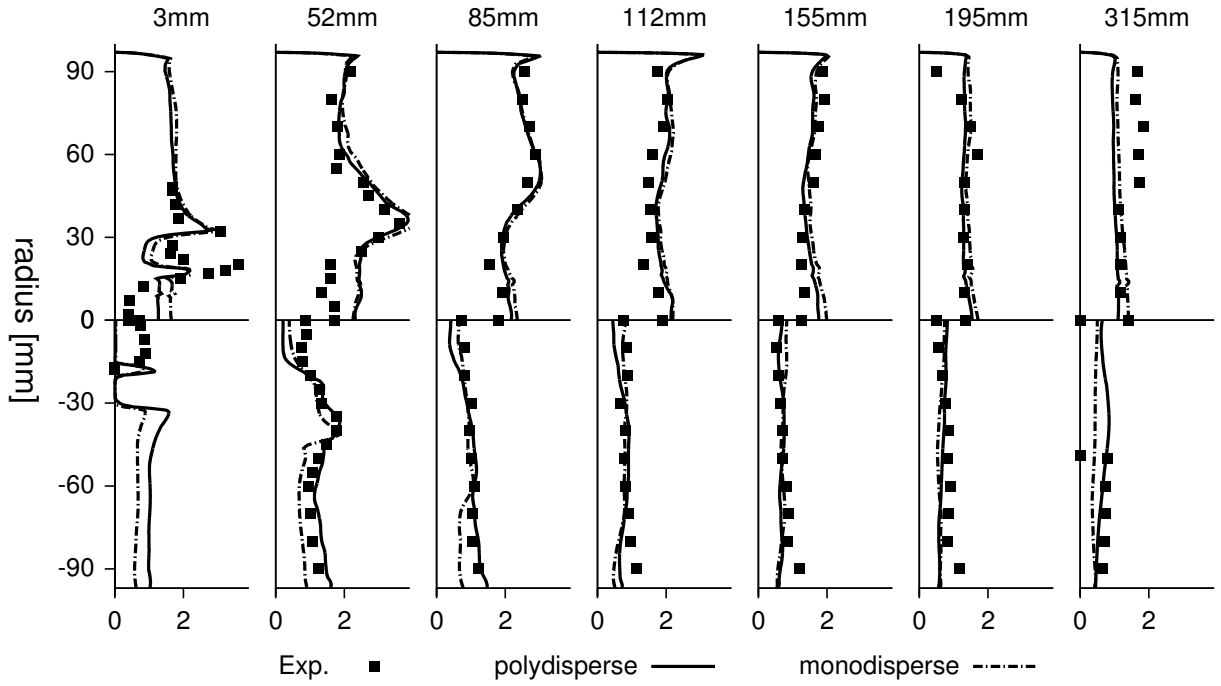

Figure 7.11: Tangential RMS velocity component (m/s) of **Upper Half** gas phase **Lower Half** dispersed phase.

The same fact is confirmed by the particle mass flux as shown in Fig. 7.12, which remains higher and is still present more downstream into the recirculation zone. Here, the larger amount of mass is imported by the large particles. Comparing the axial velocity and the particle mass flux with the experimental data, however, neither the monodisperse nor the polydisperse results match more exclusively to the experimental data. This might be due to the approximation made for the moment transport velocity within the term to the power of 0.687 in the drag formulation (Eqn. 4.42). Beside that, it could be influenced by any other neglected sub-grid scale velocity correlation as well, which is difficult to quantify as long as no comparison is made with results considering those terms. Although pro-

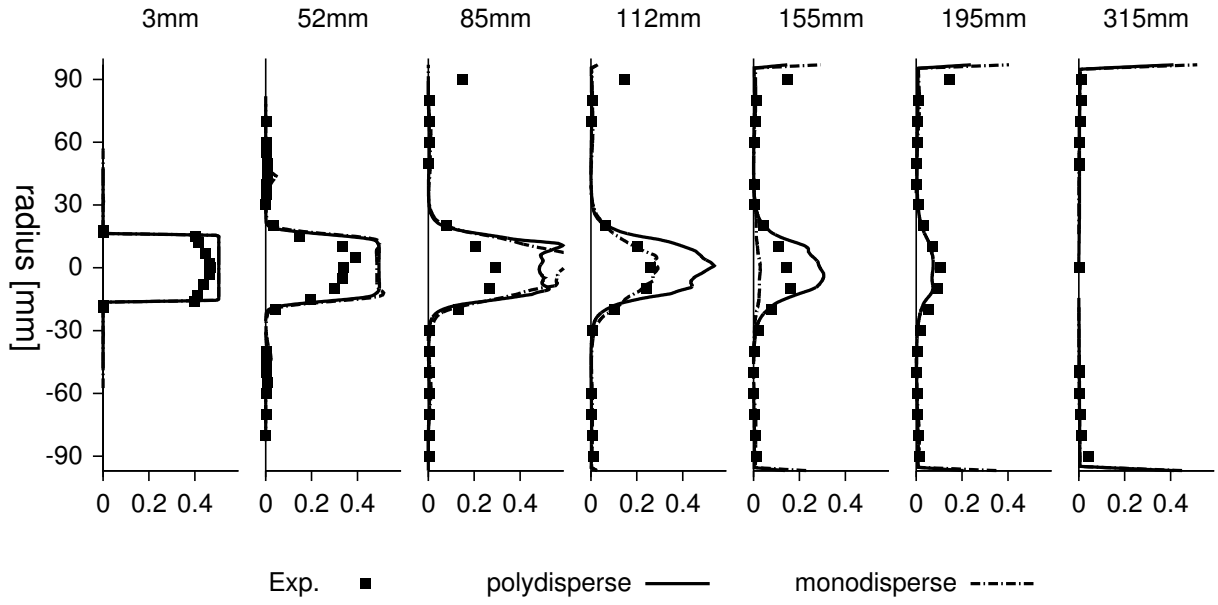

Figure 7.12: Dispersed phase mass flux ($\mathrm{kg}/(\mathrm{m}^2\,\mathrm{s})$).

ducing very similar overall results, only the polydisperse model is able to determine the spatial and temporal development of the mean diameters. Figure 7.13 shows this development with a good agreement between the polydisperse results and the experimental data. The increase of D_{10} along the centre line is captured very well, although the sudden drop is not captured by the mean values (in contrast to the instantaneous values, as visible in the instantaneous contour plot in Fig. 7.5, left column at the bottom). The deviations at the outer radii up to 112 mm are of no

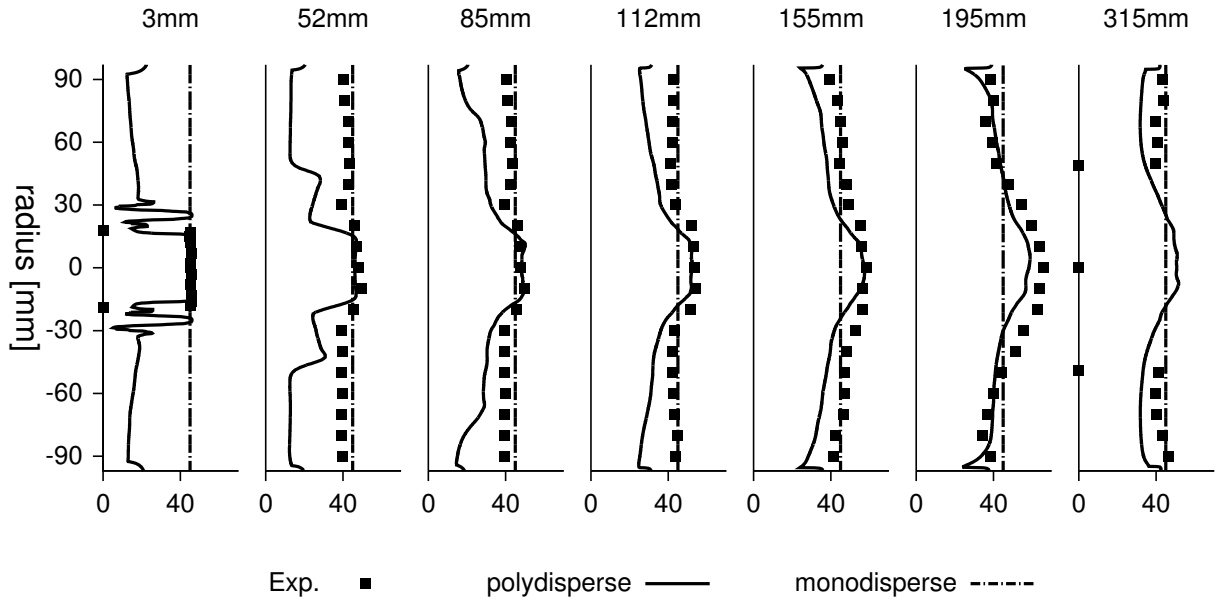

Figure 7.13: Arithmetic mean diameter D_{10} (µm).

importance, since in these regions only very few droplets are present.

Summarising, the small differences between the mono- and the polydisperse results suggest, that the effort using the moments model in this specific test case would not be justified in a real application, but its applicability is nicely verified from an academic point of view.

7.2 Sydney Spray Burner - Evaporation Only Case

Validation of the effects of size dependent vaporisation rates has different requirements on the configuration. To decouple polydisperse motion dynamics from polydisperse vaporisation, a configuration has been chosen which does not explicitly feature significantly different behaviour of monodisperse compared to polydisperse particle motion. With that, the focus is solely on the size conditioned vaporisation rate. The spray jet data base by the group of Prof. Masri at the University of Sydney (Chen et al., 2002, 2006) meets this criterion inasmuch as the particle motion is mainly along the jet axis with similar velocities as the gas phase. Polydis-

perse motion occurs mainly perpendicular to the axis through turbulent dispersion, which is, however, of minor relevance in this case. Hence, the vaporisation degree along the jet axis depends mainly on the particle size but only marginally on the spatial distribution of the particles. A monodisperse particle population is expected to have a faster overall mass loss along the jet axis compared to a polydisperse description, where the droplets which are larger than the mean droplet size are expected to have a longer lifetime. This results in a higher amount of liquid mass at positions downstream compared to the monodisperse case, where all liquid is already vaporised. Hence, the droplet mass flux is expected to have a significantly different development comparing mono- and polydisperse simulation results. Besides that, the development of the moments and mean diameters of the polydisperse vaporisation simulation are of specific interest in this case, on the one hand in order to validate the accurate description of the decrease of those values due to the vaporisation, and on the other hand, because they can be calculated from the measured quantities and explicitely validated.

7.2.1 Setup

The experimental setup of this configuration is as follows. A droplet laden air jet is surrounded by a slow air coflow. The droplets are injected by a pressurised injector 200 mm upstream of the jet exit. This ensures a homogeneous distribution of the droplets over the jet cross section but implies prevaporisation automatically. In the case considered, SP3, the mass fraction of the acetone vapour reaches a value of $Y_v = 0.017$ at the jet exit, which means, that 60 % of the droplet mass is vaporised at this position. A sketch of the simulation domain considered is given in Fig. 7.14, where the measurement plane positions are indicated for which the numerical results have been compared to the experimental data. For detailed information about the arrangement of the spray nozzle and the air flow supply which creates the jet, the reader is referred to the original publications.

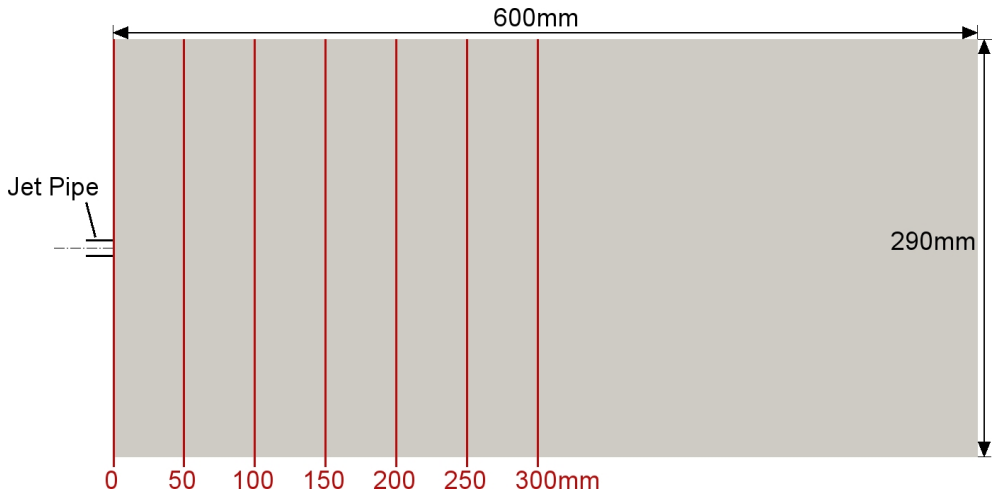

Figure 7.14: Geometrical dimensions and arrangement of the numerical domain representing the experimental configuration of Chen et al. (2002, 2006).

For this case, the dependence of the moments model on the mesh resolution has been investigated. A first mesh has been created with a more or less typical resolution compared to the other cases shown in this work with 1 015 137 computational volumes. Based on this mesh, hereafter called *coarse mesh*, a *fine mesh* has been created, not by homogeneous refinement but mainly local refinement of the jet region including the shear layer. Nevertheless, the remaining domain experienced a moderate refinement as well. This fine mesh consists of 2 515 559 computational volumes and is shown in Fig. 7.15. The comparison of the results of both meshes and their agreement with the experimental data is given later on. The flow properties and inlet values are listed in Tab. 7.1. The numerical boundary conditions are similar to those given in Tab. 6.1.

Table 7.1: Particle phase and gas phase conditions at the jet exit plane x=0 (inlet of the simulation domain).

ρ_p	$= 785\,\mathrm{kg/m^3}$	$M^{(0)}$	$= 6.790\,609 \times 10^{9}\,\mathrm{m^{-3}}$	Re	$= 20\,700$
$\dot{m}_c$	$= 150\,\mathrm{g/min}$	$M^{(1)}$	$= 1.654\,046 \times 10^{5}\,\mathrm{m^{-2}}$	ν_c	$= 1.74\,\mathrm{m^2/s}$
$\dot{m}_v$	$= 27.1\,\mathrm{g/min}$	$M^{(2)}$	$= 5.470\,325\,\mathrm{m^{-1}}$	ρ_c	$= 1.43\,\mathrm{kg/m^3}$
$\dot{m}_p$	$= 17.9\,\mathrm{g/min}$	$M^{(3)}$	$= 2.269\,83 \times 10^{-4}$	T_c	$= -5.5\,^{\circ}\mathrm{C}$

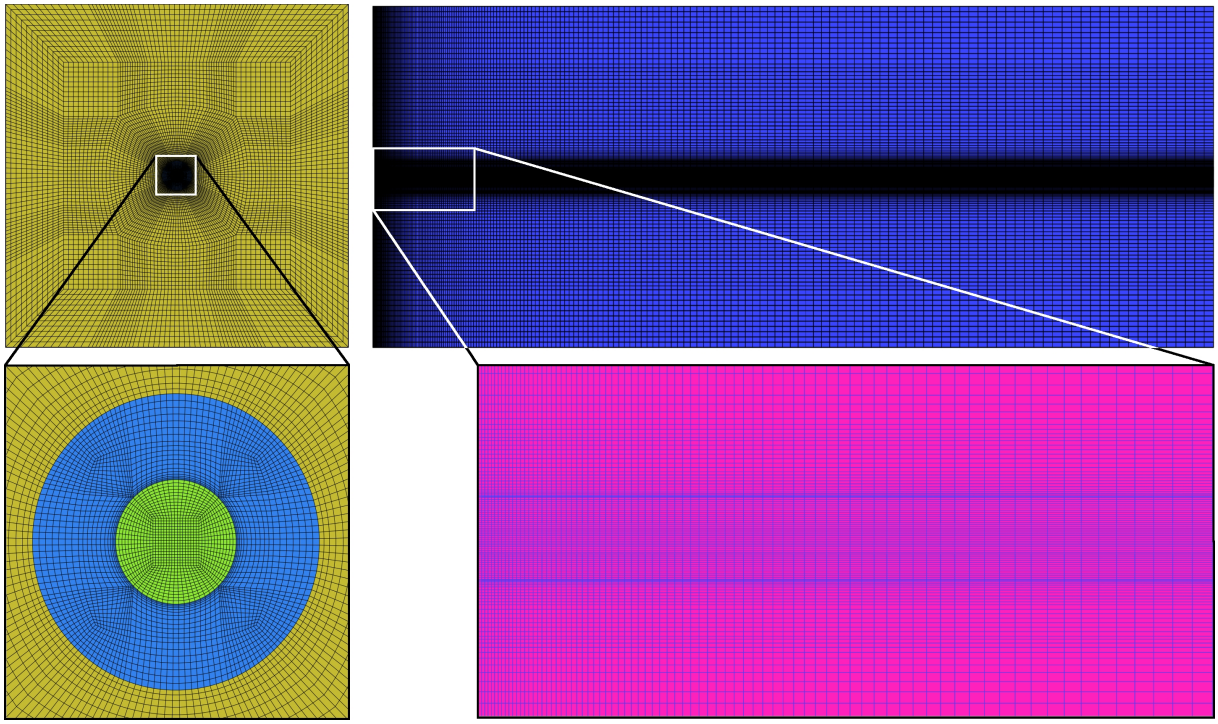

Figure 7.15: The numerical mesh created with ANSYS Icem CFD. Fine mesh with 2 515 559 cells.

7.2.2 Results

The geometry of the configuration is particularly simple. The development of the flow depends solely on the previously developed pipe turbulence and the shear layer interaction with the coflow. Hence, it is evident to either capture the upstream development of the jet before its exit or to apply an appropriate turbulent inlet condition. The former approach proved to be inapplicable with the current setup due to problems with acoustic fields numerically developing, which could not properly handled so far. The latter approach has been followed by using a turbulence generator boundary condition (Klein et al., 2004, di Mare et al., 2006) imposed onto the mean velocity profile of the pipe flow. The resulting development of the jet is shown in Fig. 7.16, with the gaseous velocity magnitude at the top and the dispersed phase velocity at the bottom, i.e. the third moment transport velocity $\mathbf{u}^{(3)}$. No turbulent fluctuations have been imposed on the mass weighted dispersed phase ve-

locity. Particularly inert to the gas phase turbulent fluctuations, the dispersed phase velocity develops straight into the domain but is affected by the large scale dispersion perpendicular to the jet axis. Comparing numerical and experimental results, the velocity fields (Figures 7.17 to 7.20) do not represent correctly the turbulent dynamics of the jet. While the axial mean component (Fig. 7.17) is slightly underestimated for the gas phase and over-predicted for the dispersed phase velocity, the radial mean and root-mean-square (rms) components reveal serious deficiencies in the pipe turbulence defined and imposed by the inlet condition (Figures 7.19 and 7.20). Issues with the mesh resolution can be excluded, because the results show effectively no difference between the coarse and the fine mesh. Hence, the correct consideration of the pipe turbulence and boundary layer development seems to be the most important issue to achieve better agreement.

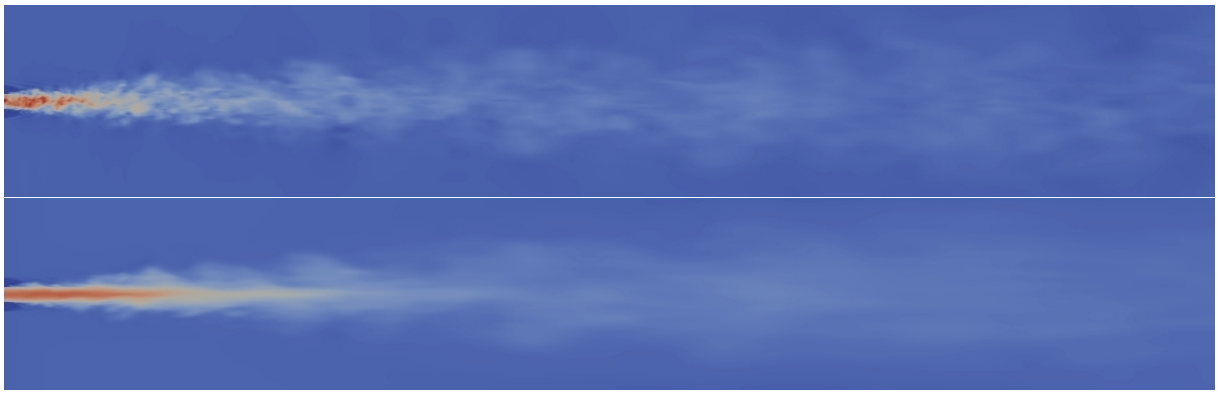

Figure 7.16: Instantaneous contour plots of **Top u** $(0 - 40\,\mathrm{m/s})$ and **Bottom** $\mathbf{u}^{(3)}$ $(0 - 30\,\mathrm{m/s})$, fine mesh, polydisperse.

Besides this issue, a significant difference can be already seen between the polydisperse and the monodisperse simulation results. The axial velocity component of the monodispersed particles adapts much faster to the gaseous one, since it is based on the drag force of droplets having a uniform size locally, i.e. the mean diameter D_{32}. Since the particle relaxation time of particles with diameter D_{32} is smaller than $\boldsymbol{\tau}^{(3)}$, they are decelerated faster. Additionally, the monodispersed droplets adapt faster to the gas phase turbulent velocity fluctuations, which result in rms com-

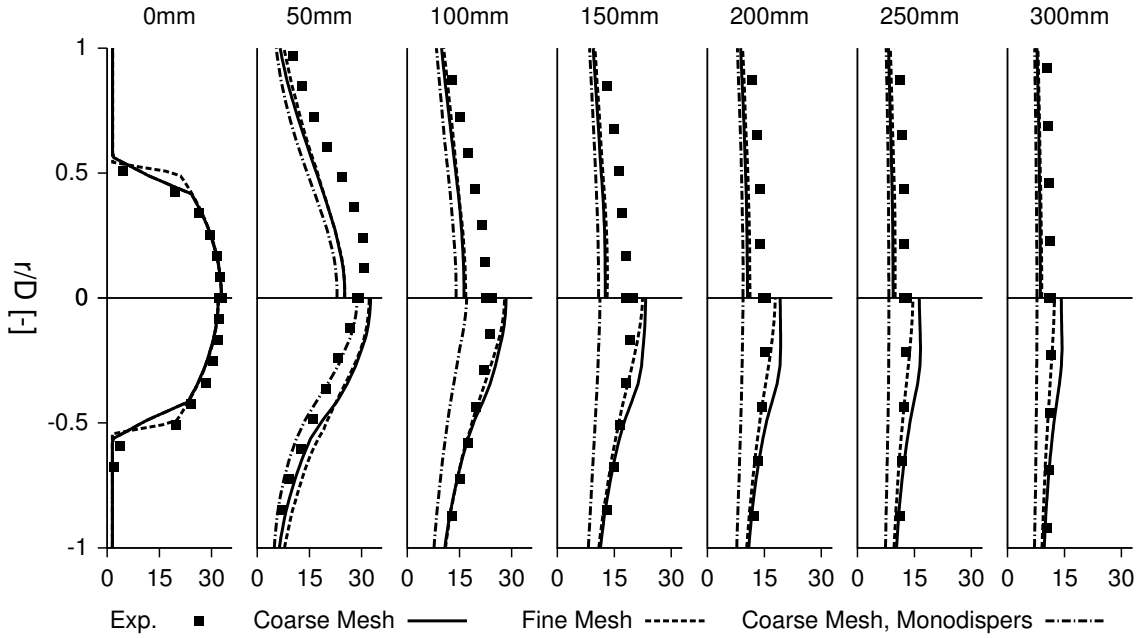

Figure 7.17: Axial mean velocity component (m/s) of **Upper Half** gas phase **Lower Half** dispersed phase.

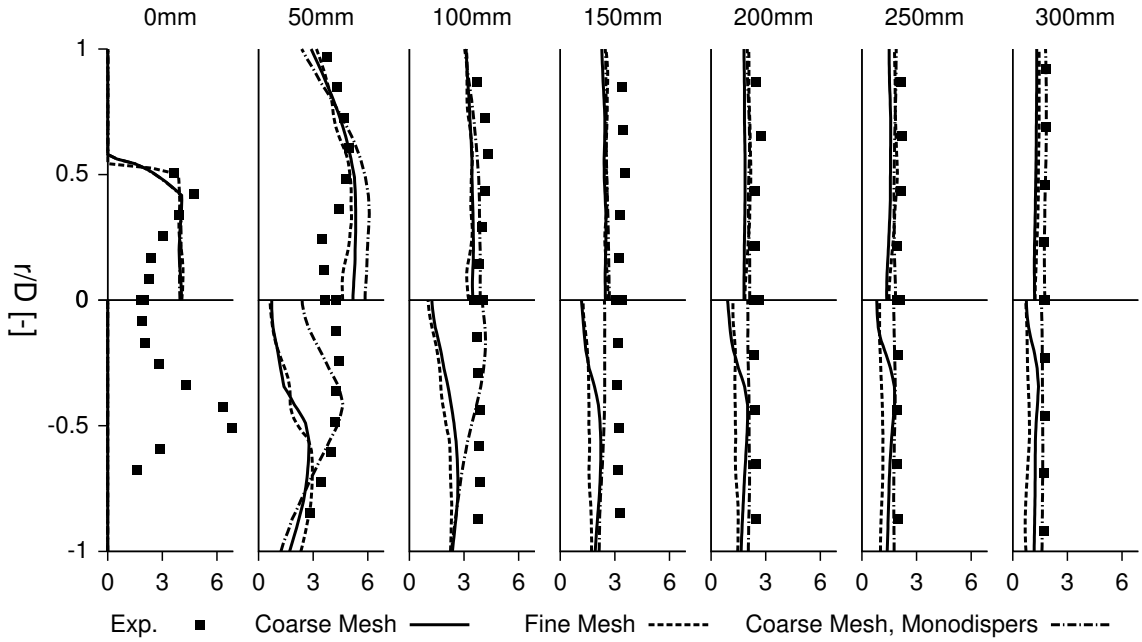

Figure 7.18: Axial RMS velocity component (m/s) of **Upper Half** gas phase **Lower Half** dispersed phase.

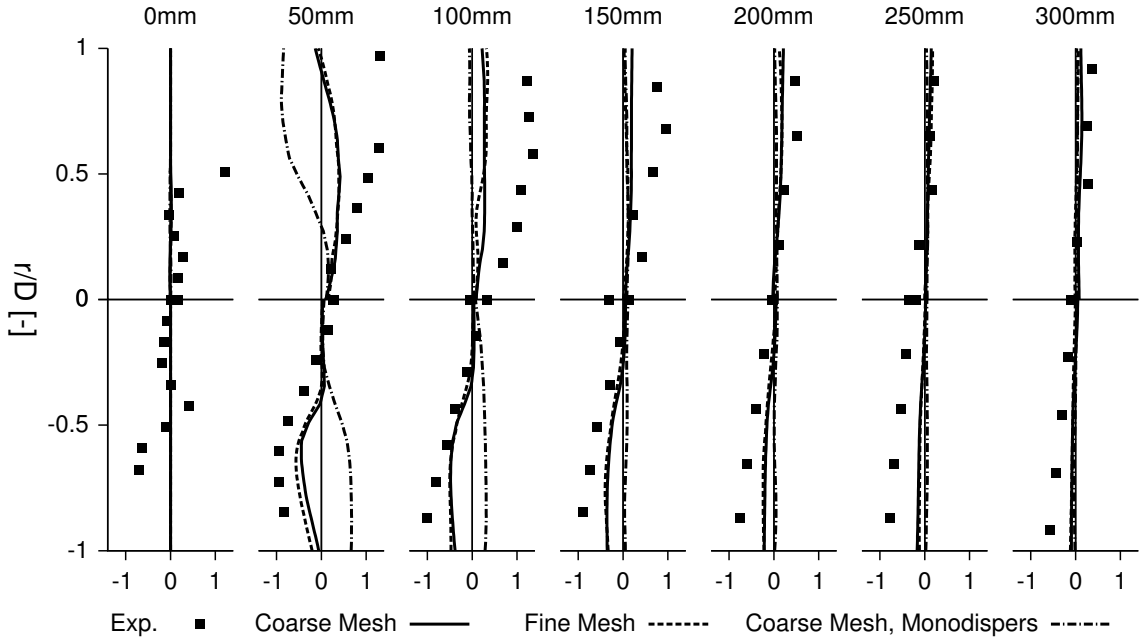

Figure 7.19: Radial mean velocity component (m/s) of **Upper Half** gas phase **Lower Half** dispersed phase.

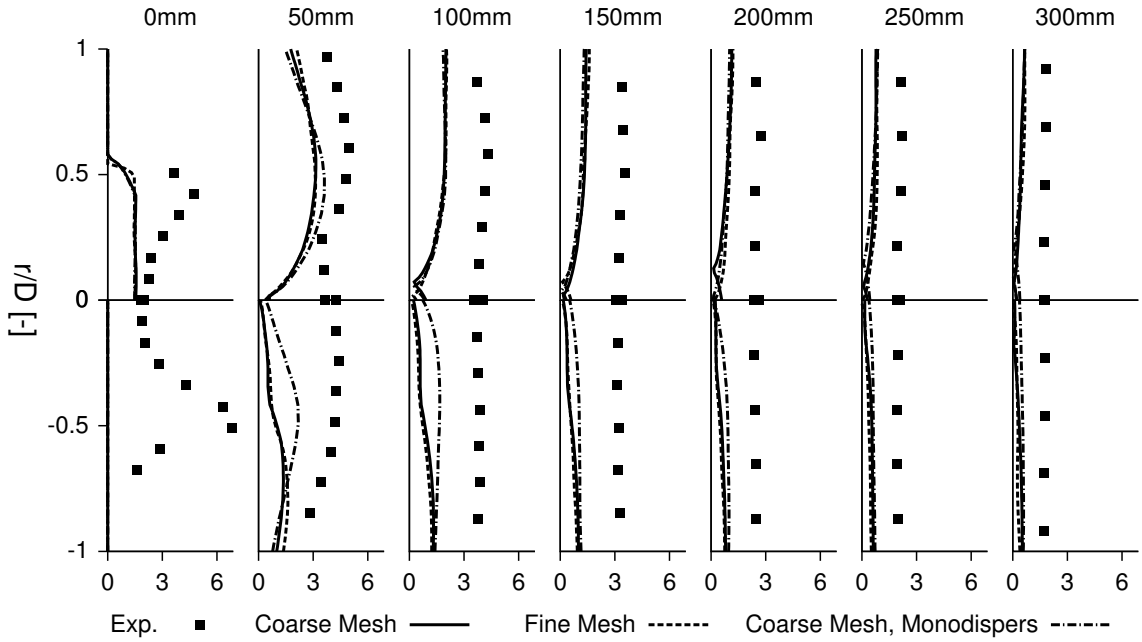

Figure 7.20: Radial RMS velocity component (m/s) of **Upper Half** gas phase **Lower Half** dispersed phase.

ponents closer to the gas phase ones compared to those of the polydisperse description. Rather curious is the significantly different dynamic of the radial velocity component, which is of reversed mean direction throughout the jet penetration. It is not clear how it does correlate with the different treatment of the particle size distribution.

As stated before, the droplets are prevaporised when entering the simulation domain, which results in an acetone vapour mass fraction of $Y_v = 0.017$ at the jet exit plane. Due to further vaporisation, Y_v continues to increase locally, but mixes with the air coflow. This results in a frayed appearance of the vapour mass fraction field (Fig. 7.21). The mass vaporisation rate is the largest at the entrance and does decrease with increasing penetration due to the decreasing droplet mass fraction, although some warmer air of the coflow contributes to an increased heat transfer into the droplets.

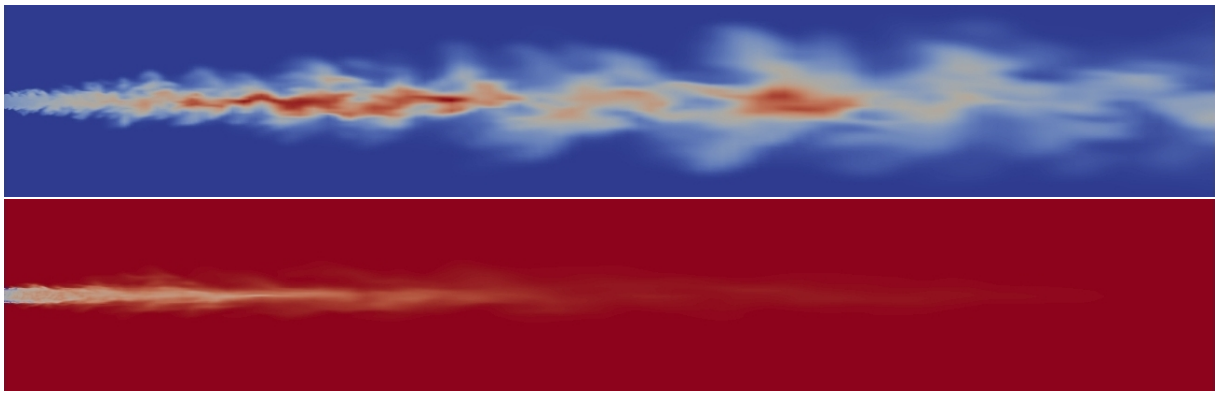

Figure 7.21: Instantaneous contour plots of **Top** Y_v $(0 - 0.032)$ and **Bottom** mass exchange rate $\Gamma_{M^{(3)}}$ $(0 - 15\,\mathrm{kg}/(\mathrm{m}^3\,\mathrm{s}))$, fine mesh, polydisperse.

In Fig. 7.22 the qualitative development of the moments $M^{(3)}$ to $M^{(0)}$ is shown, where the field of $M^{(3)}$ is effectively identical with that of α_d. All moments decrease with increasing distance to the injection, however, each moment with a different relative rate, i.e. the smaller the order of the moment the faster the descrease towards zero. This relies mainly on the effect of the polydisperse evaporation. Since the diameter of small droplets decreases faster than that of large droplets for a given

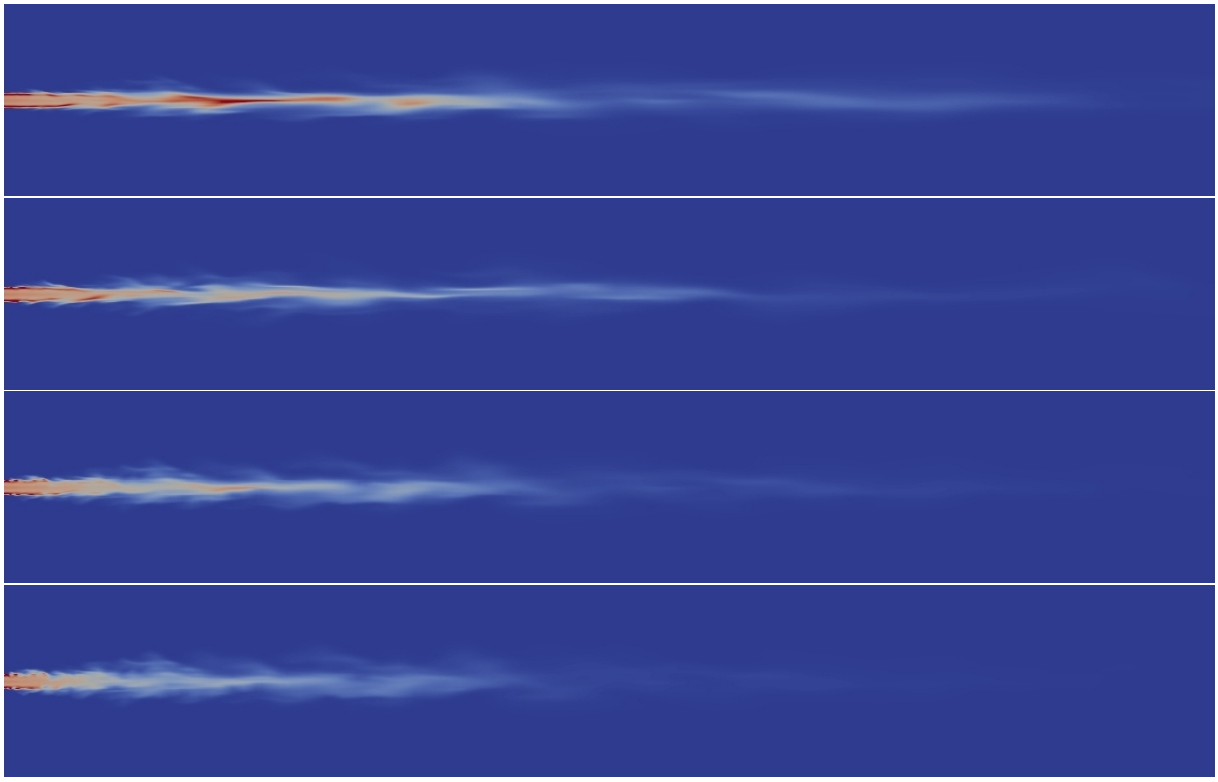

Figure 7.22: Instantaneous contour plots of **From top to bottom** $M^{(3)}$ to $M^{(0)}$, fine mesh, polydisperse. Maximum values are 1.5x the inlet values.

mass vaporisation rate, the droplet population looses the small droplets faster than the large droplets. Hence, polydispersed vaporisation does not mean that the NDF remains unchanged and moves only towards smaller diameters, but is stretched in size space, the stronger the smaller D is. Therefore, according to the characteristics of the moments, the moments of low order, which represent the dynamics of the small droplets, decrease faster than the higher order moments. The $M^{(0)}$ field is an a posteriori calculated quantity, because of the problem of finding an adequate sink term due to evaporation for this specific moment (see Section 4.4.3). Hence, only the moments $M^{(1)}$ to $M^{(3)}$ are transported in the underlying simulation. With that, the reduction of the number density can be achieved, otherwise it would remain constant[1], which is nonphysical.

[1] despite rarefaction and turbulent dispersion effects

Another effect contributes to the development of the moment fields, which is due to the inertia of the droplets: the smaller the order of the moment becomes, the stronger is the radial dispersion and the overall adaption to the gas phase velocity field.

Qualitative comparison of the moment fields with those calculated from the measured mean diameters are given in Figures 7.23 to 7.26. The "experimental" moments are calculated from the experimental mean diameters via relation 4.9, whereas the "numerical" mean diameters are calculated a posteriori from the averaged moment fields. Hence, the graphs of the moments and those of the mean diameters in Figures 7.27, 7.28 and 7.29 contain the same data/information. In the monodisperse simulation the local value of the particle diameter, i.e. D_{32}, can be calculated by the ratio of the transported moments $M^{(3)}$ and $M^{(2)}$ with help of the same relation 4.9. Transporting both moments with the same dispersed phase velocity and using vaporisation rates based on D_{32}, this approach is equivalent to considering a transport equation for D_{32} directly.

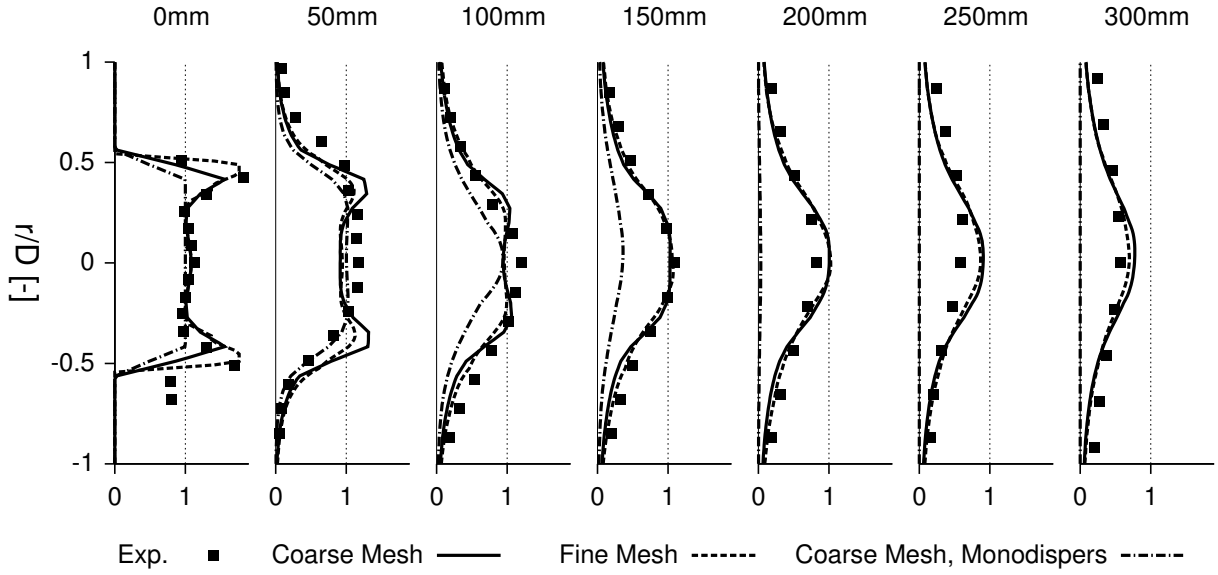

Figure 7.23: Dispersed phase volume fraction α_d, $M^{(3)}$ (-).

The vaporisation rate calculated on the fine mesh is in good agreement with the experimental data. The results obtained from the coarse mesh show larger deviations, which can be contributed to the discretisation

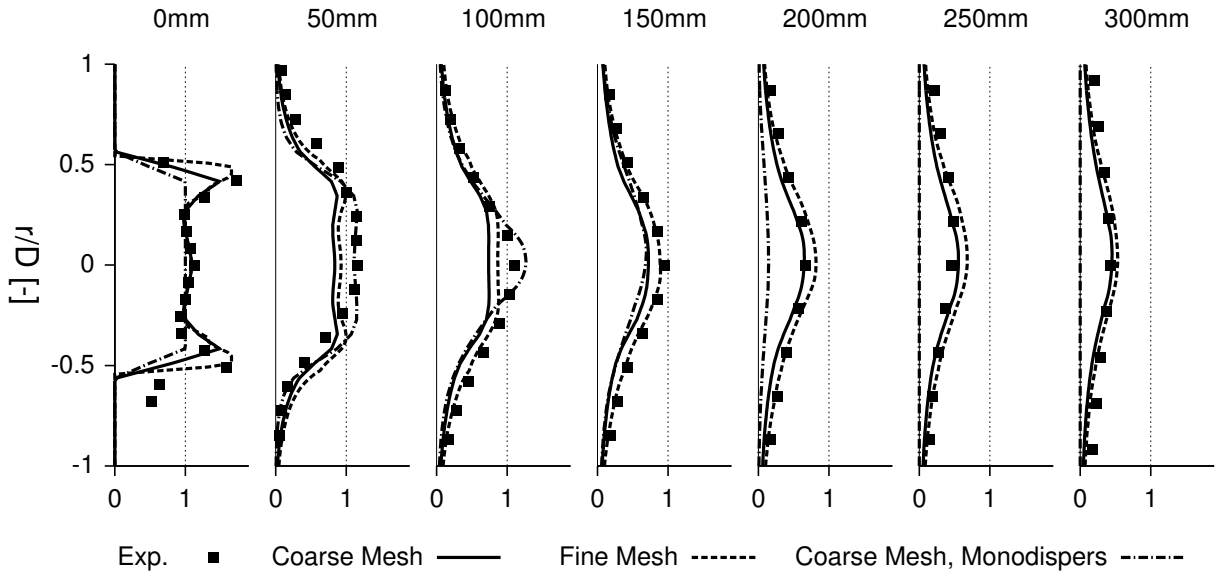

Figure 7.24: Second moment $M^{(2)}$ $(1/\mathrm{m})$.

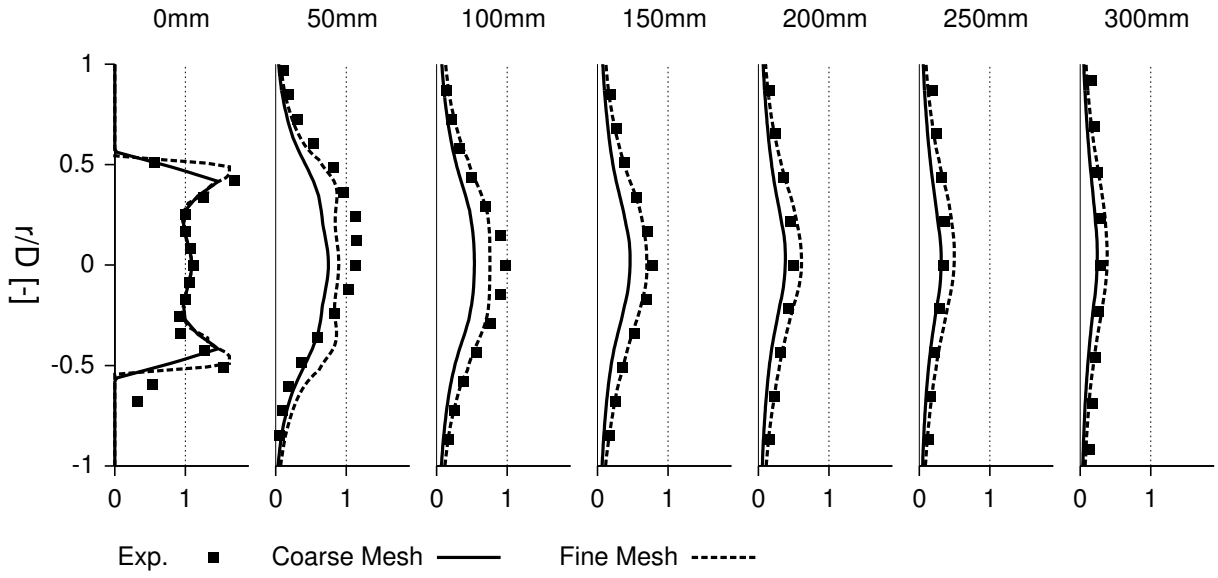

Figure 7.25: First moment $M^{(1)}$ $(1/\mathrm{m}^2)$.

scheme used for the moments, which is simple upwind discretisation. Obviously, the mesh resolution of the coarse mesh is not fine enough for the use of upwind discretisation. Nevertheless, no valid higher order discretisation scheme has been implemented, making the use of the fine mesh inevitable in this case (see also Section 6.3). Significantly differ-

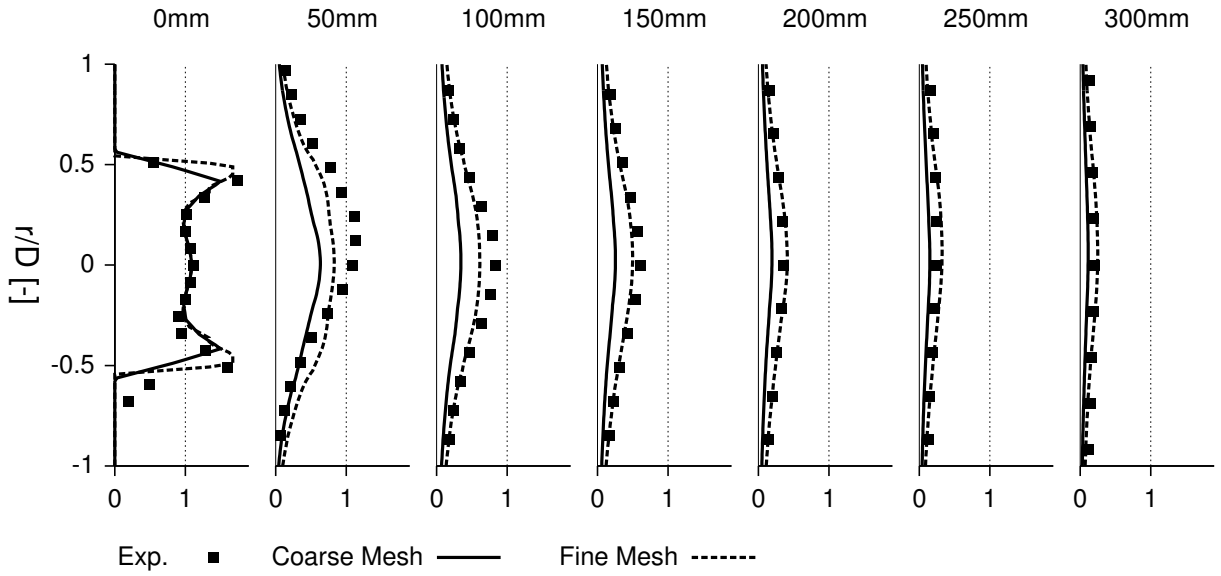

Figure 7.26: Zeroth moment $M^{(0)}$ $(1/\mathrm{m}^3)$.

ent are the moments $M^{(3)}$ and $M^{(2)}$ from the monodisperse calculation. There, the liquid mass is almost vaporised at $x = 200\,\mathrm{mm}$ and completely vanished from $x = 250\,\mathrm{mm}$ onwards. Since droplets larger than D_{32} are not considered, the characteristic of the D-square law yields a faster overall vaporisation of the liquid mass. The peaks at the inlet are not considered in the monodisperse simulation, but this does not contribute to the matter as a comparison for the polydisperse simulation has revealed (which is not presented here). Considering the graphs especially for $M^{(3)}$, a deficit in radial dispersion of the liquid mass can be observed. This can result from three reasons. First, the deviations in gas phase turbulence, especially the radial mean and rms component, second, droplet-turbulence and droplet-wall interaction within the pipe, which result in particle velocities not exclusively coaxial with the jet axis, and third, neither any sub-grid scale droplet-turbulence interaction nor the random uncorrelated motion of the droplets has been considered. Keeping in mind these simplifications, steps to improve the results must tackle these issues of the modelling. For the small droplets ($M^{(0)}$), the mean dispersion is represented more accurate, which is rather the result of the diffusive numerics than an evidence of the validity of neglecting corresponding sub-grid scale closure.

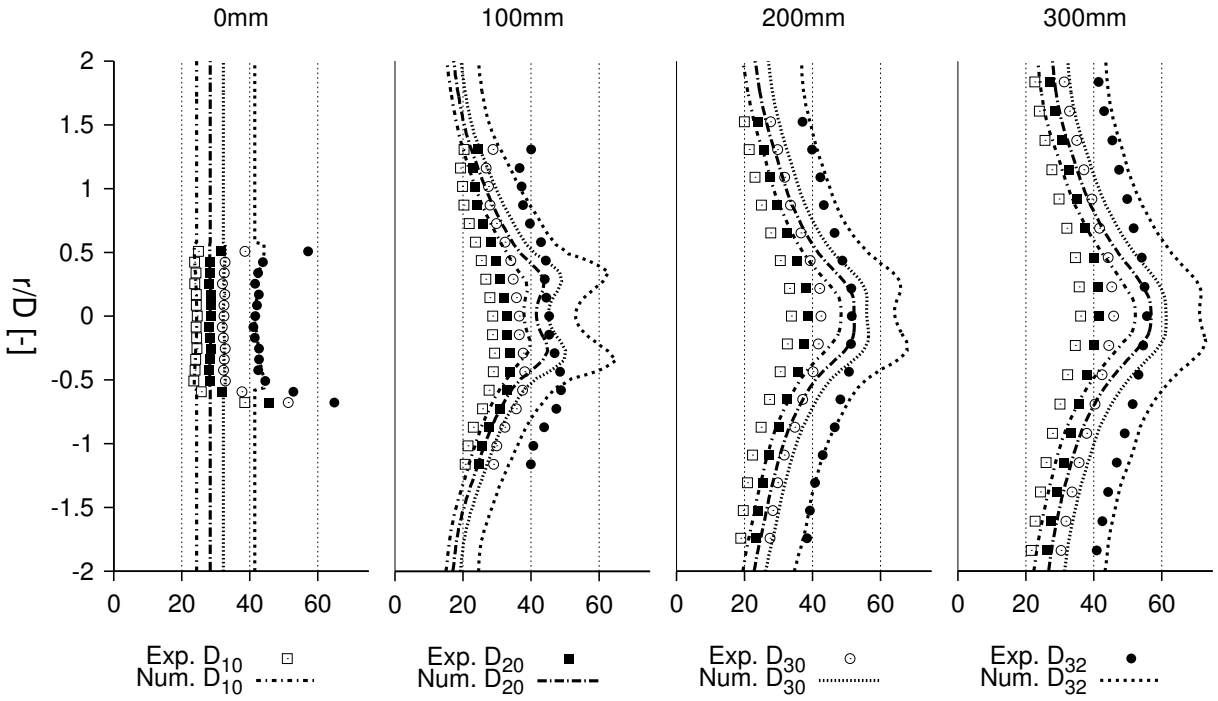

Figure 7.27: Mean diameters D_{10}, D_{20}, D_{30}, D_{32} (µm), coarse mesh.

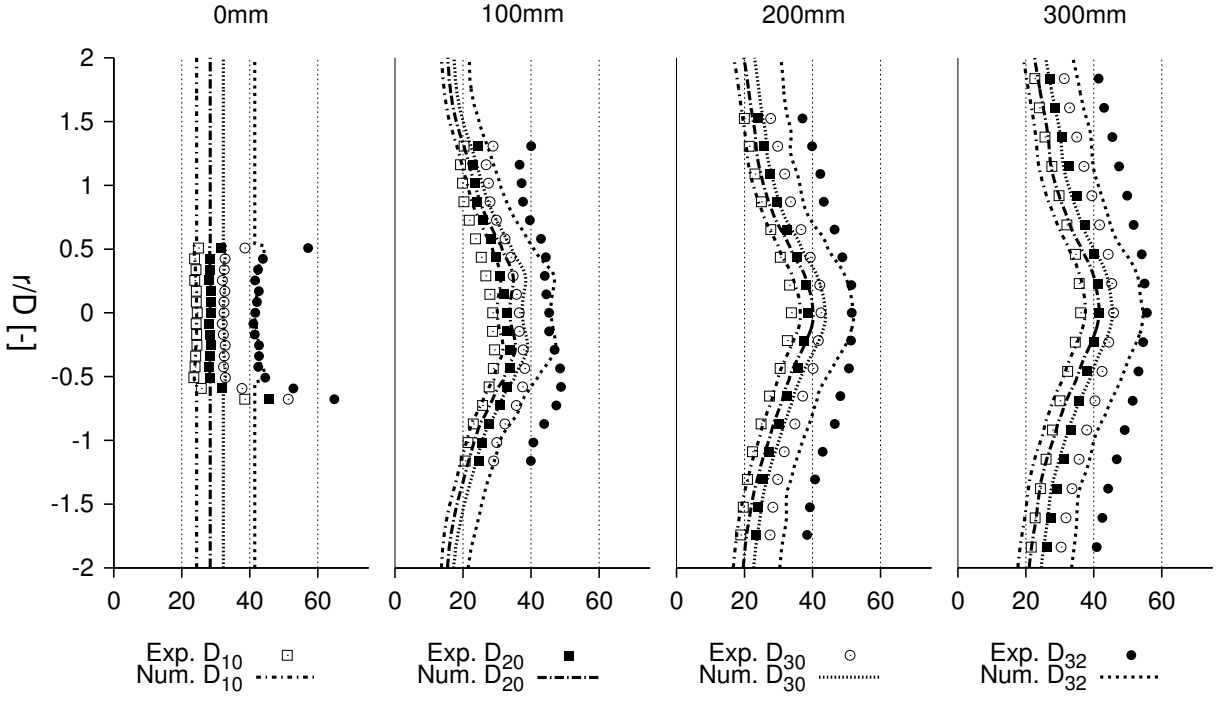

Figure 7.28: Mean diameters D_{10}, D_{20}, D_{30}, D_{32} (µm), fine mesh.

The mean diameters D_{10}, D_{20}, D_{30} and D_{32} confirm these issues very well. The fine mesh delivers the better results as it is obvious comparing Fig. 7.27 to Fig. 7.28. Furthermore, the vaporisation rate of the monodisperse calculation is much too fast compared to the one predicted by the polydisperse description. The Sauter mean diameter D_{32} decreases much faster in the monodisperse case (Fig. 7.29) than in the polydisperse counterpart. The artificial increase at $x = 250\,\text{mm}$ and $x = 300\,\text{mm}$ is due to vanishing moments, which underlie bounding routines and is not physical.

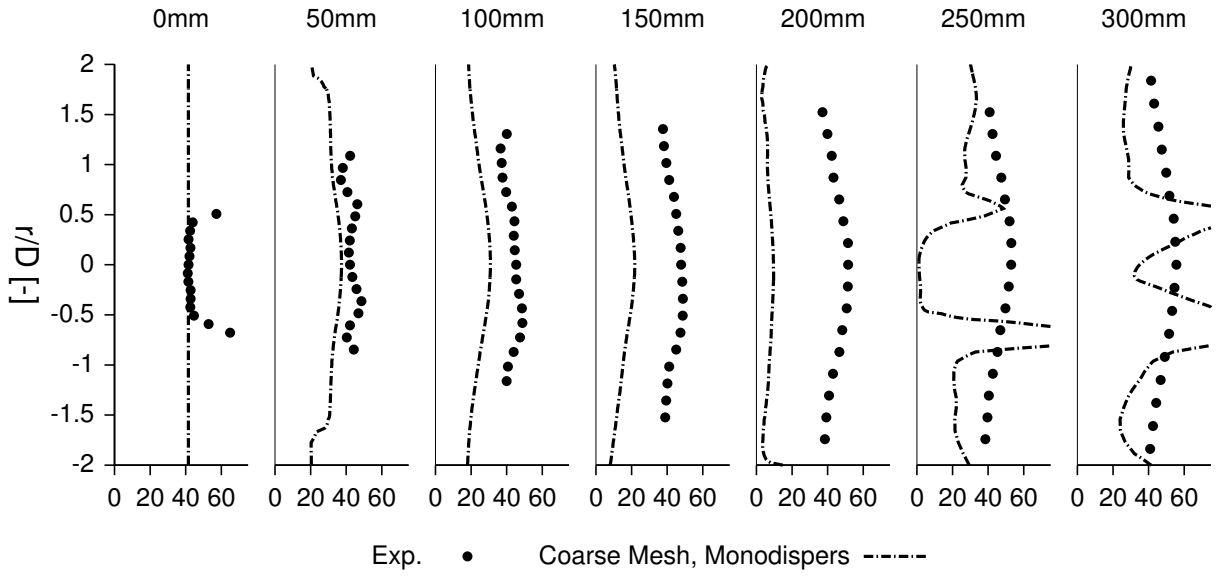

Figure 7.29: Mean diameter D_{32} (µm) from the monodisperse simulation, coarse mesh.

7.3 NASA LDI Spray Burner

As described in Section 5.1, various types of liquid fuelled flames exist and are used in numerous technical applications. With the background of this project being positioned in the field of tool development for dry oil combustion in stationary gas turbines, an experimental setup has been chosen, which features some relevant aspects of such a spray flame. First, a typical configuration must be found, which injects swirled oxidising

air into a combustion chamber such that a flame stabilising recirculation zone is generated. Second, data must be available to be able to comprehensively validate the numerical results. The configuration finally used is described next.

7.3.1 Experimental Setup

To investigate the Lean Direct Injection (LDI) combustor concept for gas turbines operating at high temperatures and pressures, the group of Jeng (Cai et al., 2005, Fu et al., 2005a,b) developed a model combustor for spray combustion. It consists of a simple coaxial swirler, a pressure swirl atomiser to generate the kerosene spray, a converging-diverging venturi and a square cross section combustor housing, which is open to the atmosphere. The spray nozzle is placed close to the narrowest cross section of the venturi. Both the venturi and the hollow spray have a cone angle of 90°. The venturi causes the swirling flow to be attached to the walls when entering the chamber, which leads to a very large recirculation zone extended almost across the whole cross section. The geometrical dimensions and the arrangement are given in Fig. 7.30 and the location of the measurement planes in Fig. 7.31. The blue lines mark the measurement planes for the cold single phase data, the red lines have been additionally or alternatively used for the reacting case. Not every quantity has been measured, however, on each plane. The locations finally used are given above every graph in the figures shown later on. Further details on the detailed dimensions can be found in the original literature Cai et al. (2005). The spray quantities have been measured using the Phase Doppler Particle Analyser (PDPA) technique.

The simulation domain starts a short distance upstream of the swirler and ends beyond the combustor within the open environment to enable the interaction of the flow exiting the chamber with the quiescent surrounding. The geometrical dimensions of the experimental setup are not uniquely determined, i.e. the measures provided by the original authors are partially inconsistent or incomplete, the geometrical dimensions used

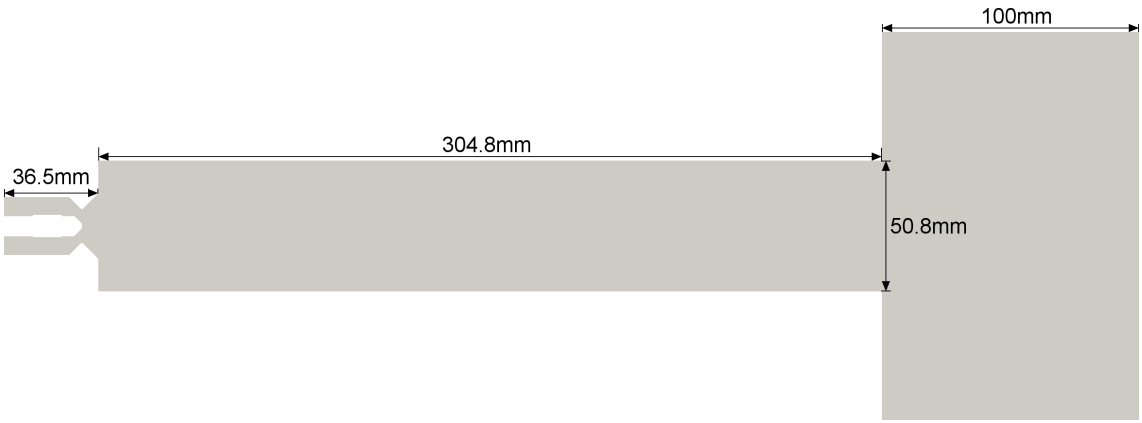

Figure 7.30: Geometrical dimensions of the LDI burner simulation domain.

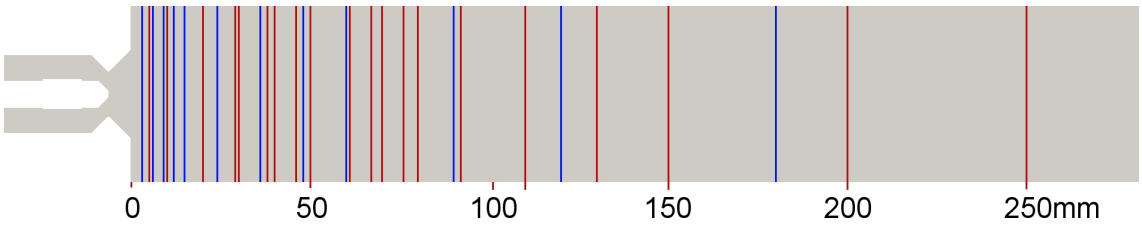

Figure 7.31: Measurement planes for cold case (blue) and additional/alternative ones for the reacting case (red).

in subsequent reciting literature are not consistent either. Therefore, the geometry used in the simulations is an individual compromise of what has been given in literature. Furthermore, the thickness of the swirler vanes has not been considered directly, but implicitly. In fact the vanes have a constant angle of 60° at the outer radius, where they are attached to the outer pipe, compared to the axial direction. For the simulation domain, the vane angle has been increased to an amount giving the same cross section area, which is approximately 65° with zero thickness of the vanes compared to 60° with thickness. The mesh arrangement and density can be seen in Fig. 7.32 for the interesting part of the domain. The red cells indicate the crossing lines of the vanes.

This experimental configuration has been used for validation of spray CFD solvers by several groups. Kirtaş et al. (2006) used the Euler-Lagrangian description for the spray with LES for the gas phase and a

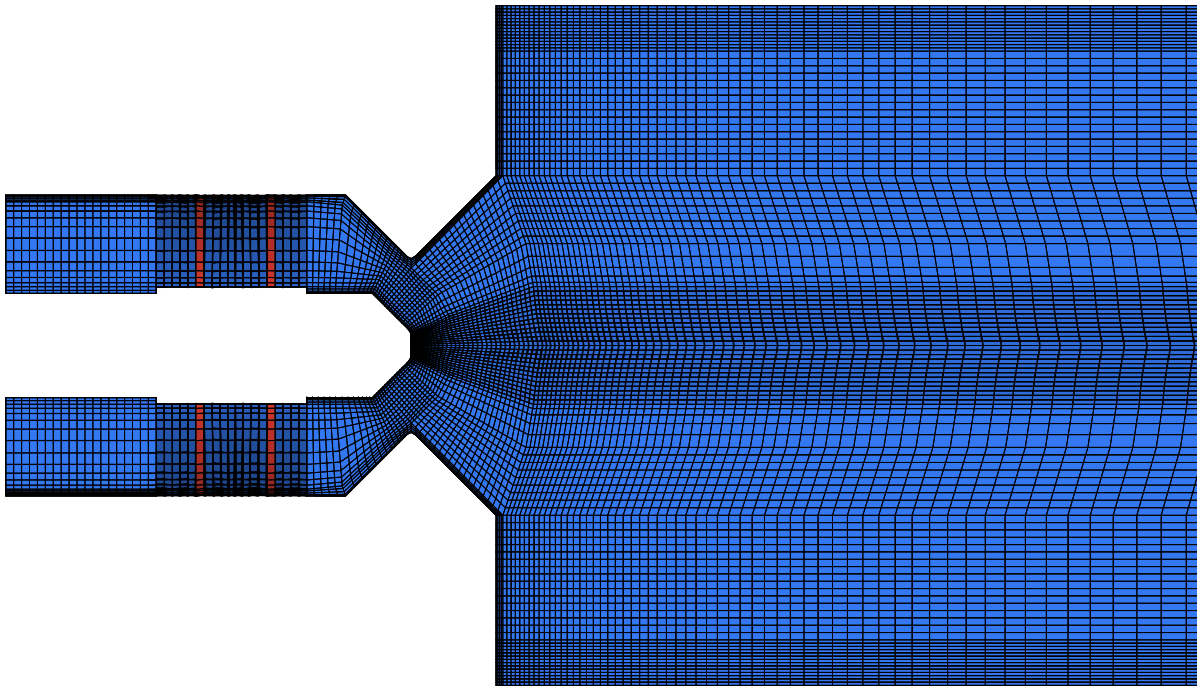

Figure 7.32: Part of the numerical mesh for the LDI burner. It consists of 734 187 computational cells.

sub-grid scale Eddy Break Up combustion model with three step chemistry. A similar modelling approach has been used by Patel and Menon (2008), however, using finite rate laminar chemistry. With a similar combustion model, Iannetti et al. (2008) investigated this setup using different turbulence models for the gas phase, i.e. RANS, Very Large Eddy Simulation and LES. Simulation results using a multi-regime flamelet model for the spray combustion and EL-LES have been presented also by Knudsen and Pitsch (2010). All of these publications made use of the Lagrangian description of the spray. Although varying in the grade of agreement between numerical and experimental data, these cases can be used as reference of what is possible using LES for that spray combustion setup.

7.3.2 Cold Gas Flow Validation

The purpose of the separate validation of the cold flow is two-fold. On the one hand, the accuracy of the solver setup (discretisation, sub-grid scale

models, mesh resolution) of calculating the isothermal flow field can be estimated, excluding influences of the additional physics and its modelling (spray interaction, combustion). On the other hand, the validity of the approximation of modelling the thickness of the vanes and the uncertainties in the geometrical dimensions can be verified. As shown in the following, they are acceptable for our purposes, considering two reasons. First, the aim of the presented results is to show in a first step the capability of the polydisperse spray model to simulate such a configuration with a reasonable computational cost. Second, the current LES simulation setup for the gas phase is rather basic compared to what is possible, i.e. it lacks of advanced LES features as high order discretisation, appropriate wall treatment, refined and adjusted inlet conditions for gas phase turbulence and spray, comprehensive mesh resolution study, etc.

Based on the available experimental data, the same operational point has been used for cold and reacting flow simulations, whose conditions for the gas phase are given in Tab. 7.2.

Table 7.2: Gas phase properties

Air mass flow	$0.0185\,\mathrm{lb/s} = 8.391\,46 \times 10^{-3}\,\mathrm{kg/s}$
Air temperature	$70°\mathrm{F} = 21.111\,°\mathrm{C}$
Static pressure at the outlet	$101\,325\,\mathrm{Pa}$

Figures 7.33 to 7.37 compare the numerical results for the mean and rms velocity components taken from the measurement planes at axial positions $z = 3, 6, 9, 15, 36, 60, 180\,\mathrm{mm}$ downstream of the coordinate origin. The coordinate origin coincide with the plane where the venturi ends and the squared housing starts, i.e. 6.35 mm downstream the nozzle. The additional axial positions $z = 12, 24, 48, 90, 120\,\mathrm{mm}$ does not provide further details of the development of the flow and are not shown here. Figures 7.33, 7.35 and 7.37 show the mean axial, radial and azimuthal velocity components, respectively, Figures 7.34, 7.36 and 7.38 the root mean square of each component. Measurements have been taken in both the $x - z$ and $y - z$ plane and are compared here to the corresponding values

from the simulation results.

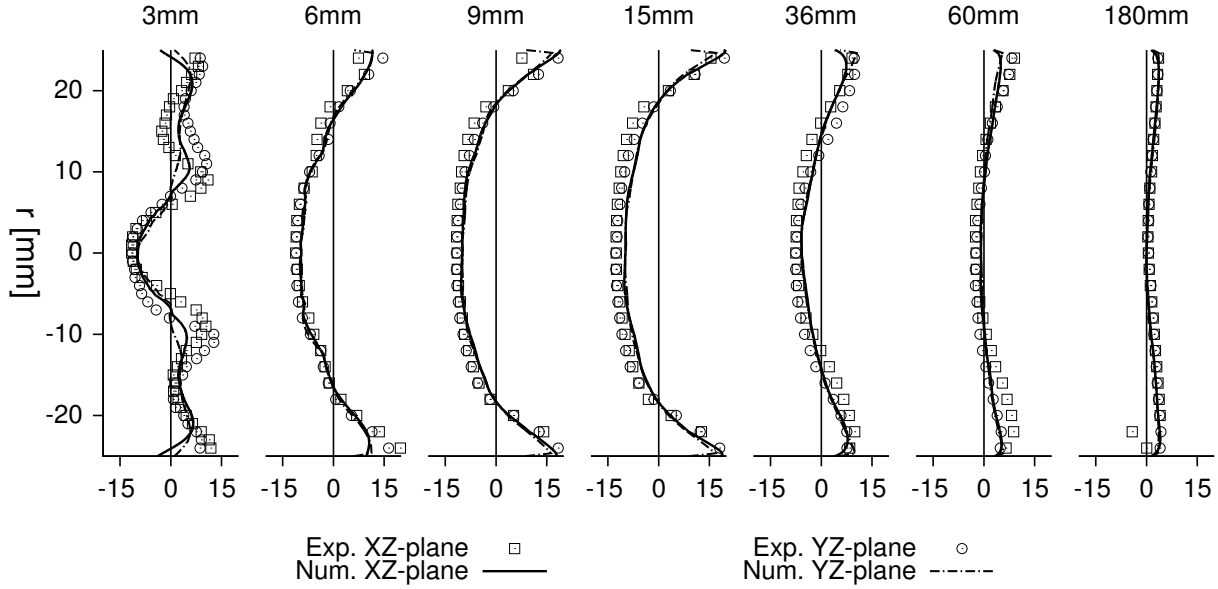

Figure 7.33: Non-reacting, cold air flow. Mean axial component of gas phase velocity ($1/m^2$).

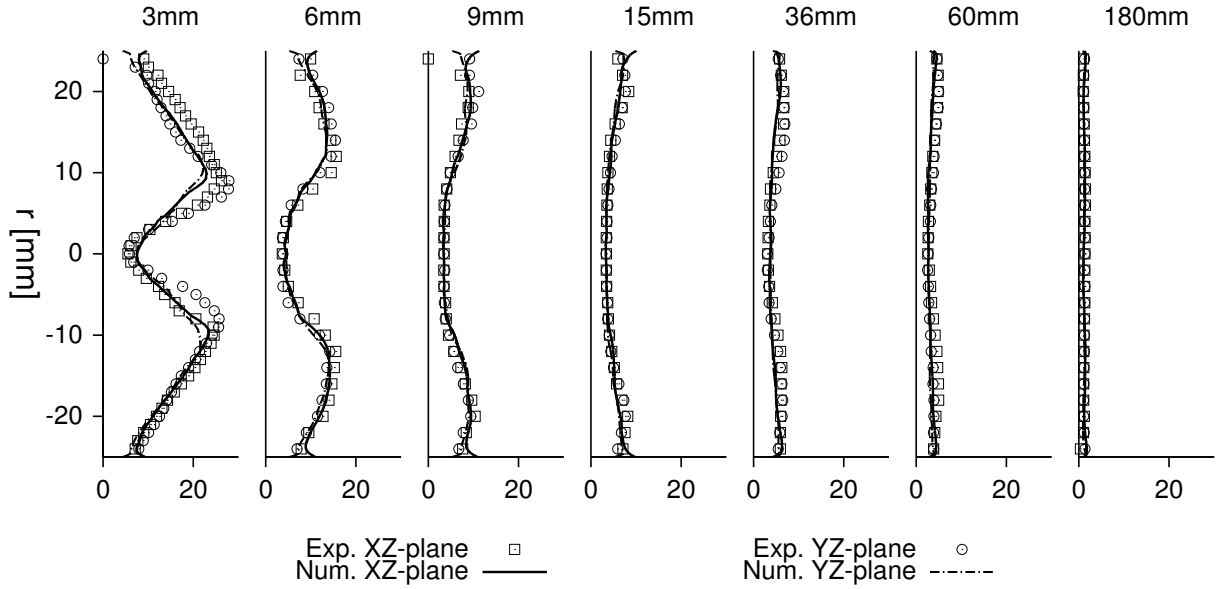

Figure 7.34: Non-reacting, cold air flow. RMS axial component of gas phase velocity ($1/m^2$).

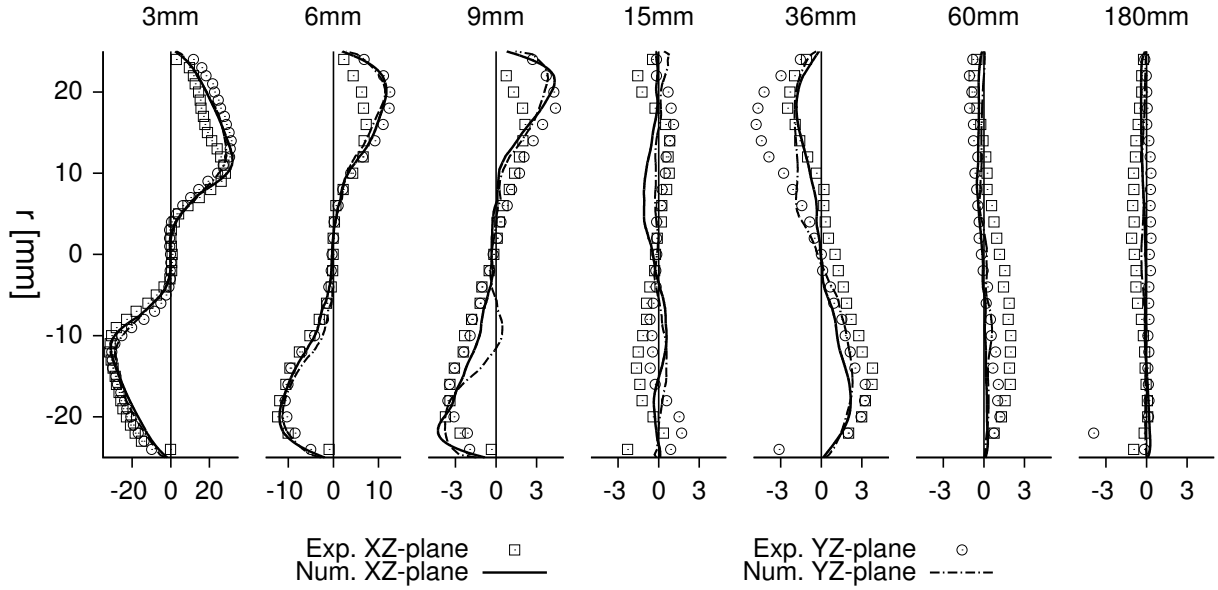

Figure 7.35: Non-reacting, cold air flow. Mean radial component of gas phase velocity ($1/m^2$).

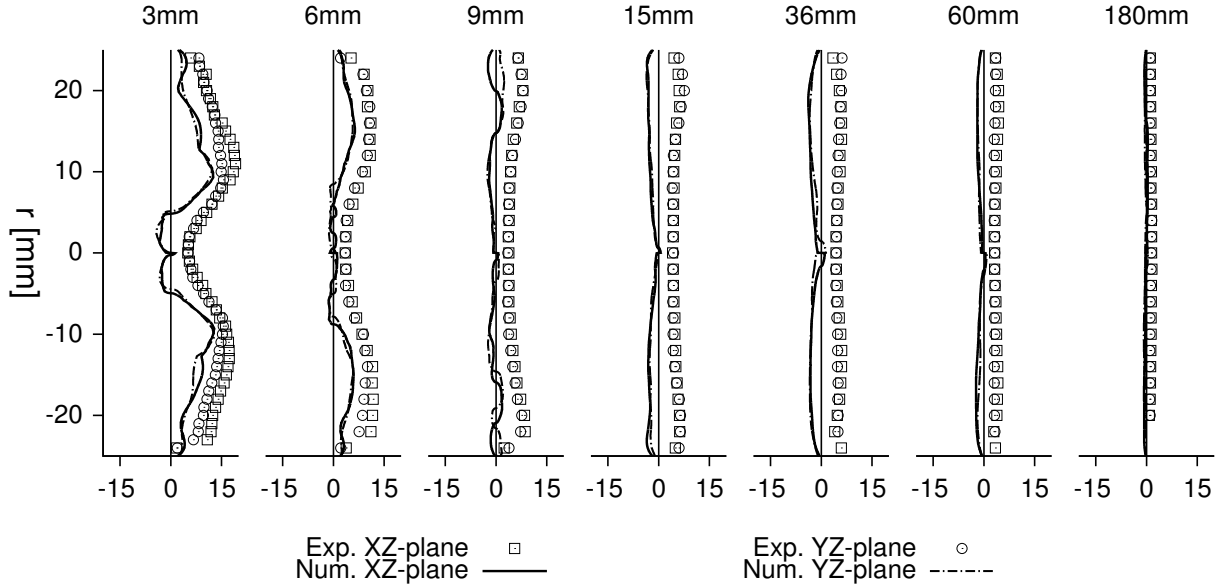

Figure 7.36: Non-reacting, cold air flow. RMS radial component of gas phase velocity ($1/m^2$).

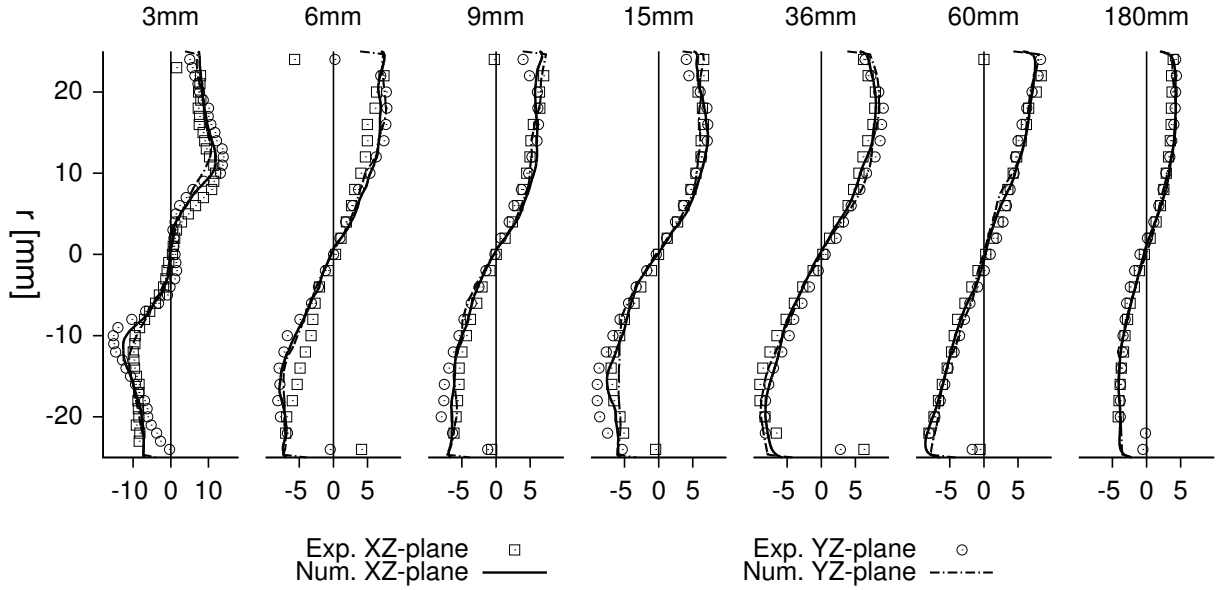

Figure 7.37: Non-reacting, cold air flow. Mean azimuthal component of gas phase velocity ($1/m^2$).

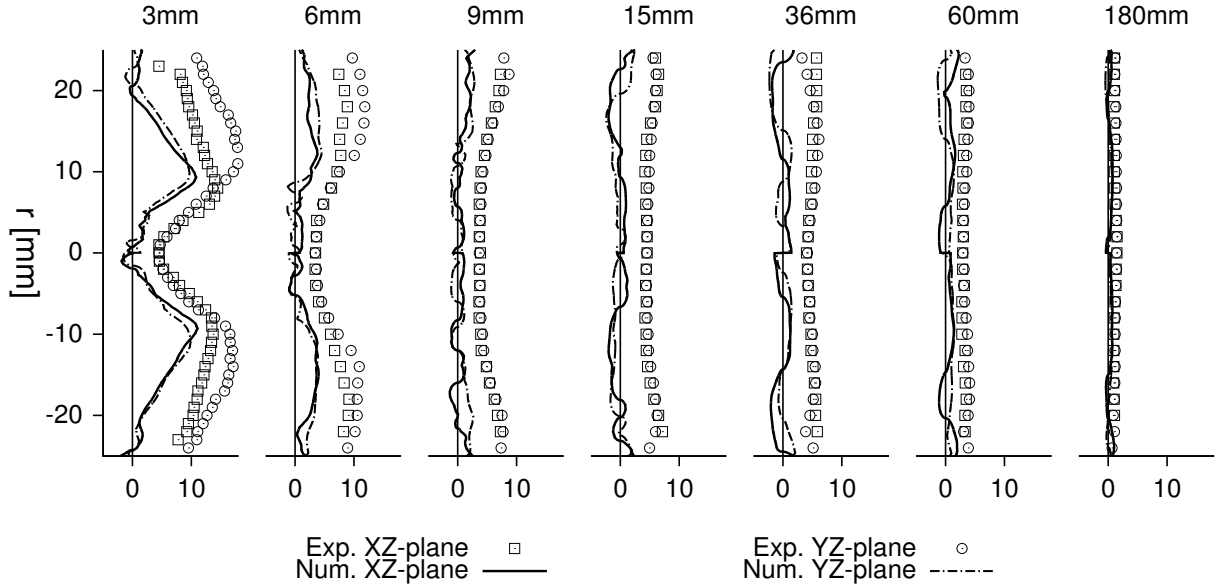

Figure 7.38: Non-reacting, cold air flow. RMS azimuthal component of gas phase velocity ($1/m^2$).

As in the experiment, significant differences are not present, although the $y-z$ plane coincidents with the trailing edge of the vanes and the $x-z$ plane is placed between two vanes (the swirler consists of six vanes in total). Although the experimental data show some differences at $z = 3\,\mathrm{mm}$ for all components and at few regions downstream, it must be considered, that the experimental data are not throughout symmetrical, which leads to the fact that at one side (of the axis) the $x-z$ and $y-z$ data differ, on the other side not. Hence, a final conclusion on the magnitude of the circumferential heterogeneity of the experimental values cannot be drawn. The numerical values are nearly identical in both planes, which suggests that considering the thickness of the vanes might contribute to the better separation of the $x-z$ and $y-z$ values (where applicable) in that sense, that the trailing edge turbulence and the wider stagnation area increase the circumferential heterogeneity.

In general, all components show sufficient agreement, with some deficiencies in the radial mean and rms and the azimuthal rms values. The shape and dynamic of the recirculation zone is captured well, whereas the intensity of the turbulent fluctuations is predicted too low, especially the radial and circumferential component. This might stem from the mesh resolution, the chosen sub-grid scale turbulent viscosity model, underpredicted trailing edge turbulence intensity and the spatial and temporal constant velocity at the domain inlet upstream the swirler or other reasons as mentioned at the beginning of this paragraph. A study on these parameters would be necessary to optimise the results, but for our needs the performance of the gas phase solver is satisfactory regarding the following two points. First, the approximated geometry of the vanes provides the correct swirl and vortex breakup, and second, the flow field is predicted very well in the sense that it will not contribute considerably to potential deviations of numerical and experimental results in subsequent simulations originating from the spray or combustion models.

7.3.3 Cold Spray Flow Validation

Cai et al. (2005) provided measurements of the spray quantities for the cold spray dynamics without any gaseous flow. This is very valuable to adjust the boundary conditions of the spray quantities at the numerical spray inlet. The spray nozzle is positioned 6.35 mm upstream of the area expansion. Hence, if the nozzle is mounted into the experimental setup, measurements are only possible from a relative position larger than 7 mm downstream of the nozzle. Spray data are only at our disposal for $z = 7$ mm and $z = 11.6$ mm, although measurements have been reported in Cai et al. (2005) at four additional positions, the first being at $z = 5$ mm downstream of the nozzle. This value indicates, that the spray has been measured without being mounted in the venturi to obtain values closer to the nozzle. Obviously, spray data as close as possible to the nozzle are of increasing value to be able to reconstruct proper inlet conditions for the simulation, but the density of the spray might impede meaningful measurements. Therefore, proper inlet conditions must be estimated by adjusting the values iteratively until satisfactory agreement is obtained at the given measurement positions. This could become, however, a longsome process, which could not be undertaken for the present results in a satisfactory manner.

The present spray inlet conditions for the simulations have been obtained by a rough adaption of the spray velocity to the measured one at $z = 7$ mm. To realise the spray angle of 90° and the deviation around that value due to dispersion, an artificial geometrical part has been introduced whose surface is used as spray inlet in the simulations as sketched in Fig. 7.39. The additional volume is marked dark grey. The upstream circumference is correctly circular, but the downstream circumference had to be adapted to the innermost block-structure of the mesh, which is hexagonal due to the o-grid constraints (Fig. 7.40 and Fig. 7.41). Since the hexagon has a diameter of 1.0 mm, any smaller structure to obtain a circular circumference is not practical. This approach, however, divides the circumferentially homogeneous spray into 6 sections separated by wedges without spray, which increase with larger radii and when moving from

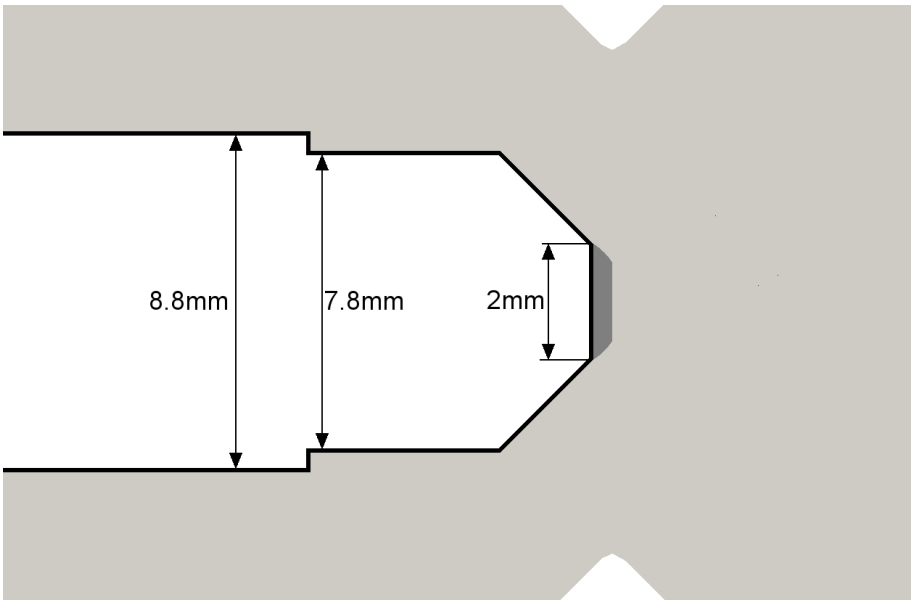

Figure 7.39: Sketch of the additional geometrical part used as spray inlet.

the circular towards the hexagonal circumference of the inlet face. The impact of the resulting circumferential heterogeneity of the spray on the combustion dynamics has not been investigated so far. This issue relaxes to a certain amount since the swirling air may reduce the heterogeneity due to its significantly higher velocity. Numerical values are taken from the $x - z$ plane, which lies within the spray. Values should be decreased when using a circumferential average.

Additionally, the default value of the spray angle being 90° is actually altered throughout the surface as well. Besides these objectionable geometrical deviations, the spray patch is not straight but intentionally curved perpendicular to the circumference, as it can be seen in Fig. 7.41 on the right. This ensures a spray spreading not only exactly at 45° but to mimic a deviation and dispersion[2] of the mass flux according to the experimental data. The curvature simplifies the definition of the spray inlet velocity significantly, i.e. the OpenFOAM inlet condition `surfaceNormalFixedValue` could be simply used for the spray velocity. Its magnitude is uniform across the inlet, which is also an approximation.

[2]The use of upwind discretisation for the moment transport contributes a significant amount by numerical dispersion anyway.

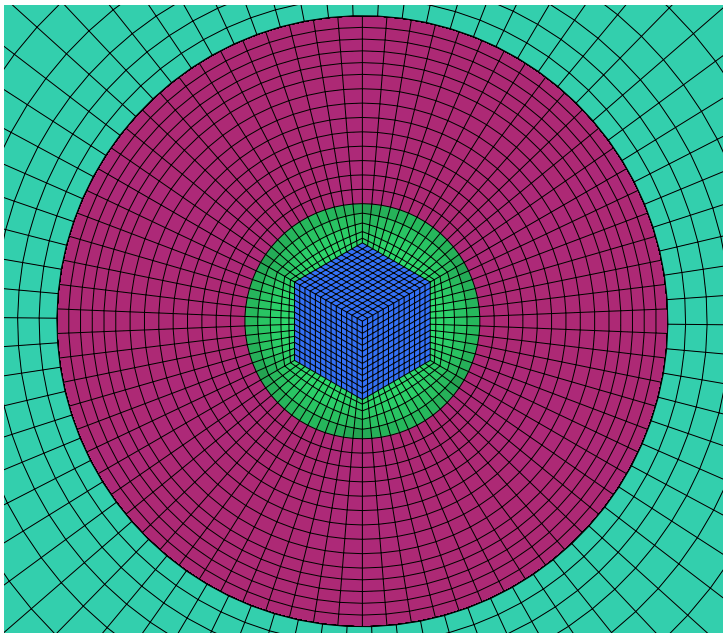

Figure 7.40: Part of the numerical mesh at the spray nozzle. Upstream view. The light green surface is the artificial spray inlet as shown in Fig. 7.41.

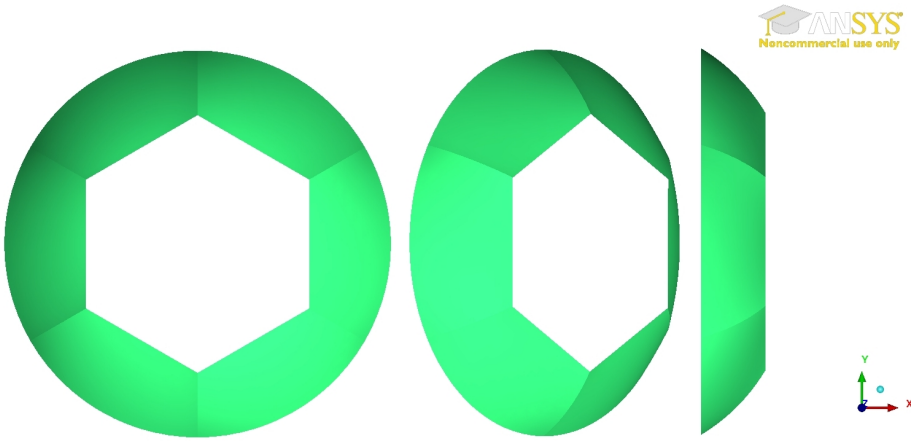

Figure 7.41: Geometrical faces of the spray inlet **Left** front view **Centre** rotated **Right** side view.

With help of the estimated spray velocity at the inlet, the liquid mass flux and the surface area of that inlet face, the volume fraction α_d has been determined. Considering the difference of the measured mean diameters D_{32} and D_{10} between $z = 7\,\text{mm}$ and $z = 11.6\,\text{mm}$, their values at the nozzle position have been estimated. These two values provide the information to calculate the moments $M^{(2)}$ to $M^{(0)}$ at the spray inlet. D_{32} allows to calculate $M^{(2)}$ from α_d and D_{10} the value of $M^{(0)}$ if $M^{(1)}$ is known. To link $M^{(2)}$ and $M^{(1)}$, an arbitrarily chosen value of $q = 3$ has been used for the parameter q of the Gamma distribution, which is in the range of typical initial spray distributions. The values obtained are summarised in Tab. 7.3.

Table 7.3: Inlet conditions for the dispersed phase.

Liquid mass flow	$0.0249\,\text{kg/min} = 4.150 \times 10^{-4}\,\text{kg/s}$
Air/spray temperature	$78°\text{F} = 25.556\,°\text{C} = 298.7\,\text{K}$, used: $300\,\text{K}$
Moments	$\alpha_d = 3.205\,137 \times 10^{-2}$
	$M^{(3)} = 6.121\,347\,4 \times 10^{-2}$
	$M^{(2)} = 8.161\,796\,5 \times 10^{2}\,\text{m}^{-1}$
	$M^{(1)} = 1.360\,299\,4 \times 10^{7}\,\text{m}^{-2}$
	$M^{(0)} = 5.914\,345\,3 \times 10^{11}\,\text{m}^{-3}$
Estimated mean diameters	$D_{32} = 75\,\mu\text{m}$
	$D_{10} = 23\,\mu\text{m}$

The comparison of numerical and experimental profiles of the spray quantities is shown in the following graphs in Fig. 7.42. Despite the same mass flux at the inlet, the mass flux predicted downstream seems much too high in the numerical results. The numerical peak values at the measurement planes are a factor of 5-7 higher than the experimental ones, but also at lower radii. Furthermore, a mean value averaged about the circumference might match the given experimental data better. The spray velocity at the inlet has been estimated to be $7\,\text{m/s}$, its development, as visible in Fig. 7.42, gives reason to be improved, especially the dispersion perpendicular to the cone is underestimated. Additionally, the spray calculation has been conducted with a fixed quiescent gas phase flow field, therefore drag and hence the deceleration of the droplets should be

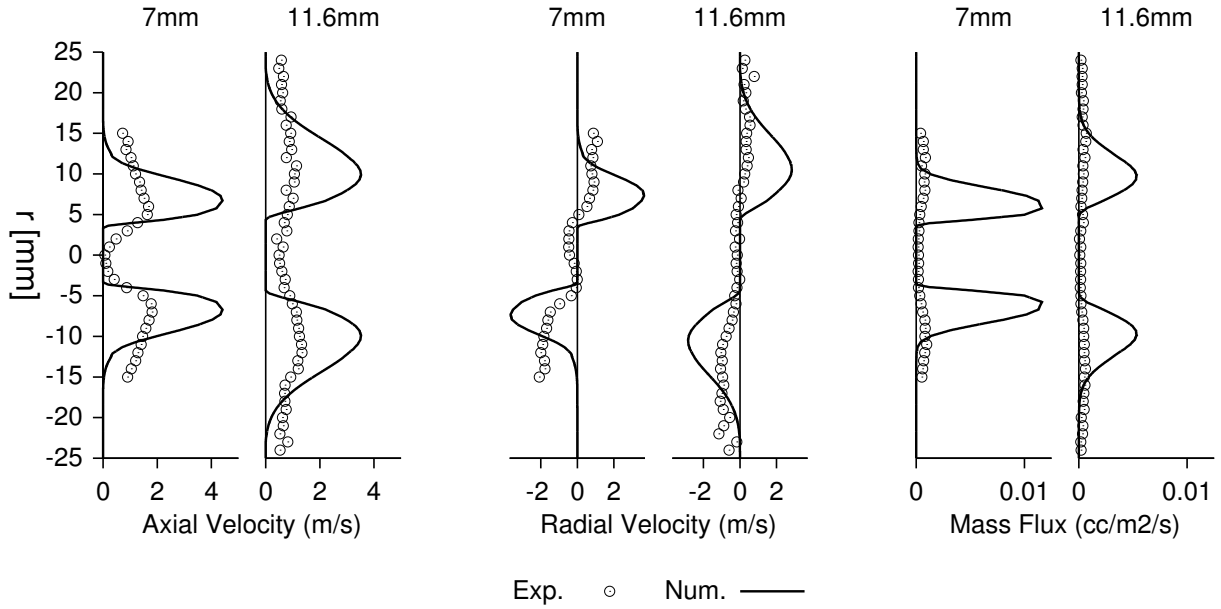

Figure 7.42: Non-reacting, cold spray flow. **Left** Axial and **Centre** radial component of the mass averaged spray velocity $\mathbf{u}^{(3)}$. **Right** Mass flux.

slightly overestimated.

Obviously, this first estimate of the spray values at the spray inlet is far from satisfactory and a comprehensive adaption must be undertaken in future steps. In this work, the correspondence of the mass flow, the spray angle and the approximately correct velocity magnitude, have been taken as sufficient to be used for the combustion simulation, as they should provide at least adequately conserved species mass fractions, temperatures and velocities.

7.3.4 Reacting Flow Validation

The LDI spray burner operates without preheating, prevaporisation or any kind of pilot flame to stabilise the spray flame. Hence, the flame position and stabilisation depends on the spray formation, vaporisation progress and the recirculation zone dynamic. The latter determines the ignition and stabilisation of the flame by recirculation of hot products

and by the low and reversed flow velocity, respectively. In such a situation the validity of the Thickened Flame Model is questionable since a thickening in a counterflow configuration is rather impracticable. Hence, the results are based on non-thickened flame calculations using the OpenFOAM PaSR combustion model (Nordin, 2001) with default settings. Radiation and droplet heat-up through radiation is not considered as well as heat loss through the walls.

Operating Conditions

The gas and spray boundary conditions are equal to those given in Section 7.3.2 and Section 7.3.3. Only the gas inlet temperature is higher in the reacting case, i.e. 80°F = 26.667 °C = 299.8 K, where the value of 300 K has been used. The overall equivalence ratio becomes $\phi = 0.73$.

Reaction Schemes

The most difficult task in order to obtain simulation results is to find a chemical mechanism, which, on the one hand, includes the slow CO to CO_2 reaction, but, on the other hand, is neither too costly nor too stiff. First, an appropriate surrogate for kerosene must be found. There exist many schemes using $C_{13}H_{26}$ or $C_{12}H_{xx}$ as surrogates for kerosene, however, the literature for the LDI burner consistently used $C_{12}H_{23}$, i.e. the work of Iannetti et al. (2008), Kirtaş et al. (2006), Patel and Menon (2008), Knudsen and Pitsch (2010). Second, an appropriate mechanism must be found and implemented. Last, a stable chemical solver must be evaluated. Especially the chemical solvers of OpenFOAM are not very stable regarding the choice of the Arrhenius parameters, especially the species mass fraction exponents. OpenFOAM provides four options, i.e. the ordinary differential equation (ode) solvers `SIBS` (Semi-Implicit Bulirsh-Stoer), `RK` which is based on a Runge-Kutta scheme and `KRR4` (Kaps-Rentrop), as well as an implicit solver named `EulerImplicit`, which gives best stability but is tremendously more costly than the ode solvers (up to

50 times and more dependent on the number of reactions) and cannot be used for the present case. Hence a choice must be made between the ode solvers. The `SIBS` is standard, but the most unstable, the `KRR4` and `RK` are more stable but the `RK` can become very costly as well.

In the following, the chosen schemes and the specific experience made using them for the present case are outlined. Initially, the Arrhenius coefficients given in Gokulakrishnan et al. (2013) have been used for the $C_{12}H_{23}$ to CO reaction, which are optimised for laminar flame speed and the combined use with the forward and backward CO oxidation reactions by Westbrook and Dryer (1981). Tab. 7.4 summarises the reactions and the parameters.

Table 7.4: 3-step mechanism given in Gokulakrishnan et al. (2013).

	A	n	Ea
$C_{12}H_{23}{}^{0.95} + 11.75\ O_2{}^{2.3} \longrightarrow 12\,CO + 11.5\ H_2O$	6.0763×10^{16}	2.0	37 893.5 cal/mol
$CO + 0.5\ O_2{}^{0.25} + H_2O^{0.5} \longrightarrow CO_2 + H_2O$	4×10^{14}	0.0	40 000 cal/mol
$CO_2 \longrightarrow CO + 0.5\ O_2$	5×10^{8}	0.0	40 000 cal/mol

The $C_{12}H_{23}$ reaction given by Gokulakrishnan et al. (2013) worked fine with the CO forward reaction only, but diverges when using the backward reaction as given by Westbrook and Dryer (1981) and using the OpenFOAM ode solver `KRR4` (when using `SIBS` even faster). The coefficients for the fuel reaction referred by Patel and Menon (2008) from Westbrook and Dryer (1981) (which are actually given for $C_{10}H_{22}$) have been tested as well but they behave similar. The problem can be attributed to the OpenFOAM specific implementation by defining both equations as two irreversible equations (instead of a reversible definition) rather than the mechnism itself. When neglecting the backward reaction of CO, there occurs only a considerable CO concentration at a thin line close to the main reaction front, whereas the experimental data show high CO concentrations long time after. To improve the poor CO concentration profiles and the wrong flame dynamics (significant deviations in the flow field), a 10-step mechanism given by Iannetti et al. (2008) has been tested.

This one is also unstable with the original $C_{12}H_{23}$ reaction, but proved more (but not unconditionally) stable with the one used by Patel and Menon (2008) using either of the ode solvers. Therefore, the NO_x reactions have been removed, which result in a much less stiff system, but lacks a proper equilibrium of the species O.

Furthermore, the 1-step scheme given in Iannetti et al. (2008) has been tested, which reads

Table 7.5: 1-step mechanism given in Iannetti et al. (2008).

	A	n	Ea
$C_{12}H_{23}{}^{0.1} + 17.75\ O_2{}^{1.65} \longrightarrow 12\,CO_2 + 11.5\ H_2O$	8.6×10^{11}	0.0	30 000 cal/mol

Using mechanisms with mass fraction exponents (much) less than unity, however, are handled (to the author's experience) somehow erroneous in OpenFOAM. It has been observed in several test cases, that using such values the mass conservation is corrupted. In the reacting simulation for the Sydney spray burner (not shown herein) a 12 % mass loss of O_2 has been observed.

To relax that issue a bit, the 2-step scheme for an artificial kerosene surrogate given by Franzelli et al. (2010) has been tested, which features an exponent of at least 0.55 for $C_{12}H_{23}$ and reads

Table 7.6: 2-step mechanism given in Franzelli et al. (2010).

	A	n	Ea
$C_{12}H_{23}{}^{0.55} + 17.75\ O_2{}^{0.9} \longrightarrow 12\,CO_2 + 11.5\ H_2O$	8×10^{11}	0.0	41 500 cal/mol
$CO + 0.5\ O_2{}^{0.5} \longrightarrow CO_2$	4.5×10^{10}	0.0	20 000 cal/mol

With that choice, two additional problems that arise according to the authors experience using Arrhenius computation in OpenFOAM are avoided. First, this 2-step scheme is given without a backward reaction for CO, which avoids the necessity of defining a forward and backward reaction (as briefly mentioned before). Second, temperature exponents

larger than zero often tend to be unstable and produce, in combination with the ode solvers, non-physically rising temperatures. The result is the crash of the simulation, since these locally extreme values can not be smoothed anymore. Using this scheme, however, the flame could not be stabilised in some initial tests. Either this scheme is too weak using $\mathbf{F} = 1$ (no thickening) or the start conditions were not appropriate.

Numerical Ignition and Heat Release Limiter

Ignition of the flame can become a difficult task as well, depending on the specific case. The following strategies have been tested. First, in order to force ignition, a time dependent, direct modification of the Arrhenius parameters has been undertaken to increase the initial heat release. Second, the reaction rate has been initially reduced, when using an artificially area of high temperature. Both attempts failed, because they are much too sensitive resulting either in distinction or "explosion" of the flame. The only practicable process is to use a small region of high temperature close to the fuel vapour in the recirculation zone, in combination with the originally given Arrhenius parameters and naturally developed species fields. Artificial modifications in the species fields, e.g. setting small region to burnt, etc., are often very contraproductive to ensure a stable solution of the reaction mechanism. Nevertheless, a reaction rate limiter is evident to avoid the nonphysical increase of the temperatures. The algorithm, which has been applied is detailed in Appendix A.4.3.

Reacting Flow Results

The presented results are based on the scheme reported by Gokulakrishnan et al. (2013) and given in Tab. 7.4. As described, the backward CO reaction has not been considered and the reaction rate limiter was applied as described in Appendix A.4.3. It acts significantly in the start-up process but reduces later on to a few small regions with a vanish-

ing amount of reaction[3]. As described in the section before, the proper choice of a reaction scheme and the issues with the OpenFOAM chemical solvers did not allow a satisfactory validation of the reacting LDI burner so far. Hence, the results discussed below must be considered as work in progress, reminding that also the inlet conditions for the spray are still matter of future improvement and better adaption to the experimentally observed values. Only the single phase flow is satisfactorily validated and is not seen as a reason for the poor agreement of the reacting simulation results with the experimental data. Nevertheless, the results are presented to show the capability to combine the moments spray model with the chemical reaction. This is of specific importance, since the development of the fuel vapour is solely depending on the moments model, i.e. no prevaporised amount of fuel does contribute to the vapour field or the stabilisation of the flame.

The simulations have been conducted for the case of an overall equivalence ratio of $\phi = 0.75$. The contour plots in Fig. 7.43 show the droplet volume fraction ($M^{(3)}$), the heat release rate density and the gas phase temperature (from left to right). Initially, the spray develops according to the predetermined nozzle spray angle but is rapidly blown towards the axial direction by the gas flow, which acts as a kind of crossflow in the

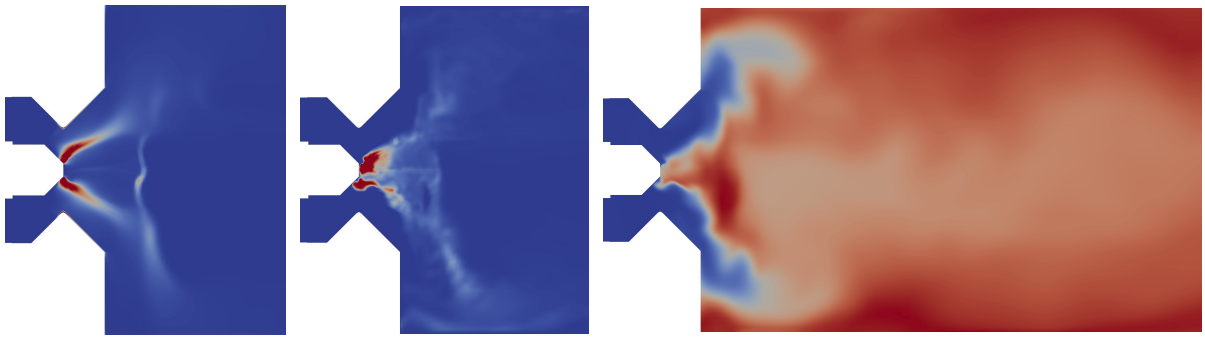

Figure 7.43: Instantaneous contour plots of **Left** droplet volume fraction $(0 - 0.002\,[\text{-}])$ **Centre** heat release rate density $(0 - 1 \times 10^{10}\,\text{J}/(\text{m}^3\,\text{s}))$ **Right** gas phase temperature $(286 - 2600\,\text{K})$.

[3]It applies there only, because the calculated reaction rate is higher than the physically possible.

direct proximity of the nozzle. Further downstream, the spray is completely stopped by the reverse gas flow in the inner part of recirculation zone. Due to the hot gases within the recirculation zone, which are transported upstream into the stagnation point situation near the nozzle, the main region of combustion establishes there in the simulation. Also the experimentally measured temperature profile has its maximum in this region as represented by the values at 5 mm in Fig. 7.49.

In comparison to the single phase flow field, the reacting flow develops quite different. This is due to the significant volume expansion of the gas due to the low density resulting from the high temperature and the approxiamately isobaric process. This volume expansion occurs mainly at the outer radii within the first 10 to 20 mm downstream the venturi (beginning of the housing). As a result, the flow is accelerated and keeps its high axial velocity of approximately 20 $\mathrm{m\,s^{-1}}$ in the proximity of the walls. At the same time, the transition between the outer downstream flow and the recirculating upstream flow becomes much sharper than compared to the single phase flow as it is clearly visible in the experimental data of the axial gas phase velocity component in Fig. 7.44.

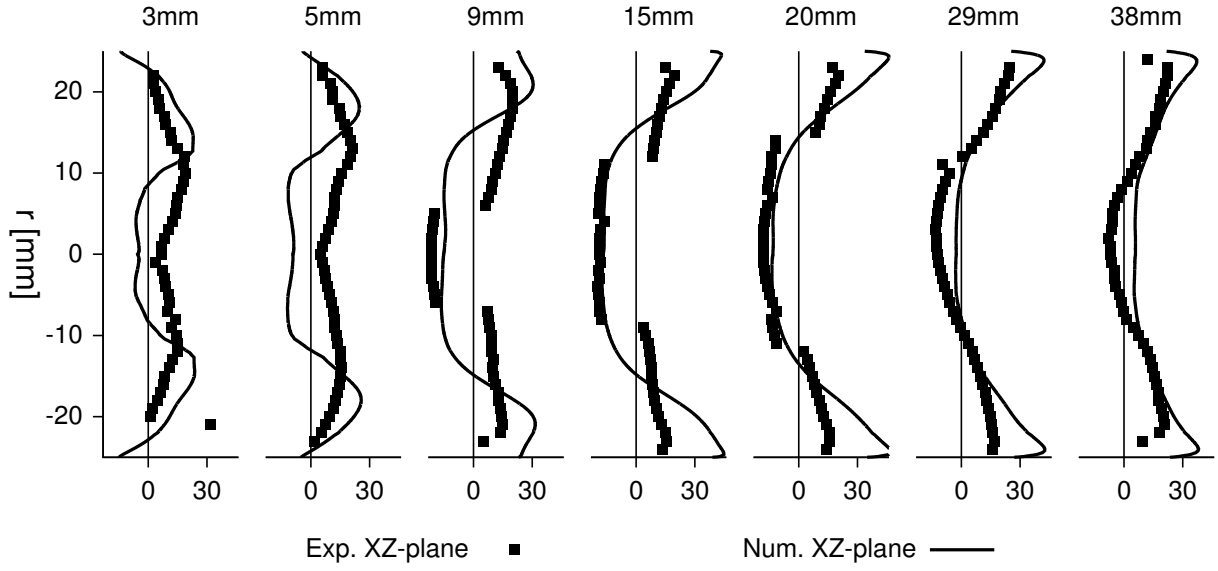

Figure 7.44: Reacting two-phase flow. Axial component of the gas phase velocity (m/s).

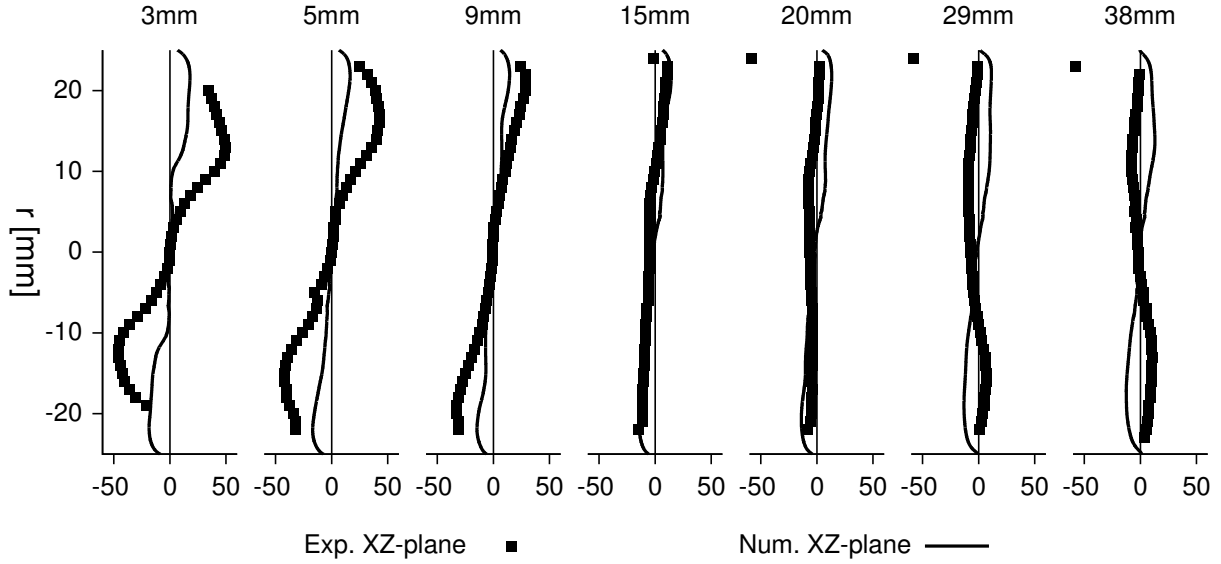

Figure 7.45: Reacting two-phase flow. Radial component of the gas phase velocity (m/s).

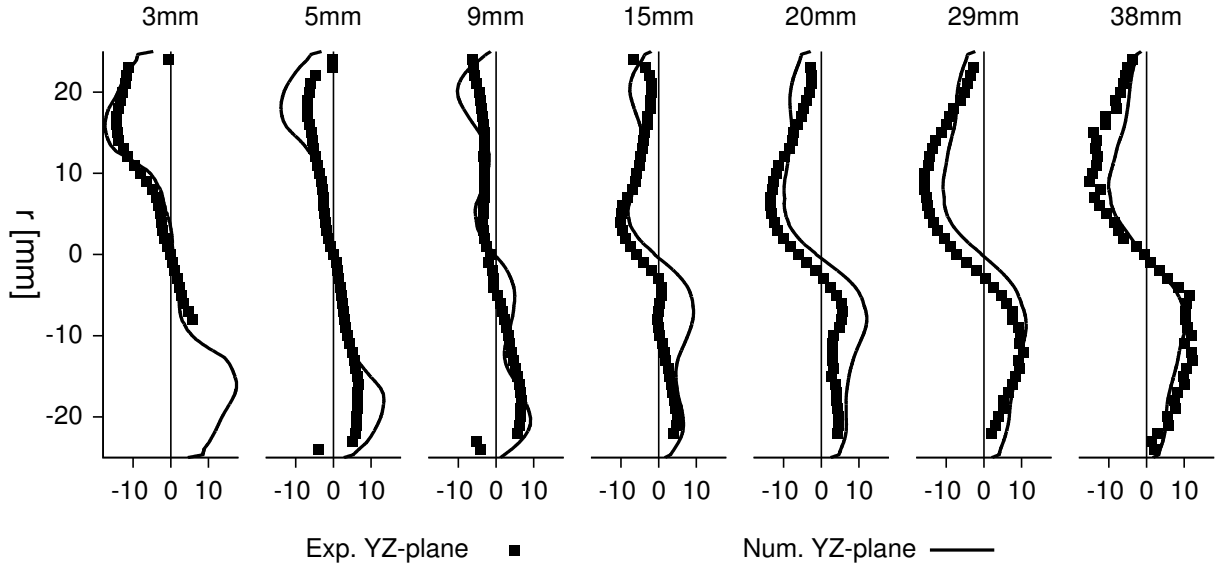

Figure 7.46: Reacting two-phase flow. Azimuthal component of the gas phase velocity (m/s).

The simulation is able to fit the magnitude of the recirculating air, however, the overall flame dynamic and interaction with the recirculation zone is quite different. This is additionally confirmed by the radial gas phase velocity component (Fig. 7.45). The azimuthal component (Fig. 7.46) is rather independent of the development of the former components and confirms the validity of the chosen setup for the swirler geometry. A detailed discussion on the flow effects due to the reaction can be found in the original literature Cai et al. (2005).

The dispersed phase axial velocity profiles show a rather reasonable agreement with the experiment at the first measurement position (Fig. 7.47), but develop divergently. Obviously, the mismatch in the inner recirculation zone is due to that of the single phase. As discussed in Section 7.3.3, the spray development suffers from properly adjusted inlet conditions as well. Hence, the computed particle mass flux profiles as

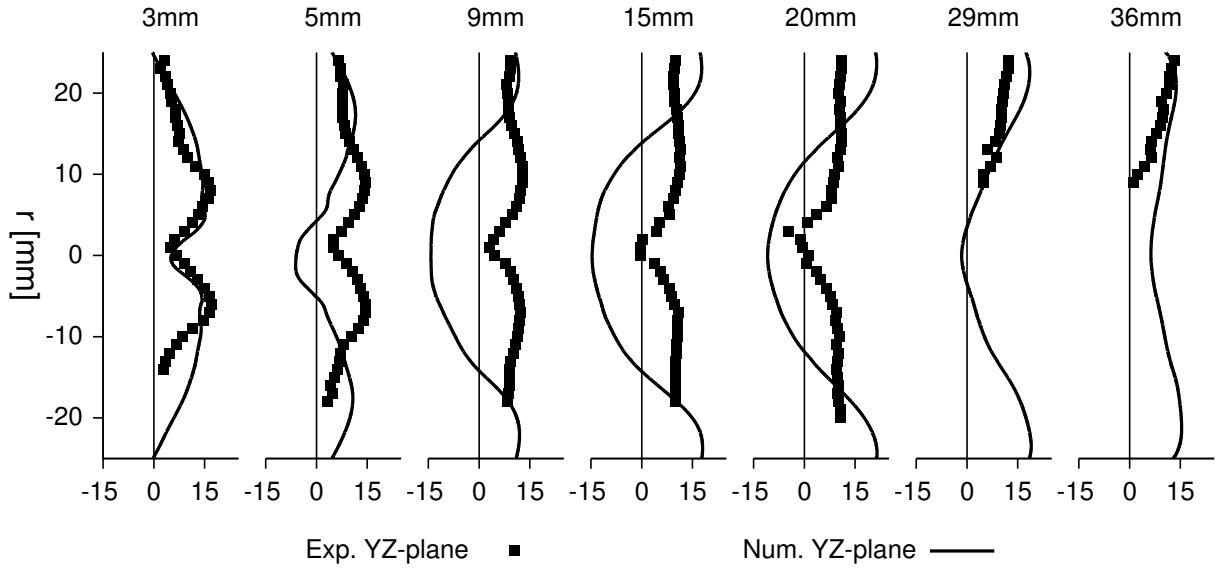

Figure 7.47: Reacting two-phase flow. Axial component of the spray velocity (m/s).

shown in Fig. 7.48, differ from the measured ones. Additionally to that, the enforcement through the gas phase is not represented correct, which would increase the axial magnitude of the particle velocity due to the cross flow arrangement (the spray angle is larger than the gas phase ve-

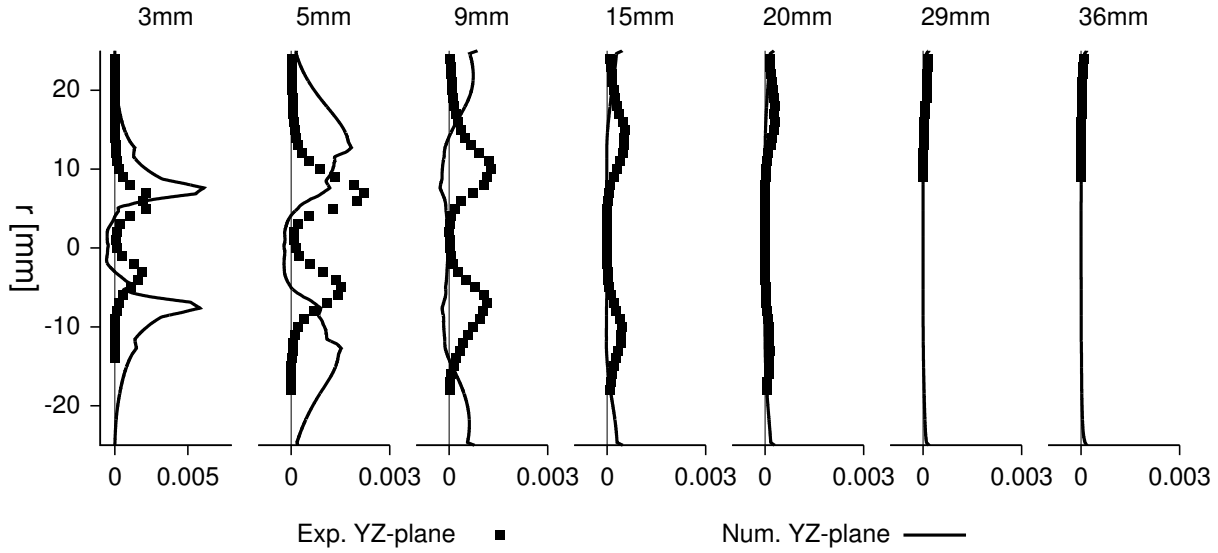

Figure 7.48: Reacting two-phase flow. Liquid volume flux ($\mathrm{kg}/(\mathrm{m}^2\,\mathrm{s})$).

locity vector in the region of the nozzle).

The experimentally measured temperature is more or less homogeneous across the cross sections throughout the domain (Fig. 7.49). The simulation predicts similar temperature levels. Towards the walls, the predicted temperature increases, which results from continuous vaporisation and

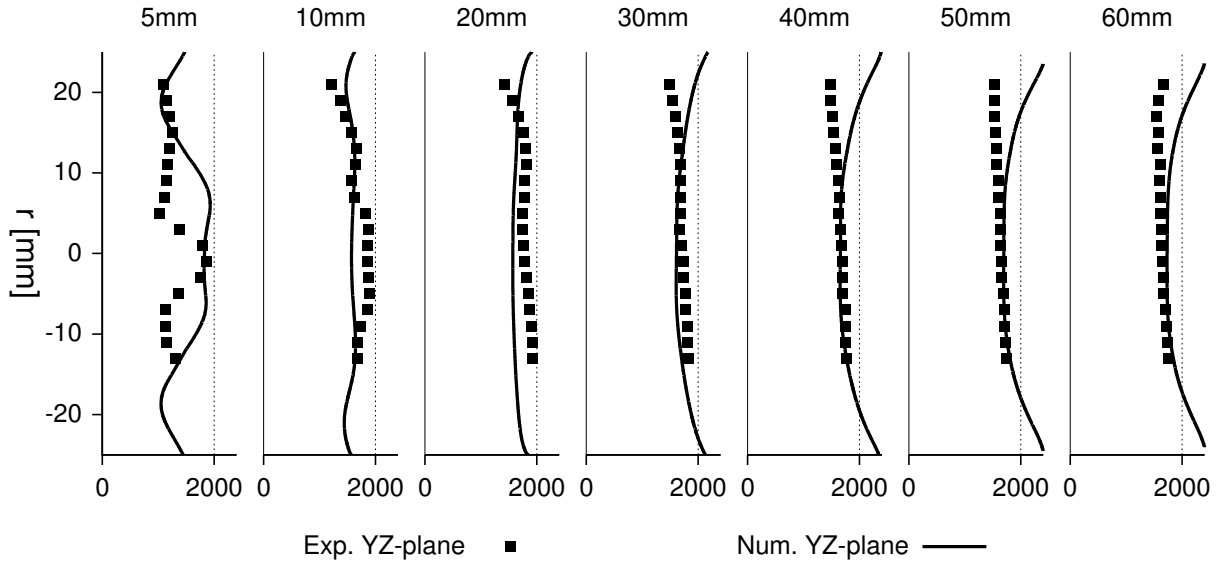

Figure 7.49: Reacting two-phase flow. Gas phase temperature (K).

combustion of some liquid, which accumulates at the walls. Whether this behaviour is physical or has been observed in the experiments is not clear. The same issue applies for the species profiles for O_2 (Fig. 7.50) and CO_2 (Fig. 7.51). Comparing particle size distribution quantities as, e.g., moments or mean diameters, does not make sense at this point. For that,

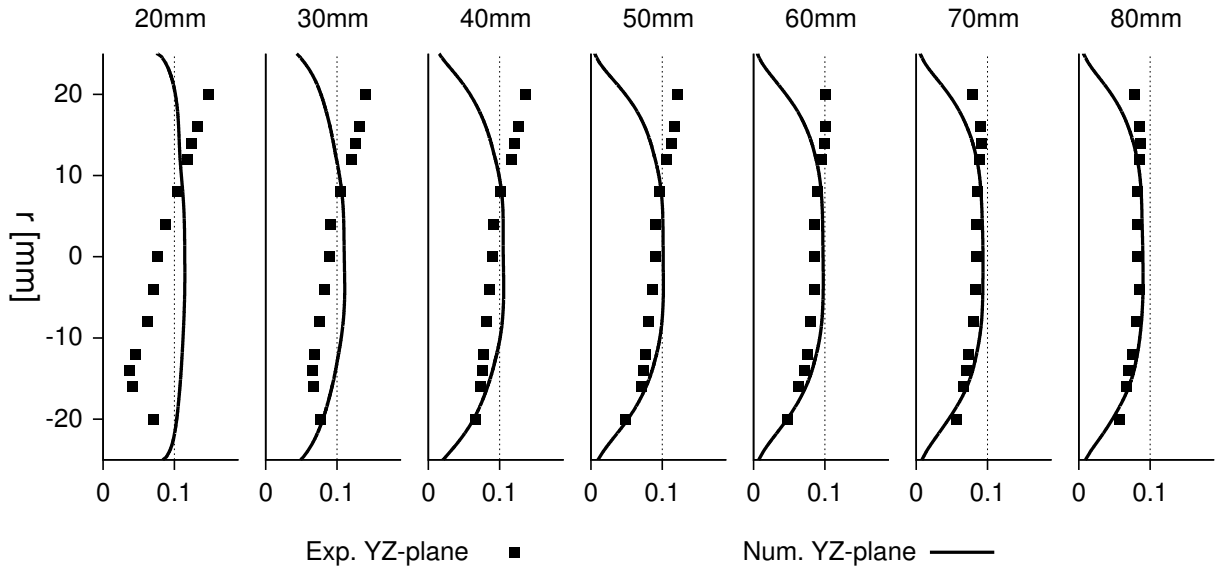

Figure 7.50: Reacting two-phase flow. O_2 mass fraction (-).

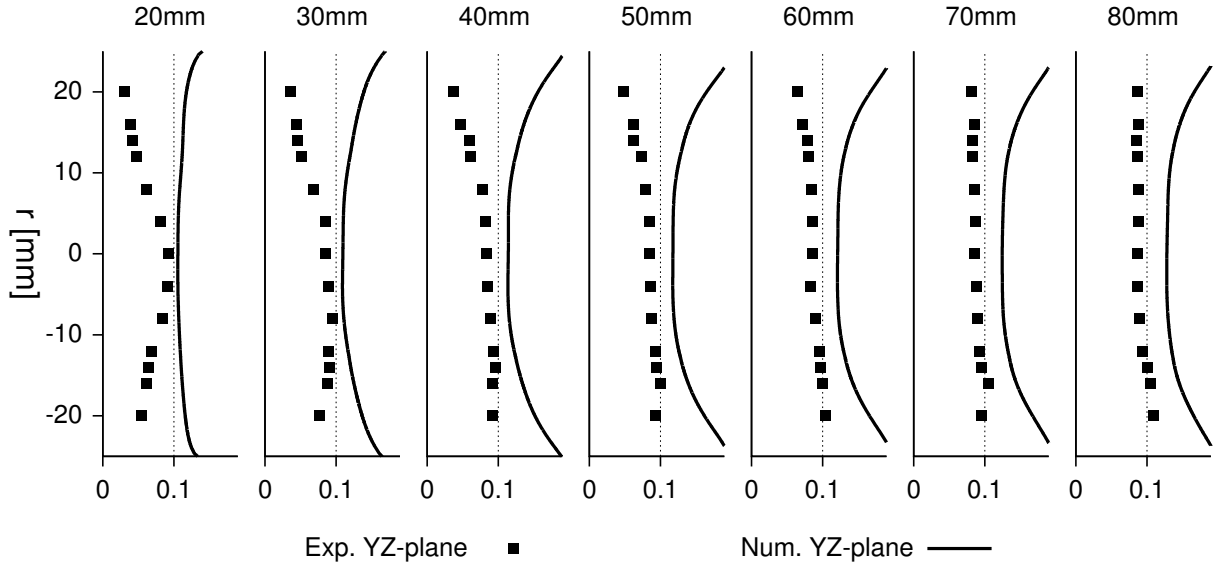

Figure 7.51: Reacting two-phase flow. CO_2 mass fraction (-).

the fit of the main quantities (i.e. actually the reaction) must be improved beforehand as well as the spray inlet conditions.

To summarise, the coupled simulation of the spray with help of the moments model and a reacting LES solver has been shown to be possible in principle. A satisfactory validation failed so far due to difficulties in finding an appropriate and meaningful setup for the combustion modelling. This must be left for comprehensive future work. Furthermore, considering the physical aspects, one must keep in mind, that the combustion is clearly in the heterogeneous regime, probably implying different modes (group combustion, single droplet combustion), but treated here in the simulation as homogeneous with vaporising droplet within the flame zone. Hence, the improvement of the modelling itself, is the subsequent step.

8 Conclusion

8.1 Summary

The present work aimed to develop, implement and validate a polydisperse, dilute droplet-air two-phase flow model for the application to spray combustion using Large Eddy Simulation and OpenFOAM. It is a following work of that done by Gharaibah and Polifke (2004), Gharaibah (2008) and Carneiro et al. (2008, 2009, 2010), Carneiro (2012). In its basics, it inherited Carneiro's moment model to describe a spray polydispersed in droplet size, especially the closures for the source terms due to motion and vaporisation and the relaxation time approach to determine moment transport velocities other than that of the third moment $M^{(3)}$. The latter closure, among others, distinguishes Carneiro's work from the work of Beck (2000), Beck and Watkins (2002, 2003), Watkins (2007), which is similarly based on volume average based RANS equations with presumed function closure.

The significant difference between the present and Carneiro's work is the reformulation of the whole moment model from RANS to LES and from volume average based equations to ensemble average based equations for the dispersed phase and to equations based on a combined operation of volume average and spatial filtering for the gas phase. The latter idea has been adopted from the work of Carrara and DesJardin (2006) and Sirignano (2005, 2010), where the present derivation follows closely that outlined in Sirignano (2010). A kinetic description based on a filtered number density function built from the ensemble of a large number of dispersed phase flow realisations for a given continuous phase flow realisation was used to describe the spray dynamics. The derivation of the transport equation for this NDF was done in line with the

common approach to define a fine grained phase space density function, whose derivatives with respect to the phase space coordinates yields the wanted equation. Its integration over the particle phase space implies several imporant aspects. First, no subsequent filtering of the resulting moment equations is necessary, because the NDF has been filtered beforehand (filtered density function approach). At this point, this work differs from the closely related work by Riber et al. (2005, 2006) and subsequent work, where the ensemble based NDF is integrated first and the resulting moment equations are filtered afterwards. Besides that, the related work of that group is polydisperse in velocity but not in particle size, except that presented by Mossa (2005). The phase space integration carried out therein acted as a reference for that done in the present work from a mathematical point of view. Both theses differ in the specific closures for the moment problem, the spray source terms and the closure of moment transport velocities. Furthermore the work of Mossa (2005) was neither concerned with the application of spatial filtering to the dispersed phase equations and the specification of the arising terms nor the combustion of the spray.

Along with the integration of the NDF over phase space, several correlations of residual components of the particle velocity arise due to the ensemble average, the spatial filtering and the phase space integration itself. These unknown terms were identified and available closure suggestions were presented and discussed. In this work, the extension of the closure for the Random Uncorrelated Velocity tensor to a size dependent formulation has been sketched but preliminary attempts to include this closure in the simulations were not straighforward. Closure for the other correlations was not attempted. Beside the dispersed phase quantities, sub-filter fluctuations of the gas phase quantities arise as well as unknown terms describing the unresolved interaction with the droplets. For LES, Mashayek and Pandya (e.g. Mashayek and Pandya, 2003) derived moment equations including a closure for the phase space diffusion current. Due to the difficulties of handling the resulting equations in 3D CFD (history integrals over time), it was not attempted to realise their implementation into the present solver. To the authors knowledge,

Mashayek and Pandya themselves have not presented related simulation results for complex spray applications so far.

Closure for the moment equations was obtained using the presumed function approach by adopting many of the closures given by Carneiro. Hence, the NDF over particle size space is represented by the Gamma and Beta distribution, whereas the particle velocity is uniquely linked to the particle diameter and the temperature space adopts only a single value locally. Each moment is transported by its respective moment transport velocity, for which closure was obtained using the relaxation time approach.

Spray combustion modelling and simulation is a field of recent research. Here, a two-phase thickened flame model as skeched by Kaufmann (2004) was applied and verified. Its usage in the combustion simulations, however, did not deliver different results or flame dynamics. Additionally, an Eulerian single droplet combustion model was proposed and its implementation verified using a simple 1D, non-prevaporised two-phase flame. This model, however, has not been tested in a 3D test case so far.

The numerical results were compared to experimental data of isothermal, vaporising and reacting polydispersed spray flows. The results indicate that considering polydispersity in size space delivers superior results compared to a monodisperse description. The development of particle phase quantities as the particle mass flux and the mean diameters is captured well and distinguished from the monodisperse formulation. The results lack quantitative accuracy, however, especially in terms of turbulent particle dispersion and the combustion modelling.

Summarising, the present work attempted to establish the consideration of polydispersity in Eulerian two-phase LES for reacting sprays, where recent work is still focused mainly on the Lagrangian description of the particles.

8.2 Outlook

Comprehensive modelling of polydispersed two-phase flows is still a challenging task regarding theoretical modelling and closure as well as numerical implementation and stable simulation. Many issues came into focus during this work, but were mostly out of the scope to be investigated. Some of them have been sketched in the appendix, which is noted below if applicable. Some points are straightforward and rather close to a solution, others represent long-term objectives. For the sake of clarity, those issues are sorted into several subtopics.

Stochastic Modelling

Using the stochastic and kinetic approach, the formulation of dispersed particle flows is a quite sophisticated framework, which is able to describe a wide range of physics and phenomena from the mesoscopic up to the macroscopic level. As shown in chapters 3 and 4, the main concern is on the closure of the numerous unknown correlations of gas and dispersed phase quantities, especially the correlations of velocity fluctuations due to the different averages, i.e. ensemble average, spatial filtering and phase space average (moment models). Some of the correlations can be assigned clearly to one or the other phase, some represent interaction of both. The following points refer, first, to the dispersed phase, and second to the gas phase and gas/dispersed phase interaction.

In many applications of sprays and spray combustion, the phase space of particle size, velocity and temperature is the most relevant regarding spray behaviour and system dynamics. These dimensions of the property space have been adopted in this work. Hence we confined ourselves to discuss only those aspects which are related to these quantities. Considering both simultaneously, the dispersed phase size and velocity space, has been attempted at the most in a weakly coupled manner so far. In most of the reported applications, only one of them is considered. Obviously preferable is a fully coupled size-velocity space formulation. Devel-

opment of this aspect in Quadrature based Moment Methods is mainly concerned with developing moment inversion algorithms which are able to handle two or more phase space dimensions. For PMOM, an approach might be the extension of the *Random Uncorrelated Motion* modelling to include the size space dependency. Besides the work of Mossa (2005), a diameter dependent RUM formulation as sketched in Appendix A.2.4 could the basis for further development. Other closures of the velocity correlation terms might be considered, e.g. developing transport equations for the velocity correlations similar to the Reynolds stress model in RANS. Finally, the temperature space is important to be considered for vaporisation and other related physics. As a first step, a size conditioned temperature $T(D)$ could be adopted, similar to the velocity law used in this work, in combination with a corresponding thermal relaxation approach (Watkins, 2005).

Besides dispersed phase quantities, the residual quantities of the continuous phase produce various unknown terms. Sub-grid scale velocity fluctuations are source of the turbulent dispersion of particles, enhanced vaporisation and others, for which models have to be included in the present framework, i.e. methods like LHDI (e.g. the macroscopic moment formulation by Pandya and Mashayek, 2003a,b). Along with that, comprehensive mesoscopic models for drag, vaporisation, etc. might result in more accurate results. Some references are given in Section 3.2.3. Especially the non-Stokes formulations for drag and mass and heat exchange rates have been closed using significant simplifications on both, the spatial and the phase space averages. Hence, future work must be related to that issue. Throughout this work, the dispersed phase averages are conditioned on a single continuous phase realisation. Incorporation of the ensemble average over a large number of gas phase realisations is the next step to a comprehensive formulation, resulting in a joint particle-gas phase NDF. Some work in literature has been already dedicated to such an approach, but restricted to a Lagrangian way of solving the NDF.

Moments Model

The moments model as used in this work might be improved tackling the following aspects.

- Using a less restrained dependency of the size conditioned mean particle velocity $\mathbf{u}(D)$, e.g. as proposed by Carneiro (2012) using an incomplete Gamma distribution, quantitatively similar to Mossa (2005) and discussed further by Vié et al. (2013).

- When following the presumed shape approach further, attempts might be made to use 2-dimensional Gamma or Beta distributions for considering the full size-velocity space.

- When considering other moment closures, the maximum entropy reconstruction seems very promising besides the Quadrature based Moment Methods.

- Beneficial would be a formulation of the vaporisation rate for $M^{(0)}$ other than that proposed by Massot et al. (2010), because of its compulsorily use of the maximum entropy reconstruction in the presented form, which might become too restrictive.

- The current formulation of the relaxation approach is valid only for Stokes drag. An extended formulation is required for liquid particles similar to the one proposed by Acher (2013) for bubbles.

- The non-Stokes formulations for drag and heat and mass transfer represent approximations. More exact formulations (e.g. Tayler expansions) might give better results.

- Stefan flow can influence the drag significantly. Corresponding correlations could be incorporated.

Combustion

Combustion modelling has been conducted in a rather simple approach in this work, which gives reason to extensive future work on this topic. Besides the incorporation of specific spray combustion models, both homogeneous and heterogeneous, the formulation of the vaporisation can be refined using non-equilibrium evaporation models as the Langmuir-Knudsen type or multi-component evaporation, which becomes relevant for liquid fuels consisting of different species with significant different boiling temperatures and vaporisation rates. Some concrete points are the comprehensive validation of the Eulerian, polydisperse single droplet combustion model as proposed in Section 5.3.2 and the investigation of spray combustion dynamics with and without acoustic-spray interaction for academical and realistic industrial liquid fuelled combustion devices.

Numerics

CFD theory, which is concerned with numerical mathematics, i.e. equation solvers, matrices handling, discretisation, i.a., is a specific topic and not trivial even for typical single phase incompressible and compressible applications. The characteristic of two-phase flow equations might behave even different from those, e.g. pressure less behaviour, and therefore the equations require careful treatment. Here only some points are proposed to be tackled in the future concerning problems with the present implementation of the model. To be mentioned are

- the implementation of moment space preserving discretisation schemes,
- the implementation of more sophisticated time advancing and spatial discretisation schemes in OpenFOAM (Runge-Kutta, Lax-Wendroff, etc.),
- the use of appropriate compressible boundary conditions (LODI),

- the comparison with Lagrangian simulations,
- mesh resolution studies, especially to quantify the dependence of the moment fields on the resolution,
- the applicability on unstructured meshes,
- a version for ANSYS Fluent via the User-Defined-Function (UDF) functionality, which can be beneficial in order to have access to a wider range of combustion models, acoustics, etc. compared to OpenFOAM,
- the evaluation of the mass flux equation vs. the particle velocity equation (Section 6.1.1),
- the evaluation of more sophisticated solvers, e.g. shock-handling solvers as well as
- the potential use of a variable density solver instead of a compressible solver to exclude related issues, which can be avoided when dealing with low mach number, non-isothermal flows.

The comprehensive derivation and formulation of the two-phase equation system to be used with Large Eddy Simulation indicates the multitude of unanswered questions and non-solved issues, especially the closure of unknown terms and the challenges due to its numerical implementation as listed above. It illustrates the need for continued research within this challenging and exciting branch of CFD.

Bibliography

B. Abramzon and W.-A. Sirignano. Droplet Vaporization Model for Spray Combustion Calculations. *Int. J. Heat and Mass Transfer*, 32(9):1605–1618, 1989.

T. Acher. Internal document, 2013.

M. Ackermann and F.A. Williams. Simplified Model for Droplet Combustion in a Slow Convective Flow. *Combustion and Flame*, 143:599–612, 2005.

C. Allouis, F. Beretta, and A. Amoresano. Experimental Study of Lean Premixed Prevaporized Combustion Fluctuations in a Gas Turbine Burner. *Combustion Science and Technology*, 180:900–909, 2008. doi: 10.1080/00102200801894323.

T.G. Almeida and F. Jaberi. Large-Eddy Simulation of a Dispersed Particle-Laden Turbulent Round Jet. *Int. J. Heat Mass Transfer*, 51:683–695, 2008. doi: 10.1016/j.ijheatmasstransfer.2007.04.023.

C. Angelberger, F. Veynante, D. Egolfopoulos, and T. Poinsot. Large Eddy Simulation of Combustion Instabilities in Turbulent Premixed Flames. In *Proc. of the Summer Program*, pages 61–82. Center for Turbulence Research, NASA-Ames/Stanford University, 1998.

S.-V. Apte, K. Mahesh, P. Moin, and J.-C. Oefelein. Large-Eddy Simulation of Swirling Particle-Laden Flows in a Coaxial-Jet Combustor. *International Journal of Multiphase Flow*, 29:1311–1331, 2003.

V. Armenio, U. Piomelli, and V. Fiorotto. Effect of the Subgrid Scales on Particle Motion. *Phys. Fluids*, 11(10):3030–3042, 1999.

Y. Baba and R. Kurose. Analysis and Flamelet Modelling for Spray Combustion. *Journal of Fluid Mechanics*, 612:45–79, 2008. doi: 10.1017/S0022112008002620.

S. Baessler, K. Moesl, and T. Sattelmayer. NOx Emissions of a Premixed Partially Vaporized Kerosene Spray Flame. *Journal of Engineering for Gas Turbines and Power*, 129:695–702, 2007.

S. Balachandar and J.K. Eaton. Turbulent Dispersed Multiphase Flow. *Annu. Rev. Fluid Mech.*, 42:111–133, 2010. doi: 10.1146/annurev.fluid.010908.165243.

J. C. Beck. *Computational Modelling of Polydisperse Sprays Without Segregation into Droplet Size Classes*. PhD thesis, UMIST, Manchester, UK, 2000.

J.-C. Beck and A.-P. Watkins. On the Development of Spray Sub-Models Based on Droplet Size Moments. *J. of Computational Physics*, 182:586–621, 2002.

J.-C. Beck and A.-P. Watkins. On the Development of a Spray Model Based on Drop-Size Moments. *Proc. R. Soc. Lond. A.*, 459:1365–1394, 2003.

C. Bekdemir, L.M.T. Somers, and L.P.H. de Goey. Numerical Modeling of Diesel Spray Formation and Combustion. In *Proceedings of the 4th European Combustion Meeting (ECM 2009)*, 14-17 April 2009, Vienna, Austria, 2009.

C. Bekdemir, E.P. Rijk, L.M.T. Somers, L.P.H. de Goey, and B.A. Albrecht. On the Application of the Flamelet Generated Manifold (FGM) Approach to the Simulation of an Igniting Diesel Spray. In *SAE Technical Papers*, 2010. Paper no. 2010-01-0358.

C. Bekdemir, L.M.T. Somers, and L.P.H. de Goey. Modeling Diesel Engine Combustion Using Pressure Dependent Flamelet Generated Manifolds. *Proceedings of the Combustion Institute*, 33(2):2887–2894, 2011.

J. Bellan and K. Harstad. Analysis of the Convective Evaporation of Nondilute Clusters of Drops. *Int. J. of Heat and Mass Transfer*, 30(1): 125–136, 1987. doi: 10.1016/0017-9310(87)90065-2.

J. Bellan and M. Summerfield. Theoretical Examination of Assumptions Commonly Used for the Gas Phase Surrounding a Burning Droplet. *Combustion and Flame*, 33:107–122, 1978.

R. Belt and O. Simonin. Quadrature Method of Moments for the PDF Modeling of Droplet Coalescence in Turbulent Two-Phase Flows. In *Proc. of the FEDSM2009*, Vail, Colorado, UAS, August 2-6 2009. ASME 2009 Fluids Engineering Division Summer Meeting. Paper no. FEDSM2009-78095.

M. Bini and W.P. Jones. Large-Eddy Simulation of Particle-Laden Turbulent Flows. *J. Fluid Mech.*, 614:207–252, 2008.

M. Birouk and I. Gökalp. Current Status of Droplet Evaporation in Turbulent Flows. *Progress in Energy and Combustion Science*, 32:408–432, 2006.

M. Boileau, S. Pascaud, E. Riber, B. Cuenot, L.-Y.-M. Gicquel, T. Poinsot, and M. Cazalens. Investigations of Two-Fluid Methods for Large Eddy Simulation of Spray Combustion in Gas Turbines. *Flow, Turbulence and Combustion*, 80(3):291–321, 2008.

M. Boivin, O. Simonin, and K.D. Squires. Direct Numerical Simulation of Turbulence Modulation by Particles in Isotropic Turbulence. *J. Fluid Mech.*, 375:235–263, 1998.

M. Boivin, O. Simonin, and K.D. Squires. On the Prediction of Gas-Solid Flows with Two-Way Coupling using Large Eddy Simulation. *Phys. Fluids*, 12(8):2080–2090, 2000. doi: 10.1063/1.870453.

P. Bollweg, A. Kaufmann, and W. Polifke. Derivation and Application of a Poly-Celerid Method for Polydispersed Two-Phase Flows. In *6th International Conference on Multiphase Flow, Leipzig, Germany*, 2007.

R. Borghi. The Links Between Turbulent Combustion and Spray Combustion and their Modelling. In *Proc. of the 8th Symposium on Transport Phenomena in Combustion (ISTP-VIII)*, pages 1–18, 1995.

R. Borghi. Background on Droplet and Sprays. In *Combustion and Turbulence in Two-Phase Flows, VKI Lecture Series*, volume 1996-02. van Karman Institute, Brussels, 1996.

F. Bouchut. On Zero Pressure Gas Dynamics. *Advances in Kinetic Theory and Computing*, pages 171–190, 1994.

F. Bouchut, S. Jin, and X. Li. Numerical Approximations of Pressureless and Isothermal Gas Dynamics. *SIAM Journal of Numerical Analysis*, 41: 135–158, 2003.

S. Bove, T. Solberg, and B.H. Hjertager. A Novel Algorithm for Solving Population Balance Equations: the Parallel Parent and Daughter Classes. Derivation, Analysis and Testing. *Chem. Eng. Sci.*, 60:1449–1464, 2005.

S. Braun, C. Höfler, R. Koch, and H.-J. Bauer. Modeling Fuel Injection in Gas Turbines Using the Meshless Smoothed Particle Hydrodynamics Method. In *ASME Proceedings. Combustion, Fuels and Emission*, San Antonio, Texas, USA, 2013. ASME. doi: 10.1115/GT2013-94027.

C.E. Brennen. *Fundamentals of Multiphase Flows*. Cambridge University Press, 2005.

T.A. Brzustowski, E.M. Twardus, S. Wojcicki, and A. Sobiesiak. Interaction of Two Burning Fuel Droplets of Arbitrary Size. *AIAA Journal*, 17 (11):1234–1242, 1979.

A.D. Burns, T. Frank, I. Hamill, and J.-M. Shi. The Favre Averaged Drag Model for Turbulent Dispersion in Eulerian Multi-Phase Flows. In *Proc. of ht 5th Int. Conf. on Multiphase Flow*, Yokohama, Japan, 2004. ICMF'04. Paper no. 392.

R. Cabra, Y. Hamano, J.Y. Chen, R.W. Dibble, F. Acosta, and D. Holve. Ensemble Diffraction Measurements of Spray Combustion in a Novel

Viviated Coflow Turbulent Jet Flame Burner. In *Proc. of the Spring Meeting of the Western States Section of the Combustion Institute*, Colorado School of Mines, Golden, Colorado, 2000.

J. Cai, S.-M. Jeng, and R. Tacina. The Structure of a Swirl-Stabilized Reacting Spray Issued from an Axial Swirler. In *Proc. of the AIAA Aerospace Sciences Meeting & Exhibit*. AIAA, 2005. Paper no. AIAA 2005-1424.

J.N.E. Carneiro. *Development of a Presumed Function Method of Moments with Application to Polydisperse Sprays*. PhD thesis, Lehrstuhl für Thermodynamik, TU München, Germany, 2012.

J.N.E. Carneiro, V. Kaufmann, and W. Polifke. Implementation of a Moments Model in OpenFOAM for Polydispersed Multiphase Flows. In *Open Source CFD International Conference, Berlin, Germany*, 2008.

J.N.E. Carneiro, V. Kaufmann, and W. Polifke. Numerical Simulation of Droplet Dispersion and Evaporation with a Moments-based CFD Model. In *Proceedings of COBEM*, 2009.

J.N.E. Carneiro, P. Dems, V. Kaufmann, and W. Polifke. Eulerian Simulations of Polydisperse Flows Using a Moments Model with a Relaxation Approach for the Moment Transport Velocities. In *7th ICMF 2010, Tampa, FL*, 2010.

M.D. Carrara and P.E. DesJardin. On Subgrid Scale Modeling of Evaporating Droplets Using Probability Density Function Methods. In *Proc. of the AIAA Aerospace Science Meeting*, pages 365–384. AIAA, 2005. Paper no. 1426.

M.D. Carrara and P.E. DesJardin. A Filtered Mass Density Function Approach for Modeling Separated Two-Phase Flows for LES I: Mathematical Formulation. *J. of Multiphase Flow*, 32:365–384, 2006.

M.D. Carrara and P.E. DesJardin. A Filtered Mass Density Function Approach for Modeling Separated Two-Phase Flows for LES II: Simulation of a Droplet Laden Temporally Developing Mixing Layer. *J. of Multiphase Flow*, 34:748–766, 2008.

T.-L. Chan, Y.-H. Liu, and C.-K. Chan. Direct Quadrature Method of Moments for the Exhaust Particle Formation and Evolution in the Wake of the Studied Ground Vehicle. *Journal of Aerosol Science*, 41:553–568, 2010.

C.-S. Chang, Y. Zhang, K.N.C. Bray, and B. Rogg. Modelling and Simulation of Autoignition Under Simulated Diesel-Engine Conditions. *Combustion Science Technology*, 113:205–219, 1996.

G. Chen and A. Gomez. Counterflow Diffusion Flames of Quasi-Monodisperse Electrostatic Sprays. *Symposium (International) on Combustion*, 24(1):1531–1539, 1992.

G. Chen and A. Gomez. Dilute Laminar Spray Diffusion Flames near the Transition from Group Combustion to Individual Droplet Burning. *Combustion and Flame*, 110:392–404, 1997.

N.-H. Chen, B. Rogg, and K.N.C. Bray. Modelling Laminar Two-Phase Counterflow Flames with Detailed Chemistry and Transport. *Symposium (International) on Combustion*, 24:1513–1521, 1992.

Y.-C. Chen, S. H. Stårner, and A. R. Masri. Characteristics of Turbulent Spray Combustion in a Piloted Jet Flame Burner. In *Proc. of the Combustion Institute*, volume 29, pages 625–632, 2002.

Y.-C. Chen, S. H. Stårner, and A. R. Masri. A Detailed Experimental Investigation of Well-Defined, Turbulent Evaporating Spray Jets of Acetone. *Int. J. of Multiphase Flow*, 32:389–412, 2006.

Z.H. Chen, T.H. Lin, and S.H. Sohrab. Combustion of Liquid Fuel Sprays in Stagnation-Point Flow. *Combustion Science and Technology*, 60:63–77, 1988.

N. Chigier. Group Combustion Models and Laser Diagnostic Methods in Spray: A Review. *Combustion and Flame*, 51:127–139, 1983.

H.H. Chiu. Advances and Challenges in Droplet and Spray Combustion. I. Towards a Unified Theory of Droplet Aerothermochemistry. *Progress Energy and Combustion Science*, 26:381–416, 2000.

H.H. Chiu and J.-S. Huang. Multiple-State Phenomena and Hysteresis of a Combusting Isolated Droplet. *Atomization and Sprays*, 6(1):1–26, 1996.

H.H. Chiu and T.M. Liu. Group Combustion of Liquid Droplets. *Combustion Science and Technology*, 17:127–142, 1977.

H.H. Chiu, H.Y. Kim, and E.J. Croke. Internal Group Combustion of Liquid Droplets. In *Proc. of the Nineteenth Symposion (Int.) on Combustion*, volume 26, pages 1961–1967. The Combustion Institute, 1996.

M. Chrigui, M. Hage, A. Sadiki, J. Janicka, and A. Dreizler. Experimental and Numerical Analysis of Spray Dispersion and Evaporation in a Combustion Chamber. *Atomization and Spray*, 12:929–955, 2009.

M. Chrigui, K. Moesl, W. Ahmadi, A. Sadiki, and J. Janicka. Partially Premixed Prevaporized Kerosene Spray Combustion in Turbulent Flow. *Experimental Thermal and Fluid Science*, 34(3):308–315, 2010a. doi: 10.1007/s00231-010-0635-1.

M. Chrigui, A. Zghal, A. Sadiki, and J. Janicka. Spray Evaporation and Dispersion of n-Heptane Droplets within Premixed Flame. *Heat and Mass Transfer*, 46:869–880, 2010b. doi: 10.1007/s00231-010-0635-1.

M. Chrigui, J. Gounder, A. Sadiki, A. Masri, and J. Janicka. Partially Premixed Reacting Acetone Spray Using LES and FGM Tabulated Chemistry. *Combustion and Flame*, 159(8):2718–2741, 2012.

M. Chrigui, A.R. Masri, A. Sadiki, and J. Janicka. Large Eddy Simulation of a Polydisperse Ethanol Spray Flame. *Flow Turbulence Combustion*, 90: 813–832, 2013. doi: 10.1007/s10494-013-9449-9.

A. Colagrossi and M. Landrini. Numerical Simulation of Interfacial Flow by Smoothed Particle Hydrodynamics. *J. of Computational Physics*, 191 (2):448–475, 2003.

O. Colin, F. Ducos, D. Veynante, and T. Poinsot. A Thickened Flame Model for Large Eddy Simulations of Turbulent Premixed Combustion. *Physics of Fluids*, 12(7):1843–1863, 2000.

P.J. Colucci, F.A. Jaberi, P. Givi, and S.B. Pope. Filtered Density Function for Large Eddy Simulation of Turbulent Reacting Flows. *Physics of Fluids*, 10(2):499–515, 1998.

G. Continillo and W.A. Sirignano. Counterflow Spray Combustion Modeling. *Combustion and Flame*, 81:325–340, 1990.

C. Crowe, M. Sommerfeld, and Y. Tsuji. *Multiphase Flows with Droplet and Particles*. CRC Press, 1998.

C.T. Crowe. On Models for Turbulence Modulation in Fluid-Particle Flows. *Int. J. of Multiphase Flow*, 26:719–727, 2000.

C.T. Crowe, M.P. Sharma, and D.E. Stock. The Particle-Source-In-Cell (PSI-CELL) Model for Gas-Droplet Flows. *J. Fluids Eng.*, 99(2):325–332, 1977.

B. Cuenot, M. Boileau, S. Pascaud, J.-B. Mossa, E. Riber, T. Poinsot, and C. Bérat. Large Eddy Simulation of Two-Phase Reacting Flows. In *EC-COMAS CFD 2006*, Egmond Aan Zee, The Netherlands, 2006.

N. Darabiha, F. Lacas, J. C. Rolon, and S. Candel. Laminar Counterflow Spray Diffusion Flames : A Comparison Between Experimental Results and Complex Chemistry Calculations. *Combustion and Flame*, 95:267–275, 1992.

S. de Chaisemartin, L. Fréret, D. Kah, F. Laurent, R. O. Fox, J. Reveillon, and M. Massot. Turbulent Combustion of Polydisperse Evaporating Spray with Droplet Crossing: Eulerian Modeling and Validation in the Infinite Knudsen Limit. In *Proceedings of the Summer Program, Center for Turbulence Research*, 2008.

F.-X. Demoulin and R. Borghi. Assumed PDF Modeling of Turbulent Spray Combustion. *Combustion Science and Technology*, 158:249–271, 2000.

P. Dems, J.N.E. Carneiro, and W. Polifke. Large Eddy Simulation of Particle-Laden Swirling Flow with a Presumed Function Method of Moments. *Progress in CFD*, 12:92–102, 2012a.

P. Dems, J.N.E. Carneiro, and W. Polifke. Large Eddy Simulation of a Polydisperse, Evaporating Spray Jet with a Presumed Method of Moments. In *ICLASS 2012, 12th Triennial Int. Conf. on Liquid Atomization and Spray Systems*, Heidelberg, Germany, 2-6 September 2012b.

I.V. Derevich. Statistical Modelling of Mass Transfer in Turbulent Two-Phase Dispersed Flows - 1. Model Development. *Int. J. Heat Mass Transfer*, 43:3709–3723, 2000.

O. Desjardins, R.-O. Fox, and P. Villedieu. A Quadrature-Based Moment Method for Dilute Fluid-Particle Flows. *J. of Computational Physics*, 227: 2514–2539, 2008.

H. Dette and W.J. Studden. *The Theory of Canonical Moments with Applications in Statistics, Probability and Analysis*. John Wiley and Sons Inc., NY, 1997. ISBN 978-0-471-10991-4.

E. Deutsch and O. Simonin. Large Eddy Simulation Applied to the Motion of Particles in Stationary Homogeneous Fluid Turbulence. In *Turbulence Modification in Multiphase Flow*, volume 110, pages 35–42. ASME-FED, 1991.

D. Dewanji, A.G. Rao, M. Pourquie, and J.P. van Buijtenen. Investigation of Flow Characteristics in Lean Direct Injection Combustors. *J. of Propulsion and Power*, 28(1):181–196, 2012. doi: 10.2514/1.B34264.

I. Dhuchakallaya and A.-P. Watkins. Development and Application of the Drop Number Size Moment Modelling to Spray Combustion Simulations. *Applied Thermal Engineering*, 30:1215–1224, 2010.

L. di Mare, M. Klein, W.P. Jones, and J. Janicka. Synthetic Turbulence Inflow Conditions for Large Eddy Simulation. *Physics of Fluids*, 18: 025107/1–11, 2006. doi: 10.1063/1.2130744.

M.D. Donsker. On Function Space Integrals. In W.A. Martin and I. Segal, editors, *Analysis in Function Space*. Cambridge, MA:MIT, 1964.

J.K. Dukowicz. A Particle-Fluid Numerical Model for Liquid Sprays. *J. Comp. Physics*, 35:229–253, 1980.

I. Düwel, H.-W. Ge, H. Kronemayer, R. Dibble, E. Gutheil, C. Schulz, and J. Wolfrum. Experimental and Numerical Characterization of a Turbulent Spray Flame. *Proc. of the Combustion Institute*, 31:2247–2255, 2007.

H.A. Dwyer. Calculations of Droplet Dynamics in High Temperature Environments. *Progress Energy and Combustion Science*, 15(2):131–158, 1989.

U. Egüz, S. Ayyapureddi, C. Bekdemir, L.M.T. Somers, and L.P.H. de Goey. Modeling Fuel Spray Auto-Ignition Using the FGM Approach: Effect of Tabulation Method. In *SAE Technical Papers*, 2012. Paper no. 2012-01-0157.

U. Egüz, S. Ayyapureddi, C. Bekdemir, L.M.T. Somers, and L.P.H. de Goey. Manifold Resolution Study of the FGM Method for an Igniting Diesel Spray. *Fuel*, 113:228–238, 2013.

S. Elghobashi. On Predicting Particle-Laden Turbulent Flows. In M. Sommerfeld, editor, *Proc. 7th Workshop on Two-Phase Flow Predictions*, 1994.

S.E. Elghobashi and T.W. Abou Arab. A Two-Equation Turbulence Model for Two-Phase Flows. *Phys. of Fluids*, 26:931–938, 1989. doi: 10.1063/1.864243.

S.E. Elghobashi, T.W. Abou Arab, M. Rizk, and A. Mostafa. Prediction of the Particle-Laden Jet with a Two-Equation Turbulence Model. *Int. J. of Multiphase Flow*, 10(6):697–710, 1984. doi: 10.1016/0301-9322(84)90006-5.

M.W. Evans and F.H. Harlow. *The Particle-In-Cell Method for Hydrodynamic Calculations*. Los Alamos Scientific Laboratory of the University of California, 1957.

F. Fachini Filho. An Analytical Solution for the Quasi-Steady Droplet Combustion. *Combustion and Flame*, 116:302–306, 1999.

G. Faeth. Current Status of Droplet and Liquid Combustion. *Progress Energy and Combustion Science*, 3(4):191–224, 1977.

G. Faeth. Evaporation and Combustion of Sprays. *Progress Energy and Combustion Science*, 9:1–76, 1983.

G.M. Faeth. Spray combustion phenomena. In *Twenty-Sixth Symposium (International) on Combustion*, pages 1593–1612. The Combustion Institute, 1996.

R. Fan, D.-L. Marchisio, and R.O. Fox. Application of the Direct Quadrature Method of Moments to Polydisperse Gas-Solid Fluidized Beds. *Powder Technology*, 139:7–20, 2004.

P. Fede and O. Simonin. Numerical Study of the Sub grid Fluid Turbulence Effects on the Statistics of Heavy Colliding Particles. *Phys. Fluids*, 18(045103):1–17, 2006. doi: 10.1063/1.2189288.

W. Feller. *An Introduction to Probability Theory and its Applications*, volume 2. Wiley, NY, 1971.

F.E. Fendell. Decompositional Burning of a Droplet in a Small Peclet Number Flow. *AIAA Journal*, 6:1946–1953, 1968. doi: 10.2514/3.4905.

F.E. Fendell, M.L. Sprankle, and D.S. Dodson. Thin-Flame Theory for a Fuel Droplet in Slow Viscous Flow. *J. Fluid Mech.*, 26(2):267–280, 1966.

J. Ferry and S. Balachandar. A First Eulerian Method for Disperse Two-Phase Flow. *Int. J. of Multiphase Flow*, 27:1199–1226, 2001.

J. Ferry and S. Balachandar. Equilibrium Expansion for the Eulerian Velocity of Small Particles. *Powder Technology*, 125:131–139, 2002.

P. Février, O. Simonin, and K.D. Squires. Partitioning of Particle Velocities an Gas-Solid Turbulent Flow into a Continuous Field and a Spatially Uncorrelated Random Distribution: Theoretical Formalism and Numerical Study. *J. of Fluid Mechanics*, 533:1–46, 2005.

R.-O. Fox. Bivariate Direct Quadrature Method of Moments for Coagulation and Sintering of Particle Populations. *Aerosol Science*, 37:1562–1580, 2006.

R.-O. Fox. Large-Eddy-Simulation Tools for Multiphase Flows. *Annu. Rev. Fluid Mech.*, 44:47–76, 2012.

R.-O. Fox, F. Laurent, and M. Massot. Numerical Simulation of Spray Coalescence in an Eulerian Framework: Direct Quadrature Method of Moments and Multi-Fluid Method. *J. of Computational Physics*, 227:3058–3088, 2008.

B. Franzelli, E. Riber, M. Sanjosé, and T. Poinsot. A Two-Step Chemical Scheme for Kerosene-Air Premixed Flames. *Combustion and Flame*, 157: 1364–1373, 2010.

B. Franzelli, B. Fiorina, and N. Darabiha. Modeling the Chemical Structure of Spray Flames Using Tabulated Chemistry Method. In *Proc. of the ICLASS 2012*, 2012.

B. Franzelli, A. Vié, B. Fiorina, and N. Darabiha. Large Eddy Simulation of Swirling Kerosene/Air Spray Flame Using Tabulated Chemistry. In *Proc. of the ASME Turbo Expo 2013*. ASME, 2013. Paper no. GT2013-94451.

M. Frenklach. Method of Moments with Interpolative Closure. *Chem. Eng. Science*, 57:2229–2239, 2002.

M. Frenklach and S.J. Harris. Aerosol Dynamics Modeling Using the Method of Moments. *J. of Colloid and Interface Science*, 118:252–261, 1987.

M. Frenklach and S.J. Harris. Detailed Mechanism and Modeling of Soot Particle Formation. In H. Bockhorn, editor, *Soot Formation in Combustion - Mechanisms and Models*, pages 165–192. Springer-Verlag, Berlin, 1994.

J.A. Friedman and M. Renksizbulut. Investigating a Methanol Spray Flame Interacting with an Annular Air Jet Using Phase-Doppler Interferometry and Planar Laser-Induced Fluorescence. *Combustion and Flame*, 117:661–684, 1999.

Y. Fu, J. Cai, A.M. Elkady, and S.-M. Jeng. Fuel and Equivalence Ratio Effects on Spray Combustion of a Counter-Rotating Swirler. In *Proc. of the AIAA Aerospace Sciences Meeting & Exhibit*. AIAA, 2005a. Paper no. AIAA 2005-0354.

Y. Fu, S.-M. Jeng, and R. Tacina. Characteristics of the Swirling Flow Generated by an Axial Swirler. In *Proc. of the AIAA Aerospace Sciences Meeting & Exhibit*. AIAA, 2005b. Paper no. AIAA 2005-68728.

A. Fujita, H. Watanabe, R. Kurose, and S. Komori. Two-Dimensional Direct Numerical Simulation of Spray Flames - Part 1: Effects of Equivalence Ratio, Fuel Droplet Size and Radiation, and Validity of Flamelet Model. *Fuel*, 104:515–525, 2013.

K. Furutsu. On the Statistical Theory of Electromagnetic Waves in a Fluctuating Medium (I). *J. of Research of the National Bureau of Standards - D. Radio Propagation*, 67D(3):303–323, 1963.

F. Gao. A Large-Eddy Simulation Scheme for Turbulent Reacting Flows. In *Annual Research Briefs*, pages 187–194. Center for Turbulence Research, 1993.

L.P. Gao, Y. D'Angelo, I. Silverman, A. Gomez, and M.D. Smooke. Quantitative Comparison of Detailed Numerical Computations and Experiments in Counterflow Spray Diffusion Flames. In *Proc. of the Twenty-Sixth Symposion (Int.) on Combustion*, pages 1739–1746. The Combustion Institute, 1996.

A. Garmory, E.S. Richardson, and E. Mastorakos. Micromixing Effects in a Reacting Plume by the Stochastic Fields Method. *Atmospheric Environment*, 40:1078–1091, 2006. doi: 10.1016/j.atmosenv.2005.11.002.

E. Garnier, N. Adams, and P. Sagaut. *Large Eddy Simulation for Compressible Flows*. Springer Science+Business Media B.V., 2009. doi: 10.1007/978-90-481-2819-8.

P. Gerlinger. *Numerische Verbrennungssimulation*. Springer, 2005.

E. Gharaibah. *Entwicklung und Validierung eines Modells polydisperser Zweiphasenströmungen unter Berücksichtigung von Koaleszenz und Dispersion*. PhD thesis, Lehrstuhl für Thermodynamik, TU München, Germany, 2008.

E. Gharaibah and W. Polifke. A Numerical Model of Dispersed Two Phase Flow in Aerated Stirred Vessels based on Presumed Shape Number Density Functions. In *Bubbly Flows: Analysis, Modelling, and Calculation*, pages 295–305. Springer, 2004.

L.Y.M. Gicquel, P. Givi, F.A. Jaberi, and S.B. Pope. Velocity Filtered Density Function for Large Eddy Simulation of Turbulent Flows. *Physics of Fluids*, 14(3):1196–1213, 2002.

R.A. Gingold and J.J. Monaghan. Smoothed Particle Hydrodynamics: Theory and Application to Non-Spherical Stars. *Monthly Notices of the Royal Astronomical Society*, 181:375–389, 1977.

G. Godsave. Studies of the Combustion of Drops in a Fuel Spray: The Burning of Single Drops of Fuel. In *Proc. of the Fourth Symposion (Int.) on Combustion*, pages 818–830. The Combustion Institute, Pittsburg, PA., 1954.

G. Gogos, S.S. Sadhal, P.S. Ayyaswamy, and T. Sundararajan. Thin-Flame Theory for the Combustion of a Moving Liquid Drop: Effects Due to Variable Density. *J. of Fluid Mechanics*, 171:121–144, 1986.

P. Gokulakrishnan, R. Joklik, D. Viehe, A. Trettek, E. Gonzalez-Juez, and M. Klassen. Optimization of Reduced Kinetic Models for Reactive Flow Simulations. In *Proc. of ASME Turbo Expo 2013*. ASME, 2013. Paper no. GT2013-95215.

M. Goldsmith and S.S. Penner. On the Burning of Single Drops of Fuel in an Oxidizing Atmosphere. *Jet Propulsion*, 24:245–251, 1954.

J.D. Gounder, A. R. Masri, and S. H. Stårner. On the Effects of Droplet Loading on the Structure of Spray Jets. In *Proc. of the 16th Australasian Fluid Mechanics Conference*, Crwon Plaza, Gold Coast, Australia, 2007.

J.B. Greenberg and N. Sarig. Coupled Evaporation and Transport Effects in Counterflow Spray Diffusion Flames. *Combustion Science and Technology*, 92:1–33, 1993.

J.B. Greenberg and N. Sarig. An Analysis of Multiple Flames in Counterflow Spray Combustion. *Combustion and Flame*, 104:431–459, 1996.

W. Gumprich and A. Sadiki. Numerical Study of Dense Turbulent Sprays Using a Coupling of the Direct Quadrature Method of Moments with an Eulerian Multi-Size Moment Model. In *ICLASS 2012, 12th Triennial Int. Conf. on Liquid Atomization and Spray Systems*, Heidelberg, Germany, 2-6 September 2012.

Y.C. Guo, C.K. Chan, and K.S. Lau. A Pure Eulerian Model for Simulating Dilute Spray Combustion. *Fuel*, 81:2131–2144, 2002.

E. Gutheil. Structure and Extinction of Laminar Ethanol-Air Spray Flames. *Combust. Theory Modelling*, 5:131–145, 2001.

E. Gutheil. Issues in Computational Studies of Turbulent Spray Combustion. In *Experiments and Numerical Simulation of Diluted Spray Turbulent Combustion*, pages 1–39. ERCOFTAC Series Volume 17, 2011.

E. Gutheil and W.A. Sirignano. Counterflow Spray Combustion Modeling with Detailed Transport and Detailed Chemistry. *Combustion and Flame*, 113:92–105, 1998.

C.W. Hirt and B.D. Nichols. Volume of Fluid (VOF) Method for the Dynamics of Free Boundaries. *J. of Computational Physics*, 39:201–225, 1981.

C. Höfler, S. Braun, R. Koch, and H.-J. Bauer. Modeling Spray Formation in Gas Turbines - A New Meshless Approach. *J. of Engineering for Gas Turbines and Power*, 135, 2013. doi: 10.1115/1.4007378.

C. Hollmann and E. Gutheil. Modeling of Turbulent Spray Diffusion Flames Including Detailed Chemistry. *Proc. of the Combustion Institute*, pages 1731–1738, 1996.

C. Hollmann and E. Gutheil. Flamelet-Modeling of Turbulent Spray Diffusion Flames Based on a Laminar Spray Flame Library. *Comb. Sci. and Tech.*, 135:175–192, 1998.

X.Y. Hu and N.A. Adams. A Multi-Phase SPH Method for Macroscopic and Mesoscopic Flows. *J. of Computational Physics*, 213(2):844–861, 2006.

X.Y. Hu and N.A. Adams. A Constant-Density Approach for Incompressible Multi-Phase SPH. *J. of Computational Physics*, 228(6):2082–2091, 2009.

G.L. Hubbard, J.C. Buell, and A.F. Mills. Droplet Evaporation: Effects of Transient and Variable Properties. *Int. J. of Heat and Mass Transfer*, 18: 1003–1008, 1975.

S.-M. Hwang, F. Akamatsu, and H.-S. Park. Evaluation of Combustion Mechanism of Droplet Cluster by Simultaneous Time-Series Measurement in Premixed Spray Flame. *J. Ind. Eng. Chem.*, 13(2):206–213, 2007.

K.E. Hyland, S. McKee, and M.W. Reeks. Derivation of a pdf Kinetic Equation for the Transport of Particles in Turbulent Flows. *J. Phys. A: Math.Gen.*, 32:6169–6190, 1999.

J. Hylkema and P. Villedieu. A Random Particle Method to Simulate Coalescence Phenomena in Dense Liquid Sprays. *Lecture Notes in Physics*, 515:488–493, 1998.

A.C. Iannetti, N.-S. Liu, and F. Davoudzadeh. The Effect of Spray Initial Conditions on Heat Release and Emissions in LDI CFD Calculations. Technical Memo NASA/TM-2008-215422, Glenn Research Center, 2008. URL http://ntrs.nasa.gov.

R. I. Issa and P. J. Oliveira. Assessment of a Particle-Turbulence Interaction Model in Conjunction with an Eulerian Two-Phase Flow Formalism. In T.W.J. Peeters K. Hanjalić, editor, *2nd Int. Symposium on Turbulence, Heat and Mass Transfer*, pages 749–770. Delft University Press, 1997.

F.A. Jaberi, P.J. Colucci, S. James, P. Givi, and S.B. Pope. Filtered Mass Density Function for Large Eddy Simulation of Turbulent Reacting Flows. *J. Fluid Mech.*, 401:85–121, 1999.

E.T. Jaynes. Information Theory and Statistical Mechanics. *Physical Review*, 106(4):620–630, 1957.

P. Jenny, D. Roekaerts, and N. Beishuizen. Modeling of Turbulent Dilute Spray Combustion. *Progress in Energy and Combustion Science*, 38:846–887, 2012.

W.P. Jones and S. Navarro-Martinez. Study of Hydrogen Auto-Ignition in a Turbulent Air Co-Flow Using a Large Eddy Simulation Approach. *Computers and Fluids*, 37(7):802–808, 2008.

W.P. Jones and V.N. Prasad. Large Eddy Simulation of Piloted Methane Jet Flame with High Levels of Extinction (Sandia Flame E) Using Eulerian Stochastic Fields Method. In *Proceedings of the European Combustion Meeting*, 2009.

D. Kah, F. Laurent, L. Fréret, S. de Chaisemartin, R.-O. Fox, J. Reveillon, and M. Massot. Eulerian Quadrature-Based Moment Models for Dilute Polydisperse Evaporating Sprays. *Flow, Turbulence and Combustion*, 85 (3–4):649–676, 2010.

D. Kah, F. Laurent, M. Massot, and S. Jay. A High Order Moment Method Simulating Evaporation and Advection of a Polydisperse Liquid Spray. *Journal of Aerosol Science*, 231:394–422, 2012.

A.N. Karpetis and A. Gomez. An Experimental Investigation of Non-Premixed Turbulent Spray Flames and Their Self-Similar Behaviour. In *Proc. of the Twenty-Seventh Symposion (Int.) on Combustion*, pages 2001–2008. The Combustion Institute, 1998.

A.N. Karpetis and A. Gomez. Self-Similarity, Momentum Scaling and Reynolds Stress in Non-Premixed Turbulent Spray Flames. *J. of Fluid Mechanics*, 397:231–258, 1999. doi: 10.1017/S0022112099006102.

D.R. Kassoy and F.A. Williams. Variable Property Effects on Liquid Droplet Combustion. *AIAA Journal*, 6(10):1961–1965, 1968. doi: 10.2514/3.4907.

A. Kaufmann. *Vers la Simulation des Grand Echelles en Formulation Euler-Euler des Ecoulements Reactifs Diphasiques*. PhD thesis, CERFACS TH/CFD/04/11, No.2089, France, 2004.

A. Kaufmann, O. Simonin, and T. Poinsot. Direct Numerical Simulation of Particle-Laden Homogeneous Isotropic Turbulent Flows Using a Two-Fluid Model Formulation. In *5th Int. Conf. on Multiphase Flow*, 2004.

J.F. Kenney. *Mathematics of Statistics. Part I*. Chapman&Hall, Ltd., London, 1939.

M.K. King. Title not found. In *Proc. of the Combustion Institute*, volume 26, pages 1961–1967. The Combustion Institute, 1996.

M. Kirtaş, N. Patel, V. Sankaran, and S. Menon. Large-Eddy Simulation of a Swirl-Stabilized, Lean Direct Injection Spray Combustor. In *Proc. of ASME Turbo Expo 2006*. ASME, 2006. Paper no. GT2006-91310.

T. Kitano, T. Nakatani, R. Kurose, and S. Komori. Two-Dimensional Direct Numerical Simulation of Spray Flames - Part 2: Effects of Ambient Pressure and Lift, and Validity of Flamelet Model. *Fuel*, 104:526–535, 2013.

M. Klein, A. Sadiki, and J. Janicka. A Digital Filter Based Generation of Inflow Data for Spatially Developing Direct Numerical or Large Eddy Simulation. *J. Comp. Phys.*, 186:652–665, 2004. doi: DOI:10.1016/S0021-9991(03)00090-1.

E. Knudsen and H. Pitsch. Large-Eddy-Simulation of a Spray Combustor Using a Multi-Regime Flamelet Approach, 2010.

D.I. Kolaitis and M.A. Founti. A Comparative Study of Numerical Models for Eulerian-Lagrangian Simulations of Turbulent Evaporating Sprays. *Int. J. of Heat and Fluid Flow*, 27:424–435, 2006.

R.H. Kraichnan. Irreversible Statistical Mechanics of Incompressible Hydromagnetic Turbulence. *The Physical Review*, 109(5):1407–1422, 1958. doi: http://dx.doi.org/10.1063/1.1761271.

R.H. Kraichnan. The Structure of Isotropic Turbulence at Very High Reynolds Numbers. *Fluid Mech.*, 5:497–543, 1959.

R.H. Kraichnan. Lagrangian-History Closure Approximation for Turbulence. *Physics of Fluids*, 8:575–598, 1965. doi: http://dx.doi.org/10.1063/1.1761271.

R.H. Kraichnan. Eulerian and Lagrangian Renormalization in Turbulence Theory. *J. Fluid Mech.*, 2:349–374, 1977. doi: http://dx.doi.org/10.1017/S0022112077001232.

K.K. Kuo. *Principles of Combustion*. Wiley-Interscience, 1986.

K.K. Kuo and R. Acharya. *Fundamentals of Turbulent Multi-Phase Combustion*. John Wiley and Sons, 2012. doi: 10.1002/9781118107683.

S. Laín and C.A. Grillo. Comparison of Turbulent Particle Dispersion Models in Turbulent Shear Flows. *Brazilian Journal of Chemical Engineering*, 24(3):351–363, 2007.

F. Laurent and M. Massot. Multi-Fluid Modeling of Laminar Poly-Dispersed Spray Flames: Origin, Assumptions and Comparison of Sectional and Sampling Methods. *Combustion Theory and Modelling*, 5:537–572, 2001.

F. Laurent, M. Massot, and P. Villedieu. Eulerian Multi-Fluid Modeling for the Numerical Simulation of Coalescence in Polydisperse Dense Liquid Sprays. *J. of Computational Physics*, 194:505–543, 2004.

C. Law. Recent Advances in Droplet Vaporization and Combustion. *Progress Energy and Combustion Science*, 8(3):171–201, 1982.

N. Le Lostec, R.O. Fox, O. Simonin, and P. Villedieu. Numerical Description of Dilute Particle-Laden Flows by a Quadrature-Based Moment Method. In *Proc. of the Summer Program*, pages 209–221. Center for Turbulence Research, 2008.

R. Lecourt, G. Linassier, and G. Lavergne. Detailed Characterization of a Swirled Air/Kerosene Spray in Reactive and Non-Reactive Conditions Downstream from an Actual Turbojet Injection System. In *Proc. of the ASME Turbo Expo 2011: Power for Land, Sea and Air*. ASME, 2011.

J.P. Legier, T. Poinsot, and D. Veynante. Dynamically Thickened Flame LES Model for Premixed and Non-Premixed Turbulent Combustion. In *Proc. of the Summer Program*, pages 157–168. Center for Turbulence Research, 2000.

R.J. LeVeque. *Finite Volume Methods for Hyperbolic Problems*. Cambridge Univ. Press, 2002.

S.C. Li. Spray Stagnation Flames. *Progress in Energy Combustion Science*, 23:303–347, 1997.

J.-C. Lin and T.-H. Lin. Structure and Temperature Distribution of a Stagnation-Point Diesel Spray Premixed Flame. *Energy Conversion and Management*, 46:2892–2906, 2005.

M.B. Liu and G.R. Liu. Smoothed Particle Hydrodynamics (SPH): An Overview and Recent Developments. *Arch. Comput. Methods in Eng.*, 17 (1):25–76, 2010. doi: 10.1088/0034-4885/68/8/R01.

Y. Liu, C. Zheng, and L. Zhou. A Joint PDF Model for Turbulent Spray Evaporation/Combustion. *Proc. of the Combustion Institute*, 29:561–568, 2002.

Y. Liu, L.X. Zhou, and C.X. Xu. Large-Eddy Simulation of Swirling Gas-Particle Flows Using a USM Two-Phase SGS Stress Model. *Powder Technology*, 198:183–188, 2010.

L.B. Lucy. A Numerical Approach to Testing the Fission Hypothesis. *Astronomical Journal*, 82:1013–1024, 1977. doi: 10.1086/112164.

D.-L. Marchisio and R.-O. Fox. Solution of Population Balance Equations Using the Direct Quadrature Method of Moments. *J. Aerosol Sci.*, 36: 43–73, 2005.

D.-L. Marchisio, J.T. Pikturna, R.O. Fox, and R.D. Vigil. Quadrature Method of Moments for Population-Balance Equations. *AIChE Journal*, 49(5):1266–1276, 2003a.

D.-L. Marchisio, R.D. Vigil, and R.-O. Fox. Implementation of the Quadrature Method of Moments in CFD Codes for Aggregation-Breakage Problems. *Chem. Eng. Sci.*, 58:3337–3351, 2003b.

S.K. Marley, K.M. Lyons, and K.A. Watson. Leading-Edge Reaction Zones in Lifted-Jet Gas and Spray Flames. *Flow, Turbulence and Combustion*, 72: 29–47, 2004a.

S.K. Marley, E.J. Welle, K.M. Lyons, and W.L. Roberts. Effects of Leading Edge Entrainment on the Double Flame Structure in Lifted Ethanol Spray Flames. *Experimental Thermal and Fluid Science*, 29:23–31, 2004b. doi: 10.1016/j.expthermflusci.2004.01.009.

F. Mashayek. Droplet-Turbulence Interactions in Low-Mach-Number Homogeneous Shear Two-Phase Flows. *J. Fluid Mech.*, 367:163–203, 1998a.

F. Mashayek. Direct Numerical Simulation of Evaporating Droplet Dispersion in Forced Low Mach Number Turbulence. *Int. J. Heat Mass Transfer*, 41:2601–2617, 1998b.

F. Mashayek and F. Jaberi. Particle Dispersion in Forced Isotropic Low-Mach-Number Turbulence. *Int. J. Heat Mass Transfer*, 42:2823–2836, 1999.

F. Mashayek and R.-V.-R. Pandya. Analytical Description of Particle/Droplet-Laden Turbulent Flows. *Progress in Energy and Combustion Science*, 29:329–378, 2003.

E. Masi, B. Bédat, M. Moreau, and O. Simonin. Euler-Euler Large-Eddy Simulation Approach for Non-Isothermal Particle-Laden Turbulent Jet. In *Proceedings of FEDSM2008, ASME Fluids Engineering Conference*, 2008.

E. Masi, O. Simonin, and B. Bédat. The Mesoscopic Eulerian Approach for Evaporating Droplets Interacting with Turbulent Flows. *Flow Turbulence Combustion*, 86:563–583, 2011.

A. R. Masri and J.D. Gounder. Turbulent Spray Flames of Acetone and Ethanol Approaching Extinction. *Combustion Science and Technology*, 182:702–715, 2010. doi: 10.1080/00102200903467754.

M. Massot. Eulerian Multi-Fluid Models for Polydisperse Evaporating Sprays. In D.L. Marchisio and R.O. Fox, editors, *Multiphase Reacting Flows: Modelling and Simulations*, chapter 3. CISM - International Centre for Mechanical Sciences - Courses and Lecture Series, 2007.

M. Massot, M. Kumar, M.D. Smooke, and A. Gomez. Spray Counterflow Diffusion Flames of Heptane: Experiments and Computations with Detailed Kinetics and Transport. In *27th Symposium (International) on Combustion*, pages 1975–1983. The Combustion Institute, 1998.

M. Massot, F. Laurent, D. Kah, and S. de Chaisemartin. A Robust Moment Method for Evaluation of the Disappearance Rate of Evaporating Sprays. *SIAM Journal on Applied Mathematics*, 70(8):3203–3243, 2010.

L. Mazzei, D.-L. Marchisio, and P. Lettieri. Direct Quadrature Method of Moments for the Mixing of Inert Polydisperse Fluidized Powders and the Role of Numerical Diffusion. *Ind. Eng. Chem. Res.*, 49(11):5141–5152, 2010.

R. McGraw. Description of Aerosol Dynamics by the Quadrature Method of Moments. *Aerosol Science and Technology*, 27:255–265, 1997.

R. McGraw. Correcting Moment Sequences for Errors Associated with Advective Transport. http://www.ecd.bnl.gov/pubs/momentcorrection_mcgraw2006.pdf, 2006.

R. McGraw and D.L. Wright. Chemically Resolved Aerosol Dynamics for Internal Mixtures by the Quadrature Method of Moments. *J. Aerosol Sci.*, 34:189–209, 2003.

L.R. Mead and N. Papanicolaou. Maximum Entropy in the Problem of Moments. *J. Math. Phys.*, 25(8):2404–2417, 1984.

C. Meneveau and T. Poinsot. Stretching and Quenching of Flamelets in Premixed Turbulent Combustion. *Combustion and Flame*, 86:311–332, 1991.

M. Mikami, K. Yamamoto, O. Moriue, and N. Kojima. Combustion of Partially Premixed Spray Jets. *Proc. of the Combustion Institute*, 30:2021–2028, 2005.

R.S. Miller and J. Bellan. Direct Numerical Simulation of a Confined Three-Dimensional Gas Mixing Layer with one Evaporating Hydrocarbon-Droplet-Laden Stream. *J. Fluid Mech.*, 384:293–338, 1999.

R.S. Miller and J. Bellan. Direct Numerical Simulation and Subgrid Analysis of Transitional Droplet Laden Mixing Layer. *Phys. Fluids*, 12(2): 650–671, 2000.

R.S. Miller, K. Harstad, and J. Bellan. Evaluation of Equilibrium and Non-Equilibrium Evaporation Models for Many-Droplet Gas-Liquid Flow Simulations. *Int. J. Multiphase Flow*, 24:1025–1055, 1998.

S. Mimouni, F. Archambeau, M. Boucker, J. Laviéville, and C. Morel. A Second-Order Turbulence Model Based on a Reynolds Stress Approach for Two-Phase Flow - Part I: Adiabatic Cases. *Science and Technology of Nuclear Installations*, 2009:1–14, 2009. doi: 10.1155/2009/792395.

J.-P. Minier and E. Peirano. The PDF Approach to Turbulent Polydispersed Two-Phase Flows. *Physics Reports*, 352:1–214, 2001.

J.J. Monaghan. Simulating Free Surface Flows with SPH. *J. Comput. Phys.*, 110(2):399–406, 1994.

J.J. Monaghan. Smoothed Particle Hydrodynamics. *Reports on Progress in Physics*, 68:1703–1759, 2005. doi: 10.1088/0034-4885/68/8/R01.

J.J. Monaghan and A. Kocharyan. SPH Simulation of Multi-Phase Flow. *Computer Physics Communications*, 87(1-2):225–235, 1995.

M. Moreau, B. Bedat, and O. Simonin. A Priori Testing of Subgrid Stress Models for Euler-Euler Two-Phase LES from Euler-Lagrange Simulations of Gas-Particle Turbulent Flow. In *18th Ann. Conf. on Liquid Atomization and Spray Systems, ILASS Americas*, 2005.

M. Moreau, O. Simonin, and B. Bédat. Development of Gas-Particle Euler-Euler LES Approach: A Priori Analysis of Particle Subgrid Models in Homogeneous Isotropic Turbulence. *Flow Turbulence Combustion*, 84:295–324, 2010.

H. Moriai, R. Kurose, H. Watanabe, and Y. Yano. Large-Eddy Simulation of Turbulent Spray Combustion in a Subscale Aircraft Jet Engine Combustor - Predictions of NO and Soot Concentrations. *J. of Eng. for Gas Turbines and Power*, 135:2135–2142, 2013.

J.P. Morris. Simulating Surface Tension with Smoothed Particle Hydrodynamics. *Numerical Methods in Fluids*, 33(3):333–353, 2000.

M. Mortensen and R.W. Bilger. Derivation of the Conditional Moment Closure Equations for Spray Combustion. *Combustion and Flame*, 156: 62–72, 2009.

J.-B. Mossa. *Extension Polydisperse pour la Description Euler-Euler des Ecoulements Diphasiques Reactifs*. PhD thesis, EDyF, L'Institut National Polytechnique de Toulouse, November 2005.

A. Mostafa and S.E. Elghobashi. A Two-Equation Turbulence Model for Jet Flows Laden with Vaporizing Droplets. *Int. J. of Multiphase Flow*, 11 (4):515–533, 1985. doi: 10.1016/0301-9322(85)90073-4.

L. Muñiz and M.G. Mungal. Instantaneous Flame-Stabilization Velocity in Lifted-Jet Diffusion Flames. *Combustion and Flame*, 111:16–31, 1997.

M.E. Mueller, G. Blanquart, and H. Pitsch. Hybrid Method of Moments for Modelling Soot Formation and Growth. *Combustion and Flame*, 156: 114–1155, 2009. doi: 10.1016/j.combustflame.2009.01.025.

R. Mustata, L. Valiño, C. Jiménez, W.P. Jones, and S. Bondi. A Probability Density Function Eulerian Monte Carlo Field Method for Large Eddy

Simulations: Application to a Turbulent Piloted Methane/Air Diffusion Flame (Sandia D). *Combustion and Flame*, 145(1–2):88–104, 2006.

A. Neophytou and E. Mastorakos. Simulations of Laminar Flame Propagation in Droplet Mists. *Combustion and Flame*, 156:1627–1640, 2009.

A. Neophytou, E. Mastorakos, and R.S. Cant. Complex Chemistry Simulations of Spark Ignition in Turbulent Spray. *Proc. of the Combustion Institute*, 33:2135–2142, 2011.

F. Nicoud and F. Ducros. Subgrid-Scale Stress Modelling Based on the Square of the Velocity Gradient Tensor. *Flow, Turbulence and Combustion*, 62:183–200, 1999.

H. Nomura, M. Hayasaki, and Y. Ujiie. Effects of Fine Fuel Droplets on a Laminar Flame Stabilized in a Partially Prevaporized Spray Stream. *Proc. of the Combustion Institute*, 31:2265–2272, 2007. doi: 10.1016/j.proci.2006.07.080.

P.A. Nordin. *Complex Chemistry Modeling of Diesel Spray Combustion*. PhD thesis, Chalmers University of Technology, Dept. of Thermo and Fluid Dynamics, Göteborg, 2001.

E.A. Novikov. Functionals and the Random-Force Method in Turbulence Theory. *Soviet Physics JETP*, 20(5):1290–1294, 1965.

E.E. O'Brian. The Probability Density Function (PDF) Approach to Reacting Turbulent Flows. In P.A. Libby and F.A. Williams, editors, *Turbulent Reactive Flows, Topics in Applied Physics*, volume 44, pages 185–218. Springer, Heidelberg, 1980.

J.-C. Oefelein. Large Eddy Simulation of Turbulent Combustion Processes in Propulsion and Power Systems. *Progress is Aerospace Sciences*, 42:2–37, 2006.

N.A. Okong'o and J. Bellan. Consistent Large-Eddy Simulation of a Temporal Mixing Layer Laden with Evaporating Drops. Part 1. Direct Numerical Simulation, Formulation and a priori Analysis. *J. Fluid Mech.*, 499:1–47, 2004. doi: 10.1017/S0022112003007018.

J.-P. Oliveira and R.-I. Issa. Numerical Prediction of Particle Dispersion in a Mixing Layer Using an Eulerian Two-Phase Flow Model. In *Proceedings of FEDSM98 ASME Fluids Engineering Division Summer Meeting, Washington DC*, 1998.

S. Osher and R.P. Fedkiw. Level Set Methods: An Overview and Some Recent Results. *J. of Computational Physics*, 169(2):463–502, 2001.

S. Osher and J.A. Sethian. Fronts Propagating with Curvature Dependent Speed: Algorithms Based on Hamilton-Jacobi Formulations. *J. of Computational Physics*, 79:12–49, 1988.

M.G. Pai and S. Subramaniam. Modeling Droplet Dispersion and Interphase Turbulent Kinetic Energy Transfer Using a New Dual-Timescale Langevin Model. *Int. J. of Multiphase Flow*, 33:252–281, 2007. doi: 10.1016/j.ijmultiphaseflow.2006.08.007.

R.-V.-R. Pandya and F. Mashayek. Probability Density Function Modeling of Evaporating Droplets Dispersed in Isotropic Turbulence. *AIAA Journal*, 39:1909–1915, 2001. doi: 10.2514/6.2001-333.

R.-V.-R. Pandya and F. Mashayek. Two-Fluid Large-Eddy Simulation Approach for Particle-Laden Turbulent Flows. *International Journal of Heat and Mass Transfer*, 45:4753–4759, 2002.

R.-V.-R. Pandya and F. Mashayek. Kinetic Equation for Particle Transport and Heat Transfer in Non-Isothermal Turbulent Flows. *AIAA Journal*, 41(5):841–847, 2003a.

R.-V.-R. Pandya and F. Mashayek. Non-Isothermal Dispersed Phase of Particles in Turbulent Flow. *J. Fluid Mech.*, 475:205–245, 2003b.

S. Pannala and S. Menon. On LEM/LES Methodology for Two-Phase Flows. In *Proc. of 35th AIAA/ASME/SAE/ASEE Joint Propulsion Conference and Exhibit*, Los Angeles, California, 1999. AIAA. Paper no. AIAA 99-2209.

N. Patel and S. Menon. Simulation of Spray-Turbulence-Flame Interaction in a Lean Direct Injection Combustor. *Combustion and Flame*, 153: 228–257, 2008.

E. Peirano, S. Chibbaro, J. Pozorski, and J.P. Minier. Mean-Field/PDF Numerical Approach for Polydispersed Turbulent Two-Phase Flows. *Progress Energy and Combustion Science*, 32:315–371, 2006.

M. Petitti, A. Nasuti, D.-L. Marchisio, M. Vanni, G. Baldi, N. Mancini, and F. Podenzani. Bubble Size Distribution Modeling in Stirred Gas-Liquid Reactors with QMOM Augmented by a new Correction Algorithm. *AIChe Journal*, 56:36–53, 2010.

C. Pichard, Y. Michou, C. Chauveau, and I. Gökalp. Average Droplet Vaporization Rates in Partially Prevaporized Turbulent Spray Flames. *Proc. of the Combustion Institute*, 29:527–533, 2002.

T. Poinsot and D. Veynante. *Theoretical and Numerical Combustion*. Edwards Inc., Philadelphia, PA, USA, 2 edition, 2005.

T. Poinsot, D. Veynante, and S. Candel. Quenching Processes and Premixed Turbulent Combustion Diagrams. *J. Fluid Mechanics*, 228:561–606, 1991.

S.B. Pope. The Transport Equation for the Joint Probability Density Function of Velocity ans Scalars in Turbulent Flow. *Physics of Fluid*, 24(4): 588–596, 1981.

S.B. Pope. PDF Methods for Turbulent Reactive Flows. *Progress in Energy and Combustion Science*, 11:119–192, 1985.

J. Pozorski and S.-V. Apte. Filtered Particle Tracking in Isotropic Turbulence and Stochastic Modeling of Subgrid-Scale Dispersion. *International Journal of Multiphase Flow*, 35:118–128, 2009. doi: 10.1016/j.ijmultiphaseflow.2008.10.005.

C. Presser, A.K. Gupta, and H.G. Semerjian. Aerodynamic Characteristics of Swirling Spray Flames: Pressure-Jet Atomizer. *Combustion and Flame*, 92:25–44, 1992.

C. Presser, A.K. Gupta, C.T. Avedisian, and H.G. Semerjian. Droplet Transport in a Swirl-Stabilized Spray Flame. *J. of Propulsion and Power*, 10:631–638, 1994.

M.W. Reeks. Eulerian Direct Interaction Applied to the Statistical Motion of Particles in a Turbulent Field. *J. Fluid Mech.*, 97(3):569–590, 1980. doi: 10.1017/S0022112080002704.

M.W. Reeks. The Transport of Discrete Particles in Inhomogeneous Turbulence. *J. Aerosol Sci.*, 14(6):729–739, 1983. doi: 10.1016/0021-8502(83)90055-1.

M.W. Reeks. On the Continuum Equations for Dispersed Particles in Nonuniform Flows. *Physics of Fluids A*, 4(6):1290–1303, 1992. doi: http://dx.doi.org/10.1063/1.858247.

J. Reveillon and F.-X. Demoulin. Effects of the Preferential Segregation of Droplets on Evaporating and Turbulent Mixing. *J. Fluid Mech.*, 583:273–302, 2007. doi: 10.1017/S0022112007006180.

J. Réveillon and L. Vervisch. Accounting for Spray Vaporization in Turbulent Combustion Modeling. In *Proceedings of the Summer Program*, pages 25–38. Center for Turbulence Research, 1998.

J. Réveillon and L. Vervisch. Analysis of Weakly Turbulent Dilute-Spray Flames and Spray Combustion Regimes. *J. Fluid Mech.*, 537:317–347, 2005. doi: 10.1017/S0022112005005227.

J. Réveillon, M. Massot, and C. Pera. Analysis and Modeling of the Dispersion of Vaporizing Polydispersed Sprays in Turbulent Flows. In *Proceedings of the Summer Program, Center for Turbulence Research*, pages 393–404, 2002.

E. Riber, M. Moreau, O. Simonin, and B. Cuenot. Towards Large Eddy Simulation of Non-Homogeneous Particle Laden Turbulent Gas Flows Using Euler-Euler Approach. In *Proc. of 11th Workshop on Two-Phase Flow Predictions, Merseburg, Germany*, 2005.

E. Riber, M. Moreau, O. Simonin, and B. Cuenot. Development of Euler-Euler LES Approach for Gas-Particle Turbulent Jet Flow. In *Proceedings of FEDSM2006, ASME Joint U.S. - European Fluids Engineering Summer Meeting*, 2006.

E. Riber, V. Moureau, M. García, T. Poinsot, and O. Simonin. Evaluation of Numerical Strategies for Large Eddy Simulation of Particulate Two-Phase Recirculating Flows. *J. of Computational Physics*, 228:539–564, 2009.

G.A. Richards, P.E. Sojka, and A.H. Lefebvre. Flame Speeds in Fuel Spray with Hydrogen Addition. In *Transactions of the ASME*, Gas Turbine and Aeroengine Congress and Exposition, Amsterdam, The Netherlands, 1988.

M.A. Rizk and S.E. Elghobashi. A Two-Equation Turbulence Model for Dispersed Dilute Confined Two-Phase Flow. *Int. J. Multiphase Flow*, 15: 119–133, 1989.

H. Rusche. *Computational Fluid Dynamics of Dispersed Two-Phase Flows at High Phase Fractions*. PhD thesis, Imperial College of Science, Technology and Medicine, UK, 2002.

V. Sabel'nikov, M. Gorokhovski, and N. Baricault. The Extended IEM Mixing Model in the Framework of the Composition ODF Approach: Applications to Diesel Spray Combustion. *Combustion Theory and Modelling*, 10:155–169, 2006.

P. Sagaut. *Large Eddy Simulation for Incompressible Flows*. Springer Berlin Heidelberg, 3 edition, 1998.

V. Sankaran and S. Menon. LES of Spray Combustion in Swirling Flows. *J. Turbulence*, 3(1):11–23, 2002.

S.S. Sazhin. Advanced Models of Fuel Droplet Heating and Evaporation. *Prog. in Energy and Combustion Science*, 32:162–214, 2006.

L. Schiller and A. Nauman. A Drag Coefficient Correlation. *V.D.I. Zeitung*, 77:318–320, 1935.

D. Schlotz and E. Gutheil. Modeling of Laminar Mono- and Bidisperse Liquid Oxygen/Hydrogen Spray Flames in the Counterflow Configuration. *Comb. Sci. and Tech.*, 158:195–210, 2000.

J.S. Serafini. Impingement of Water Droplets on Wedges and Double Wedge Airfoils at Supersonic Speeds. Technical Report 1159, National Advisory Committee for Aeronautics, 1954.

K. Seshadri, C. Trevino, and M.D. Smooke. Analysis of the Structure and Mechanisms of Extinction of a Counterflow Methanol-Air Diffusion Flame. *Combustion and Flame*, 76:111–132, 1989.

C.E. Shannon. A Mathematical Theory of Communication. *The Bell System Technical Journal*, 27:379–423, 623–656, 1948.

M.R.H. Sheikhi, T.G. Drozda, P. Givi, and S.B. Pope. Velocity-Scalar Filtered Density Function for Large Eddy Simulation of Turbulent Flows. *Physics of Fluids*, 15(8):2321–2337, 2003.

T.H. Shih and J.L. Lumley. Second-Order Modelling of Particle Dispersion in a Turbulent Flow. *J. Fluid Mech.*, 163:349–363, 1986.

J.A. Shohat and J.D. Tamarkin. The Problem of Moments. *American Mathematical Society Mathematical Surveys*, 1, 1943.

B. Shotorban and F. Mashayek. Modeling Subgrid-Scale Effects on Particles by Approximate Deconvolution. *Phys. Fluids*, 17(081701):1–4, 2005. doi: 10.1063/1.2001691.

B. Shotorban and F. Mashayek. On Stochastic Modeling of Heavy Particle Dispersion in Large-Eddy Simulation of Two-Phase Turbulent Flow. In S. Balachandar and A. Prosperetti, editors, *Proc. of the IUTAM Symposium on Computational Approaches to Multiphase Flow, Fluid Mechanics and its Applications*, volume 81, pages 373–380. Springer, Netherlands, 2006a.

B. Shotorban and F. Mashayek. A Stochastic Model for Particle Motion in Large-Eddy Simulation. *J Turbulence*, 7(18):1–13, 2006b.

O. Simonin, E. Deutsch, and J.P. Minier. Eulerian Prediction of the Fluid/Particle Correlated Motion in Turbulent Flows. *Appl. Sci. Reseach*, 51:275–283, 1993.

O. Simonin, E. Deutsch, and M. Boivin. Large Eddy Simulation and Second-Moment Closure Model of Particle Fluctuating Motion in Two-Phase Turbulent Shear Flows. In F. Durst, N. Kasagi, B. Launder, F. Schmidt, and J. Whitelaw, editors, *Turbulent Shear Flows*, volume 9, pages 85–115. Springer Berlin Heidelberg, 1995.

O. Simonin, P. Février, and J. Laviéville. On the Spatial Distribution of Heavy-Particle Velocities in Turbulent Flow: From Continuous Field to Particulate Chaos. *J. of Turbulence*, 3:40ff, 2002. doi: 10.1088/1468-5248/3/1/040.

W.-A. Sirignano. Fuel Droplet Vaporisation and Spray Combustion Theory. *Progress Energy Combustion Science*, 9:291–322, 1983.

W.-A. Sirignano. Computational Spray Combustion. In *Numerical Modeling in Combustion*. Taylor & Francis, Bristol, PA, 1993.

W.-A. Sirignano. Volume Averaging for the Analysis of Turbulent Spray Flows. *Int. J. of Multiphase Flow*, 31:675–705, 2005.

W.-A. Sirignano. *Fluid Dynamics and Transport of Droplets and Sprays*. Cambridge University Press, 2 edition, 2010.

N.S.A. Smith, C.M. Cha, H. Pitsch, and J.C. Oefelein. Simulation and Modelling of the Behavior of Conditional Scalar Moments in Turbulent Spray Combustion. In *Proceedings of the Summer Program 2000*, pages 207–218. Center for Turbulence Research, 2000.

M. Sommerfeld and H.-H. Qiu. Detailed Measurements in a Swirling Particulate Two-Phase Flow by a Phase-Doppler Anemometer. *Int. J. Heat and Fluid Flow*, 12(1), 1991.

M. Sommerfeld, G. Kohnen, and M. Rüger. Some Open Questions and Inconsistencies of Lagrangian Particle Dispersion Models. In *Proc. of*

the 9th Symposium on Turbulent Shear Flows, volume 136, pages 31–62, Kyoto, Japan, 1993.

D. Spalding. The Combustion of Liquid Fuels. In *Proc. of the Fourth Symposion (Int.) on Combustion*, pages 847–864. The Combustion Institute, Pittsburg, PA., 1954.

K.D. Squires and J.K. Eaton. Particle Response and Turbulence Modification in Isotropic Turbulence. *Physics of Fluids A*, 2(7):1191–1203, 1990. doi: 10.1063/1.857620.

K.D. Squires and J.K. Eaton. Preferential Concentration of Particles by Turbulence. *Physics of Fluids A*, 3(5):1169–1178, 1991a. doi: 10.1063/1.858045.

K.D. Squires and J.K. Eaton. Measurements of Particle Dispersion from Direct Numerical Simulations of Isotropic Turbulence. *J. Fluid Mech.*, 226:1–35, 1991b. doi: 10.1017/S0022112091002276.

K.D. Squires and O. Simonin. Application of DNS and LES to Dispersed Two-Phase Turbulent Flow. In M. Sommerfeld, editor, *Proc. of the 10th Workshop on Two-Phase Flow Predictions*, pages 152–163, Merseburg, DE, 2002.

S. H. Stårner, J. Gounder, and A. R. Masri. Effects of Turbulence and Carrier Fluid on Simple, Turbulent Spray Jet Flames. *Combustion and Flame*, 143:420–432, 2005.

T.-J. Stieltjes. Recherches sur les Fractions Continues. *Annales de la faculté des sciences de Toulouse*, 8(4):1–122, 1894.

M. Sussman. A Second Order Coupled Level Set and Volume-Of-Fluid Method for Computing Growth and Collapse of Vapor Bubbles. *J. of Computational Physics*, 187(1):110–136, 2003.

M. Sussman and E.G. Puckett. A Coupled Level Set and Volume-Of-Fluid Method for Computing 3D and Axisymmetric Incompressible Two-Phase Flows. *J. of Computational Physics*, 162(2):301–337, 2000.

M. Sussman, P. Smereka, and S. Osher. A Level Set Approach for Computing Solutions to Incompressible Two-Phase Flow. *J. of Computational Physics*, 114(1):146–159, 1994.

S. Tenneti, R. Garg, C.M. Hrenya, R.O. Fox, and S. Subramaniam. Direct Numerical Simulation of Gas-Solid Suspensions at Moderate Reynolds Number: Quantifying the Coupling Between Hydrodynamic Forces and Particle Velocity Fluctuations. *Powder Technology*, 203:57–69, 2010.

J. Tillou, J.-B. Michel, C. Angelberger, and D. Veynante. Assessing LES Models Based on Tabulated Chemistry for the Simulation of Diesel Spray Combustion. *Combustion and Flame*, 161(2):525–540, 2014.

G. Tryggvason, B. Bunner, A. Esmaeeli, D. Juric, N. Al-Rawahi, W. Tauber, J. Han, S. Nas, and Y.J. Jan. A Front-Tracking Method for the Computation of Multiphase Flow. *J. of Computational Physics*, 169:708–759, 2001.

E.M. Twardus and T.A. Brzustowski. The Interaction Between Two Burning Fuel Droplets. *Archiwum Processor Spalania*, 8:347–358, 1977.

S. Ulzama and E. Specht. An Analytical Study of Droplet Combustion Under Microgravity: Quasi-Steady Transient Approach. In *Proc. of the Combustion Institute*, volume 31, pages 2301–2308. The Combustion Institute, 2007. doi: 10.1016.

A. Umemura and S. Takamori. Percolation Theory for Flame Propagation in Non- or Less-Volatile Fuel Spray: A Conceptual Analysis to Group Combustion Excitation Mechanism. *Combustion and Flame*, 141:336–349, 2005.

S.O. Unverdi and G. Tryggvason. A Front-Tracking Method for Viscous, Incompressible, Multi-Fluid Flows. *J. of Computational Physics*, 100:25–37, 1992.

J. Urzay. A Revised Spray-Combustion Diagram of Diffusion-Controlled Burning Regimes in Fuel-Spray Clouds. *Annual Research Briefs*, pages 193–198, 2011.

L. Valiño. A Field Monte Carlo Formulation for Calculating the Probability Density Function of a Single Scalar in a Turbulent Flow. *Flow, Turbulence and Combustion*, 60:157–172, 1998.

N.G. van Kampen. *Stochastic Processes in Physics and Chemistry*. Elsevier, Amsterdam, The Netherlands, 1997.

M. van Sint Annaland, N.G. Deen, and J.A.M. Kuipers. Numerical Simulation of Gas Bubbles Behaviour Using a Tgree-Dimensional Volume of Fluid Method. *Chem. Eng. Science*, 60(11):2999–3011, 2005.

A. Vié, M. Sanjosé, S. Jay, C. Angelberger, B. Cuenot, and M. Massot. Evaluation of a Multi-Fluid Mesoscopic Eulerian Formalism on the Large Eddy Simulation of an Aeronautical-Type Configuration. In *Proc. of the 7th Int. Conf. on Multiphase Flow*, Tampa, Florida, May 30 - June 4 2010.

A. Vié, F. Laurent, and M. Massot. Size-Velocity Correlations in High Order Moment Methods for Polydisperse Evaporating Sprays: Modeling and Numerical Issues. *Journal of Computational Physics*, 237:177–210, 2013. doi: 10.1016/j.jcp.2012.11.043.

V. Vikas, Z.J. Wang, A. Passalacqua, and R.O. Fox. Development of High-Order Realizable Finite-Volume Schemes for Quadrature-Based Moment Method. In *48th AIAA Aerospace Science Meeting Including the New Horizons Forum and AeroSpace Exposition*, Orlando, Florida, 4-7 January 2010. American Institute of Aeronautics and Astronautics. Paper no. FEDSM2009-78095.

V. Vikas, Z.J. Wang, A. Passalacqua, and R.O. Fox. Realizable High-Order Finite-Volume Schemes for Quadrature-Based Moment Methods. *J. of Computational Physics*, 230:5328–5352, 2011.

I. Vinkovic, C. Aguirre, S. Simoëns, and M. Gorokhovski. Large Eddy Simulation of Droplet Dispersion for Inhomogeneous Turbulent Wall Flow. *Int. J. of Multiphase Flow*, 32:344–364, 2006. doi: 10.1016/j.ijmultiphaseflow.2005.10.005.

L.A. Vulis. *Thermal Regimes of Combustion*. New York: McGraw-Hill, 1961.

F. Wang, A.I. Sayma, Z.J. Peng, and Y. Huang. A Multi-Section Droplet Combustion Model for Spray Combustion. In *Proceedings of ASME Turbo Expo 2011*, June 6-10, Vancouver, British Columbia, Canada, 2011. Paper no. GT2011-45023.

L. P. Wang and D. E. Stock. Dispersion of Heavy Particles by Turbulent Motion. *J. Atmos. Sci.*, 50:1897–1913, 1993.

Q. Wang and K.D. Squires. Large Eddy Simulation of Particle Deposition in a Vertical Turbulent Channel Flow. *Int. J. Multiphase Flow*, 22(4):667–683, 1996a.

Q. Wang and K.D. Squires. Large Eddy Simulation of Particle-Laden Turbulent Channel Flow. *Phys. Fluids*, 8(5):1207–1223, 1996b.

H. Watanabe, R. Kurose, S.-M. Hwang, and F. Akamatsu. Characteristics of Flamelets in Spray Flames Formed in a Laminar Counterflow. *Combustion and Flame*, 148(4):234–248, 2007.

A.-P. Watkins. The Application of Gamma and Beta Number Size Distributions to the Modelling of Sprays. In *Proceedings of the 20th ILASS-Europe, Orléans, France, September*, 2005.

A.-P. Watkins. Modelling the Mean Temperatures used for Calculating Heat and Mass Transfer in Sprays. *Int. J. of Heat and Fluid Flow*, 28: 388–406, 2007.

H.-G. Weller. Derivation, Modelling and Solution of the Conditionally Averaged Two-Phase Flow Equations. Technical Report TR/HGW/02, OpenCFD Ltd., 2005.

C.K. Westbrook and F.L. Dryer. Simplified Reaction Mechanisms for the Oxidation of Hydrocarbon Fuels in Flames. *Combustion Science and Technology*, 27:31–43, 1981.

J.F. Widmann and C. Presser. A Benchmark Experimental Database for Multiphase Combustion Model Input and Validation. *Combustion and Flame*, 129:47–86, 2002.

A. Williams. Combustion of Droplets of Liquid Fuels: A Review. *Combustion and Flame*, 21(1):1–31, 1973.

Y.M. Wright, G. De Paola, K. Boulouchos, and E. Mastorakos. Simulations of Spray Autoignition and Flame Establishment with Two-Dimensional CMC. *Combustion and Flame*, 143:402–419, 2005.

D.L. Wright Jr. Numerical Advection of Moments of the Particle Size Distribution in Eulerian Models. *J. of Aerosol Science*, 38:1352–369, 2007. doi: 10.1016/j.jaerosci.2006.11.011.

D.L. Wright Jr., R. McGraw, and D.E. Rosner. Bivariate Extension of the Quadrature Method of Moments for Modeling Simultaneous Coagulation and Sintering of Particle Populations. *J. of Colloid and Interface Science*, 236:242–251, 2001. doi: 10.1006/jcis.2000.7409.

D. Wunsch, R. Belt, P. Fede, and O. Simonin. DNS/DPS of Inertial Droplet Coalescence in Homogeneous Isotropic Turbulence and Comparison with PDF Model Predictions Using Direct Quadrature Method of Moments. In *Proc. of the FEDSM2009*, Vail, Colorado, UAS, August 2-6 2009. ASME 2009 Fluids Engineering Division Summer Meeting. Paper no. FEDSM2009-78091.

C.Y. Yang and U. Lei. The Role of the Turbulent Scales in the Settling Velocity of Heavy Particles in Homogeneous Isotropic Turbulence. *J. Fluid Mech.*, 371:179–205, 1998.

F. Yeh and U. Lei. On the Motion of Small Particles in a Homogeneous Isotropic Turbulent Flow. *Phys. Fluids A*, 3(11):2571–2586, 1991.

C. Yoon and R. McGraw. Representation of Generally Mixed Multivariate Aerosols by the Quadrature Method of Moments: II. Aerosol Dynamics. *J. of Aerosol Science*, 35:577–598, 2004. doi: 10.1016/j.aerosci.200.11.012.

D.L. Youngs. Time-Dependent Multi-Material Flow with Large Fluid Distortion. *Numerical Methods for Fluid Dynamics*, pages 273–285, 1982.

C. Yuan, F. Laurent, and R.-O. Fox. An Extended Quadrature Method of Moments for Population Balance Equations. *J. of Aerosol Science*, 51: 1–23, 2012.

S. Yuu, T. Ueno, and T. Umekage. Numerical Simulation of the High Reynolds Number Slit Nozzle Gas-Particle Jet Using Subgrid-Scale Coupling Large Eddy Simulation. *Chem. Eng. Science*, 56:4293–4307, 2001.

L.I. Zaichik. A Statistical Model of Particle Transport and Heat Transfer in Turbulent Shear Flows. *Physics of Fluids*, 11(6):1521–1534, 1999. doi: 10.1063/1.870015.

D.Z. Zhang and A. Prosperetti. Averaged Equations for Inviscid Dispersed Two-Phase Flow. *J. Fluid Mech.*, 267:185–219, 1994.

D.Z. Zhang and A. Prosperetti. Momentum and Energy Equations for Disperse Two-Phase Flows and Their Closure for Dilute Suspensions. *Int. J. on Multiphase Flow*, 23(3):425–453, 1997.

L.X. Zhou. Developing Multiphase and Reacting Turbulence Models. In *Proc. of the 7th Int. Conf. on CFD in the Minerals and Process Industries*. CSIRO, Melbourne, Australia, 2009.

L.X. Zhou and Y. Liu. Two-Phase Subgrid-Scale (SGS) Stress Models for Two-Fluid Large-Eddy Simulation of Gas-Particle Flows. In *7th Int. Conf. on Multiphase Flow*, Tampa, Florida, USA, May 30- June 4 2010.

X.Y. Zhou and J.F.C. Pereira. Large Eddy Simulation (2D) of a Reacting Plan Mixing Layer Using Filtered Density Function. *Flow, Turbulence, Combustion*, 64:279–, 2000.

A. Zucca, D.-L. Marchisio, A.A. Barresi, and R.O. Fox. Implementation of the Population Balance Equation in CFD Codes for Modelling Soot Formation in Turbulent Flames. *Chem. Eng. Sci.*, 61:87–95, 2006.

A Appendix

A.1 Appendix to Chapter 3

A.1.1 Connection Between Sensible Enthalpy, Inner and Total Energy Equation

The equation of the total energy without chemical energy $E = e + \frac{k}{\rho}$, where e is the inner energy and k the kinetic energy $k = \frac{1}{2}\rho\mathbf{u}^2$, reads

$$\frac{\partial(\rho E)}{\partial t} + \nabla\cdot(\rho E\mathbf{u}) + \nabla\cdot(p\mathbf{u}) + \nabla\dot{q}_{\text{rad}} + \nabla\cdot\left(\sum_m \rho\mathbf{V}_m h_m Y_m\right) = \nabla\cdot(\lambda\nabla T) + \nabla\cdot(\boldsymbol{\tau}\cdot\mathbf{u}) + \sum_m \rho\dot{\omega}_m Q_m\,. \quad \text{(A.1)}$$

Subtracting the kinetic energy equation

$$\frac{\partial k}{\partial t} + \nabla\cdot(k\mathbf{u}) = -\mathbf{u}\nabla p + \mathbf{u}\nabla\cdot\boldsymbol{\tau} \quad \text{(A.2)}$$

gives the equation for only the inner energy e:

$$\frac{\partial(\rho e)}{\partial t} + \nabla\cdot(\rho e\mathbf{u}) + p\nabla\cdot\mathbf{u} + \nabla\dot{q}_{\text{rad}} + \nabla\cdot\left(\sum_m \rho\mathbf{V}_m h_m Y_m\right) = \nabla\cdot(\lambda\nabla T) + \boldsymbol{\tau} : (\nabla\mathbf{u}) + \sum_m \rho\dot{\omega}_m Q_m\,. \quad \text{(A.3)}$$

Adding the moving boundary work (or pressure-volume (pV-) work), i.e.

$e + \frac{p}{\rho} = h$, results in the equation for the enthalpy h

$$\frac{\partial(\rho h)}{\partial t} - \frac{\partial p}{\partial t} + \nabla\cdot(\rho h\mathbf{u}) - \nabla\cdot(p\mathbf{u}) + p\nabla\cdot\mathbf{u} + \nabla\dot{q}_{\text{rad}} + \nabla\cdot\left(\sum_m \rho\mathbf{V}_m h_m Y_m\right) = \nabla\cdot(\lambda\nabla T) + \boldsymbol{\tau} : (\nabla\mathbf{u}) + \sum_m \rho\dot{\omega}_m Q_m \quad \text{(A.4)}$$

$$\frac{\partial(\rho h)}{\partial t} + \nabla\cdot(\rho h\mathbf{u}) + \nabla\dot{q}_{\text{rad}} + \nabla\cdot\left(\sum_m \rho\mathbf{V}_m h_m Y_m\right) = \underbrace{\frac{\partial p}{\partial t} + \underbrace{\nabla\cdot(p\mathbf{u}) - p\nabla\cdot\mathbf{u}}_{\mathbf{u}\cdot\nabla p}}_{\frac{dp}{dt}} + \nabla\cdot(\lambda\nabla T) + \boldsymbol{\tau} : (\nabla\mathbf{u}) + \sum_m \rho\dot{\omega}_m Q_m \quad \text{(A.5)}$$

$$\frac{\partial(\rho h)}{\partial t} + \nabla\cdot(\rho h\mathbf{u}) + \nabla\dot{q}_{\text{rad}} + \nabla\cdot\left(\sum_m \rho Y_m\mathbf{V}_m h_m\right) = \frac{dp}{dt} + \nabla\cdot(\lambda\nabla T) + \boldsymbol{\tau} : (\nabla\mathbf{u}) + \sum_m \rho\dot{\omega}_m Q_m\,. \quad \text{(A.6)}$$

A.1.2 Parts of Vaporisation Modelling (Section 3.2.1)

Diffusion Controlled Mass Rate

Reformulation of the mass change rate in terms of the temporal derivative of particle diameter. The contribution due to forced convection in the Stokes flow regime (S) develops as

$$\dot{m}_{M,nc}^{(n)} = 2\pi\rho^{@\mathbf{x}_p^{(n)}}\mathfrak{D}D^{(n)}\ln(1+\mathrm{B}_M^{@\mathbf{x}_p^{(n)}})$$
$$\frac{dD_{\mathrm{S}}^{(n)^3}}{dt} = -12\frac{\rho^{@\mathbf{x}_p^{(n)}}}{\rho_p}\mathfrak{D}D^{(n)}\ln(1+\mathrm{B}_M^{@\mathbf{x}_p^{(n)}})$$

$$3D^{(n)2}\frac{dD_{\mathrm{S}}^{(n)}}{dt} = -12\frac{\rho^{@\mathbf{x}_p^{(n)}}}{\rho_p}\mathfrak{D}D^{(n)}\ln(1+\mathrm{B}_M^{@\mathbf{x}_p^{(n)}})$$
$$\frac{dD_{\mathrm{S}}^{(n)}}{dt} = -4\frac{\rho^{@\mathbf{x}_p^{(n)}}}{\rho_p D^{(n)}}\mathfrak{D}\ln(1+\mathrm{B}_M^{@\mathbf{x}_p^{(n)}}) \tag{A.7}$$

and the part for higher Reynolds numbers (nS) as

$$\dot{m}_{M,wc}^{(n)} = 0.552\left(\frac{(\mathbf{u}^{@\mathbf{x}_p^{(n)}} - \mathbf{v}_p^{(n)})D^{(n)}}{\nu^{@\mathbf{x}_p^{(n)}}}\right)^{1/2}\mathrm{Sc}^{1/3}\pi\rho^{@\mathbf{x}_p^{(n)}}\mathfrak{D}D^{(n)}\frac{\ln(1+\mathrm{B}_M^{@\mathbf{x}_p^{(n)}})}{F_{\mathrm{M}}}$$

$$\dot{m}_{M,wc}^{(n)} = 0.552\pi\rho^{@\mathbf{x}_p^{(n)}}\mathfrak{D}\left(\frac{(\mathbf{u}^{@\mathbf{x}_p^{(n)}} - \mathbf{v}_p^{(n)})}{\nu^{@\mathbf{x}_p^{(n)}}}\right)^{1/2}\mathrm{Sc}^{1/3}D^{(n)3/2}\frac{\mathrm{B}_{\mathrm{M}}^{@\mathbf{x}_p^{(n)}}}{(1+\mathrm{B}_{\mathrm{M}}^{@\mathbf{x}_p^{(n)}})^{0.7}}$$

$$\frac{\pi}{6}\rho_p\frac{dD_{\mathrm{nS}}^{(n)3}}{dt} = -0.552\pi\rho^{@\mathbf{x}_p^{(n)}}\mathfrak{D}\left(\frac{(\mathbf{u}^{@\mathbf{x}_p^{(n)}} - \mathbf{v}_p^{(n)})}{\nu^{@\mathbf{x}_p^{(n)}}}\right)^{1/2}\mathrm{Sc}^{1/3}D^{(n)3/2}\frac{\mathrm{B}_{\mathrm{M}}^{@\mathbf{x}_p^{(n)}}}{(1+\mathrm{B}_{\mathrm{M}}^{@\mathbf{x}_p^{(n)}})^{0.7}}$$

$$\frac{dD_{\mathrm{nS}}^{(n)3}}{dt} = -0.552\cdot 6\frac{\rho^{@\mathbf{x}_p^{(n)}}}{\rho_p}\mathfrak{D}\left(\frac{(\mathbf{u}^{@\mathbf{x}_p^{(n)}} - \mathbf{v}_p^{(n)})}{\nu^{@\mathbf{x}_p^{(n)}}}\right)^{1/2}\mathrm{Sc}^{1/3}D^{(n)3/2}\frac{\mathrm{B}_{\mathrm{M}}^{@\mathbf{x}_p^{(n)}}}{(1+\mathrm{B}_{\mathrm{M}}^{@\mathbf{x}_p^{(n)}})^{0.7}}$$

$$3D^{(n)2}\frac{dD_{\mathrm{nS}}^{(n)}}{dt} = -0.552\cdot 6\frac{\rho^{@\mathbf{x}_p^{(n)}}}{\rho_p}\mathfrak{D}\left(\frac{(\mathbf{u}^{@\mathbf{x}_p^{(n)}} - \mathbf{v}_p^{(n)})}{\nu^{@\mathbf{x}_p^{(n)}}}\right)^{1/2}\mathrm{Sc}^{1/3}D^{(n)3/2}\frac{\mathrm{B}_{\mathrm{M}}^{@\mathbf{x}_p^{(n)}}}{(1+\mathrm{B}_{\mathrm{M}}^{@\mathbf{x}_p^{(n)}})^{0.7}}$$

$$\frac{dD_{\mathrm{nS}}^{(n)}}{dt} = -0.552\cdot 2\frac{\rho^{@\mathbf{x}_p^{(n)}}}{\rho_p}\mathfrak{D}\left(\frac{(\mathbf{u}^{@\mathbf{x}_p^{(n)}} - \mathbf{v}_p^{(n)})}{\nu^{@\mathbf{x}_p^{(n)}}}\right)^{1/2}\frac{\mathrm{Sc}^{1/3}}{D^{(n)1/2}}\frac{\mathrm{B}_{\mathrm{M}}^{@\mathbf{x}_p^{(n)}}}{(1+\mathrm{B}_{\mathrm{M}}^{@\mathbf{x}_p^{(n)}})^{0.7}}\,. \tag{A.8}$$

Heat Conduction Controlled Mass Rate

Simplification of the mass change rate to be used for the derivation of the temporal derivatives of the particle temperature is shown next. The

Stokes part (S) develops accordingly as shown above as

$$\dot{m}_{T,S}^{(n)} = 2\pi \frac{\lambda^{@\mathbf{x}_p^{(n)}}}{c_{\mathrm{p}v}^{@\mathbf{x}_p^{(n)}}} D^{(n)} \ln(1 + \mathrm{B}_T^{@\mathbf{x}_p^{(n)}})$$
$$\frac{dD_S^{(n)}}{dt} = -4 \frac{\lambda^{@\mathbf{x}_p^{(n)}}}{\rho_p c_{\mathrm{p}v}^{@\mathbf{x}_p^{(n)}} D^{(n)}} \ln(1 + \mathrm{B}_T^{@\mathbf{x}_p^{(n)}}) \tag{A.9}$$

and the non-Stokes part (nS) as

$$\dot{m}_{T,\mathrm{nS}}^{(n)} = 0.552 \left(\frac{(\mathbf{u}^{@\mathbf{x}_p^{(n)}} - \mathbf{v}_p^{(n)}) D^{(n)}}{\nu^{@\mathbf{x}_p^{(n)}}} \right)^{1/2} \mathrm{Pr}^{1/3} \pi \frac{\lambda^{@\mathbf{x}_p^{(n)}}}{c_{\mathrm{p}v}^{@\mathbf{x}_p^{(n)}}} D^{(n)} \frac{\ln(1 + \mathrm{B}_T^{@\mathbf{x}_p^{(n)}})}{F_{\mathrm{T}}^{@\mathbf{x}_p^{(n)}}}$$
$$\dot{m}_{T,\mathrm{nS}}^{(n)} = 0.552\pi \frac{\lambda^{@\mathbf{x}_p^{(n)}}}{c_{\mathrm{p}v}^{@\mathbf{x}_p^{(n)}}} \left(\frac{(\mathbf{u}^{@\mathbf{x}_p^{(n)}} - \mathbf{v}_p^{(n)})}{\nu^{@\mathbf{x}_p^{(n)}}} \right)^{1/2} \mathrm{Pr}^{1/3} {D^{(n)}}^{3/2} \frac{\mathrm{B}_{\mathrm{T}}^{@\mathbf{x}_p^{(n)}}}{(1 + \mathrm{B}_{\mathrm{T}}^{@\mathbf{x}_p^{(n)}})^{0.7}} \tag{A.10}$$

$$\frac{dD_{\mathrm{nS}}^{(n)}}{dt} = -0.552 \cdot 2 \frac{\lambda^{@\mathbf{x}_p^{(n)}}}{\rho_p c_{\mathrm{p}v}^{@\mathbf{x}_p^{(n)}}} \left(\frac{(\mathbf{u}^{@\mathbf{x}_p^{(n)}} - \mathbf{v}_p^{(n)})}{\nu^{@\mathbf{x}_p^{(n)}}} \right)^{1/2} \frac{\mathrm{Pr}^{1/3}}{{D^{(n)}}^{1/2}} \frac{\mathrm{B}_{\mathrm{T}}^{@\mathbf{x}_p^{(n)}}}{(1 + \mathrm{B}_{\mathrm{T}}^{@\mathbf{x}_p^{(n)}})^{0.7}} . \tag{A.11}$$

A.1.3 Derivation of the W_p Transport Equation

In two-phase context using Lagrangian particle equations, W_p is favourably written as "Lagrangian PDF" (see Minier and Peirano, 2001, Sec. 6.4.2f), i.e. the physical location is included in the phase space as $\delta(\mathbf{x} - \mathbf{x}_p^{(n)})$. Therefore (in line with Février et al. (2005), Hyland et al. (1999), etc., W_p is written as

$$W_p^{(n)}(D, \mathbf{c}_p, \zeta_p; \mathbf{x}, t, \mathcal{H}_p | \mathcal{H}_f)$$
$$= \delta(\mathbf{x} - \mathbf{x}_p^{(n)}(t)) \delta(D - D_p^{(n)}(t)) \delta(\mathbf{c}_p - \mathbf{v}_p^{(n)}(t)) \delta(\zeta_p - T_p^{(n)}(t)) \tag{A.12}$$

and the temporal derivative reads

$$\frac{\partial W_p}{\partial t} = -\frac{\partial}{\partial x_i}\left(W_p \frac{dx_{p,i}^{(n)}}{dt}\right) - \frac{\partial}{\partial D}\left(W_p \frac{dD^{(n)}}{dt}\right) - \frac{\partial}{\partial c_{p,j}}\left(W_p \frac{dv_{p,j}^{(n)}}{dt}\right) - \frac{\partial}{\partial \zeta_p}\left(W_p \frac{dT_p^{(n)}}{dt}\right) , \tag{A.13}$$

where the first term on the rhs can be reformulated with help of Eqn. 3.36 as

$$-\frac{\partial}{\partial x_i}\left(W_p \frac{dx_{p,i}^{(n)}}{dt}\right) = -\frac{\partial}{\partial x_i}\left(W_p v_{p,i}^{(n)}\right) . \tag{A.14}$$

This yields the transport equation for W_p:

$$\frac{\partial W_p}{\partial t} + \frac{\partial W_p v_{p,i}^{(n)}}{\partial x_i} = - \frac{\partial}{\partial D}\left(W_p \frac{dD^{(n)}}{dt}\right) - \frac{\partial}{\partial c_{p,j}}\left(W_p \frac{dv_{p,j}^{(n)}}{dt}\right) - \frac{\partial}{\partial \zeta_p}\left(W_p \frac{dT_p^{(n)}}{dt}\right) . \tag{A.15}$$

Since $v_{p,i}^{(n)}$ is not a function of $\mathbf{x}$, one can write

$$\frac{\partial W_p v_{p,i}^{(n)}}{\partial x_i} = v_{p,i}^{(n)} \frac{\partial W_p}{\partial x_i} , \tag{A.16}$$

however, applying an average/filter yields only a meaningful solution for $\frac{\partial W_p v_{p,i}^{(n)}}{\partial x_i}$, since $\langle v_{p,i}^{(n)} \frac{\partial W_p}{\partial x_i} | \boldsymbol{\mathcal{I}} \rangle^{\mathcal{E}}$ must be recasted to the former version in any case:

$$\langle v_{p,i}^{(n)} \frac{\partial W_p}{\partial x_i} | \boldsymbol{\mathcal{I}} \rangle^{\mathcal{E}} = \langle \frac{\partial W_p v_{p,i}^{(n)}}{\partial x_i} | \boldsymbol{\mathcal{I}} \rangle^{\mathcal{E}} = \frac{\partial \langle W_p v_{p,i}^{(n)} | \boldsymbol{\mathcal{I}} \rangle^{\mathcal{E}}}{\partial x_i} = \frac{\partial \breve{f} \langle v_{p,i}^{(n)} | \boldsymbol{\mathcal{I}} \rangle^{\mathcal{E}}}{\partial x_i} . \tag{A.17}$$

Now, this equation can be ensemble averaged over particle phase realisations, or gas phase realisations, or both, and optionally filtered subsequently, or the latter without any ensemble average. We want to apply an

ensemble average over particle phase realisations for a given gas phase realisation and subsequent filtering. First, applying an ensemble average over a large number of particle phase realisations $\mathcal{H}_p$ for a given fluid flow realisation $\mathcal{H}_p$ only, Eqn. A.15 yields

$$\begin{aligned}\frac{\partial\langle W_p|\boldsymbol{\mathcal{I}}\rangle^{\mathcal{E}}}{\partial t}+\frac{\partial\langle W_p v_{p,i}^{(n)}|\boldsymbol{\mathcal{I}}\rangle^{\mathcal{E}}}{\partial x_i}=&-\frac{\partial}{\partial D}\left(\langle W_p\frac{dD^{(n)}}{dt}|\boldsymbol{\mathcal{I}}\rangle^{\mathcal{E}}\right)\\&-\frac{\partial}{\partial c_{p,j}}\left(\langle W_p\frac{dv_{p,j}^{(n)}}{dt}|\boldsymbol{\mathcal{I}}\rangle^{\mathcal{E}}\right)\\&-\frac{\partial}{\partial \zeta_p}\left(\langle W_p\frac{dT_p^{(n)}}{dt}|\boldsymbol{\mathcal{I}}\rangle^{\mathcal{E}}\right)\end{aligned}\tag{A.18}$$

and, since phase space is still distinguished, gas phase variables are invariant (i.e. conditioned on a single gas phase realisation) and all source terms $\frac{d}{dt}$ are only a function of those and not, e.g., of their gradients (which would make things more difficult), the ensemble average is rather without effect but improves only the quality of the statistics of W_p and yields the ensemble average based NDF (EbNDF) $\breve{f}$:

$$\begin{aligned}\frac{\partial\breve{f}}{\partial t}+\frac{\partial\breve{f}c_{p,i}}{\partial x_i}=&-\frac{\partial}{\partial D}\left(\breve{f}\langle\frac{dD^{(n)}}{dt}|\boldsymbol{\mathcal{I}}\rangle^{\mathcal{E}}\right)\\&-\frac{\partial}{\partial c_{p,j}}\left(\breve{f}\langle\frac{dv_{p,j}^{(n)}}{dt}|\boldsymbol{\mathcal{I}}\rangle^{\mathcal{E}}\right)\\&-\frac{\partial}{\partial \zeta_p}\left(\breve{f}\langle\frac{dT_p^{(n)}}{dt}|\boldsymbol{\mathcal{I}}\rangle^{\mathcal{E}}\right)\ ,\end{aligned}\tag{A.19}$$

with $c_{p,i}=\langle v_{p,i}^{(n)}|\boldsymbol{\mathcal{I}}\rangle^{\mathcal{E}}$. One could omit writing the ensemble average notation around the Lagrangian derivatives, i.e. $\langle\frac{d}{dt}|\boldsymbol{\mathcal{I}}\rangle^{\mathcal{E}}$, but we keep the notation to indicate that the operation has been already applied.

Filtering becomes interesting, since gas phase variables are taken actually from different locations, i.e. they vary although conditioned on phase

space. Applying spatial filtering yields

$$\begin{aligned}\frac{\partial \bar{f}}{\partial t} + \frac{\partial \bar{f} c_{p,i}}{\partial x_i} = &- \frac{\partial}{\partial D}\left(\langle W_p \frac{dD^{(n)}}{dt} | \boldsymbol{\mathcal{I}} \rangle^{\mathcal{F}}\right) \\ &- \frac{\partial}{\partial c_{p,j}}\left(\langle W_p \frac{dv_{p,j}^{(n)}}{dt} | \boldsymbol{\mathcal{I}} \rangle^{\mathcal{F}}\right) \\ &- \frac{\partial}{\partial \zeta_p}\left(\langle W_p \frac{dT_p^{(n)}}{dt} | \boldsymbol{\mathcal{I}} \rangle^{\mathcal{F}}\right)\end{aligned} \tag{A.20}$$

$$\begin{aligned}\frac{\partial \bar{f}}{\partial t} + \frac{\partial \bar{f} c_{p,i}}{\partial x_i} = &- \frac{\partial}{\partial D}\left(\bar{f}\langle \frac{dD^{(n)}}{dt} | \boldsymbol{\mathcal{I}} \rangle^{\mathcal{F}}\right) \\ &- \frac{\partial}{\partial c_{p,j}}\left(\bar{f}\langle \frac{dv_{p,j}^{(n)}}{dt} | \boldsymbol{\mathcal{I}} \rangle^{\mathcal{F}}\right) \\ &- \frac{\partial}{\partial \zeta_p}\left(\bar{f}\langle \frac{dT_p^{(n)}}{dt} | \boldsymbol{\mathcal{I}} \rangle^{\mathcal{F}}\right) \ ,\end{aligned} \tag{A.21}$$

where the result distinguishes itself from the ensemble averaged version only by the definition of the density function and the Lagrangian derivatives.

The combination of both using the operations from Section 3.2.2, i.e.

$$\langle \cdot | D, \mathbf{c}_p, \zeta_p, \mathcal{H}_f \rangle^{\mathcal{E}} = \frac{\lim_{\mathcal{N}_p \to \infty}\left[\frac{1}{\mathcal{N}_p}\sum_{\mathcal{H}_p}\sum_{n=1}^{N_p} \cdot W_p^{(n)}(D, \mathbf{c}_p, \zeta_p; \boldsymbol{\xi}, t, \mathcal{H}_p | \mathcal{H}_f)\right]}{\breve{f}(D, \mathbf{c}_p, \zeta_p; \mathbf{x}, t | \mathcal{H}_f)} \ , \tag{A.22}$$

$$\langle \cdot | D, \mathbf{c}_p, \zeta_p \rangle^{\mathcal{F}} = \iiint_{\infty} G(\mathbf{x} - \boldsymbol{\xi}) \cdot \ \mathrm{d}^3\boldsymbol{\xi} \ , \tag{A.23}$$

and

$$\langle \cdot | D, \mathbf{c}_p, \zeta_p, \mathcal{H}_f \rangle^{\mathcal{E}\mathcal{F}} = \langle \langle \cdot | D, \mathbf{c}_p, \zeta_p, \mathcal{H}_f \rangle^{\mathcal{E}} | D, \mathbf{c}_p, \zeta_p, \rangle^{\mathcal{F}} \ , \tag{A.24}$$

reads

$$\frac{\partial\langle W_p|\boldsymbol{\mathcal{I}}\rangle^{\mathcal{EF}}}{\partial t}+\frac{\partial\langle W_p v_{p,i}^{(n)}|\boldsymbol{\mathcal{I}}\rangle^{\mathcal{EF}}}{\partial x_i}=-\frac{\partial}{\partial D}\left(\langle W_p\frac{dD^{(n)}}{dt}|\boldsymbol{\mathcal{I}}\rangle^{\mathcal{EF}}\right)-\frac{\partial}{\partial c_{p,j}}\left(\langle W_p\frac{dv_{p,j}^{(n)}}{dt}|\boldsymbol{\mathcal{I}}\rangle^{\mathcal{EF}}\right)-\frac{\partial}{\partial \zeta_p}\left(\langle W_p\frac{dT_p^{(n)}}{dt}|\boldsymbol{\mathcal{I}}\rangle^{\mathcal{EF}}\right) \tag{A.25}$$

and yields

$$\frac{\partial\breve{\breve{f}}(\boldsymbol{\mathcal{I}})}{\partial t}+\frac{\partial\breve{\breve{f}}(\boldsymbol{\mathcal{I}})c_{p,i}}{\partial x_i}=-\frac{\partial}{\partial D}\left(\langle\breve{f}\langle\frac{dD^{(n)}}{dt}|\boldsymbol{\mathcal{I}}\rangle^{\mathcal{E}}|\boldsymbol{\mathcal{I}}\rangle^{\mathcal{F}}\right)-\frac{\partial}{\partial c_{p,j}}\left(\langle\breve{f}\langle\frac{dv_{p,j}^{(n)}}{dt}|\boldsymbol{\mathcal{I}}\rangle^{\mathcal{E}}|\boldsymbol{\mathcal{I}}\rangle^{\mathcal{F}}\right)-\frac{\partial}{\partial \zeta_p}\left(\langle\breve{f}\langle\frac{dT_p^{(n)}}{dt}|\boldsymbol{\mathcal{I}}\rangle^{\mathcal{E}}|\boldsymbol{\mathcal{I}}\rangle^{\mathcal{F}}\right)\ . \tag{A.26}$$

A.1.4 Parts of LES Closure (Section 3.2.3)

The LES filtered Lagrangian derivatives imply only sgs-fluctuations of the gas phase, i.e. since the conditioned filtering only counts particles with identical phase space position actually, the gas phase properties at the position of each individual particle vary from particle to particle only. Therefore, we would have to apply the density weighted Favre splitting to all gas phase quantities except the gas phase mass density itself. It becomes obvious, that splitting all gas phase variables, i.e. the material properties and the velocity, results in terms which are hardly to handle. Therefore we restrict ourselves on splitting only the gas phase velocity in a spatial, Favre-averaged mean velocity $\tilde{\mathbf{u}}$ and a residual component

$\mathbf{u}'^{@\mathbf{x}_p^{(n)}}(\mathbf{x},t)$, which represents the difference between the mean velocity and the local gas phase velocity at the position of the individual particle:

$$\mathbf{u}^{@\mathbf{x}_p^{(n)}}(\mathbf{x},t) = \tilde{\mathbf{u}}(\mathbf{x},t) + \mathbf{u}'^{@\mathbf{x}_p^{(n)}}(\mathbf{x},t)\ . \tag{A.27}$$

Velocity Derivative (Drag Term)

Inserting this decomposition in the Stokes drag term yields a closed expression containing only filtered properties. The non-linear drag law extension by Schiller-Naumann reads

$$\begin{aligned}\langle \frac{dv_{p,j,\mathrm{nS}}^{(n)}}{dt} | \boldsymbol{\mathcal{I}} \rangle^{\mathcal{EF}} &= 0.15 \frac{18 D^{0.687}}{\rho_d D^2} \langle \eta^{@\mathbf{x}_p^{(n)}} \left(\frac{|u_j^{@\mathbf{x}_p^{(n)}} - v_{p,j}^{(n)}|}{\nu^{@\mathbf{x}_p^{(n)}}} \right)^{0.687} (u_j^{@\mathbf{x}_p^{(n)}} - v_{p,j}^{(n)}) | \boldsymbol{\mathcal{I}} \rangle^{\mathcal{EF}} \\ &= 0.15 \frac{18\bar{\rho}}{\rho_d} \left(\frac{\bar{\nu}}{D} \right)^{1.313} \langle |\tilde{u}_j + u_j' - v_{p,j}^{(n)}|^{0.687} (\tilde{u}_j + u_j' - v_{p,j}^{(n)}) | \boldsymbol{\mathcal{I}} \rangle^{\mathcal{EF}} \\ &= \dots\ , \end{aligned} \tag{A.28}$$

which directly shows the challenge in deriving distinguished expressions for the different correlations. Actually, it becomes even more complicated (at least to identify and model the terms), since the triple decomposition of the particle velocity must be incorporated as well (see Appendix A.2.5), which gives a multitude of first order correlations between gas/gas, gas/dispersed and dispersed/dispersed phase.

Temperature Derivative with Distinguished Mass Terms

Details for the temperature term

$$\frac{dT_p^{(n)}(t)}{dt} = \frac{1}{m_p^{(n)} c_{\mathrm{pl}}} \left(\dot{m}_T^{(n)} \frac{c_{\mathrm{p}v}^{@\mathbf{x}_p^{(n)}} (T^{@\mathbf{x}_p^{(n)}} - T_p^{(n)})}{\mathrm{B}_T^{@\mathbf{x}_p^{(n)}}} - \dot{m}_M^{(n)} \Delta h_v^{(n)} \right) : \tag{A.29}$$

Stokes part (S):

$$\begin{aligned}
\langle \frac{dT_{p,S}^{(n)}}{dt} | \boldsymbol{\mathcal{I}} \rangle^{\mathcal{EF}} &= \langle \frac{12\lambda^{@\mathbf{x}_p^{(n)}}}{\rho_p {D^{(n)}}^2 c_{\mathrm{pl}}} (T^{@\mathbf{x}_p^{(n)}} - T_p^{(n)}) \frac{\ln(1+\mathrm{B}_T^{@\mathbf{x}_p^{(n)}})}{\mathrm{B}_T^{@\mathbf{x}_p^{(n)}}} | \boldsymbol{\mathcal{I}} \rangle^{\mathcal{EF}} \\
&\quad - \langle \frac{12\rho^{@\mathbf{x}_p^{(n)}} \mathfrak{D}}{\rho_p {D^{(n)}}^2 c_{\mathrm{pl}}} \Delta h_v^{(n)} \ln(1+\mathrm{B}_M^{@\mathbf{x}_p^{(n)}}) | \boldsymbol{\mathcal{I}} \rangle^{\mathcal{EF}} \\
&= \frac{12}{\rho_d D^2 c_{\mathrm{pl}}} \langle \lambda^{@\mathbf{x}_p^{(n)}} (T^{@\mathbf{x}_p^{(n)}} - T_p^{(n)}) \frac{\ln(1+\mathrm{B}_T^{@\mathbf{x}_p^{(n)}})}{\mathrm{B}_T^{@\mathbf{x}_p^{(n)}}} | \boldsymbol{\mathcal{I}} \rangle^{\mathcal{EF}} \\
&\quad - \frac{12}{\rho_d D^2 c_{\mathrm{pl}}} \mathfrak{D} \Delta h_v(\zeta_p) \langle \rho^{@\mathbf{x}_p^{(n)}} \ln(1+\mathrm{B}_M^{@\mathbf{x}_p^{(n)}}) | \boldsymbol{\mathcal{I}} \rangle^{\mathcal{EF}}
\end{aligned}$$

Even with setting the mass and heat transfer numbers to be constant, a meaningful decomposition into the individual correlations is not productive. Therefore, all quantities are assumed to be invariant to ensemble average and filtering, which yields

$$\begin{aligned}
&\approx \frac{12}{\rho_d D^2 c_{\mathrm{pl}}} \bar{\lambda} (\bar{T} - \zeta_p) \frac{\ln(1+\bar{\mathrm{B}}_\mathrm{T})}{\bar{\mathrm{B}}_\mathrm{T}} \\
&\quad - \frac{12}{\rho_d D^2 c_{\mathrm{pl}}} \bar{\rho} \mathfrak{D} \Delta h_v(\zeta_p) \ln(1+\tilde{\mathrm{B}}_M) \\
&\approx \frac{12}{\rho_d D^2 c_{\mathrm{pl}}} \left(\bar{\lambda} (\bar{T} - \zeta_p) \frac{\ln(1+\bar{\mathrm{B}}_\mathrm{T})}{\bar{\mathrm{B}}_\mathrm{T}} - \bar{\rho} \mathfrak{D} \Delta h_v(\zeta_p) \ln(1+\tilde{\mathrm{B}}_M) \right) ,
\end{aligned} \tag{A.30}$$

and higher Reynolds number forced convection (nS) (Frössling)

$$
\begin{aligned}
&\Big\langle \frac{dT_{p,\mathrm{nS}}^{(n)}}{dt} | \boldsymbol{\mathcal{I}} \Big\rangle^{\mathcal{EF}} \\
&= \Big\langle 0.552 \cdot 6 \frac{1}{{D^{(n)}}^3 \rho_p c_{\mathrm{pl}}} \frac{\lambda^{@\mathbf{x}_p^{(n)}}}{c_{\mathrm{p}v}^{@\mathbf{x}_p^{(n)}}} \left(\frac{(\mathbf{u}^{@\mathbf{x}_p^{(n)}} - \mathbf{v}_p^{(n)})}{\nu^{@\mathbf{x}_p^{(n)}}} \right)^{1/2} \mathrm{Pr}^{1/3} {D^{(n)}}^{3/2} \\
&\qquad \frac{\mathrm{B}_{\mathrm{T}}^{@\mathbf{x}_p^{(n)}}}{(1+\mathrm{B}_{\mathrm{T}}^{@\mathbf{x}_p^{(n)}})^{0.7}} \frac{c_{\mathrm{p}v}^{@\mathbf{x}_p^{(n)}} (T^{@\mathbf{x}_p^{(n)}} - T_p^{(n)})}{\mathrm{B}_T^{@\mathbf{x}_p^{(n)}}} | \boldsymbol{\mathcal{I}} \Big\rangle^{\mathcal{EF}} \\
&- \Big\langle 0.552 \cdot 6 \frac{1}{{D^{(n)}}^3 \rho_p c_{\mathrm{pl}}} \rho^{@\mathbf{x}_p^{(n)}} \mathfrak{D} \left(\frac{(\mathbf{u}^{@\mathbf{x}_p^{(n)}} - \mathbf{v}_p^{(n)})}{\nu^{@\mathbf{x}_p^{(n)}}} \right)^{1/2} \mathrm{Sc}^{1/3} {D^{(n)}}^{3/2} \\
&\qquad \frac{\mathrm{B}_{\mathrm{M}}^{@\mathbf{x}_p^{(n)}}}{(1+\mathrm{B}_{\mathrm{M}}^{@\mathbf{x}_p^{(n)}})^{0.7}} \Delta h_v^{(n)} | \boldsymbol{\mathcal{I}} \Big\rangle^{\mathcal{EF}} \\
&= \Big\langle 0.552 \cdot 6 \frac{\lambda^{@\mathbf{x}_p^{(n)}} \mathrm{Pr}^{1/3}}{{D^{(n)}}^{3/2} \rho_p c_{\mathrm{pl}}} \left(\frac{(\mathbf{u}^{@\mathbf{x}_p^{(n)}} - \mathbf{v}_p^{(n)})}{\nu^{@\mathbf{x}_p^{(n)}}} \right)^{1/2} \frac{(T^{@\mathbf{x}_p^{(n)}} - T_p^{(n)})}{(1+\mathrm{B}_{\mathrm{T}}^{@\mathbf{x}_p^{(n)}})^{0.7}} | \boldsymbol{\mathcal{I}} \Big\rangle^{\mathcal{EF}} \\
&- \Big\langle 0.552 \cdot 6 \frac{\rho^{@\mathbf{x}_p^{(n)}} \mathfrak{D}\, \mathrm{Sc}^{1/3}}{{D^{(n)}}^{3/2} \rho_p c_{\mathrm{pl}}} \left(\frac{(\mathbf{u}^{@\mathbf{x}_p^{(n)}} - \mathbf{v}_p^{(n)})}{\nu^{@\mathbf{x}_p^{(n)}}} \right)^{1/2} \frac{\mathrm{B}_{\mathrm{M}}^{@\mathbf{x}_p^{(n)}} \Delta h_v^{(n)}}{(1+\mathrm{B}_{\mathrm{M}}^{@\mathbf{x}_p^{(n)}})^{0.7}} | \boldsymbol{\mathcal{I}} \Big\rangle^{\mathcal{EF}} \\
&= 0.552 \cdot 6 \frac{\mathrm{Pr}^{1/3}}{D^{3/2} \rho_d c_{\mathrm{pl}}} \Big\langle \lambda^{@\mathbf{x}_p^{(n)}} \left(\frac{(\mathbf{u}^{@\mathbf{x}_p^{(n)}} - \mathbf{v}_p^{(n)})}{\nu^{@\mathbf{x}_p^{(n)}}} \right)^{1/2} \frac{(T^{@\mathbf{x}_p^{(n)}} - T_p^{(n)})}{(1+\mathrm{B}_{\mathrm{T}}^{@\mathbf{x}_p^{(n)}})^{0.7}} | \boldsymbol{\mathcal{I}} \Big\rangle^{\mathcal{EF}} \\
&- 0.552 \cdot 6 \frac{\Delta h_v(\zeta_p) \mathfrak{D}\, \mathrm{Sc}^{1/3}}{D^{3/2} \rho_d c_{\mathrm{pl}}} \Big\langle \rho^{@\mathbf{x}_p^{(n)}} \left(\frac{(\mathbf{u}^{@\mathbf{x}_p^{(n)}} - \mathbf{v}_p^{(n)})}{\nu^{@\mathbf{x}_p^{(n)}}} \right)^{1/2} \frac{\mathrm{B}_{\mathrm{M}}^{@\mathbf{x}_p^{(n)}}}{(1+\mathrm{B}_{\mathrm{M}}^{@\mathbf{x}_p^{(n)}})^{0.7}} | \boldsymbol{\mathcal{I}} \Big\rangle^{\mathcal{EF}}
\end{aligned}
$$

... as above...

$$= 0.552 \cdot 6 \frac{\bar{\lambda} \mathrm{Pr}^{1/3}}{D^{3/2} \rho_d c_{\mathrm{pl}}} \left(\frac{(\bar{\mathbf{u}} - \mathbf{c}_p)}{\bar{\nu}} \right)^{1/2} (\bar{T} - \zeta_p) \frac{1}{(1 + \bar{\mathrm{B}}_{\mathrm{T}})^{0.7}}$$
$$- 0.552 \cdot 6 \frac{\bar{\rho} \mathfrak{D} \, \mathrm{Sc}^{1/3}}{D^{3/2} \rho_d c_{\mathrm{pl}}} \left(\frac{(\tilde{\mathbf{u}} - \mathbf{c}_p)}{\bar{\nu}} \right)^{1/2} \Delta h_v(\zeta_p) \frac{\tilde{\mathrm{B}}_{\mathrm{M}}}{(1 + \tilde{\mathrm{B}}_{\mathrm{M}})^{0.7}} \, . \tag{A.31}$$

Size Derivative with Distinguished Mass Terms

Stokes part (S):

$$\begin{aligned} \langle \frac{dD_{\mathrm{S}}^{(n)}}{dt} | \boldsymbol{\mathcal{I}} \rangle^{\mathcal{EF}} &= -\langle 2 \, \mathrm{Sh}_{\mathrm{S}}^{*} \frac{\rho^{@\mathbf{x}_p^{(n)}}}{\rho_p D^{(n)}} \mathfrak{D} \ln(1 + \mathrm{B}_M^{@\mathbf{x}_p^{(n)}}) | \boldsymbol{\mathcal{I}} \rangle^{\mathcal{EF}} \\ &= -\frac{4\mathfrak{D}}{\rho_d D} \langle \rho^{@\mathbf{x}_p^{(n)}} \ln(1 + B_M^{@\mathbf{x}_p^{(n)}}) | \boldsymbol{\mathcal{I}} \rangle^{\mathcal{EF}} \, . \end{aligned}$$

Replacing unfiltered with filtered quantities yields

$$\approx -4 \frac{\bar{\rho} \mathfrak{D}}{\rho_d D} \ln(1 + \tilde{\mathrm{B}}_{\mathrm{M}}) \, . \tag{A.32}$$

Non-Stokes part (nS):

$$\begin{aligned} &\langle \frac{dD_{\mathrm{nS}}^{(n)}}{dt} | \boldsymbol{\mathcal{I}} \rangle^{\mathcal{EF}} \\ &= -\langle 0.552 \cdot 2 \frac{\rho^{@\mathbf{x}_p^{(n)}}}{\rho_p} \mathfrak{D} \left(\frac{(\mathbf{u}^{@\mathbf{x}_p^{(n)}} - \mathbf{v}_p^{(n)})}{\nu^{@\mathbf{x}_p^{(n)}}} \right)^{1/2} \frac{\mathrm{Sc}^{1/3}}{D^{(n)1/2}} \frac{\mathrm{B}_{\mathrm{M}}^{@\mathbf{x}_p^{(n)}}}{(1 + \mathrm{B}_{\mathrm{M}}^{@\mathbf{x}_p^{(n)}})^{0.7}} | \boldsymbol{\mathcal{I}} \rangle^{\mathcal{EF}} \\ &= -0.552 \cdot 2 \frac{\mathfrak{D}}{\rho_d} \frac{\mathrm{Sc}^{1/3}}{D^{1/2}} \langle \rho^{@\mathbf{x}_p^{(n)}} \left(\frac{(\mathbf{u}^{@\mathbf{x}_p^{(n)}} - \mathbf{v}_p^{(n)})}{\nu^{@\mathbf{x}_p^{(n)}}} \right)^{1/2} \frac{\mathrm{B}_{\mathrm{M}}^{@\mathbf{x}_p^{(n)}}}{(1 + \mathrm{B}_{\mathrm{M}}^{@\mathbf{x}_p^{(n)}})^{0.7}} | \boldsymbol{\mathcal{I}} \rangle^{\mathcal{EF}} \end{aligned}$$

... as above...

$$\begin{aligned}
&\approx -0.552 \cdot 2\frac{\mathfrak{D}}{\rho_d}\frac{\mathrm{Sc}^{1/3}}{D^{1/2}}\bar{\rho}\left(\frac{(\tilde{\mathbf{u}}-\mathbf{c}_p)}{\bar{\nu}}\right)^{1/2}\frac{\tilde{\mathrm{B}}_\mathrm{M}}{(1+\tilde{\mathrm{B}}_\mathrm{M})^{0.7}} \\
&\approx -0.552 \cdot 2\frac{\bar{\rho}}{\rho_d}\mathfrak{D}\frac{\mathrm{Sc}^{1/3}}{D^{1/2}}\left(\frac{(\tilde{\mathbf{u}}-\mathbf{c}_p)}{\bar{\nu}}\right)^{1/2}\frac{\tilde{\mathrm{B}}_\mathrm{M}}{(1+\tilde{\mathrm{B}}_\mathrm{M})^{0.7}}\,. \qquad \text{(A.33)}
\end{aligned}$$

The Latter Two with only one Mass Term $\dot{m}_T$

Details for the temperature term

$$\frac{dT_p^{(n)}(t)}{dt} = \frac{\dot{m}_T^{(n)}}{m_p^{(n)}c_{\mathrm{p}l}}\left(\frac{c_{\mathrm{p}v}^{@\mathbf{x}_p^{(n)}}(T^{@\mathbf{x}_p^{(n)}}-T_p^{(n)})}{\mathrm{B}_T^{@\mathbf{x}_p^{(n)}}}-\Delta h_v^{(n)}\right)\,: \qquad \text{(A.34)}$$

Stokes part (S):

$$\begin{aligned}
\langle\frac{dT_{p,S}^{(n)}}{dt}|\boldsymbol{\mathcal{I}}\rangle^{\mathcal{EF}} &= \langle\frac{12\lambda^{@\mathbf{x}_p^{(n)}}\ln(1+\mathrm{B}_T^{@\mathbf{x}_p^{(n)}})}{D^{(n)^2}\rho_p c_{\mathrm{p}l}c_{\mathrm{p}v}^{@\mathbf{x}_p^{(n)}}}\left(\frac{c_{\mathrm{p}v}^{@\mathbf{x}_p^{(n)}}(T^{@\mathbf{x}_p^{(n)}}-T_p^{(n)})}{\mathrm{B}_T^{@\mathbf{x}_p^{(n)}}}-\Delta h_v^{(n)}\right)|\boldsymbol{\mathcal{I}}\rangle^{\mathcal{EF}} \\
&= \frac{12}{\rho_d c_{\mathrm{p}l}}\langle\frac{\lambda^{@\mathbf{x}_p^{(n)}}\ln(1+\mathrm{B}_T^{@\mathbf{x}_p^{(n)}})}{D^{(n)^2}c_{\mathrm{p}v}^{@\mathbf{x}_p^{(n)}}}\left(\frac{c_{\mathrm{p}v}^{@\mathbf{x}_p^{(n)}}(T^{@\mathbf{x}_p^{(n)}}-T_p^{(n)})}{\mathrm{B}_T^{@\mathbf{x}_p^{(n)}}}-\Delta h_v^{(n)}\right)|\boldsymbol{\mathcal{I}}\rangle^{\mathcal{EF}} \\
&\approx \frac{12\bar{\lambda}}{\rho_d c_{\mathrm{p}l}\bar{c}_{p,v}}\frac{\ln(1+\bar{\mathrm{B}}_\mathrm{T}(\zeta_p))}{D^2}\left(\frac{\bar{c}_{p,v}(\bar{T}-\zeta_p)}{\bar{\mathrm{B}}_\mathrm{T}(\zeta_p)}-\Delta h_v(\zeta_p)\right)
\end{aligned} \qquad \text{(A.35)}$$

and higher Reynolds number convection (nS) (Frössling)

$$\begin{aligned}
\langle \frac{dT_{p,\mathrm{nS}}^{(n)}}{dt} | \boldsymbol{\mathcal{I}} \rangle^{\mathcal{EF}} = & - \langle 0.552 \cdot 6 \frac{\lambda^{@\mathbf{x}_p^{(n)}}}{c_{\mathrm{p}v}^{@\mathbf{x}_p^{(n)}} D^{(n)^{3/2}} c_{\mathrm{p}l}} \left(\frac{(\mathbf{u}^{@\mathbf{x}_p^{(n)}} - \mathbf{v}_p^{(n)})}{\nu^{@\mathbf{x}_p^{(n)}}} \right)^{1/2} \mathrm{Pr}^{1/3} \\
& \frac{\mathrm{B}_{\mathrm{T}}^{@\mathbf{x}_p^{(n)}}}{(1+\mathrm{B}_{\mathrm{T}}^{@\mathbf{x}_p^{(n)}})^{0.7}} \left(\frac{c_{\mathrm{p}v}^{@\mathbf{x}_p^{(n)}} (T^{@\mathbf{x}_p^{(n)}} - T_p^{(n)})}{\mathrm{B}_T^{@\mathbf{x}_p^{(n)}}} - \Delta h_v^{(n)} \right) | \boldsymbol{\mathcal{I}} \rangle^{\mathcal{EF}} \\
= & - 0.552 \cdot 6 \frac{\mathrm{Pr}^{1/3}}{D^{3/2} c_{\mathrm{p}l}} \langle \frac{\lambda^{@\mathbf{x}_p^{(n)}}}{c_{\mathrm{p}v}^{@\mathbf{x}_p^{(n)}}} \left(\frac{(\mathbf{u}^{@\mathbf{x}_p^{(n)}} - \mathbf{v}_p^{(n)})}{\nu^{@\mathbf{x}_p^{(n)}}} \right)^{1/2} \\
& \frac{\mathrm{B}_{\mathrm{T}}^{@\mathbf{x}_p^{(n)}}}{(1+\mathrm{B}_{\mathrm{T}}^{@\mathbf{x}_p^{(n)}})^{0.7}} \left(\frac{c_{\mathrm{p}v}^{@\mathbf{x}_p^{(n)}} (T^{@\mathbf{x}_p^{(n)}} - T_p^{(n)})}{\mathrm{B}_T^{@\mathbf{x}_p^{(n)}}} - \Delta h_v^{(n)} \right) | \boldsymbol{\mathcal{I}} \rangle^{\mathcal{EF}} \\
\approx & - 0.552 \cdot 6 \frac{\mathrm{Pr}^{1/3}}{D^{3/2} c_{\mathrm{p}l}} \frac{\bar{\lambda}}{\bar{c}_{p,v}} \left(\frac{(\bar{\mathbf{u}} - \mathbf{c}_p)}{\bar{\nu}} \right)^{1/2} \\
& \frac{\bar{\mathrm{B}}_{\mathrm{T}}(\zeta_p)}{(1+\bar{\mathrm{B}}_{\mathrm{T}}(\zeta_p))^{0.7}} \left(\frac{\bar{c}_{p,v}(\bar{T} - \zeta_p)}{\bar{\mathrm{B}}_{\mathrm{T}}(\zeta_p)} - \Delta h_v(\zeta_p) \right) . \qquad \text{(A.36)}
\end{aligned}$$

Details for mass term:

Stokes flow (S):

$$\begin{aligned}
\langle \frac{dD_{\mathrm{S}}^{(n)}}{dt} | \boldsymbol{\mathcal{I}} \rangle^{\mathcal{EF}} = & - \langle 4 \frac{\lambda^{@\mathbf{x}_p^{(n)}}}{\rho_p c_{\mathrm{p}v}^{@\mathbf{x}_p^{(n)}} D^{(n)}} \ln(1 + \mathrm{B}_T^{@\mathbf{x}_p^{(n)}}) | \boldsymbol{\mathcal{I}} \rangle^{\mathcal{EF}} \\
= & -4 \frac{1}{\rho_d D} \langle \frac{\lambda^{@\mathbf{x}_p^{(n)}}}{c_{\mathrm{p}v}^{@\mathbf{x}_p^{(n)}}} \ln(1 + \mathrm{B}_T^{@\mathbf{x}_p^{(n)}}) | \boldsymbol{\mathcal{I}} \rangle^{\mathcal{EF}} \\
\approx & -4 \frac{\bar{\lambda}}{\rho_d \bar{c}_{p,v} D} \ln(1 + \bar{\mathrm{B}}_{\mathrm{T}}(\zeta_p)) \qquad \text{(A.37)}
\end{aligned}$$

and for higher Reynolds numbers (nS)

$$\begin{aligned}\langle\frac{dD_{\mathrm{nS}}^{(n)}}{dt}|\boldsymbol{\mathcal{I}}\rangle^{\mathcal{EF}} &= -\langle 0.552\cdot 2\frac{\lambda^{@\mathbf{x}_p^{(n)}}}{\rho_p c_{\mathrm{p}v}^{@\mathbf{x}_p^{(n)}}}\left(\frac{(\mathbf{u}^{@\mathbf{x}_p^{(n)}}-\mathbf{v}_p^{(n)})}{\nu^{@\mathbf{x}_p^{(n)}}D^{(n)}}\right)^{1/2}\mathrm{Pr}^{1/3}\frac{\mathrm{B}_{\mathrm{T}}^{@\mathbf{x}_p^{(n)}}}{(1+\mathrm{B}_{\mathrm{T}}^{@\mathbf{x}_p^{(n)}})^{0.7}}|\boldsymbol{\mathcal{I}}\rangle^{\mathcal{EF}}\\ &= -0.552\cdot 2\frac{\mathrm{Pr}^{1/3}}{\rho_d D^{1/2}}\langle\frac{\lambda^{@\mathbf{x}_p^{(n)}}}{c_{\mathrm{p}v}^{@\mathbf{x}_p^{(n)}}}\left(\frac{(\mathbf{u}^{@\mathbf{x}_p^{(n)}}-\mathbf{v}_p^{(n)})}{\nu^{@\mathbf{x}_p^{(n)}}}\right)^{1/2}\frac{\mathrm{B}_{\mathrm{T}}^{@\mathbf{x}_p^{(n)}}}{(1+\mathrm{B}_{\mathrm{T}}^{@\mathbf{x}_p^{(n)}})^{0.7}}|\boldsymbol{\mathcal{I}}\rangle^{\mathcal{EF}}\\ &\approx -0.552\cdot 2\frac{\mathrm{Pr}^{1/3}}{\rho_d D^{1/2}}\frac{\bar{\lambda}}{\bar{c}_{p,v}}\left(\frac{(\bar{\mathbf{u}}-\mathbf{c}_p)}{\bar{\nu}}\right)^{1/2}\frac{\bar{\mathrm{B}}_{\mathrm{T}}(\zeta_p)}{(1+\bar{\mathrm{B}}_{\mathrm{T}}(\zeta_p))^{0.7}}\,.\end{aligned} \tag{A.38}$$

The approximation $\mathfrak{D}^{@\mathbf{x}_p^{(n)}} = \mathfrak{D} = const.$ is usually done anyway (also in gas phase equation derivation).

A.2 Appendix to Chapter 4

This section mainly deals with sketching the incorporation of the first central moment of the dispersed phase velocity, i.e. the particle velocity co-variance tensor, for two different cases. The first case is the spatial filtering of a single particle phase realisation for a given continuous phase realisation, where we refer to the co-variance as *dispersed phase stress tensor* $\boldsymbol{\tau}_d$. The second case deals with deriving the so-called *Random Uncorrelated Velocity* (RUV) tensor $\delta\mathbf{R}_d$ which is the pointwise first order central moment of the particle phase velocity distribution gained from a sample accumulation over a large number of particle phase realisations.

In any case, the particle temperature is set to be phase space independent, that means that all particles of any size or velocity have the same temperature T_d locally, i.e. $f(D,\mathbf{c}_p,\zeta_p)$ can be assumed as

$$f(D,\mathbf{c}_p,\zeta_p) = f^{**}(D,\mathbf{c}_p)\delta(\zeta_p - T_d)\,. \tag{A.39}$$

Furthermore, we have to distinguish between different versions of the

number density function depending on its dimensionality due to partial integration over sub-spaces of the phase space. Hence

$$f^{**}(D, \mathbf{c}_p) \overset{\text{def.}}{=} \int f(D, \mathbf{c}_p, \zeta_p) \mathrm{d}\zeta_p \ , \tag{A.40}$$

$$f^{*}(D) \overset{\text{def.}}{=} \int f^{**}(D, \mathbf{c}_p) \mathrm{d}\mathbf{c}_p \ , \tag{A.41}$$

$$M^{(0)} \ = \ \int f^{*}(D) \, \mathrm{d}D \ , \tag{A.42}$$

where the density functions, despite from its phase space dimension, distinguish themselves from each other by the particle number implied, i.e. something like $f^{*}(D) \hat{=} f^{**}(D) N^{*}(D) \hat{=} f^{**}(D, \mathbf{c}_p)$. The notation is only for illustration and does not aim for mathematical correctness at this point.

The next three section are ordered as, first, the spatial filtering solely, followed by the sample accumulation correspondingly and finally the sequential application of both.

A.2.1 Including the Co-Variance of the SGS Particle Phase Velocity FNDF

The filtered number density function (without underlying sample accumulation) consists of a spatial summation of delta peaks indicating individual particles. Hence, the individual particle velocity $\mathbf{v}_p^{(n)}(t, \mathcal{H}_p | D)$ can be split in a spatially averaged velocity $\bar{\mathbf{u}}(D; \mathbf{x}, t)$ shared by all particles being present within the spatial support of the filter and the deviation of the individual particle $\bar{\mathbf{u}}'^{(n)}(D, \mathbf{c}_p; \mathbf{x}, t, \mathcal{H}_p)$ from this mean velocity, i.e.

$$\mathbf{v}_p^{(n)}(t, \mathcal{H}_p | D) = \bar{\mathbf{u}}(D; \mathbf{x}, t) + \bar{\mathbf{u}}'^{(n)}(D, \mathbf{c}_p; \mathbf{x}, t, \mathcal{H}_p) \ . \tag{A.43}$$

Replacing the phase space variable $\mathbf{c}_p$, which is actually the sample space of the individual particle velocities, by the this ansatz we obtain the fol-

lowing expression for a linear term in $\mathbf{c}_p$:

$$
\begin{aligned}
&\iiint D^k \mathbf{c}_p \bar{f}(D, \mathbf{c}_p, \zeta_p)\, \mathrm{d}\zeta_p \mathrm{d}\mathbf{c}_p \mathrm{d}D \\
&= \iiint D^k \mathbf{c}_p \bar{f}^{**}(D, \mathbf{c}_p) \delta(\zeta_p - T_d)\, \mathrm{d}\zeta_p \mathrm{d}\mathbf{c}_p \mathrm{d}D \\
&= \iint D^k \mathbf{c}_p \bar{f}^{**}(D, \mathbf{c}_p) \left(\underbrace{\int \zeta_p^0 \delta(\zeta_p - T_d) \mathrm{d}\zeta_p}_{=1} \right) \mathrm{d}\mathbf{c}_p \mathrm{d}D \\
&= \iint D^k \left[\bar{\mathbf{u}}(D; \mathbf{x}, t) + \bar{\mathbf{u}}'^{(n)}(D, \mathbf{c}_p; \mathbf{x}, t, \mathcal{H}_p) \right] \bar{f}^{**}(D, \mathbf{c}_p)\, \mathrm{d}\mathbf{c}_p \mathrm{d}D \\
&= \iint D^k \bar{\mathbf{u}}(D) \bar{f}^{**}(D, \mathbf{c}_p)\, \mathrm{d}\mathbf{c}_p \mathrm{d}D + \iint D^k \bar{\mathbf{u}}'^{(n)}(D, \mathbf{c}_p) \bar{f}^{**}(D, \mathbf{c}_p)\, \mathrm{d}\mathbf{c}_p \mathrm{d}D \\
&= \int D^k \bar{\mathbf{u}}(D) \bar{f}^{*}(D)\, \mathrm{d}D \\
&\overset{\text{def.}}{=} \bar{M}^{(k)} \bar{\mathbf{u}}^{(k)} \,.
\end{aligned}
\tag{A.44}
$$

The first order term in $\bar{\mathbf{u}}'^{(n)}(D, \mathbf{c}_p)$ becomes zero, since the velocity space integration directly corresponds to the conditioned spatial averaging procedure.

Applying the same procedure to a non-linear term in $\mathbf{c}_p$ yields (with skipping the step of integration over temperature space):

$$
\begin{aligned}
&\iiint D^k \mathbf{c}_p \mathbf{c}_p \bar{f}(D, \mathbf{c}_p, \zeta_p)\, \mathrm{d}\zeta_p \mathrm{d}\mathbf{c}_p \mathrm{d}D \\
&= \iiint D^k \mathbf{c}_p \mathbf{c}_p \bar{f}^{**}(D, \mathbf{c}_p) \delta(\zeta_p - T_d)\, \mathrm{d}\zeta_p \mathrm{d}\mathbf{c}_p \mathrm{d}D \\
&= \iint D^k \left[\underbrace{\bar{\mathbf{u}}(D; \mathbf{x}, t)^* + \bar{\mathbf{u}}'^{(n)}(D, \mathbf{c}_p; \mathbf{x}, t, \mathcal{H}_p)^*}_{=\mathbf{c}_p} \right]^2 \bar{f}^{**}(D, \mathbf{c}_p)\, \mathrm{d}\mathbf{c}_p \mathrm{d}D \\
&= \iint D^k \bar{\mathbf{u}}(D) \bar{\mathbf{u}}(D) \bar{f}^{**}(D, \mathbf{c}_p)\, \mathrm{d}\mathbf{c}_p \mathrm{d}D \\
&\qquad + \iint D^k \bar{f}^{**}(D, \mathbf{c}_p) \bar{\mathbf{u}}'^{(n)}(D, \mathbf{c}_p) \bar{\mathbf{u}}'^{(n)}(D, \mathbf{c}_p)\, \mathrm{d}\mathbf{c}_p \mathrm{d}D \,,
\end{aligned}
$$

which gives by rewriting the second term as

$$\int D^k \underbrace{\int \bar{f}^{**}(D,\mathbf{c}_p)\bar{\mathbf{u}}'^{(n)}(D,\mathbf{c}_p)\bar{\mathbf{u}}'^{(n)}(D,\mathbf{c}_p)\mathrm{d}\mathbf{c}_p}_{\boldsymbol{\tau}_d(D)\bar{f}^*(D)}\,\mathrm{d}D$$

and including the moment velocity splitting discussed in Section 4.3.2

$$= \iint D^k \left[\underbrace{\bar{\mathbf{u}}^{(k)}(\mathbf{x},t)+\bar{\mathbf{u}}'(D;\mathbf{x},t)}_{\bar{\mathbf{u}}(D;\mathbf{x},t)}\right]^2 \bar{f}^{**}(D,\mathbf{c}_p)\,\mathrm{d}\mathbf{c}_p\mathrm{d}D + \int D^k\boldsymbol{\tau}_d(D)\bar{f}^*(D)\,\mathrm{d}D$$

$$\begin{aligned}
&= \iint D^k\bar{\mathbf{u}}^{(k)}\bar{\mathbf{u}}^{(k)}\bar{f}^{**}(D,\mathbf{c}_p)\,\mathrm{d}\mathbf{c}_p\mathrm{d}D \\
&\quad + \int D^k\bar{\mathbf{u}}'(D)\bar{\mathbf{u}}'(D)\bar{f}^*(D)\,\mathrm{d}D + \int D^k\boldsymbol{\tau}_d(D)\bar{f}^*(D)\,\mathrm{d}D \\
&\overset{\text{def.}}{=} \bar{M}^{(k)}\bar{\mathbf{u}}^{(k)}\bar{\mathbf{u}}^{(k)} + \int D^k\bar{\mathbf{u}}'\bar{\mathbf{u}}'\bar{f}^*(D)\,\mathrm{d}D + \int D^k\boldsymbol{\tau}_d(D)\bar{f}^*(D)\,\mathrm{d}D\,. \qquad \text{(A.45)}
\end{aligned}$$

$\boldsymbol{\tau}_d(D)$ can be interpreted as a diameter dependent, spacial "particle phase stress tensor", which, however, does imply totally different behaviour than any kind of continuous phase turbulent stresses. Transport equations for these particle phase stresses can be derived, for which the closure problem is only transferred to higher order correlations. In this case, closure is often gained by neglecting the third order correlations (see, e.g. Pandya and Mashayek, 2002). Simply using turbulent viscosity models as in single phase LES does often not justice to the character of the particle phase physics.

A.2.2 Including the Co-Variance of the Particle Phase Velocity EbNDF (Random Uncorrelated Velocity Tensor)

In this section, we make a similar derivation for the size conditioned first central moment of the velocity distribution, i.e. the Random Uncorrelated

Velocity tensor (Riber et al., 2006), which is part of the *Random Uncorrelated Motion* concept (denotation introduced by Kaufmann et al. (2004), formerly known as Quasi-Brownian motion). The formalism is very similar to the one shown before for the spatial filtering, although the meaning of operations and variables, especially the fluctuations and NDFs, is different. The ensemble-sampled number density function $\check{f}(D, \mathbf{c}_p, \zeta_p)$, here abbreviated as EbNDF, consists, similar to the FNDF, of a summation of delta peaks indicating individual particles, but gained from a large number of particle phase realisations $\mathcal{H}_p$ for a given continuous phase realisation $\mathcal{H}_f$. As in the section before, we aim to derive formally the size conditioned co-variance of the particle phase velocity distribution.

The individual particle velocity $\mathbf{v}_p^{(n)}$ can be divided into a mean velocity $\breve{\mathbf{u}}(D; \mathbf{x}, t)$, in the framework of the Random Uncorrelated Motion formalism usually called *Mesoscopic Eulerian Velocity*, and a residual velocity component $\breve{\mathbf{u}}'^{(n)}(D, \mathbf{c}_p; \mathbf{x}, t, \mathcal{H}_p)$, which is the deviation of the velocity of the individual particle to the ensemble mean velocity shared by all particles at physical space point $\mathbf{x}$ at time t. The decomposition reads

$$\mathbf{v}_p^{(n)} = \mathbf{v}_p^{(n)}(t, \mathcal{H}_p | D) = \breve{\mathbf{u}}(D; \mathbf{x}, t) + \breve{\mathbf{u}}'^{(n)}(D, \mathbf{c}_p; \mathbf{x}, t, \mathcal{H}_p) \; . \tag{A.46}$$

Here again, the integration over phase space is equivalent to the sample accumulation over particle phase realisations, which yields linear terms in $\mathbf{c}_p$ to be zero. Again, skipping the temperature space integration, this reads

$$\begin{aligned}
&\iiint D^k \mathbf{c}_p \check{f}(D, \mathbf{c}_p, \zeta_p) \, \mathrm{d}\zeta_p \mathrm{d}\mathbf{c}_p \mathrm{d}D \\
&= \iiint D^k \mathbf{c}_p \check{f}^{**}(D, \mathbf{c}_p) \delta(\zeta_p - T_d) \, \mathrm{d}\zeta_p \mathrm{d}\mathbf{c}_p \mathrm{d}D \\
&= \iint D^k \left[\breve{\mathbf{u}}(D; \mathbf{x}, t) + \breve{\mathbf{u}}'^{(n)}(D, \mathbf{c}_p; \mathbf{x}, t, \mathcal{H}_p) \right] \check{f}^{**}(D, \mathbf{c}_p) \, \mathrm{d}\mathbf{c}_p \mathrm{d}D \\
&= \iint D^k \breve{\mathbf{u}}(D) \check{f}^{**}(D, \mathbf{c}_p) \, \mathrm{d}\mathbf{c}_p \mathrm{d}D + \underbrace{\iint D^k \breve{\mathbf{u}}'^{(n)}(D, \mathbf{c}_p) \check{f}^{**}(D, \mathbf{c}_p) \, \mathrm{d}\mathbf{c}_p \mathrm{d}D}_{=0}
\end{aligned}$$

$$= \int D^k \breve{\mathbf{u}}(D) \breve{f}^*(D)\, \mathrm{d}D$$
$$\stackrel{\text{def.}}{=} \breve{M}^{(k)} \breve{\mathbf{u}}^{(k)} \,. \tag{A.47}$$

Worth to clarify is that the term containing the fluctuation becomes already zero if integrating first over the subspace of velocity only. Hence, the integration over the size spectrum becomes superfluous. The nonlinear term of second order develops accordingly to the one shown for spatial filtering as

$$\begin{aligned}
&\iiint D^k \mathbf{c}_p \mathbf{c}_p \breve{f}(D, \mathbf{c}_p, \zeta_p)\, \mathrm{d}\zeta_p \mathrm{d}\mathbf{c}_p \mathrm{d}D \\
&= \iiint D^k \mathbf{c}_p \mathbf{c}_p \breve{f}^{**}(D, \mathbf{c}_p) \delta(\zeta_p - T_d)\, \mathrm{d}\zeta_p \mathrm{d}\mathbf{c}_p \mathrm{d}D \\
&= \iint D^k \left[\breve{\mathbf{u}}(D; \mathbf{x}, t) + \breve{\mathbf{u}}'^{(n)}(D, \mathbf{c}_p; \mathbf{x}, t, \mathcal{H}_p) \right]^2 \breve{f}^{**}(D, \mathbf{c}_p)\, \mathrm{d}\mathbf{c}_p \mathrm{d}D \\
&= \iint D^k \breve{\mathbf{u}}(D) \breve{\mathbf{u}}(D) \breve{f}^{**}(D, \mathbf{c}_p)\, \mathrm{d}\mathbf{c}_p \mathrm{d}D \\
&\qquad + \iint D^k \breve{f}^{**}(D, \mathbf{c}_p) \breve{\mathbf{u}}'^{(n)}(D, \mathbf{c}_p) \breve{\mathbf{u}}'^{(n)}(D, \mathbf{c}_p)\, \mathrm{d}\mathbf{c}_p \mathrm{d}D \,,
\end{aligned}$$

where the second term is treated correspondingly as shown in the section before. Using again the moment velocity decomposition (Section 4.3.2) for the first term, we finally arrive at

$$\stackrel{\text{def.}}{=} \breve{M}^{(k)} \breve{\mathbf{u}}^{(k)} \breve{\mathbf{u}}^{(k)} + \int D^k \breve{\mathbf{u}}' \breve{\mathbf{u}}' \breve{f}^*(D)\, \mathrm{d}D + \int D^k \delta\mathbf{R}_d(D) \breve{f}^*(D)\, \mathrm{d}D \,. \tag{A.48}$$

$\delta\mathbf{R}_d(D)$ is the so-called *Random Uncorrelated Velocity* tensor, here dependent on particle size, since we are dealing with polydisperse flows. It reads in terms of the actual and mean particle velocity

$$\delta\mathbf{R}_d(D) = \frac{1}{\breve{f}^*(D)} \int D^k (\mathbf{c}_p - \breve{\mathbf{u}}(D))(\mathbf{c}_p - \breve{\mathbf{u}}(D)) \breve{f}^{**}(D, \mathbf{c}_p) \mathrm{d}\mathbf{c}_p \,. \tag{A.49}$$

Modelling of $\delta R_d(D)$ has been discussed in several publications (Simonin et al., 2002, Kaufmann, 2004, Moreau et al., 2005, Riber et al., 2005,

Masi et al., 2008, Moreau et al., 2010, Masi et al., 2011), the closure of $\int D^k \delta \mathbf{R}_d(D) \check{f}^*(D)\, \mathrm{d}D$ has not been investigated in the context of the moment model presented in this work, Mossa (2005) examined this issue within the Mesoscopic Eulerian Formalism.

A.2.3 Including the Co-Variances of the Particle Phase Velocity Filtered Ensemble based NDF (FEbNDF)

Since the EbNDF is a pointwise NDF in terms of physical space, it can vary significantly on the sub-grid scale. In order to use the sample accumulation based mesoscopic equations in Large Eddy Simulations, Moreau et al. (2005) and Riber et al. (2006) proposed to filter the moment equations, which result from the phase space integration. Another way is to filter the EbNDF first and apply the phase space integration subsequently. This approach yields moment transport equations which are already filtered, i.e. which can be resolved by a numerical mesh being appropriate for the used filter size. In this section, we sketch this approach, combining the sample accumulation and the LES filtering before conducting the integration over phase space.

Accordingly, the individual particle velocity can be expressed as a mean $\breve{\mathbf{u}}(D;\mathbf{x},t)$ and two residual contributions as

$$\mathbf{v}_p^{(n)} = \breve{\mathbf{u}}(D;\mathbf{x},t) + \breve{\mathbf{u}}'(D,\mathbf{c}_p;\mathbf{x},t) + \breve{\mathbf{u}}'^{(n)}(D,\mathbf{c}_p;\mathbf{x},t,\mathcal{H}_p)\,, \tag{A.50}$$

where $\breve{\mathbf{u}}'(D,\mathbf{c}_p;\mathbf{x},t)$ is the residual component between the spatial average of the mean ensemble values $\breve{\mathbf{u}}(D;\mathbf{x},t)$ and the individual, pointwise ensemble mean values (here not explicitly given as a mathematical expression), and $\breve{\mathbf{u}}'^{(n)}(D,\mathbf{c}_p;\mathbf{x},t,\mathcal{H}_p)$ is the residual component between an individual pointwise ensemble mean to the velocity of the individual

particle. Using this decomposition yields for the linear term

$$
\begin{aligned}
&\iiint D^k \mathbf{c}_p \breve{\breve{f}}(D, \mathbf{c}_p, \zeta_p)\, \mathrm{d}\zeta_p \mathrm{d}\mathbf{c}_p \mathrm{d}D \\
&= \iiint D^k \mathbf{c}_p \breve{\breve{f}}^{**}(D, \mathbf{c}_p) \delta(\zeta_p - T_d)\, \mathrm{d}\zeta_p \mathrm{d}\mathbf{c}_p \mathrm{d}D \\
&= \iint D^k \left[\breve{\mathbf{u}}(D; \mathbf{x}, t) + \breve{\mathbf{u}}'(D, \mathbf{c}_p; \mathbf{x}, t) + \breve{\mathbf{u}}'^{(n)}(D, \mathbf{c}_p; \mathbf{x}, t, \mathcal{H}_p) \right] \breve{\breve{f}}^{**}(D, \mathbf{c}_p)\, \mathrm{d}\mathbf{c}_p \mathrm{d}D \\
&= \iint D^k \breve{\mathbf{u}}(D) \breve{\breve{f}}^{**}(D, \mathbf{c}_p; \mathbf{x}, t)\, \mathrm{d}\mathbf{c}_p \mathrm{d}D \\
&\qquad + \iint D^k \breve{\mathbf{u}}'(D, \mathbf{c}_p; \mathbf{x}, t) \breve{\breve{f}}^{**}(D, \mathbf{c}_p)\, \mathrm{d}\mathbf{c}_p \mathrm{d}D \\
&\qquad + \iint D^k \breve{\mathbf{u}}'^{(n)}(D, \mathbf{c}_p; \mathbf{x}, t, \mathcal{H}_p) \breve{\breve{f}}^{**}(D, \mathbf{c}_p)\, \mathrm{d}\mathbf{c}_p \mathrm{d}D \\
&= \int D^k \breve{\mathbf{u}}(D) \breve{\breve{f}}^{*}(D)\, \mathrm{d}D \\
&\overset{\text{def.}}{=} \breve{M}^{(k)} \breve{\mathbf{u}}^{(k)} \,.
\end{aligned}
\tag{A.51}
$$

Both integrals containing a linear term in particle velocity fluctuation become zero. In the first term, the fluctuation refers to a spacial average of mean values, i.e. the fluctuation is constructed such that its integration becomes zero when using the "mean values" as weighting. If we replace the "mean values" by their individual multitude of sample values, i.e. $\breve{\breve{f}}^{**}(D, \mathbf{c}_p)$ instead of $\bar{f}^{**}(D, \mathbf{c}_p)$, the weighting remains the same. The second contribution becomes zero, because as soon as a each local sample of residual components becomes zero (see Eqn. A.47) also the spacial "sample" of all local samples becomes zero by integration. With that we can drop the first order contributions of fluctuations in the non-linear term as well, and keeping only the (co)variances of the velocity fluctuations.

$$
\begin{aligned}
&\iiint D^k \mathbf{c}_p \mathbf{c}_p \breve{\breve{f}}(D, \mathbf{c}_p, \zeta_p)\, \mathrm{d}\zeta_p \mathrm{d}\mathbf{c}_p \mathrm{d}D \\
&= \iiint D^k \mathbf{c}_p \mathbf{c}_p \breve{\breve{f}}^{**}(D, \mathbf{c}_p) \delta(\zeta_p - T_d)\, \mathrm{d}\zeta_p \mathrm{d}\mathbf{c}_p \mathrm{d}D \\
&= \iint D^k \left[\underbrace{\breve{\mathbf{u}}(D; \mathbf{x}, t) + \breve{\mathbf{u}}'(D, \mathbf{c}_p; \mathbf{x}, t) + \breve{\mathbf{u}}'^{(n)}(D, \mathbf{c}_p; \mathbf{x}, t, \mathcal{H}_p)}_{=\mathbf{c}_p} \right]^2 \breve{\breve{f}}^{**}(D, \mathbf{c}_p)\, \mathrm{d}\mathbf{c}_p \mathrm{d}D
\end{aligned}
$$

$$
\begin{aligned}
&= \iint D^k \breve{\mathbf{u}}(D)\breve{\mathbf{u}}(D)\breve{\breve{f}}^{**}(D,\mathbf{c}_p)\,\mathrm{d}\mathbf{c}_p\mathrm{d}D \\
&\quad + \underbrace{\iint D^k \breve{\breve{f}}^{**}(D,\mathbf{c}_p)\breve{\mathbf{u}}'^{(n)}(D,\mathbf{c}_p)\breve{\mathbf{u}}'^{(n)}(D,\mathbf{c}_p)\,\mathrm{d}\mathbf{c}_p\mathrm{d}D}_{\equiv \int D^k \delta\mathbf{B}\mathbf{B}_d(D)\breve{\breve{f}}^{*}(D)\,\mathrm{d}D} \\
&\quad + \underbrace{\iint D^k \breve{\breve{f}}^{**}(D,\mathbf{c}_p)\breve{\mathbf{u}}'^{(n)}(D,\mathbf{c}_p)\breve{\mathbf{u}}'^{(n)}(D,\mathbf{c}_p)\,\mathrm{d}\mathbf{c}_p\mathrm{d}D}_{\equiv \int D^k \delta\mathbf{C}\mathbf{C}_d(D)\breve{\breve{f}}^{*}(D)\,\mathrm{d}D} \\
&\quad + \underbrace{\iint D^k \breve{\breve{f}}^{**}(D,\mathbf{c}_p)\breve{\mathbf{u}}'^{(n)}(D,\mathbf{c}_p)\breve{\mathbf{u}}'^{(n)}(D,\mathbf{c}_p)\,\mathrm{d}\mathbf{c}_p\mathrm{d}D}_{\equiv \int D^k \delta\mathbf{B}\mathbf{C}_d(D)\breve{\breve{f}}^{*}(D)\,\mathrm{d}D} \\
&\overset{\text{def.}}{=} M^{(k)}\breve{\mathbf{u}}^{(k)}\breve{\mathbf{u}}^{(k)} + \int D^k \breve{\mathbf{u}}''\breve{\mathbf{u}}''\breve{\breve{f}}^{*}(D)\,\mathrm{d}D \\
&\quad + \int D^k(\delta\mathbf{B}\mathbf{B}_d(D) + \delta\mathbf{C}\mathbf{C}_d(D) + \delta\mathbf{B}\mathbf{C}_d(D))\breve{\breve{f}}^{*}(D)\,\mathrm{d}D\,. \qquad \text{(A.52)}
\end{aligned}
$$

where the notation for the moment velocity splitting is $\breve{\mathbf{u}}(D;\mathbf{x},t) = \breve{\mathbf{u}}^{(k)}(\mathbf{x},t) + \breve{\mathbf{u}}''(D;\mathbf{x},t)$, which slightly differs from the two case shown before. $\delta\mathbf{B}\mathbf{B}_d(D)$ is the spatial co-variance tensor of the mesoscopic Eulerian velocity field, $\delta\mathbf{C}\mathbf{C}_d(D)$ can be interpreted as the filtered, size dependent RUV tensor and the co-variance $\delta\mathbf{B}\mathbf{C}_d(D)$ eludes a proper interpretation so far. The generic naming scheme prevent misleading or inaccurate comparison with variables presented elsewhere in literature. Actually, however, $\delta\mathbf{C}\mathbf{C}_d(D)$ can be compared by trace and deviatoric parts to $\widehat{\delta\theta_d}$ and $\widehat{\delta\mathbf{R}_d}^*$ given in Riber et al. (2006), respectively, where it is simply modelled by replacing non-filtered quantities by filtered ones in the underlying models by Kaufmann et al. (2004).

Application of these operations to the time derivative and convective term of Eqn. 3.70 is straight forward since this is already shown above, actually. The source terms are not examined here, since the unknown correlations $\delta\mathbf{B}\mathbf{B}_d(D)$, $\delta\mathbf{C}\mathbf{C}_d(D)$, $\delta\mathbf{B}\mathbf{C}_d(D)$ are not considered in the simula-

tions shown in this work at all. The challenging closure for these must be left to be accomplished in future work.

A.2.4 Polydisperse RUM Formalism

In most publications, the Random Uncorrelated Velocity tensor is conditioned on size space (except Mossa, 2005). Here, we formulate the idea of considering the size space and formulate a size space averaged version of the tensor. The dependency of the Random Uncorrelated Velocity tensor reads

$$\delta R^*_{p,ij}(D) = \delta R_{p,ij}(D) - \frac{2}{3}\delta\theta_d(D)\delta_{ij} \ , \tag{A.53}$$

where

$\delta R_{p,ij}(D)$ is the polydisperse RUV tensor ,

$\delta\theta_d(D)$ is the Random Uncorrelated Energy, i.e. half the trace of $\delta R_{p,ij}(D)$,

$\delta R^*_{p,ij}(D)$ is the deviatoric part of $\delta R_{p,ij}(D)$.

For $\delta\theta_d(D)$ a transport equation is solved, in which the triple correlation $\delta S_{p,iij}(D)$ occurs. Closure could be obtained based on the proposed models as

$$\delta R^*_{p,ij}(D) = -\nu_{\mathrm{RUV}}(D)\left(\frac{\partial u_{p,i}(D)}{\partial x_j} + \frac{\partial u_{p,j}(D)}{\partial x_i} - \frac{\partial u_{p,k}(D)}{\partial x_k}\frac{\delta_{ij}}{3}\right) \ , \tag{A.54}$$

$$\delta S_{p,iij}(D) = -\kappa_{\mathrm{RUV}}(D)\frac{\partial\delta\theta_d(D)}{\partial x_j} \tag{A.55}$$

and

$$\nu_{\mathrm{RUV}}(D) = \frac{\tau_d(D)}{3}\delta\theta_d(D) \ , \tag{A.56}$$

$$\kappa_{\mathrm{RUV}}(D) = \frac{20}{27}\tau_d(D)\delta\theta_d(D) \ . \tag{A.57}$$

Integration over the diameter spectrum yields averaged terms for the corresponding moment flux transport equations implying the random uncorrelated motion of particles weighted by powers of the particle diameter. Since the uncorrelated particle velocity increases with larger particles,

this effect could be considered somehow in the relaxation approach to determine the moment transport velocities $u^{(k)}$. These steps must be left for future work.

A.2.5 Moment Integration Correlations for the Source Terms (The Time and Convective Terms are shown in Chapter 4)

Stokes Drag Closure Problem in Volume Average Based Two-Phase Equations

Instead of using moments about zero, expressing the Stokes drag term by a decomposition into mean and residual component (i.e. central moments) for both, particle size and velocity, one obtain (here again considering fluctuations in the gas phase to be in line with the general case)

$$\begin{aligned}
&\iiint 18\bar{\nu}\bar{\rho}D(\tilde{\mathbf{u}}+\mathbf{u}''-\mathbf{c}_p)\bar{f}(\boldsymbol{\mathcal{I}})\,\mathrm{d}\boldsymbol{\mathcal{I}} \\
&\quad= \iiint 18\bar{\nu}\bar{\rho}(D_{10}+D')(\tilde{\mathbf{u}}+\mathbf{u}''-(\mathbf{u}(D)+\mathbf{u}'(D))\bar{f}(\boldsymbol{\mathcal{I}})\,\mathrm{d}\boldsymbol{\mathcal{I}} \\
&\quad= 18\bar{\nu}\bar{\rho}D_{10}(\tilde{\mathbf{u}}-\mathbf{u}(D)) + \iiint 18\bar{\nu}\bar{\rho}D'(\mathbf{u}''-\mathbf{u}'(D))\bar{f}(\boldsymbol{\mathcal{I}})\,\mathrm{d}\boldsymbol{\mathcal{I}}\,.
\end{aligned} \tag{A.58}$$

The last expression on the rhs is similar to those obtained from volume average based two-phase equations. In RANS context, Burns et al. (2004) give an overview of available models proposed for closure of the non-resolved volume fraction/velocity correlations.

Non-Stokes Drag Closure Problem

Including both, ensemble average and spatial filtering, as well as the moment transport velocity splitting ($\bar{\mathbf{u}}(D;\mathbf{x},t) = \bar{\mathbf{u}}^{(k)}(\mathbf{x},t) + \bar{\mathbf{u}}'(D;\mathbf{x},t)$) by inserting the decomposition

$$\mathbf{c}_p = \breve{\mathbf{u}}(D;\mathbf{x},t) + \breve{\mathbf{u}}'(D,\mathbf{c}_p;\mathbf{x},t) + \breve{\mathbf{u}}'^{(n)}(D,\mathbf{c}_p;\mathbf{x},t,\mathcal{H}_p) \tag{A.59}$$

into

$$\iiint 18\bar{\nu}\bar{\rho}0.15\left(\frac{|\tilde{\mathbf{u}}-\mathbf{c}_p|}{\bar{\nu}}\right)^{0.687}(\tilde{\mathbf{u}}-\mathbf{c}_p)D^{1.687}\bar{f}(\boldsymbol{\mathcal{I}})\,\mathrm{d}\boldsymbol{\mathcal{I}}=\ldots\,, \tag{A.60}$$

directly shows the problem of such an attempt to derive and model all components individually.

A.3 Appendix to Chapter 5

A.3.1 Parts of Section 5.3.2

Reformulation of SDC Mass Rate to the D^2 Format (Eqn. 5.14)

$$\dot{m}=\frac{2\pi\lambda(T_f-T_s)D}{\left(1-\frac{ln(1+\nu Y_{\mathrm{ox},\infty})}{ln(1+\mathrm{B_M})}\right)\left[c_{\mathrm{p}l}(T_s-T_p)+\Delta H_v+c_{\mathrm{p}v}(T_f-T_s)\right]} \tag{A.61}$$

Formulated as a D^2-like law (with neglecting $D/D_{\mathrm{flame}}\ll 1$), it gives

$$\begin{aligned}\frac{dD^2}{dt}&=-\frac{8\lambda}{\rho_p}\frac{(T_f-T_s)}{c_{\mathrm{p}l}(T_s-T_p)+\Delta h_v+c_{\mathrm{p}v}(T_f-T_s)}\\&=-\frac{8\lambda}{\rho_p c_{\mathrm{p}v}}\frac{c_{\mathrm{p}v}(T_f-T_s)}{c_{\mathrm{p}l}(T_s-T_p)+\Delta h_v+c_{\mathrm{p}v}(T_f-T_s)}\\&=-\frac{8\lambda}{\rho_p c_{\mathrm{p}v}}\frac{\frac{c_{\mathrm{p}v}(T_f-T_s)}{c_{\mathrm{p}l}(T_s-T_p)+\Delta h_v}}{1+\frac{c_{\mathrm{p}v}(T_f-T_s)}{c_{\mathrm{p}l}(T_s-T_p)+\Delta h_v}}\\&=-\frac{8\lambda}{\rho_p c_{\mathrm{p}v}}\frac{\mathrm{B_T}}{1+\mathrm{B_T}}=-K\,.\end{aligned} \tag{A.62}$$

Comparison with a Typical Vaporisation Rate

In order to proof the similarity of the mass flow rate $\dot{m}_v$ with those of pure vaporisation, we compare it with the vaporisation rate given by Abramzon and Sirignano (1989) and used in this work (Eqn. 3.46), which reads

for Stokes flow

$$\dot{m}_T = 2\pi \frac{\lambda}{c_{\mathrm{p}v}} D \ln(1 + \mathrm{B_T}) \tag{A.63}$$

and reformulated as D^2-law

$$\frac{dD^2}{dt} = -\frac{8\lambda}{\rho_p c_{\mathrm{p}v}} \ln(1 + \mathrm{B_T}) \,. \tag{A.64}$$

The comparable formulation of the SDC model (Eqn. A.62) reads

$$\frac{dD^2}{dt} = -\frac{8\lambda}{\rho_p c_{\mathrm{p}v}} \frac{\mathrm{B_T}}{1 + \mathrm{B_T}} \,, \tag{A.65}$$

where $\mathrm{B_T}$ is the evaporative heat transfer number defined in Eqn. 3.48. Approximating $\ln(1 + \mathrm{B_T})$ as

$$\ln(1 + \mathrm{B_T}) = \frac{\mathrm{B_T}}{1 + \frac{\mathrm{B_T}}{2}} + O() \tag{A.66}$$

shows the similarity of both expressions.

A.4 Appendix to Chapter 6

A.4.1 Phase Intensive Equations

The mass balance equation for the gas phase reads (Eqn. 3.2):

$$\frac{\partial}{\partial t}(\theta \bar{\rho}) + \nabla \cdot (\theta \bar{\rho} \tilde{\mathbf{u}}) = \Gamma \,. \tag{A.67}$$

The gas phase momentum conservation (Eqn. 3.5) becomes

$$\begin{aligned} \frac{\partial}{\partial t}(\theta \bar{\rho} \tilde{\mathbf{u}}) + \nabla \cdot (\theta \bar{\rho} \tilde{\mathbf{u}} \tilde{\mathbf{u}}) = & -\theta \nabla \bar{p} + \theta \nabla \cdot \bar{\boldsymbol{\tau}} + \nabla \cdot (\theta \boldsymbol{\tau}^t) \\ & - \mathbf{M} + \Gamma \bar{\mathbf{u}}_d \\ & + \theta \bar{\rho} \mathbf{g} \end{aligned} \tag{A.68}$$

$$\tilde{\mathbf{u}}\frac{\partial}{\partial t}(\theta\bar{\rho}) + \theta\bar{\rho}\frac{\partial\tilde{\mathbf{u}}}{\partial t} + \tilde{\mathbf{u}}\nabla\cdot(\theta\bar{\rho}\tilde{\mathbf{u}}) + \theta\bar{\rho}\tilde{\mathbf{u}}\nabla\cdot\tilde{\mathbf{u}} = -\theta\nabla\bar{p} + \theta\nabla\cdot\bar{\boldsymbol{\tau}} + \nabla\cdot(\theta\boldsymbol{\tau}^t) - \mathbf{M} + \Gamma\bar{\mathbf{u}}_d + \theta\bar{\rho}\mathbf{g} \tag{A.69}$$

$$\tilde{\mathbf{u}}\underbrace{\left(\frac{\partial}{\partial t}(\theta\bar{\rho}) + \nabla\cdot(\theta\bar{\rho}\tilde{\mathbf{u}})\right)}_{=\Gamma} + \theta\bar{\rho}\frac{\partial\tilde{\mathbf{u}}}{\partial t} + \theta\bar{\rho}\tilde{\mathbf{u}}\nabla\cdot\tilde{\mathbf{u}} = -\theta\nabla\bar{p} + \theta\nabla\cdot\bar{\boldsymbol{\tau}} + \nabla\cdot(\theta\boldsymbol{\tau}^t) - \mathbf{M} + \Gamma\bar{\mathbf{u}}_d + \theta\bar{\rho}\mathbf{g} \tag{A.70}$$

$$\theta\bar{\rho}\frac{\partial\tilde{\mathbf{u}}}{\partial t} + \theta\bar{\rho}\tilde{\mathbf{u}}\nabla\cdot\tilde{\mathbf{u}} = -\theta\nabla\bar{p} + \theta\nabla\cdot\bar{\boldsymbol{\tau}} + \nabla\cdot(\theta\boldsymbol{\tau}^t) - \mathbf{M} + \Gamma(\bar{\mathbf{u}}_d - \tilde{\mathbf{u}}) + \theta\bar{\rho}\mathbf{g} \tag{A.71}$$

$$\frac{\partial\tilde{\mathbf{u}}}{\partial t} + \tilde{\mathbf{u}}\nabla\cdot\tilde{\mathbf{u}} = -\frac{1}{\bar{\rho}}\nabla\bar{p} + \frac{1}{\bar{\rho}}\nabla\cdot\bar{\boldsymbol{\tau}} + \frac{1}{\theta\bar{\rho}}\nabla\cdot(\theta\boldsymbol{\tau}^t) - \frac{1}{\theta\bar{\rho}}\left(\mathbf{M} + \Gamma(\bar{\mathbf{u}}_d - \tilde{\mathbf{u}})\right) + \mathbf{g} \tag{A.72}$$

and the sensible enthalpy (Eqn. 3.33)

$$\frac{\partial}{\partial t}(\theta\bar{\rho}\tilde{h}) + \nabla\cdot(\theta\bar{\rho}\tilde{h}\tilde{\mathbf{u}}) + \nabla\cdot\left(\frac{\bar{\rho}\nu_{\text{eff}}}{\text{Pr}_{\text{eff}}}\nabla(\theta\bar{h})\right) = \theta\left(\frac{\partial\bar{p}}{\partial t} + \tilde{\mathbf{u}}\nabla\bar{p}\right) + \Gamma(\bar{h}_s - q_{gl}) + \sum_m\langle\rho\dot{\omega}_m\rangle^{\mathcal{VF}}Q_m \tag{A.73}$$

$$\tilde{h}\left(\frac{\partial}{\partial t}(\theta\bar{\rho}) + \nabla\cdot(\theta\bar{\rho}\tilde{\mathbf{u}})\right) + \theta\bar{\rho}\frac{\partial\tilde{h}}{\partial t} + \theta\bar{\rho}\tilde{\mathbf{u}}\nabla\tilde{h} + \nabla\cdot\left(\frac{\bar{\rho}\nu_{\text{eff}}}{\text{Pr}_{\text{eff}}}\nabla(\theta\bar{h})\right) = \theta\left(\frac{\partial\bar{p}}{\partial t} + \tilde{\mathbf{u}}\nabla\bar{p}\right) + \Gamma(\bar{h}_s - q_{gl}) + \sum_m\langle\rho\dot{\omega}_m\rangle^{\mathcal{VF}}Q_m \tag{A.74}$$

$$\theta\bar{\rho}\frac{\partial\tilde{h}}{\partial t}+\theta\bar{\rho}\tilde{\mathbf{u}}\nabla\tilde{h}+\nabla\cdot\left(\frac{\bar{\rho}\nu_{\text{eff}}}{\text{Pr}_{\text{eff}}}\nabla(\theta\bar{h})\right)$$
$$=\theta\left(\frac{\partial\bar{p}}{\partial t}+\tilde{\mathbf{u}}\nabla\bar{p}\right)+\Gamma(\bar{h}_s-\tilde{h}-q_{gl})+\sum_m\langle\rho\dot{\omega}_m\rangle^{\mathcal{V}\mathcal{F}}Q_m\,. \quad \text{(A.75)}$$

Similarly, one obtains with the help of the third moment transport equation (Eqn. 4.62),

$$\frac{\partial}{\partial t}(\rho_d M^{(3)})+\nabla\cdot(\rho_d M^{(3)}\mathbf{u}^{(3)})\,,=-\Gamma_{M^{(3)}} \quad \text{(A.76)}$$

the phase intensive formulation of the dispersed phase momentum equation (Eqn. 4.63)

$$\frac{\partial}{\partial t}(\rho_d M^{(3)}\mathbf{u}^{(3)})+\nabla\cdot(\rho_d M^{(3)}(\mathbf{u}\mathbf{u})^{(3)})=\mathbf{M}^{(3)}+\mathbf{g}M^{(3)}\rho_d-\Gamma_{M^{(3)}}\mathbf{u}^{(1)} \quad \text{(A.77)}$$

$$\mathbf{u}^{(3)}\underbrace{\left(\frac{\partial}{\partial t}(\rho_d M^{(3)})+\nabla\cdot(\rho_d M^{(3)}\mathbf{u}^{(3)})\right)}_{=-\Gamma_{M^{(3)}}}$$
$$+\rho_d M^{(3)}\frac{\partial\mathbf{u}^{(3)}}{\partial t}+\rho_d M^{(3)}\mathbf{u}^{(3)}\nabla\cdot\mathbf{u}^{(3)}=\mathbf{M}^{(3)}+\mathbf{g}M^{(3)}\rho_d-\Gamma_{M^{(3)}}\mathbf{u}^{(1)} \quad \text{(A.78)}$$

$$\rho_d M^{(3)}\frac{\partial\mathbf{u}^{(3)}}{\partial t}+\rho_d M^{(3)}\mathbf{u}^{(3)}\nabla\cdot\mathbf{u}^{(3)}=\mathbf{M}^{(3)}+\mathbf{g}M^{(3)}\rho_d-\Gamma_{M^{(3)}}(\mathbf{u}^{(1)}-\mathbf{u}^{(3)}) \quad \text{(A.79)}$$

$$\frac{\partial\mathbf{u}^{(3)}}{\partial t}+\mathbf{u}^{(3)}\nabla\cdot\mathbf{u}^{(3)}=\frac{\mathbf{M}^{(3)}}{\rho_d M^{(3)}}+\mathbf{g}-\frac{1}{\rho_d M^{(3)}}\Gamma_{M^{(3)}}(\mathbf{u}^{(1)}-\mathbf{u}^{(3)})\,, \quad \text{(A.80)}$$

implying the simplification of $(\mathbf{u}\mathbf{u})^{(3)}\approx\mathbf{u}^{(3)}\mathbf{u}^{(3)}$, and the phase intensive formulation of the dispersed phase enthalpy equation (Eqn. 4.65)

$$\frac{\partial}{\partial t}(\rho_d M^{(3)}h_d)+\nabla\cdot(\rho_d M^{(3)}\mathbf{u}^{(3)}h_d)$$
$$=-\Gamma_{M^{(3)}}\left(h_d+\Delta h_v(T_d)-c_{\text{p}v}\frac{(T-T_d)}{\bar{\text{B}}_{\text{T}}}\right) \quad \text{(A.81)}$$

$$h_d \underbrace{\left(\frac{\partial}{\partial t}(\rho_d M^{(3)}) + \nabla \cdot (\rho_d M^{(3)} \mathbf{u}^{(3)}) \right)}_{=-\Gamma_{M^{(3)}}} + \rho_d M^{(3)} \frac{\partial h_d}{\partial t} + \rho_d M^{(3)} \mathbf{u}^{(3)} \nabla h_d$$

$$= -\Gamma_{M^{(3)}} \left(h_d + \Delta h_v(T_d) - c_{\mathrm{p}v} \frac{(T - T_d)}{\bar{\mathrm{B}}_{\mathrm{T}}} \right) \quad \text{(A.82)}$$

$$\rho_d M^{(3)} \frac{\partial h_d}{\partial t} + \rho_d M^{(3)} \mathbf{u}^{(3)} \nabla h_d = -\Gamma_{M^{(3)}} \left(\Delta h_v(T_d) - c_{\mathrm{p}v} \frac{(T - T_d)}{\bar{\mathrm{B}}_{\mathrm{T}}} \right) \quad \text{(A.83)}$$

$$\frac{\partial h_d}{\partial t} + \mathbf{u}^{(3)} \nabla h_d = -\frac{1}{\rho_d M^{(3)}} \Gamma_{M^{(3)}} \left(\Delta h_v(T_d) - c_{\mathrm{p}v} \frac{(T - T_d)}{\bar{\mathrm{B}}_{\mathrm{T}}} \right) . \quad \text{(A.84)}$$

A.4.2 A Simple Example of the Use of the Conservative vs. the Phase-Intensive Formulation

With a simple but effective example, the difference between using the dispersed phase momentum equation in a conservative and phase intensive formulation will be demonstrated. A 2-dimensional jet in cross flow is considered, where the jet is laden with particles having a mass density ratio $\rho/\rho_d \approx 1000$. The cross flow is physically free of particles, but with marginal values in the numerical simulation. With that the momentum of the jet particles is much larger than that of the cross flow "particles". Hence, to determine the resulting dispersed phase velocity within a computational volume, the mass weighted average of the incoming velocities as resulting from the conservative formulation is expected to have a significant different value and direction than that of the phase intensive formulation. In the former, the jet is expected to penetrate the cross flow physically correct, whereas using the phase intensive formulation, the jet is expected to adapt its flow direction immediately towards the cross flow streamlines with a speed determined by the arithmetic mean of the incoming velocity values.

In the simple example shown, both the cross flow and the jet have a velocity of 1 m/s for both phases, the former horizontally directed, the latter vertically directed. In Fig. A.1 both cases are shown, on the left the result

using the phase intensive or non-conservative formulation, on the right that of the conservative formulation. Clearly, this is an issue to consider when solving the dispersed phase momentum equation. Its impact depends on the given case.

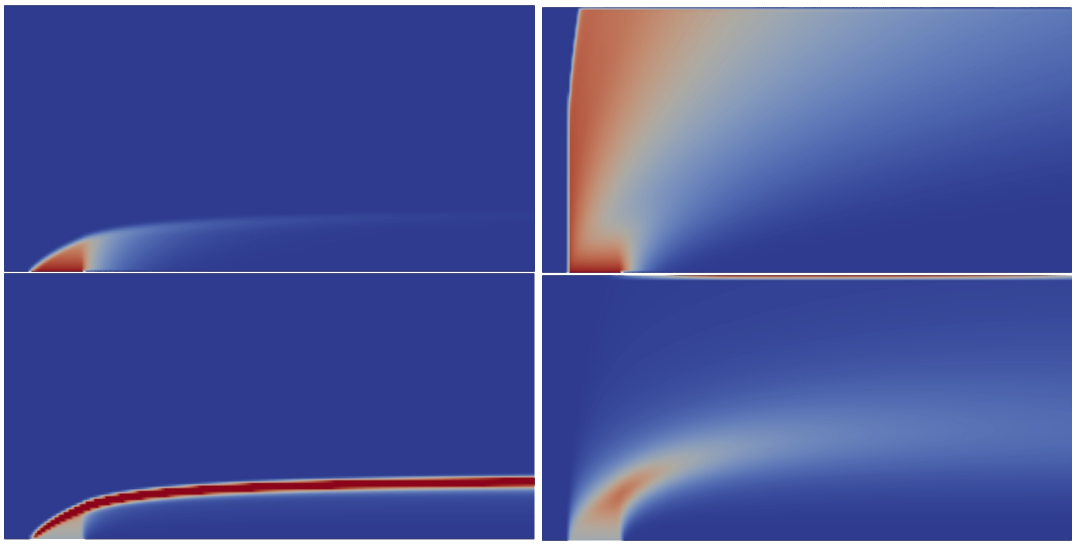

Figure A.1: Steady state contours of **Left** phase intensive based and **Right** conservative based equation formulation. **Top** Dispersed phase vertical velocity component. **Bottom** Dispersed phase volume fraction.

A.4.3 Reaction Rate Limiter

Arrhenius reaction rates are very stiff terms especially when considering only a one step, global reaction or reaction mechanisms with only a few reactions. Although the reaction rate expression provides several parameters to modify, control and adjust, the powers of the temperature and the species mass fraction does not allow this option as a practical way to ignite the flame. Especially the species mass fraction can vary very fast between many size orders down to zero, which leads in combination with the power coefficients, the time discretisation and eventually due to the missing coupling with the temperature in the chemical solver to notoriously critical values of the whole expression. In the case of the LDI

burner (see Section 7.3), it was absolutely not possible to ignite the flame without using a heat release and mass fraction change rate limiter. Hence the following limiter has been implemented and used for the simulation of the LDI burner.

Basically, the analytical, infinitely fast reaction is used when the calculated heat release is higher than the highest possible, i.e. proceed the reaction until either the present fuel (lean), oxidiser (rich) or both (stoichiometric) are zero. For those computational cells, where this criterion applies, the species mass fraction change rates and the heat release rate are artificially modified to have the whole reaction process within the current time step. The algorithm divides into the following steps:

1. Determining the maximal possible species mass fraction change rates, depending on the limiting educt species.
2. Determining the corresponding heat release via species mass fraction change rates and heat of formation.
3. Comparing this analytical heat release with the one calculated by the code. With that it can be specified for each computational cell whether the calculated or the analytical expression for species and enthalpy will be used.
4. Using, depending on this switch, the corresponding source terms for species and enthalpy transport equation.
5. When using two-step reaction mechanisms including CO, all the CO will be oxidised as long as oxidiser is available and subsequently the actual fuel in case there is still oxidiser and fuel. This, however, reduces the 2-step mechanism to a kind of 1-step mechanism in the corresponding cells.

The following expressions have been implemented for the LDI burner using the one and two step schemes for kerosene by Gokulakrishnan et al. (2013). With molar mass and mass based stoichiometric coefficients the

reactions read, respectively,

$$C_{12}H_{23} + 11.5\,O_2 = 12\,CO + 11.5\,H_2O \tag{A.85}$$
$$2\,CO + O_2 = CO_2 \tag{A.86}$$

and

$$167\,C_{12}H_{23} + 568\,O_2 = 528\,CO + 207\,H_2O \tag{A.87}$$
$$56\,CO + 32\,O_2 = 88\,CO_2\,, \tag{A.88}$$

where the molar masses are slightly approximated for simplicity.

Referring to point 1, it will be first checked whether rich or lean conditions are present in the computational cell considered. Knowing that, the species mass fraction change rate may be expressed as

$$\dot{\omega}_{O_2} = -\frac{Y_{O_2}}{\Delta t} \tag{A.89}$$
$$\dot{\omega}_{C_{12}H_{23}} = \frac{167}{568}\dot{\omega}_{O_2} \tag{A.90}$$
$$\dot{\omega}_{CO_2} = -\frac{528}{568}\dot{\omega}_{O_2} \tag{A.91}$$
$$\dot{\omega}_{H_2O} = -\frac{207}{568}\dot{\omega}_{O_2} \tag{A.92}$$

for lean conditions and as

$$\dot{\omega}_{C_{12}H_{23}} = -\frac{Y_{C_{12}H_{23}}}{\Delta t} \tag{A.93}$$
$$\dot{\omega}_{O_2} = \frac{568}{167}\dot{\omega}_{C_{12}H_{23}} \tag{A.94}$$
$$\dot{\omega}_{CO_2} = -\frac{528}{167}\dot{\omega}_{C_{12}H_{23}} \tag{A.95}$$
$$\dot{\omega}_{H_2O} = -\frac{207}{167}\dot{\omega}_{C_{12}H_{23}} \tag{A.96}$$

for rich conditions. The heat release can be determined for the one step scheme as (point 2)

$$\sum_m \rho\dot{\omega}_m Q_m = \rho(\dot{\omega}_{C_{12}H_{23}} + \dot{\omega}_{O_2})\Delta Q_c \tag{A.97}$$

with

$$\Delta Q_c = \frac{1}{735}(167 Q_{C_{12}H_{23}} + 568 Q_{O_2} + 528 Q_{CO_2} + 207 Q_{H_2O}) \tag{A.98}$$

and for the two step schemes including CO as (point 5)

$$\sum_m \rho \dot{\omega}_m Q_m = \rho(\dot{\omega}_{C_{12}H_{23}} + \dot{\omega}_{O_2}) \Delta Q_{c,C_{12}H_{23}-O_2} + \rho(\dot{\omega}_{CO} + \dot{\omega}_{O_2}) \Delta Q_{c,CO-O_2} \tag{A.99}$$

$$\sum_m \rho \dot{\omega}_m Q_m = (1 + \frac{568}{167}) \rho \dot{\omega}_{C_{12}H_{23}} \Delta Q_{c,C_{12}H_{23}-O_2} + (1 + \frac{32}{56}) \rho \dot{\omega}_{CO} \Delta Q_{c,CO-O_2} \, . \tag{A.100}$$

Since there is no mechanism included in the code to avoid extinction or blow out of the flame, sufficiently strong ignition is still required and must be taken care of.

A.4.4 Solver Structure

The main loop of the different solvers for isothermal, non-isothermal and reacting flows is structured similarly, as

```
solve(fvm::ddt(rho) + fvc::div(phi)==-Gamma_alphaD/dynTF);

// --- Pressure-velocity PIMPLE corrector loop
while (pimple.loop())
{
    #include "momsEqnGamma.H"          // Eqn. 4.62, 4.74 - 4.76 (5.7)

    #include "liftDragCoeffs.H"        // Eqn. 4.43
    #include "UdEqn.H"                 // Eqn. 4.63 (5.8)

    #include "sourceHeatEvap.H"        // Eqn. 4.51
    #include "hdEqn.H"                 // Eqn. 4.65 (5.9)

    #include "UEqn.H"                  // Eqn. 3.5 (5.5)
    #include "thickening.H"
    #include "YEqns.H"                 // Eqn. 3.19 (5.4)
    #include "hsEqn.H"                 // Eqn. 3.33 (5.6)
```

```
        // --- PISO loop
        while (pimple.correct())
        {
            #include "pEqn.H"
        }

        if (pimple.turbCorr())
        {
            turbulence->correct();
        }
    }
```

Obviously, for isothermal flows, no enthalpy, species and heat transfer equations are needed, in purely vaporising flows, the reaction is not included. The structure is naturally sequential, although a block-coupled solver, at least for the moment transport equations would be interesting to test, since the equation system of the dispersed phase is highly coupled. First theoretical attempts to rewrite the moment equations in a form which is appropriate to be used with OpenFOAM's block-coupled solver failed due to the strong (non-linear) coupling.

A.5 Appendix to Chapter 7

The discretisation used (`fvSchemes`) and the solver setup (`fvSolution`) is given next for each case. Common to all cases is `backward` time discretisation, which yielded significantly better results than `Euler` as observed in the case of Sommerfeld and Qiu (1991).

A.5.1 Sommerfeld and Qiu 1991

Discretization

```
gradSchemes
{
```

```
    default                         Gauss linear;
}

divSchemes
{
    default                         none;
    div(phi,U)                      Gauss filteredLinear2V 0.2 0;
    div(phi,h)                      Gauss filteredLinear2 0.2 0;
    div(phiU,p)                     Gauss limitedLinear 1;
    div((muEff*dev2(T(grad(U)))))   Gauss linear;

    div(phid,Ud)                    Gauss upwind;
    div(phid,m0)                    Gauss upwind;
    div(phid,m1)                    Gauss upwind;
    div(phid,m2)                    Gauss upwind;
    div(phi,alphaD)                 Gauss upwind;
}

laplacianSchemes
{
    default                         linear corrected;
}

interpolationSchemes
{
    default                         linear;
}
```

The entries `snGradSchemes` and `fluxRequired` are standard in every case.

Solver Setup

The solver setup is identical for all cases, with

```
"(p|rho)"
{
    solver                      PCG;
    preconditioner              DIC;
    tolerance                   1e-6;
    relTol                      0;
}
```

```
"(p|rho)Final"
{
    $p;
    relTol                      0;
}

  .
  .
  .

All other variables, with different tolerances:

    solver                      PBiCG;
    preconditioner              DILU;

  .
  .
  .

PIMPLE
{
    momentumPredictor           yes;
    nOuterCorrectors            2;
    nCorrectors                 2;
    nNonOrthogonalCorrectors    0;
    nAlphaCorr                  2;
    correctAlpha                yes;
    rhoMin                      rhoMin [ 1 -3 0 0 0 ] 0.1;
    rhoMax                      rhoMax [ 1 -3 0 0 0 ] 2.0;
}
```

A.5.2 Sydney Spray Burner/LDI Burner

The discretisation for the non-isothermal, vaporising and reacting cases is practically equal. The discretisation of the dispersed phase shows some "inconsistencies", e.g. the particle enthalpy could/should be discretised with `upwind` as well, which might slightly affect the solution. The `harmonic` interpolation was used sometime to try it for stabilising the simulation. Whether it makes a difference at the final version of the code has not been tested.

Discretisation

```
gradSchemes
{
    default                         Gauss linear;
    grad(Ud)                        cellLimited leastSquares 1.0;
}

divSchemes
{
    default                         none;
    div(phi,U)                      Gauss filteredLinear2V 0.2 0;
    div(phi,h)                      Gauss filteredLinear2 0.2 0;
    div(phiU,p)                     Gauss linear;
    div((muEff*dev2(T(grad(U)))))  Gauss linear;

    div(phi,alphaD)                 Gauss upwind;
    div(phid,m0)                    Gauss upwind;
    div(phid,m1)                    Gauss upwind;
    div(phid,m2)                    Gauss upwind;
    div(phi,Yv)                     Gauss vanLeer01; // for vaporisation
    div(phi,Yi_h)                   Gauss limitedLinear01 1.; // for combustion
    div(phid,Ud)                    Gauss upwind;
    div(phid,hd)                    Gauss filteredLinear2 0.2 0;
}

laplacianSchemes
{
    default                         Gauss linear corrected;
}

interpolationSchemes
{
    default                         linear;
    interpolate(alphaD)             harmonic;
    interpolate(m0)                 harmonic;
    interpolate(m1)                 harmonic;
    interpolate(m2)                 harmonic;
    interpolate(m3)                 harmonic;
    interpolate(m4)                 harmonic;
    interpolate(m5)                 harmonic;
    interpolate(m1687)              harmonic;
    interpolate(m3687)              harmonic;
    interpolate(h)                  harmonic;
}
```